

Interactions of Gold Plasmons and Vanadium Dioxide

By

Christina Lynn McGahan

Dissertation

Submitted to the Faculty of the
Graduate School of Vanderbilt University
in partial fulfillment of the requirements
for the degree of

DOCTOR OF PHILOSOPHY

in

Physics

May, 2017

Nashville, Tennessee

Approved:

Richard F. Haglund, Ph.D.

David E. Cliffler, Ph.D.

Jason G. Valentine, Ph.D.

Kalman Varga, Ph.D.

Yaqiong Xu, Ph.D.

© Copyright by Christina McGahan 2017
All Rights Reserved

ACKNOWLEDGEMENTS

This would not have been possible without the help and support of many people. First, I would like to thank the Department of Physics and The Vanderbilt Institute of Nanoscale Science and Engineering (VINSE) for their support and resources. I would like to specifically thank Tony Hmelo, Ben Schmidt, Kurt Heinrich, and Bo Choi, for their willingness to share their fabrication and characterization expertise. I am grateful for the time, and guidance provided by my committee members - Professors. David Cliffler, Jason Valentine, Kalman Varga, Yaqiong Xu, and Rizia Bardhan. I would like to thank my collaborators on this work - Dr. Yohannes Abate, Sampath Gamage, Dr. Laura Na Liu, Dr. Song Yue, and Dr. Fangfang Wen. Without them, my work on the phase coexistence of single crystals and on hydrogen doping of vanadium dioxide would not have been possible. This work was funded primarily by the United States Department of Energy (DE-FG02-01ER454916).

I would like to thank the other members of the Haglund Lab, both past and present. I am grateful to have you as friends and colleagues. I would like to specifically thank Kent Hallman for helping me to understand VO₂; Claire Marvinney for being willing to let me bounce ideas about plasmonics and beyond off of her; Zhihua Zhu for her help with electron beam lithography and process development; Kristin Engerer for the discussions about novel nanoscale materials and inventive fabrication methods; Dr. Bob Marvel for his guidance and willingness to answer my questions about vanadium dioxide; and Dr. Dan Mayo for telling me that this would be hard but that I would get through it and to just start going. I would like to acknowledge Nick Beier, for being my partner in exploring the magical mystical land of vanadium dioxide and plasmonics as well as being an excellent undergraduate researcher.

I would like to thank my family for their support. I would also like to thank Bill Smith for helping me stay sane and supporting me through this process of getting a Ph.D. The proofreading and digitizing of data were also immensely appreciated.

Finally, I would like to thank my advisor, Professor Richard Haglund, for believing in me and encouraging me when I was having doubts.

TABLE OF CONTENTS

	Page
ACKNOWLEDGEMENTS	iii
LIST OF TABLES.....	viii
LIST OF FIGURES	ix
1. INTRODUCTION	1
1.1. Introduction.....	1
1.2. Plasmonics	3
1.2.1. Brief Introduction to Plasmonics	3
1.2.2. Physics of the Localized Surface Plasmon Resonance	4
1.2.3. Influence of Nanoparticle Material on Plasmon Resonance.....	5
1.2.4. Influence of Nanoparticle Size on Plasmon Resonance	6
1.2.5. Influence of Nanoparticle Shape on Plasmon Resonance.....	7
1.2.6. Influence of the Local Dielectric Environment of the Nanoparticle on the Plasmon Resonance	8
1.2.7. Plasmon Mode Hybridization	10
1.2.8. How Plasmon Resonance is Altered in an Array.....	14
1.2.9. Uses of Plasmons	15
1.2.10. A Limitation of Metal Plasmonics	16
1.3. Phase-Change Materials	16
1.3.1. Phase-Change Materials and Their Applications.....	16
1.3.2. Advantages of VO ₂ as a Phase-Transition Material	18
1.3.3. Inducing the VO ₂ PT.....	19
1.3.4. Details of the VO ₂ PT	19
1.3.5. Influence of VO ₂ Fabrication on Material Properties.....	23

1.4. Active Plasmonics	25
1.4.1. Motivation for Combining a LSPR and a Phase-Change Material.....	25
1.4.2. Benefits of Combining VO ₂ and Au Plasmonic Particles.....	26
1.5. Structure of Dissertation	26
2. FABRICATION AND CHARACTERIZATION OF AU-VO ₂ NANOSTRUCTURES	28
2.1. Introduction.....	28
2.2. Sample Design	29
2.3. Basic Sample Fabrication	31
2.3.1. Substrate Details	31
2.3.2. Cleaning Substrates.....	32
2.3.3. VO ₂ Thin Film Deposition Mechanisms	32
2.3.4. Annealing Samples	33
2.3.5. VO ₂ Single Crystal Growth.....	34
2.3.6. Spin-coating Resist onto Samples.....	35
2.3.7. Electron Beam Lithography	35
2.3.8. Development	36
2.3.9. Gold Deposition	36
2.3.10. Liftoff	37
2.4. Sample Characterization	37
2.4.1. Scanning Electron Microscopy	37
2.4.2. Atomic Force Microscopy	38
2.4.3. Temperature-Dependent Transmission Setup.....	38
2.4.4. Small Spot-Size Spectroscopy Setup	41
2.5. Contributed Fabrication Developments.....	43
2.5.1. Non-scattering VO ₂ thin films	43
2.5.2. EBL on VO ₂ Single Crystals.....	46
2.5.3. Stacked-Structure Fabrication.....	50

2.5.3.1.	Introduction	50
2.5.3.2.	Fabrication Process and Rationale	53
2.5.4.	Significance of Contributed Fabrication Developments.....	60
3.	VO ₂ SINGLE CRYSTAL PHASE COEXISTENCE.....	62
3.1.	Introduction.....	62
3.2.	Background.....	63
3.3.	Materials and Methods	65
3.4.	Results and Discussion	69
3.4.1.	Phase Coexistence in High-Aspect-Ratio Single Crystals.....	69
3.4.2.	Phase Coexistence in Low-Aspect-Ratio Single Crystals	70
3.4.3.	Verification that Plasmonic Particles are Resonant with Excitation Source ..	75
3.4.4.	Depth Dependence of Phase Coexistence.....	76
3.4.5.	Simulated Influence of Plasmon Resonance on VO ₂	79
3.5.	Conclusions and Outlook.....	81
4.	HYDROGEN DOPING OF VO ₂ PROBED VIA PLASMONIC PARTICLES	84
4.1.	Introduction.....	84
4.2.	Background.....	85
4.3.	Sample Fabrication	89
4.4.	Experimental Setup and Measurements.....	90
4.5.	Thermal Hysteresis Data and Analysis.....	91
4.5.1.	Thermal Hysteresis Background.....	91
4.5.2.	Thermal Hysteresis Fits to Data and Analysis	94
4.6.	Dynamics Data and Analysis.....	99
4.7.	Integrating Thermal and Dynamics Results	109
4.8.	Conclusions and Outlook.....	110
5.	ACTIVE PIT IN STACKED AU-VO ₂ DOLMENS.....	111
5.1.	Introduction.....	111

5.2. Theory.....	112
5.2.1. Bright and Dark Plasmon Modes	112
5.2.2. What is Plasmon-Induced Transparency?.....	113
5.2.3. Sample Design Logic	118
5.3. Simulations	121
5.3.1. Simulation Overview	121
5.3.2. Effect of VO ₂ Thickness	122
5.3.3. Effect of Dipole-Quadrupole Gap G.....	124
5.3.4. Effect of the Pitch of the Array.....	127
5.4. Proof-of-Principle Fabrication and Characterization of Structures	129
5.5. Conclusions and Outlook.....	134
6. CONCLUSIONS AND OUTLOOK.....	137
APPENDICES	144
A Useful Lumerical Scripts	144
A.1. Parameter Sweep using Scripting.....	144
A.2. Script to run Multiple Simulations in a Row.....	145
A.3. Exporting Data from a Monitor.....	145
B Detailed Process for Single Crystal Growth	147
C Detailed Process for Writing Nanoparticles on VO ₂ Single Crystals	150
D Details of the Plasmon-Resonance Hysteresis	156
E Contributions to the Understanding of VO ₂ Not Discussed in this Dissertation.....	159
F Sensing Depth for LSPR in with Resonance in the Near-IR Wavelength Range	162
BIBLIOGRAPHY	164

LIST OF TABLES

Table	Page
1.1 Shifts in the T_c of VO ₂ with different dopants. Table redrawn from Ref. [54].....	25
4.1 Details of the samples and parameters used for hydrogen dynamics studies.	103
5.1 In-plane dimensions and pitch for stacked Au-VO ₂ dolmen nanostructures in the simulations discussed in Section 5.4. These dimensions are applicable unless it is specifically stated otherwise in one of the following simulations.	122
5.2 Maximum change in simulated transmission over the VO ₂ phase transition for Au dolmens topped with VO ₂ dolmens of varying thicknesses.....	123
5.3 Ratio of maximum local electric field values for I and M VO ₂ for Au-VO ₂ dolmens with varying values of G , the dipole-quadrupole gap.....	126
5.4 Maximum change in simulated transmission over the VO ₂ phase transition for Au-VO ₂ dolmens with varying values of G , the dipole-quadrupole gap.	126
5.5 Maximum change in simulated transmission over the VO ₂ phase transition for Au-VO ₂ dolmens with varying pitches.	128
5.6 Ratio of maximum local electric field values for I and M VO ₂ for Au-VO ₂ dolmens with varying pitches.....	129

LIST OF FIGURES

Figure	Page
1.1 Stained glass window from the Cathédrale Notre-Dame de Paris made in the 13 th century. Reproduced from Ref. [2].	3
1.2 Glass cup from 4 th century Rome, called the Lycurgus Cup. Illumination from the outside (a) produces a green color, but illumination from the inside (b) produces a red color. Reproduced from Ref. [1].	3
1.3 Simulated transmission for 100 nm long, 20 nm wide, and 20 nm thick nanorods comprised of a variety of noble metals in air. Electric field polarized parallel to long axis of rods.	6
1.4 Measured extinction for 20 nm thick Au nanodisks with increasing diameter. Figure from Ref. [15].	7
1.5 Simulated transmission for 20 nm thick and 20 nm wide Au nanorod in air with increasing length. Electric field polarized parallel to long axis of rods.	7
1.6 Simulated transmission for 20 nm thick and 120 nm long Au nanorod in air with decreasing width. Electric field polarized parallel to long axis of rods.	7
1.7 Simulated transmission for 120 nm long and 20 nm wide Au nanorod in air with decreasing thickness. Electric field polarized parallel to long axis of rods.	7
1.8 Simulated transmission for an Au rod, triangle, and disk all in air and resonant within a 10 nm range.	8
1.9 Schematic indicating direction of electric field for the Au disk, rod, and triangle simulations.	8
1.10 Simulated local electric field intensity at resonance corresponding to the transmission spectra above.	8
1.11 Simulated transmission for a 100 nm long, 60 nm wide, and 40 nm thick Au nanorod embedded in a variety of dielectric environments. Electric field polarized parallel to long axis of rods.	10
1.12 Calculated absorption efficiencies for 25 nm radius Au spheres as a function of ϵ_m'' of the dielectric environment for two constant real parts of the dielectric function (ϵ_m') of the environment. The values of ϵ_m'' used are as follows: 0, 1, 2, 3, 5, 10. Figure reproduced from Ref. [12].	10

1.13	Energy level diagram for a metal nanoshell showing the hybridized plasmon resonances showing the hybridized plasmon resonances, which can be described as the interaction of metal nanosphere and nanocavity plasmon resonances. This interaction creates a bonding (ω^-) and antibonding (ω^+) plasmon resonance. Figure reproduced from Ref. [19].	11
1.14	Plasmon mode hybridization diagram for an Au nanorod dimer formed from two non-identical nanorods. The simulated transmission for the short (blue) and long (green) nanorods, and the dimer bonding mode, indicated in purple, are shown. The nanorod and dimer plasmon modes are identified via the simulated local electric field maps at the resonant wavelengths of the dimer and nanorod as determined using the simulated transmission. The nanorods are 70 nm wide and 35 nm thick, and the nanorod dimer has a 20 nm gap. The lengths of the nanorods are 150 nm and 210 nm.	13
1.15	Simulated transmission spectra for Au nanorod (348 nm long, 129 nm wide, 60 nm thick) on glass as a function of pitch. Spectra are offset by 0.4 for clarity. Electric field polarized parallel to long axis of rods.	15
1.16	SEM of Si ring resonator with VO ₂ patch (false color) atop a section of the ring and measured transmission through the waveguide above and below the VO ₂ phase transition. Figure reproduced from Ref. [43].	18
1.17	Thermally controlled micro grabber, showing grabbing below the PT and releasing above the phase transition. Scale bar is 50 μm . Figure reproduced from Ref. [48].	18
1.18	Sensitivity of Pd-decorated VO ₂ nanowires to hydrogen gas probed through a change in current when gas is flowing. Inset shows change in current when CO gas flow is cycled on and off. Figure reproduced from Ref. [51].	18
1.19	Band structure of insulating and metallic VO ₂ . Figure reproduced from Ref. [69].	20
1.20	Crystal structure of M1 and R VO ₂ . Figure reproduced from Ref. [37].	20
1.21	Refractive index of VO ₂ in the visible to near-IR region for both M and I VO ₂ . Data were obtained using ellipsometry on an electron beam-deposited VO ₂ thin film courtesy of Sam White and Kent Hallman.	21
1.22	Refractive index of VO ₂ in the near-IR region for both M and I VO ₂ . Data were obtained using ellipsometry on a VO ₂ thin film measured by Stuart Earl and deposited by Dr. Bob Marvel.	21
1.23	Diagram indicating showing the physical definition for the switching contrast and critical temperature. The critical temperature is defined as the average temperature between the two sigmoids where the transmission is half of its maximum value.	22

1.24	Temperature-dependent transmission of a 52 nm RF-M sputtered VO ₂ thin film on glass. Data were obtained using both a 1550 nm laser and a broadband white-light source with emission between 400 and 1000 nm. The critical temperature is the same for the two curves, but the switching contrast is much higher for the data taken using the 1550 nm laser.	22
1.25	Resistivity of 52 nm RF sputtered VO ₂ thin film on glass. Data were obtained using a four point probe setup.	22
1.26	Raman spectra on a VO ₂ single crystal grown on Si as described in Chapter 2, both above (red) and below (blue) the SPT. Figure courtesy of Kent Hallman.	22
1.27	Atomic force microscopy (AFM) scans of VO ₂ thin films grown by (A) pulsed lased deposition on glass, (C) electron beam evaporation on c-cut sapphire, and (E) radio frequency magnetron sputter on silicon. AFM data have a 5 μm by 5 μm scan size. Figure reproduced from Ref. [79].	24
1.28	Shifts in the T_c and insulating crystal phase of VO ₂ with high (red) and low (blue) valence dopants. Figure reproduced from Ref. [53].	25
2.1	Optical microscopy of typical VO ₂ single crystals grown on quartz and Si. Photolithographically patterned cross markers are 30 μm by 30 μm.	34
2.2	Picture of the temperature-dependent transmission setup.	39
2.3	Image of the small spot size spectroscopy setup with relevant components labeled.	42
2.4	Dark-field scattering of Au dimers embedded in PLD VO ₂ films which are 110 nm thick and on Si, 100 nm thick and on ITO-glass, and 50 nm thick and on ITO-glass. The fourth scattering image shows Au dimers covered with low-scattering VO ₂ . This is included as a reference image, so that the locations of the Au dimers in the other images are known and it is evident what the dimers would look like if their scattering is visible. For the 110 nm VO ₂ thin film, scattering from the dimers is barely visible. For the 100 and 50 nm films, scattering from the dimers is completely hidden by scattering from the VO ₂ thin films.	44
2.5	Dark-field scattering of Au dimers embedded in EBE VO ₂ films which are 105 nm Thick (left) and 106 nm thick (center and right) with a slightly different Au dimer EBL pattern on ITO-coated glass. The left and center films were annealed for 10 minutes and the right film was annealed for 5 minutes. The scattering from the Au dimers is clearly visible (left), not visible (center), and somewhat visible (right).	45

2.6	Dark-field scattering of Au dimers embedded in RF-M sputtering VO ₂ films which are 100 nm thick (left), 108 nm thick (center), and 93 nm thick (right). The scattering from individual Au dimers can be clearly seen in all three of the images.....	46
2.7	Photolithographically patterned Cr alignment markers. Crosses are located every 200 μm, with number and letter labels indicating every other cross.	48
2.8	Schematic of development used when patterning nanoparticles on top of individual single crystals.....	50
2.9	Simulated transmission for Au disks (radius 90 nm thickness 40 nm) without VO ₂ , on 40 nm thick VO ₂ films (solid lines), and on 40 nm thick VO ₂ disks (radius 90 nm). Insulating (blue) and metallic (red) VO ₂ are simulated. Figure reproduced from Ref. [109].	51
2.10	Simulated and experimental resonance shifts for VO ₂ -Au stacked disk fabricated with one step of EBL as a function of the disk diameters. There is poor agreement below 150 nm diameter disks. Data are extracted from Ref. [110].	52
2.11	(a) Tilted SEM of Pacman particles showing Au nanoparticles and underlying VO ₂ nanoparticles of a larger diameter. (b) Tilted SEM of edge of nanoparticle array, showing “Pacman-type” nanostructures. (c) Simulated (dashed curves) and experimental (solid curves) transmission response of nanostructures; blue (red) curves indicate response with insulating (metallic) VO ₂	55
2.12	Images of the (a) flat and (b) tilted sample holders. The blue rectangles represent the locations of samples during the RF-M sputter depositions. The top images show the holders with the side being deposited on facing up. A side image of provided in (b) to show the angle of the tilted holder. The bottom images show the sample holders in place in the sputtering chamber and show the orientation of the samples with respect to the sputter gun.	56
2.13	Schematic showing the largest angles which depositing material (blue lines) can have and still reach the bottom of the EBL-patterned wells in the PMMA and deposit there to form a nanoparticle (blue). The angle of acceptance is clearly smaller for a deeper PMMA well than for the shallower well. Schematic indicating θ_{acc} is in the right panel.	57
2.14	SEMs of stacked disks and dolmens following a short liftoff procedure or a long liftoff procedure.....	58

2.15	Nano wedding cakes. On the left is an SEM of nano wedding cakes with the top Au layer (diameter 124 nm) centered on underlying VO ₂ and Au layers (diameter 197 nm). In the center are the simulated transmission spectra for metallic and insulating VO ₂ . The dimensions are those of the experimentally fabricated samples at the left. On the right is an SEM of nano wedding cakes with top Au layer (87 nm) offset from the center of the underlying VO ₂ and Au layers (diameter 158 nm).	59
2.16	Diagram showing the radius of a particle (blue) with increasing height in a two layer EBL-defined well. High molecular weight PMMA (950 PMMA) is shown in dark gray and low molecular weight PMMA (495 PMMA) is in light gray. Blue arrows show the angle of acceptance for material deposited into this well. The nanoparticle decreases in diameter as the nanoparticle thickness increases.	60
3.1	Phase coexistence patterns for VO ₂ single crystals. Perpendicular stripe pattern shown on the left and pure herringbone pattern shown on the right. All the herringbone domains form at θ from the c _R direction. Yellow domains indicate metallic VO ₂ and red domains indicated insulating VO ₂ . Arrows indicate the direction of the rutile c crystal axis of VO ₂	64
3.2	Schematic of the s-SNOM setup (a), topographic (b) and second harmonic near-field amplitude (c) images of a single crystal VO ₂ nanobeam grown on sapphire substrate recorded at temperature 50 °C and laser wavelength, $\lambda=10.7 \mu\text{m}$. Scale bar at top of (b) represents 50 nm and applies to (b) and (c). Optical amplitude image of the strained beam displays the formation of coexisting metallic (bright) and insulating (dark) domains even below the critical temperature. Figure reproduced from Ref. [128].	66
3.3	Scanning electron micrograph of VO ₂ single-crystal microbeam grown on silicon substrate. Gold nanorods were fabricated on top of the single crystal via electron beam lithography. Figure reproduced from Ref. [128].	68
3.4	Topographic (a) third harmonic near-field amplitude (b), and third harmonic phase images (c) of an individual Au nanorod resonant with the excitation laser. Amplitude and phase patterns characteristic of a dipole antenna are seen, with regions of high scattering at the rod ends in the amplitude image and a phase shift over the length of the rod. Scale bar at bottom left represents 300 nm. Figure adapted from Ref. [128]	69
3.5	Topographic (a) and second harmonic near-field amplitude images (b) of single crystal VO ₂ nanobeams with width less than 100 nm grown on sapphire substrate. Gold nanorods were fabricated on top of the single crystal via electron beam lithography. Figure reproduced from Ref. [128].	70

- 3.6 S-SNOM topography (a), second-harmonic near-field amplitude imaged at $T \sim 73^\circ\text{C}$ and recorded at laser wavelength $\lambda = 10.7 \mu\text{m}$ (b), and optical microscope (c) images of Au rods fabricated on a VO_2 microbeam grown on silicon. Scale bar at top right of (a) represents $1.5 \mu\text{m}$. Arrow in (a) indicates the direction of the c_R axis in all three figures. Regions in (b) where the metallic domain walls deviate from the herringbone structure are labelled 1, 2, 3 and 4. Large alternating regions of bright and dark rectangles in (c) are ferroelastic domains. Ferroelastic domain walls corresponding to interruptions in the herringbone structure are labelled 1, 2, 3 and 4 to match the labels in (b).72
- 3.7 Images of the Au nanorod array: (a) SEM, (b) topographic, (c) experimental second harmonic near-field amplitude, (d) FDTD simulation of electric field amplitude, (e) experimental second harmonic phase, (f) and FDTD simulated phase images of Au antennas fabricated on a VO_2 single-crystal microbeam and recorded at room temperature. (c) and (e) were recorded while excited by a laser with $\lambda = 10.7 \mu\text{m}$. Arrow in (a) indicates the direction of the c_R axis in all six figures. Figure reproduced from Ref. [128].76
- 3.8 Schematic of Au nanorod on VO_2 crystal showing the sketched s-SNOM image corresponding to a given pattern of coexisting VO_2 phases in depth as a function of increasing temperature. The plasmon dipole mode, maximum plasmon interaction depth, and s-SNOM probing depth are superimposed on the depth-dependent diagrams. Electric field is parallel to the long axis of the nanorod shown in the s-SNOM top view. One metallic domain (a) out of range of s-SNOM and plasmon field, (b) in range of s-SNOM but not plasmon field, (c) in range of both s-SNOM and plasmon field. (d)-(f) Trend toward purely metallic VO_2 progresses. Figure reproduced from Ref. [128].78
- 3.9 FEM simulations of the local electric field (V/m) in VO_2 from Au nanorod plasmon (a) scaled to visualize the characteristic dipolar electric field. The field is scaled to visualize above-threshold regions as dark red in (b). The magnitude of the local electric field is below the threshold field necessary to induce the VO_2 phase transition (b). Scale does not apply to (a).80
- 3.10 Geometry of bowtie (a) and FEM simulations of the local electric field (V/m) in VO_2 from Au bowtie plasmon (b,c). In (b) the field at the surface of the VO_2 is scaled to show the plasmonic response characteristic of a bowtie antenna. Close-ups of region in red box are shown in (c). Slices of the antenna gap electric field scaled to display above-threshold field in red are shown in (c) as a function of depth ($-z$) below the VO_2 surface. Scale only applies to (c).81
- 4.1 The crystal structure for M1, hydrogen doped M1, and R VO_2 . Blue atoms are vanadium, red atoms are oxygen, and pink atoms are hydrogen. Figure reproduced from Ref. [143].86

4.2	Schematic of the sample geometry used for hydrogenation measurements. Figure is modified from original graphic courtesy of Song Yue.	90
4.3	Schematic of experimental setup used for single particle dark-field scattering. Figure courtesy of Fangfang Wen.	91
4.4	Representative plasmon-resonance hysteresis curve. Sigmoids represent the heating (red) and cooling (blue) response. The relevant sigmoidal fit parameters for this analysis ($H-M$, $C-M$, $H-T_c$, $H-I$, and $H-S$) are overlaid on the hysteresis curve.	93
4.5	Resonant wavelength of Au dimers and monomers as a function of hydrogenation temperature when the VO_2 is fully metallic. The resonant wavelength is measured both when the sample is heated to the metallic state (left column) and when the sample is cooling but in the metallic state (right column). The resonant wavelength for metallic VO_2 is plotted after Pd deposition (grey) and after hydrogen doping (purple) for the six samples. Lines indicating the average values of $H-M$ and $C-M$ after Pd deposition (grey) and after H doping (purple) as well as shaded regions to indicate uncertainties in the average values are included.	95
4.6	Critical temperature for the heating curve ($H-T_c$) for disk dimers and disk monomers as Function of hydrogenation temperature. The critical temperature of VO_2 under heating is plotted after Pd deposition (grey) and after hydrogen doping (purple) for the five samples which exhibit heating sigmoids after hydrogenation. A line indicating the average value of $H-T_c$ after Pd deposition (grey) as well as shaded regions to indicate uncertainties in the average value are included.	96
4.7	Resonant wavelength when VO_2 is in an insulating state ($H-I$) and the sample is being heated for disk dimers and disk monomers as a function of hydrogenation temperature. The resonant wavelength for insulating VO_2 is plotted after Pd deposition (grey) and after hydrogen doping (purple) for the five samples which exhibit heating sigmoids after hydrogenation. A line indicating the average value of $H-I$ after Pd deposition (grey) as well as shaded regions to indicate uncertainties in the average value are included. The red points indicate the resonant wavelength value for Au disks and dimers after hydrogenation at 90 °C.	97
4.8	Sigmoid parameter governing the slope of the heating sigmoid ($H-S$) for disk dimers and disk monomers as a function of hydrogenation temperature. $H-S$ is plotted after Pd deposition (grey) and after hydrogen doping (purple) for the five samples which exhibit heating sigmoids after hydrogenation. Lines indicating the average values of $H-S$ after Pd deposition (grey) and after H_2 doping (purple) as well as shaded regions to indicate uncertainties in the average values are included.	99

4.9	Plasmon-resonance shifts for Au dimers embedded in a VO ₂ film as a function of time during hydrogenation. (Left) experimental data for a dimer hydrogenated at 65 °C with 100% H ₂ gas flow courtesy of Song Yue. (Left, bottom) biexponential and single exponential fits to sampled data from (Left). (Right, bottom) biexponential and single exponential fits to sampled data from a dimer hydrogenated at 65 °C with 10% H ₂ gas flow.	101
4.10	Fit parameters governing the shape of the biexponential fit to the hydrogenation dynamics data for different hydrogenation processes described in the Table 4.1. A higher fit result number corresponds to less aggressive hydrogenation. Error bars are the standard error in each fit parameter for a given hydrogenation process.	105
4.11	Ratio of the decay rates of the fast (<i>f</i>) and slow (<i>b</i>) exponentials in the biexponential fits to different hydrogen doping processes described in Table 4.1. A higher fit result number corresponds to less aggressive hydrogenation. Error bars are derived from the standard error in each of the two fit parameters for a given hydrogenation process.	106
4.12	Ratio of the initial resonance wavelength shift contributions of the fast (<i>d</i>) and slow (<i>a</i>) exponentials in the biexponential fits to different hydrogen doping processes described in Table 4.1. A higher fit result number corresponds to less aggressive hydrogenation. Error bars are derived from the standard error in each of the two fit parameters for a given hydrogenation process.....	107
4.13	Comparison of the decay rate for the slow exponential decay for the biexponential fits (blue, 1-6) with the decay rate of the exponential fit for ITO-17 (red, 7). For fit results 1 through 6, a higher fit result number corresponds to less aggressive hydrogenation.	108
4.14	Plasmon-resonance shift for an Au dimer embedded in a VO ₂ film as a function of time during hydrogenation. Experimental data for a dimer hydrogenated at 90 °C with 100% H ₂ gas flow courtesy of Song Yue.....	109
4.15	Linear fit to sampled data for Figure 4.14. The y-axis is zoomed-in for ease of visualization. A positive slope with increasing time can be seen starting at a time of 15 minutes.	109
5.1	Simulated transmission spectrum showing PIT.....	114
5.2	Schematic of a dolmen structure.....	114

5.3	Simulated transmission for Au dolmens on glass with decreasing gap size G . Stronger PIT is observed as G decreases. The spectra are each offset by 0.4 in transmission for clarity. Incident electric field polarized parallel to the dipole antenna, along the length of L_1 . In this set of simulations, the dimensions of the dolmen are $L_1 = 320$ nm, $W_1 = 135$ nm, $L_2 = 300$ nm, $W_2 = 125$ nm, $S = 50$ nm, and $T = 60$ nm.116
5.4	(a) Plasmon mode hybridization diagram for an Au dolmen formed from a dipole and a quadrupole antenna showing the bonding, PIT, and antibonding mode charge distributions. (b) The simulated local electric field maps at each of the hybrid modes described in (a) with the same color scheme. The PIT mode has no local field around the dipole antenna and the bonding mode has high electric field in the gap between the dipole and quadrupole antennas, as expected from the charge distributions. Incident electric field polarized parallel to the dipole antenna, along the length of L_1 for electric field maps.118
5.5	Simulated transmission of an Au dolmen on glass with dolmen structure imported from an SEM image. The directions of quadrupole and dipole polarized light with respect to a dolmen are indicated in the inset with borders color-coded to the appropriate spectra. Dipole (red) and quadrupole (blue) polarized spectra are shown, demonstrating the polarization-dependent PIT response of the dolmen nanostructure.115
5.6	Experimentally measured optical transmission of an Au dolmen on a VO_2 film. The light is dipole polarized. The orientation of dipole polarized light with respect to a dolmen is described in the inset of Figure 5.5.119
5.7	Simulated transmission of an Au dolmen on a VO_2 film the with dolmen structure imported from an SEM image of the sample measured in Figure 5.6. The light is dipole polarized. The orientation of dipole polarized light with respect to a dolmen is described in the inset of Figure 5.5.120
5.8	Simulated transmission spectra for Au dolmens topped with I VO_2 dolmens of varying thicknesses. Spectra are offset by 0.4 for clarity. Incident electric field polarized parallel to the dipole antenna, along the length of L_1123
5.9	Simulated transmission spectra for Au- VO_2 dolmens with varying dipole-quadrupole gaps. The VO_2 is in the insulating phase during these simulations. Spectra are offset by 1 for clarity. Incident electric field polarized parallel to the dipole antenna, along the length of L_1 125
5.10	Simulated local electric field maps for Au- VO_2 dolmens taken at the wavelength of the bonding mode of nanostructure with varying values of G . The maps are taken at a height of 30 nm. A scale of electric field enhancement is provided at the top left. Incident electric field polarized parallel to the dipole antenna, along the length of L_1126

5.11	Simulated transmission spectra for Au-VO ₂ dolmens with varying pitches. Spectra are offset by 0.5 for every 100 nm increase in pitch for clarity. Incident electric field polarized parallel to the dipole antenna, along the length of L_1	127
5.12	Simulated local electric field maps for Au-VO ₂ dolmens taken at the wavelength of the bonding mode of nanostructure with varying values of pitch. The maps are taken at a height of 30nm. A scale of electric field enhancement is provided at the top left. Incident electric field polarized parallel to the dipole antenna, along the length of L_1	129
5.13	Left and center - SEMs of stacked dolmens. Left is a magnified images of an individual dolmen and center is an array of dolmens with a pitch of 1110 nm. Right – AFM of stacked dolmen. Line profiles indicate that the full structure thickness is 78 ± 2 nm. As the Au is 60 nm thick based upon previous Au nanoparticle thickness calibration via AFM, the VO ₂ layer is 18 ± 2 nm thick.....	130
5.14	Simulated transmission spectra for an Au dolmen on a glass substrate with dimensions and pitch matching those of the fabricated Au-VO ₂ stacked dolmens. Incident electric field polarized parallel to the dipole antenna, along the length of L_1	131
5.15	Simulated transmission spectrum (black) for an Au dolmen imported from an SEM of a fabricated dolmen. The Lorentzian fit (green) represents the data reasonably well.	132
5.16	Simulated transmission spectrum (black) for an Au dolmen created by rectangles with dimensions measured from a fabricated dolmen. The Lorentzian fit (purple) does not represent the data particularly well.	132
5.17	Local electric field maps at resonance are shown below for each of the two spectra. The purple map corresponds to the measured dimensions and the green map corresponds to the SEM import. Incident electric field polarized parallel to the dipole antenna, along the length of L_1	133
5.18	Simulated transmission spectra for Au-VO ₂ dolmen for I and M phase VO ₂ . The dimensions are taken from fabricated nanostructures and a 900 nm pitch is used. Incident electric field polarized parallel to the dipole antenna, along the length of L_1	134
5.19	Simulated transmission spectra for Au-VO ₂ dolmen for I phase VO ₂ with the electric field polarized parallel to the dipole antenna (along the length of L_1) and parallel to the quadrupole antenna (along the length of L_2). The dimensions are taken from fabricated nanostructures and a 900 nm pitch is used.....	134

6.1	Schematics illustrating the principles for a broadband absorber which is actively tunable. In the top left, the absorption of nanoparticles of the same size embedded in M and I VO ₂ (red and blue, respectively) are shown in comparison to the absorption of those nanoparticles in air (black). In the bottom left, the absorption of nanoparticles of different sizes in air are shown. On the right, the absorption of nanoparticles of different sizes embedded in M and I VO ₂ (red and blue, respectively) are shown.143
B.1	Schematic of powder and substrate positions in the boat for single crystal growth. 148
C.1	Vanadium dioxide single crystals grown on Si with overlying Au photolithography markers. The left SEM shows the regularly spaced Au crosses with numbers and letters, with PMMA and Cr on top, demonstrating their visibility for EBL. The right optical micrograph shows VO ₂ single crystals on the micrometer scale randomly oriented and shaped near one particular set of photolithography markers.151
C.2	Vanadium dioxide single crystals grown on quartz with overlying Au photolithography markers and EBL-patterned Au nanorods. As can be seen, the Au nanostructures were written on the sample (boxed in red), but there is an offset on the 10's of microns order between where the structures were written and the crystal onto which they were intended to be written (pointed to with blue arrow).152
C.3	Vanadium dioxide single crystals grown on Si with overlying Au photolithography markers and EBL-patterned Au nanorods. As can be seen, the Au nanostructures have been successfully written on the sample directly on top of VO ₂ crystals.155
D.1	Thermal transmission hysteresis on the VO ₂ thin film on sample ITO-10 away from the buried Au nanoparticle arrays. The red and blue curves represent the sample response during heating and cooling, respectively.157
D.2	Plasmon resonance-hysteresis on sample ITO-10. Sigmoids represent the average heating (red) and cooling (blue) responses of 10 Au disk dimers and 9 Au disk monomers.157
D.3	Plasmon resonance-hysteresis on sample ITO-10 before Pd deposition. Sigmoids represent the average heating (red) and cooling (blue) responses of 10 Au disk dimers and 9 Au disk monomers.158
D.4	Plasmon resonance-hysteresis on sample ITO-10 after Pd deposition. Sigmoids represent the average heating (red) and cooling (blue) responses of 10 Au disk dimers and 9 Au disk monomers.158

E.1	Temperature-dependent transmission measured using a 1550 nm laser light for 8 nm, 12 nm, and 16 nm (left to right) RF-M sputtering VO ₂ films grown on Si. The oscillations in the hysteresis curves are due to the thermoelectric effect in silicon, and appear in these curves due to the underlying Si substrates.	160
E.2	Representative SEM images for 8 nm, 12 nm, and 16 nm (left to right) RF-M sputtering VO ₂ films grown on Si. Individual grains with differences in conductivity are seen.	161
E.3	Representative AFM images for 8 nm (left) and 16 nm (center and right) RF-M sputtering VO ₂ films grown on Si. The samples are film-like, with distinct grains and regions where the material appears to be balled-up. Some regions on the samples have voids, as seen in the right image.	161
F.1	Plots of plasmon resonance vs substrate-nanorod distance for substrates with $n = 1.5$ (left) and $n = 2$ (right). The resonant wavelengths become constant as the distance increases.	163

CHAPTER 1

INTRODUCTION

1.1 – Introduction

This dissertation explores the dipole and quadrupole interactions between localized surface plasmons and a phase-changing environment, the specific properties of these hybrid materials, and the challenges inherent in fabricating these complex structures. The combination of plasmonics with a phase-changing material offers a rich span of phenomena for examination, including the formation of coexisting material phases, hydrogen doping, and switchable plasmon-induced transparency. The contributions to the understanding of gold-vanadium dioxide (Au-VO₂) hybrid structures discussed in this dissertation are as follows.

Hydrogen doping of VO₂ probed with Au nanostructures:

Atomic hydrogen is sensed by optically probing the plasmon resonance of Au dimers embedded in a VO₂ film for the first time. It is observed that with increased hydrogen doping, the pure VO₂ metallic state optical properties are retained and the insulating state optical properties continuously change to become like those of pure metallic VO₂. It is also observed that the phase-transition temperature is lower for hydrogen doped VO₂ than for pure VO₂, but the temperature does not significantly decrease with increased hydrogen doping. It is also found that the time-dependent hydrogen doping of VO₂ has two distinct timescale and that their relative contributions are dependent on the temperature during hydrogen doping.

Novel phase coexistence in VO₂ single crystals probed with s-SNOM:

A novel pattern of coexisting metallic and insulating domains of VO₂ in a low-aspect ratio VO₂ single crystal is observed using scattering-scanning near-field optical microscopy (s-SNOM).

The physics underlying this pattern is connected to the physics and pattern observed in VO₂ thin films. This pattern has never before been studied on VO₂ single crystals. It is determined, for the first time, that the coexisting M and I domains in VO₂ single crystals do not extend throughout the entire depth of the crystal, but rather are depth-dependent and nucleate below the crystal surface using plasmons on the crystal surface as probes of the VO₂ phase transition.

Active Plasmon-Induced Transparency examined with simulations:

Active PIT hybrid Au-VO₂ dolmen nanostructures are simulated. The structure parameters are tuned to improve the switching contrast and determine that the sharpness of the resonance cannot be optimized while simultaneously optimizing the resonance shift over the phase transition. A stacked dolmen nanostructure is fabricated with dimensions that produce active VO₂ based upon simulations.

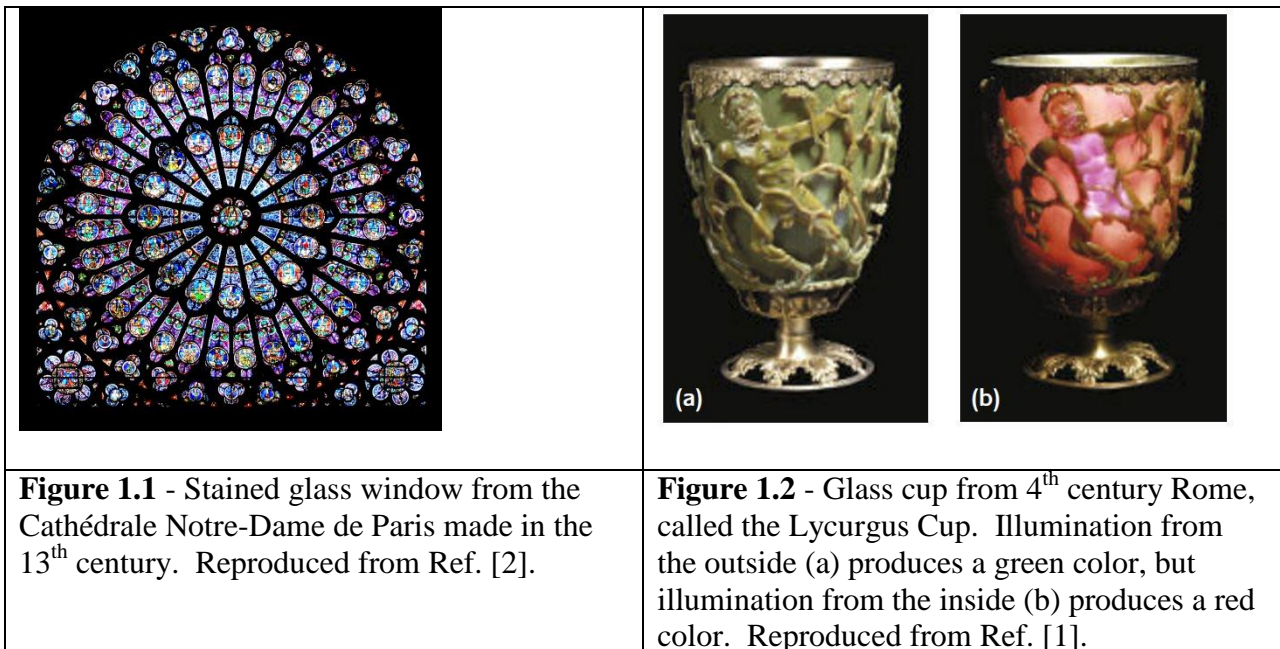
Contributions to the fabrication and characterization of hybrid Au-VO₂ nanostructures:

A method is developed to pattern Au nanorods atop VO₂ single crystals. The optimal deposition method to make VO₂ films with low scattering on top of Au dimers is discussed. A method is developed to fabricate stacked Au-VO₂ nanostructures with a variety of sizes and shapes using a single layer of electron beam lithography.

1.2 – Plasmonics

1.2.1 – Brief Introduction to Plasmonics

The properties of plasmonics particle have been applied far before anyone knew why these properties occurred regarding the underlying physics. Artisans as far back as the 4th century in Rome added small amounts of metallic powder to glass to produce bright colors for use in stained glass windows and to produce the dichroism observed in the Lycurgus Cup. In the case of the Lycurgus cup, gold-silver alloy nanospheres with diameters between 50 and 100 nm comprising less than 1% of the cup were incorporated into the glass during fabrication. This causes the cup to appear green when illuminated from the outside and red when illuminated from the inside. In Ref. [1], there is a detailed report on the composition of the cup and its history.



Michael Faraday, when examining the ruby color of colloidal gold particles in solution, proposed that the cause of the color was light interacting with particles smaller than could be

seen in any microscopes which existed at that time.[3, 4] This proved to be the case when gold colloids made with the same methods employed by Faraday were examined later and determined to contain gold (Au) nanoparticles with 6 ± 2 nm size.[4]

Gustav Mie developed a formalism based on Maxwell's equations to predict the absorption and scattering of spheres of a random radius embedded in a medium with a random index of refraction.[5] He was not the first to develop a mathematical description of light interacting with small spheres, as this was independently developed by Ludvig Lorenz,[6, 7] but he did predict the existence of multiple resonances (referred to as Mie resonances) that were not accounted for with Rayleigh scattering.[5, 8] He also used his mathematical formalism to study Au nanospheres in liquids and predicted what are now known to be localized surface plasmon modes in metal nanoparticles. Extensions were subsequently developed building on his theory to allow the resonances of nanoparticles with shapes such as ellipsoids and cylinders as well as larger nanoparticles to be calculated.[9-11] Improvements in computational modeling to examine the interaction of light with nanoscale materials have allowed the simulation of more complex geometries (coupled particles, non-spherical or ellipsoidal shapes) and contributed to the resurgence of plasmonics in recent years.

1.2.2 - Physics of the Localized Surface Plasmon Resonance

A plasmon is a collective oscillation of free electrons in a material induced by light with a wavelength where the driving frequency matches the resonant frequency of the system of free electrons. In the case of metal nanoparticles, the oscillation is localized to the nanoparticle and moves back and forth along the particle in the direction parallel to that of the exciting electric field. As with other harmonic oscillations, the electrons spend the most time at the turning points

of their orbits, that is, the edges of the nanoparticle with the restoring force provided by the nearly stationary atomic nuclei in the metal. The resonant oscillation of electrons on a metal nanoparticle is referred to as a localized surface plasmon resonance (LSPR), and is the plasmon resonance of relevance for this work.

The excitation of a plasmon resonance in a nanoparticle by light results in two major phenomena. The first is that scattering and absorption of the light at the resonant wavelength are increased. This is because the scattering and absorption cross sections increase when there is a resonance in polarizability since they are proportional to each other as described in Ref. [12]. The second is that the electric field near the nanoparticle is enhanced due to the presence of large numbers of electrons at the edges of the nanoparticle during resonance.

1.2.3 – Influence of Nanoparticle Material on Plasmon Resonance

Having a plasmon requires only the presence of free carriers that can move. Thus, plasmons can exist in both metallic and non-metallic nanostructures.[13] In this work, though, the focus is on the plasmons in metallic nanostructures, specifically those made of gold. Different metals have different dielectric functions as a function of wavelength, so these metals are resonant at different wavelengths and with different resonant widths even if when the particles are all embedded in the same medium and are identical in size and shape.

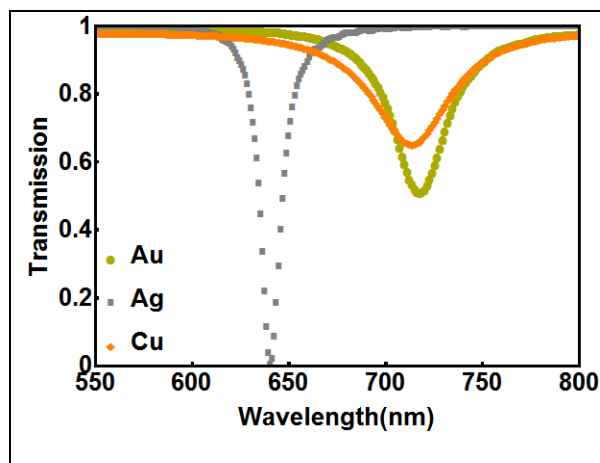


Figure 1.3 - Simulated transmission for 100 nm long, 20 nm wide, and 20 nm thick nanorods comprised of a variety of noble metals in air. Electric field polarized parallel to long axis of rods.

1.2.4 – Influence of Nanoparticle Size on Plasmon Resonance

For the simple dipole resonance, the electrons are traveling back and forth in the nanoparticle dimension parallel to the optical electric field exciting the particle. The distance the electrons have to travel is larger for a larger nanoparticle, thus, the resonant frequency is lower and the resonant wavelength is longer. For a nanorod plasmonic resonator, an increase in aspect ratio red-shifts the long axis plasmon mode and decreases its full width at half maximum (FWHM) indicating an increase in the dephasing time of the electrons driving that resonance.[14] When changing just the long axis (length) dimension of a nanorod, the long axis resonance is red-shifted as the length is increased. When changing just the short in-plane axis (width) dimension of a nanorod, the long axis resonance is blue-shifted as the width is increased. When changing just the thickness of a nanorod, the long axis resonance is blue-shifted as the thickness is increased. For the nanorod, the plasmon resonance is stronger (less transmission) when the volume of material is larger.

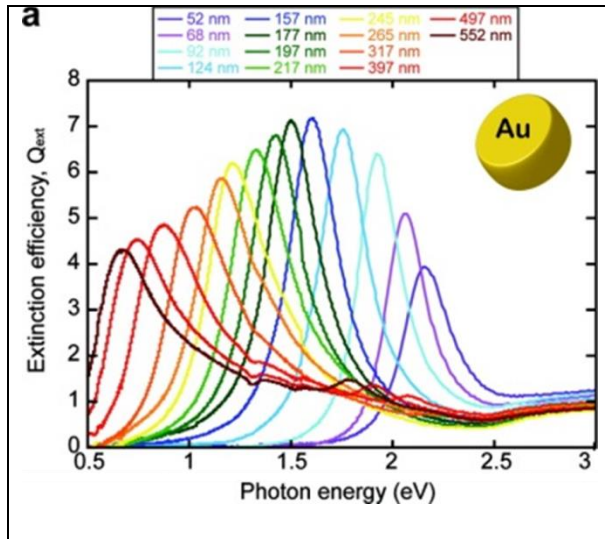


Figure 1.4 - Measured extinction for 20 nm thick Au nanodisks with increasing diameter. Figure from Ref. [15].

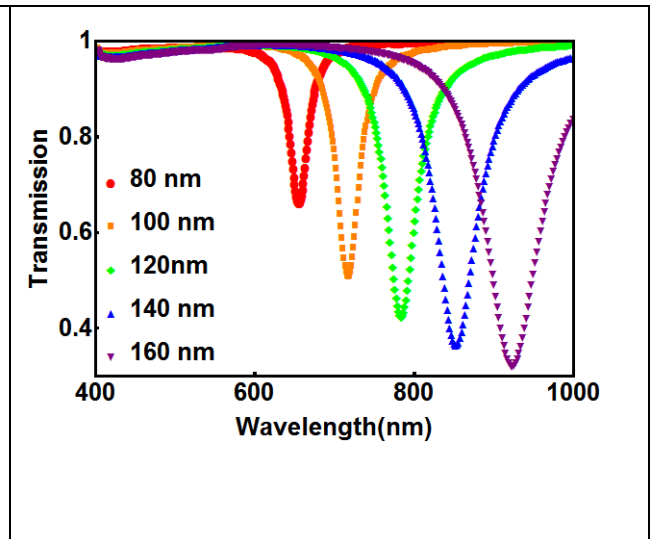


Figure 1.5 - Simulated transmission for 20 nm thick and 20 nm wide Au nanorod in air with increasing length. Electric field polarized parallel to long axis of rods.

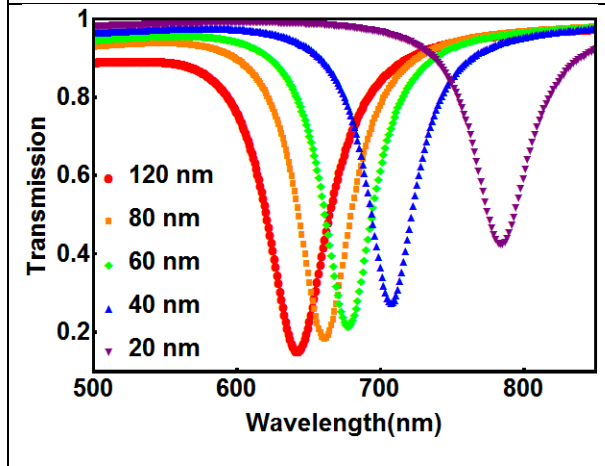


Figure 1.6 - Simulated transmission for 20 nm thick and 120 nm long Au nanorod in air with decreasing width. Electric field polarized parallel to long axis of rods.

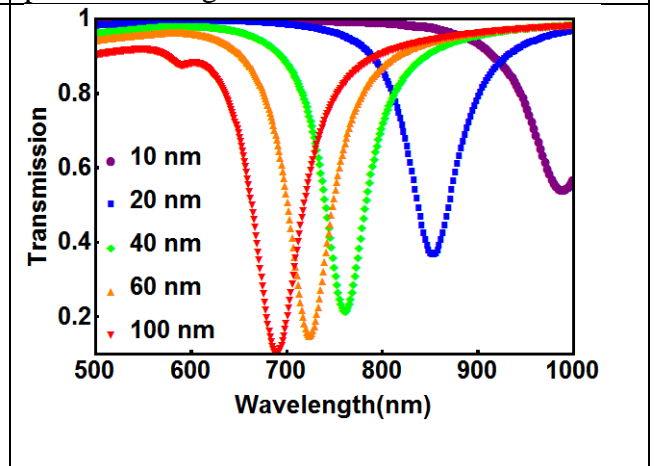
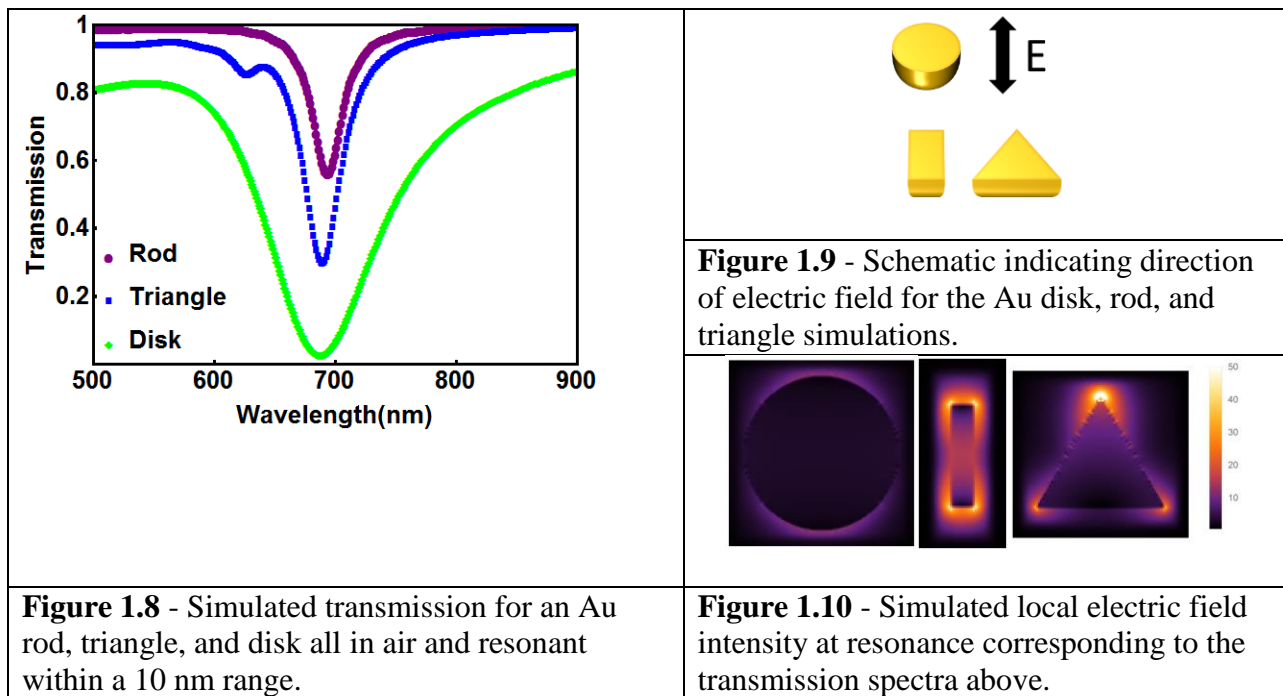


Figure 1.7 - Simulated transmission for 120 nm long and 20 nm wide Au nanorod in air with decreasing thickness. Electric field polarized parallel to long axis of rods.

1.2.5 – Influence of Nanoparticle Shape on Plasmon Resonance

The shape of a metal nanoparticle can alter the plasmon resonance primarily in two ways. First, a nanoparticle with a smaller in-plane aspect ratio will have a broader plasmon resonance than a nanoparticle with a larger in-plane aspect ratio. For example, a rod with an in-plane aspect ratio of 4.5 has a narrower plasmon resonance than a disk with an in-plane aspect ratio of

1, though both have plasmon resonances in the same 10 nm range. In Figure 1.8, the plasmon resonance is strongest (the least amount of light is transmitted) for the nanoparticle that has the largest volume. Second, a nanoparticle with sharp points or corners will have a higher local enhancement of the electric field than a particle without points or corners. For example, a triangular nanoparticle will have a higher electric field enhancement around it than a disk-shaped nanoparticle, as seen in Figure 1.10.



1.2.6 – Influence of the Local Dielectric Environment of the Nanoparticle on the Plasmon Resonance

The dielectric function of material in the local environment of a plasmonic particle influences the resonant condition of the particles. This is because the electrons comprising the plasmon oscillation are not completely confined within the nanoparticles, but rather spill out on the edges.[9] These electrons are sensitive to their local environment. Mathematically, this can

be seen in the quasi static limit, where the plasmonic particles are at least an order of magnitude smaller than the wavelength of light.[16] In this case, the polarizability, α , for a sphere as a function of wavelength is proportional to

$$\alpha \propto \frac{\varepsilon_m(\lambda) - \varepsilon_d(\lambda)}{\varepsilon_m(\lambda) + 2\varepsilon_d(\lambda)}, \#(1.1)$$

where ε_m and ε_d are the complex wavelength-dependent functions describing dielectric properties of the nanoparticle and the dielectric environment respectively.[17] There is a resonance when the real part of the denominator goes to zero, which is when

$$\varepsilon_m(\lambda) = -2\varepsilon_d(\lambda). \#(1.2)$$

When the quasi static limit no longer holds, the equation for the polarizability becomes more complex to account for account for the size effects, as described in Ref [12]. The dielectric function for the dielectric environment, though, still plays a role.

A material with a higher refractive index in the absence of absorption will shift the resonant wavelength of the particle to longer wavelengths. Physically, this is because a higher refractive index environment decreases the restoring force on the oscillating electrons, which decreases the resonant frequency and red-shifts the resonance.[18] This can be seen in Figure 1.11, where the plasmon resonance of an Au nanorod red-shifts as the local dielectric environment of the nanorod is changed from air to glass (SiO_2) to sapphire (Al_2O_3) in order of increasing refractive index.

A material with higher absorption will broaden and dampen the plasmon resonance

because more energy from the oscillator is transferred to the environment, causing the decrease in amplitude and broadening which is characteristic of a lossier plasmon resonance. This can be seen in the Figure 1.12 where the plasmon resonance of an Au nanosphere is broadened and weakened as the imaginary component of the dielectric function (ϵ_m'') of the dielectric environment is increased. The plasmon-resonance position is not influenced by changes in ϵ_m'' of the dielectric environment.

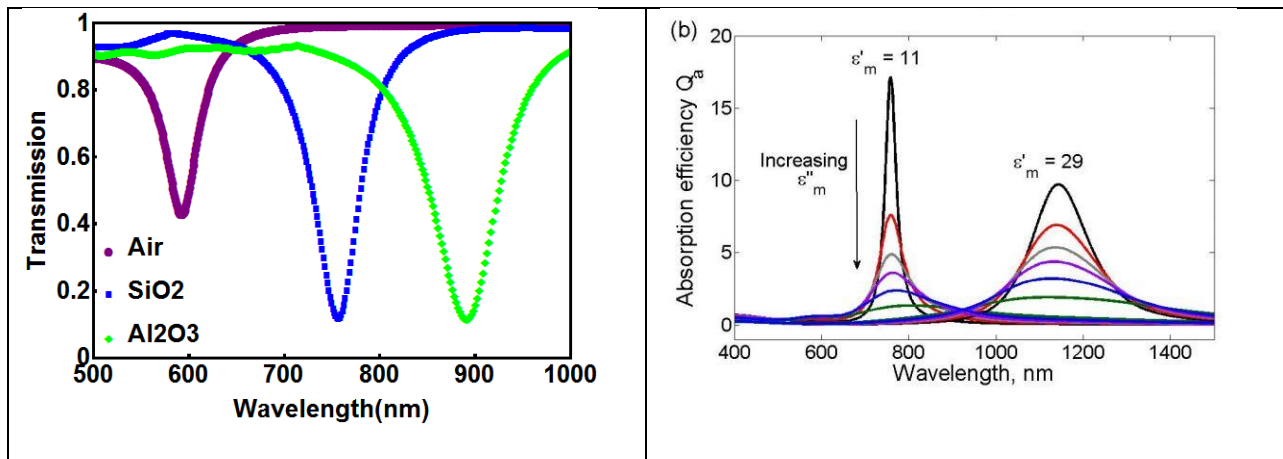


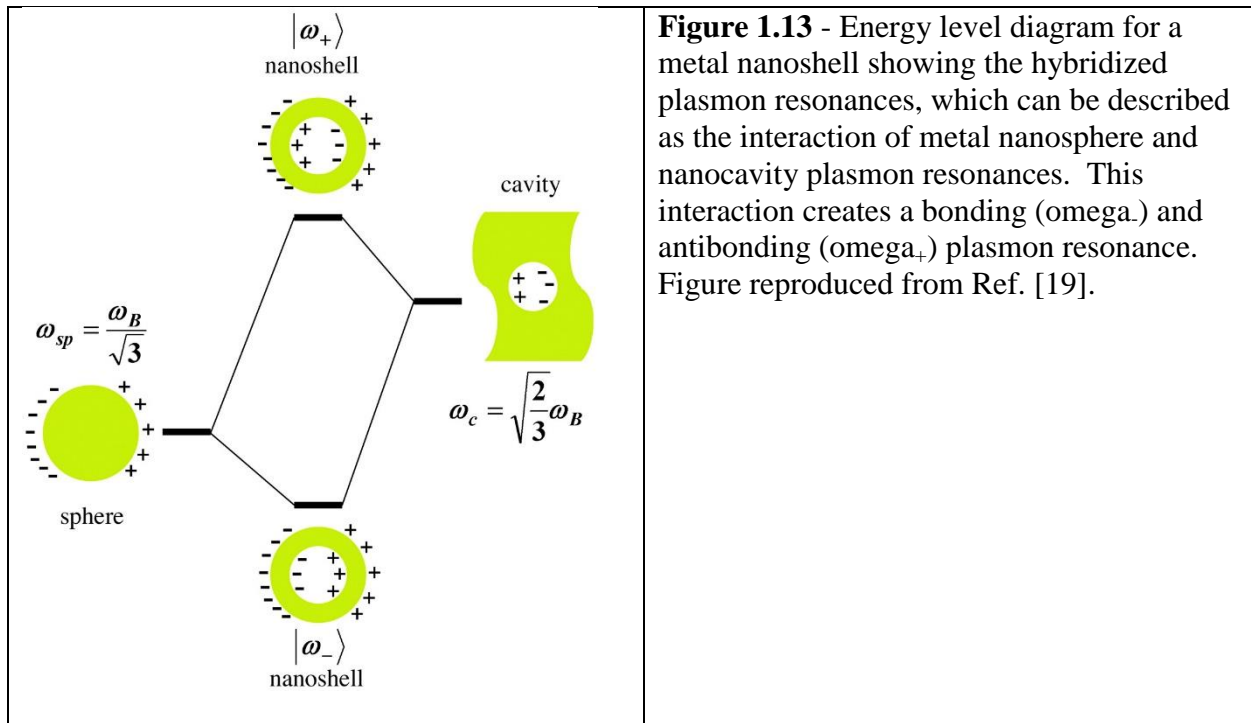
Figure 1.11 - Simulated transmission for a 100 nm long, 60 nm wide, and 40 nm thick Au nanorod embedded in a variety of dielectric environments. Electric field polarized parallel to long axis of rods.

Figure 1.12 - Calculated absorption efficiencies for 25 nm radius Au spheres as a function of ϵ_m'' of the dielectric environment for two constant real parts of the dielectric function (ϵ_m') of the environment. The values of ϵ_m'' used are as follows: 0, 1, 2, 3, 5, 10. Figure reproduced from Ref. [12].

1.2.7 - Plasmon Mode Hybridization

The plasmon modes of complex geometries (nanoshells, dimers, dolmens, etc.) come about from the interaction and thus hybridization of plasmonic modes from simpler geometries (spheres, ellipsoids, rods, cavities) where the modes are known, as described by Prodan.[19] When two nanostructures such as a nanosphere and a cavity are spatially close together and their resonant wavelengths are also close together, their resonances couple with a strength based upon

the resonators' closeness and the difference between their resonant wavelengths. This causes the modes to hybridize, meaning that they mix together to form new modes different from either of the original modes. This results in the creation of a symmetric plasmon mode and an antisymmetric plasmon mode, seen in Figure 1.13, which are both shifted in energy from the energies of the resonant modes of the constituent nanosphere and cavity. The designations for these modes are related to the relative phases of the two constituent dipole plasmon modes in each hybridized mode. In Figure 1.13, the bonding and antibonding modes of a nanoshell can be described by the hybridization of the dipole modes of a plasmonic nanosphere and a plasmonic cavity.[19] Before the innovations in computational modeling of plasmonic particles, which allow for routine computation of the plasmon modes of complex nanostructures, this method also served as a way to calculate the modes of more complex systems by using the modes of simple plasmonic structures as building blocks because their modes could be determined analytically.



With the progress in commercial physics solvers (such as Lumerical[®] FDTD), it is possible to test this hybridization framework by simulating the expected transmission spectrum and local electric field at the plasmon resonance for complex nanostructures and their component nanoparticles. In Figure 1.14, a nanorod dimer with non-identical nanorod components is considered. A hybridization diagram shows the constituent and hybrid modes, their relative energies, and their charge distributions with the short constituent nanorod indicated in blue, the long constituent nanorod in green, and the antibonding hybridized mode in purple. Using Lumerical FDTD, the transmission spectra of the short rod, long rod, and dimer (antibonding mode) were simulated. The relative positions of the plasmon resonances of these modes demonstrate that the nanorod resonances are indeed at higher energies than the dimer bonding mode (purple) and that the short nanorod resonance (blue) is a higher energy mode than the long nanorod resonance (green). A simulated local electric field map of the dimer at the resonance wavelength of the purple curve confirms that this mode is indeed the antibonding mode, with the high electric field in the gap between the nanoparticles expected given the charge distribution of this mode as seen in the hybridization diagram. The simulated local electric field maps of the short (blue) and long (green) nanorods at their resonance positions indicated that the modes are dipole modes, as expected.

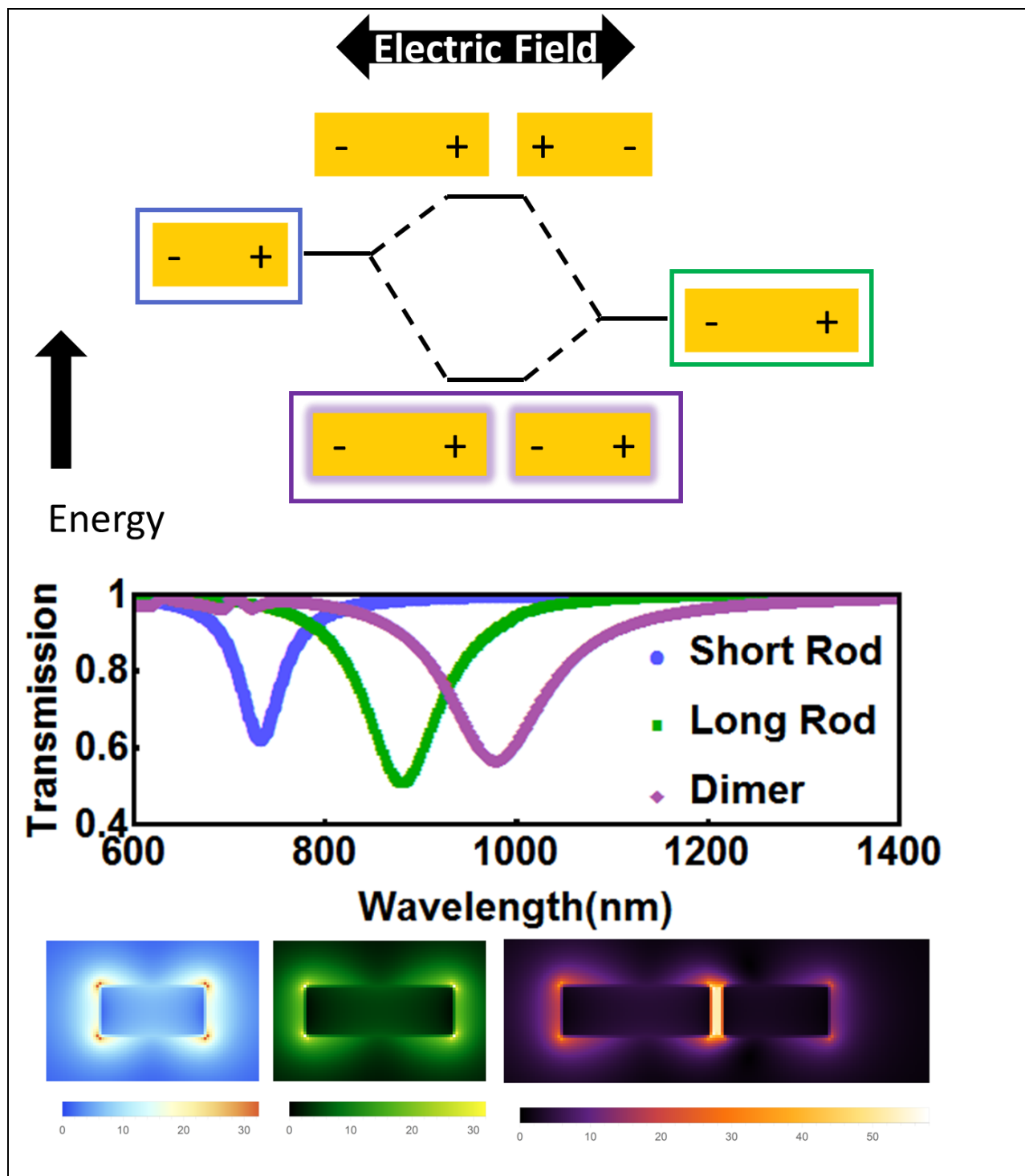


Figure 1.14 - Plasmon mode hybridization diagram for an Au nanorod dimer formed from two non-identical nanorods. The simulated transmission for the short (blue) and long (green) nanorods, and the dimer bonding mode, indicated in purple, are shown. The nanorod and dimer plasmon modes are identified via the simulated local electric field maps at the resonant wavelengths of the dimer and nanorod as determined using the simulated transmission. The nanorods are 70 nm wide and 35 nm thick, and the nanorod dimer has a 20 nm gap. The lengths of the nanorods are 150 nm and 210 nm.

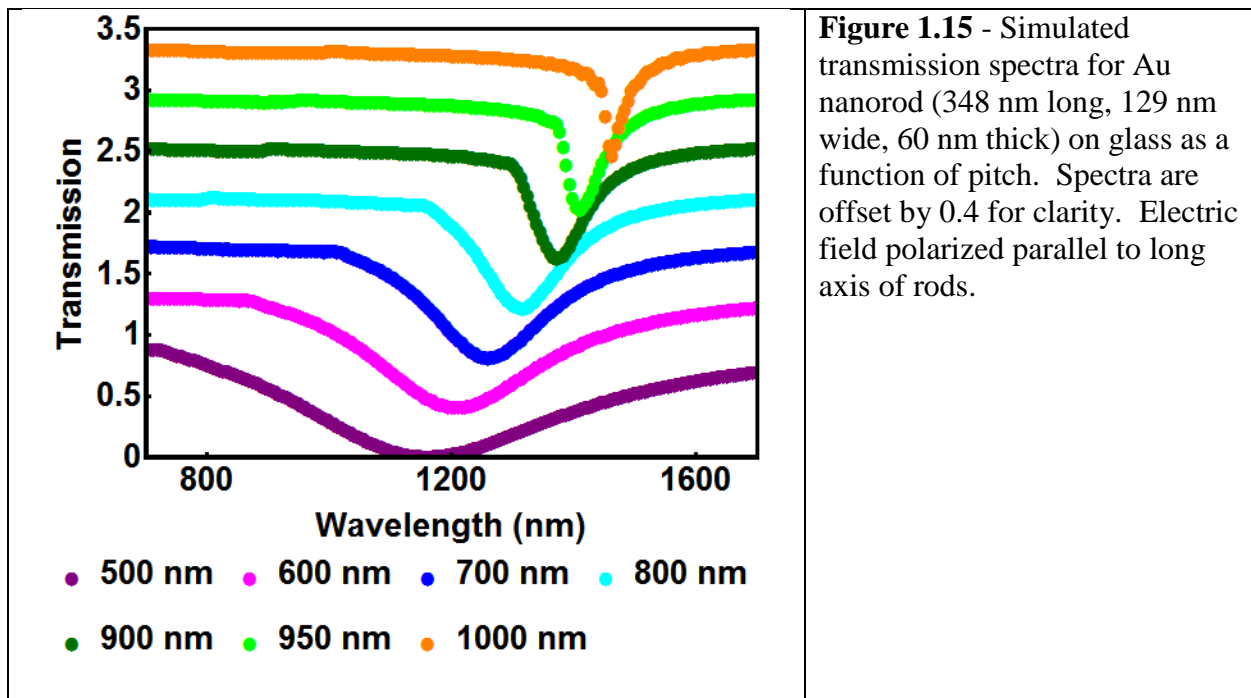
1.2.8 - How Plasmon Resonance is Altered in an Array

When plasmonic particles are arranged in an ordered array, it is necessary to consider the effect of the pitch of the array on the response of the nanoparticles. When the pitch is close to the size of the nanoparticles, the resonators couple and do not act as individual antennas. This results in a broad plasmon resonance, as can be seen in Figure 1.15 for a 500 nm pitch spectrum. As the pitch is increased, the plasmon resonance red-shifts and narrows while maintaining the same minimum transmission, observed in Figure 1.15, for pitches between 600 and 950 nm. With pitches up to 950 nm, a clear Lorentzian lineshape can be seen, which is characteristic of a dipole resonance.

A Lorentzian lineshape is not observed for the spectrum in Figure 1.15 associated with a 1000 nm pitch, and an asymmetric lineshape is observed instead. Once the wavelength of light approaches the pitch of the lattice, the Wood-Rayleigh anomaly becomes relevant. The Wood-Rayleigh anomaly occurs when light at a particular wavelength and diffraction order would be diffracted perpendicular to the grating or beyond. This light cannot be diffracted at an angle higher than 90 degrees from the direction normal to the grating and is instead redistributed back into diffraction orders that are permissible, showing up as additional light in the spectrum at that particular wavelength and permissible diffraction orders.[20-22] This comes about in nanoparticle arrays because a 2D array of nanoparticles is basically a two-dimensional diffraction grating, and thus will diffract light. If the Wood's anomaly is close in wavelength to the wavelength of the LSPR for the individual plasmonic nanoparticles, this creates a sharp resonance in transmission because the diffracted waves can couple to the plasmonic particles.[23-25] Tuning the spectral position of the Wood-Rayleigh anomaly with respect to the

spectral position of the single nanoparticle resonance by tuning the array pitch can also be used to maximize the local electric field on the nanoparticles.[23]

For the plasmon resonance of a plasmonic particle in a one-dimensional array to be equivalent to the plasmon resonance of an individual nanoparticle, the pitch of the array must be greater than five times that of the nanoparticle size.[26] Otherwise, there is still nanoparticle-nanoparticle interaction. For two-dimensional arrays, the plasmon resonance of a particle in this array has not been shown to be equivalent to an individual nanoparticle for pitch to particle size ratios up to 5:1.[26]



1.2.9 - Uses of Plasmons

Plasmons have applications in a variety of areas. Biological applications include biological imaging, such as identifying cancerous and non-cancerous cells, selectively removing cancer or bacterial infections, and biological sensing.[27] Water splitting, improved gas sensing,

and local heating can be achieved using metal plasmonics particles as well.[28, 29] Plasmonic particles can also be used to enhance solar cells.[30] Harkening back to the Lycurgus cup and stained glass windows, metal plasmons are also used to create color and thus art on the nanometer to micrometer scale.[31]

1.2.10 - A Limitation of Metal Plasmonics

A major limitation of metal plasmonics is that the plasmon resonance of a nanoparticle cannot be altered once it is fabricated. This leads naturally to a discussion of a class of materials in which the properties of these materials can be altered after fabrication - phase-change materials.

1.3 – Phase-Change Materials

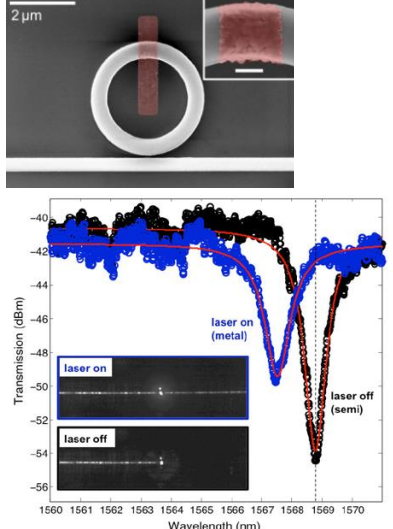
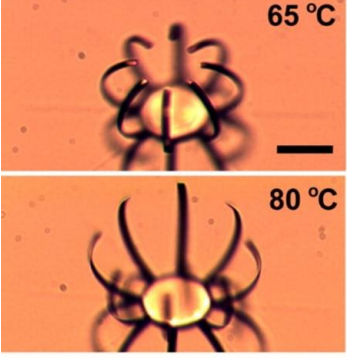
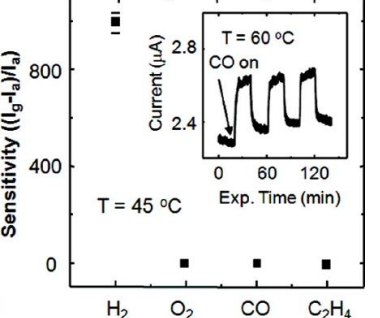
1.3.1 – Phase-Change Materials and their Applications

Phase-change materials allow for controllable modulation of the optical, electronic, magnetic, and/or structural properties of these materials. A subset of these materials is described here. The high-temperature superconductor YBaCuO undergoes the superconducting – non-superconducting transition between 80 and 93K and, therefore, has large changes in resistance and magnetic susceptibility as a function of temperature.[32] The manganite LaPrCaMnO has a large change in resistance as a function of applied magnetic field in the 2-4K range.[33] Vanadium sesquioxide undergoes an insulator-to-metal transition (IMT), a structural phase transition (SPT) from monoclinic to rhombohedral, and an antiferromagnetic to paramagnetic transition with a phase-transition temperature around 155K.[34] In $\text{Ge}_2\text{Sb}_2\text{Te}_5$, the crystalline to

amorphous phase transition causes a 30% change in the dielectric function within 100fs when switched optically, which induces changes in electrical conductivity and optical absorption. This material can also be switched from crystalline to amorphous by heating the crystalline state above the 615 °C melting point of $\text{Ge}_2\text{Sb}_2\text{Te}_5$ so that the lattice becomes disordered and then rapidly cooling the material to retain that amorphous state.[35] In VO_2 , there is an IMT and a SPT at a critical temperature (T_c) of 67 °C in bulk material which cause changes in the optical, electronic, and structural properties of the material.[36, 37]

Phase-change materials have been employed in a variety of applications. A subsection of applications using VO_2 are described here. Using the change in transmitted light over the IMT due to the change in optical properties, VO_2 thin films have been used in optical limiters to protect sensitive components from intense light.[38] The change in transmitted light over the IMT in VO_2 also is harnessed for temperature control in smart windows [39, 40] and considered to control the temperature on spacecraft.[41] The change in optical properties over the IMT has also been used to create a ring resonator structure which can be actively modulated by switching the IMT in a VO_2 patch placed over a section of the ring.[42-44] An example of this structure and the large change in transmission through the waveguide at a given wavelength as a function of the state of the VO_2 is shown In Figure 1.16. As the crystal lattice of VO_2 expands 1% along the c_R axis and shrinks by 0.6% and 0.1% along a_R and b_R axes respectively when undergoing the SPT.[37] Vanadium dioxide single crystals and patterned thin films have also been used in micro- and nanoactuators.[45-48] A micro grabber using this principle is shown in Figure 1.17. The change in resistance of VO_2 has been used in microbolometers to detect small changes in incident IR radiation.[49] This change in resistance of VO_2 over the IMT and also the sensitivity of the VO_2 T_c to dopants has been used to detect trace amounts of gases such as hydrogen,

helium, and argon.[50, 51] An example of gas sensing using a VO₂ nanowire as a probe of H₂ gas with far greater sensitivity than other gasses is shown in Figure 1.18. The utility of VO₂ as a hydrogen gas sensor will be discussed further in Chapter 4.

		
<p>Figure 1.16 - SEM of Si ring resonator with VO₂ patch (false color) atop a section of the ring and measured transmission through the waveguide above (blue) and below (black) the VO₂ phase transition. Figure reproduced from Ref. [43].</p>	<p>Figure 1.17 - Thermally controlled micro grabber, showing grabbing below the phase transition and releasing above the phase transition. Scale bar is 50 μm. Figure reproduced from Ref. [48].</p>	<p>Figure 1.18 - Sensitivity of Pd-decorated VO₂ nanowires to hydrogen gas probed through a change in current when gas is flowing. Inset shows change in current when CO gas flow is cycled on and off. Figure reproduced from Ref. [51].</p>

1.3.2 - Advantages of VO₂ as a Phase-Transition Material

Vanadium dioxide has a phase transition (PT) at 67 °C for bulk material.[37, 52] In comparison to many other PT materials such as YBaCuO, LaPrCaMnO, and V₂O₃, VO₂ has T_c much closer to room temperature (RT) and the VO₂ T_c can be depressed to or below RT via doping or strain.[53-58] The VO₂ PT is also fully reversible, unlike Ge₂Sb₂Te₅ in which the PT is not reversible if the material becomes fully amorphous.[35] Vanadium dioxide does not have

a large change in optical or electronic properties compared to other PT materials, but it is advantageous that the VO₂ PT occurs near room temperature in ambient conditions, that it can be switched on the fs time scale, and that it is fully reversible.

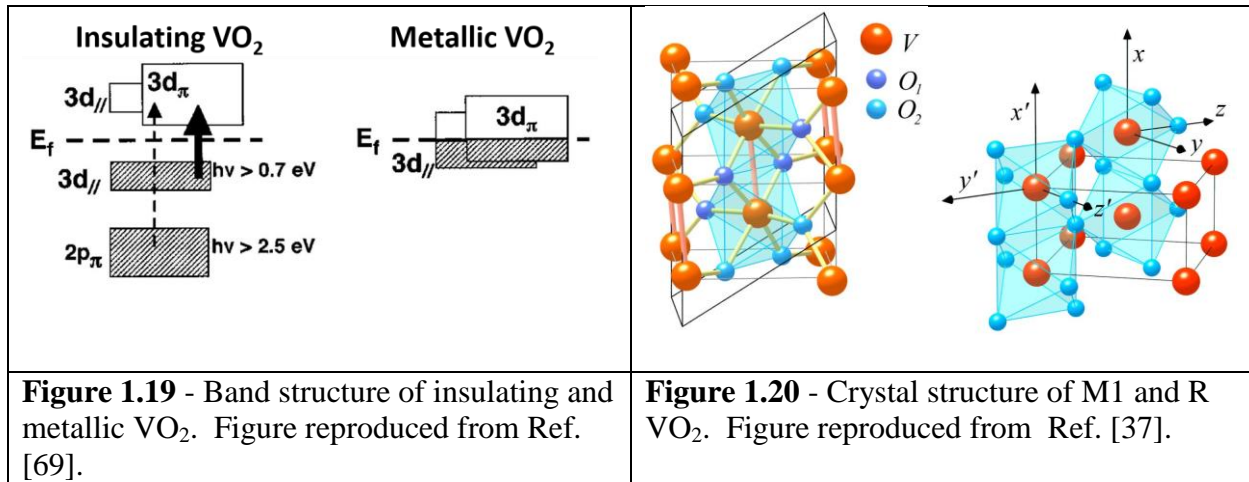
1.3.3 - Inducing the VO₂ PT

There is a variety of methods to induce the PT in VO₂, but the most common and simplest is by heating VO₂ above T_c . [59-61] Applying strain to VO₂ single crystals or thin films has also been shown to induce and alter the PT. [56-58] Applying a high electric field also induces the VO₂ PT via the Poole-Frenkel effect. [62, 63] The phase transition can also be induced in a purely optical manner, using a femtosecond laser pulse [64-66] or elevating the temperature close to that of the PT and using a decreased fluence to switch VO₂. [67] Doping VO₂ with atomic hydrogen after VO₂ fabrication either as single crystals or thin films also serves to induce the PT. [68]

1.3.4 - Details of VO₂ PT

Vanadium dioxide has a 1st order PT that is both an electronic (insulator-to-metal) and structural (monoclinic (M1) to rutile) transition. The VO₂ band structures of the insulating and metallic states are shown in Figure 1.19. In the insulating state, the 3_{d||} bands are split and a band gap exists between the lower energy 3_{d||} band and the 3_{d π} band. In the metallic state, the 3_{d π} band decreases in energy and the 3_{d||} bands merge to create a conduction band. [37, 69] The crystal structures of M1 and R VO₂ are shown in Figure 1.20. For R VO₂, the V atoms (orange) form a body-centered tetragonal lattice and the O atoms (blue) form an octahedron around each V atom. For M1 VO₂, the O atoms barely move from their R positions, but the V atoms move such that

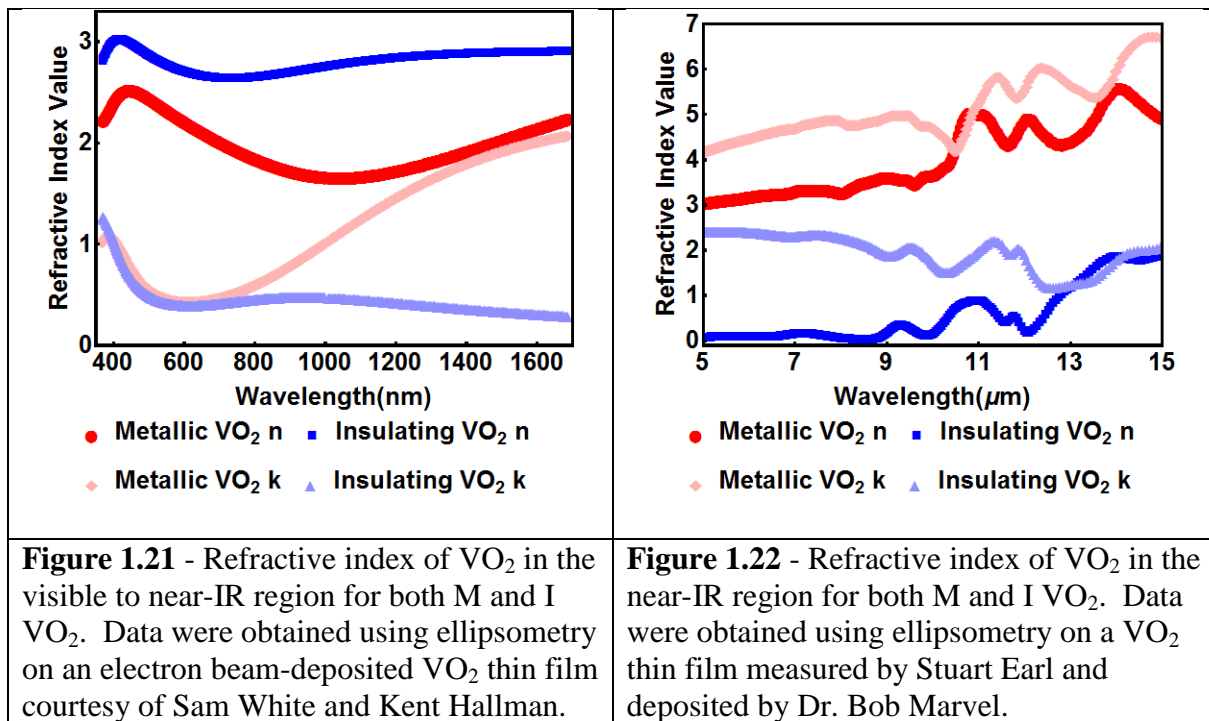
they dimerize (shorter V-V bond lengths indicated in pink) and tilt. Thus, the O atoms have two different environments and are indicated in purple (O_1) and blue (O_2).[37] There are two other insulating VO_2 crystal states, a second monoclinic phase (M2) and a triclinic phase (T), which will not be focused upon here.[37]



The IMT causes a large change in the interaction of light with VO_2 due to the large wavelength-dependent change in the real and imaginary components of the dielectric function of VO_2 , as shown in Figures 1.21 and 1.22. This leads to a change in the amount of light transmitted through or refracted by the VO_2 . The plot of this change in transmission, shown in Figure 1.23, comprises two sigmoidal curves representing heating and cooling the sample, which are offset in temperature, producing the characteristic hysteresis curve of VO_2 . The switching contrast and critical temperature, shown in Figure 1.23, are used to characterize the VO_2 hysteresis curve. This change in transmission is wavelength-dependent, as is shown in Figure 1.24, using 1550 nm laser light and a broadband white-light source with emission between 400 and 1000 nm. As the change in the dielectric function of VO_2 over the IMT is larger at 1550 nm than in the range of 400 to 1000 nm, the switching contrast over the PT is much larger for 1550nm light than for the broadband white light. It is important to note, though, that the critical

temperature for the VO₂ IMT is the same when excited with either light source, as the wavelength used to probe the transmission does not influence the temperature at which the VO₂ IMT occurs when the IMT is induced thermally. There is also a multiple-orders-of-magnitude change in the resistivity of the VO₂ over the IMT, as is shown in Figure 1.25.

The SPT yields noticeable changes in the Raman spectrum of VO₂ as the VO₂ goes from M1 to R, as shown in Figure 1.26. Vanadium dioxide in the M1 phase has many sharp, well-defined peaks whereas R VO₂ has a single broad peak.[53, 70] This work focuses on the large change in the dielectric function of VO₂ over the phase transition.



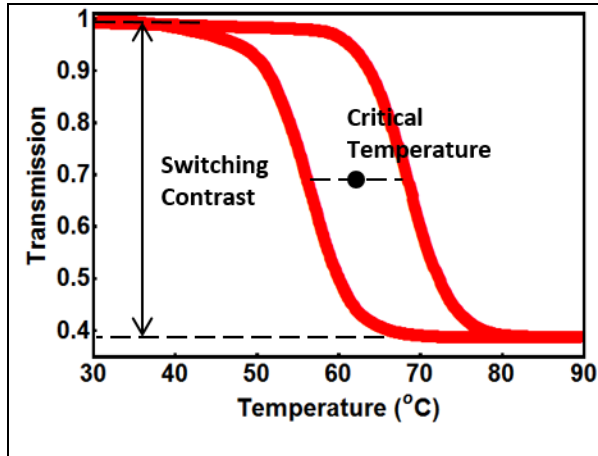


Figure 1.23 - Diagram indicating showing the physical definition for the switching contrast and critical temperature. The critical temperature is defined as the average temperature between the two sigmoids where the transmission is half of its maximum value.

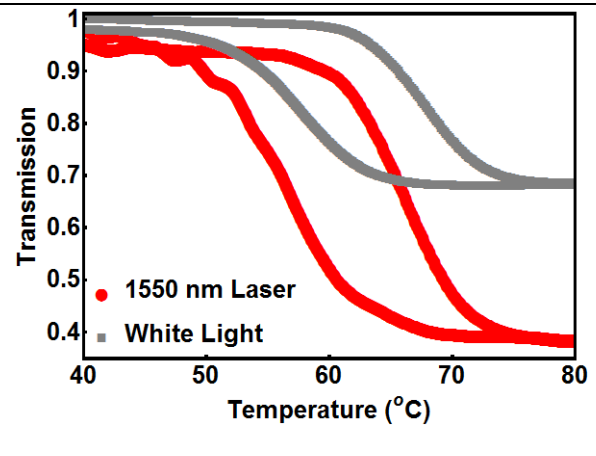


Figure 1.24 - Temperature-dependent transmission of a 52 nm RF-M sputtered VO₂ thin film on glass. Data were obtained using both a 1550 nm laser and a broadband white-light source with emission between 400 and 1000 nm. The critical temperature is the same for the two curves, but the switching contrast is much higher for the data taken using the 1550 nm laser.

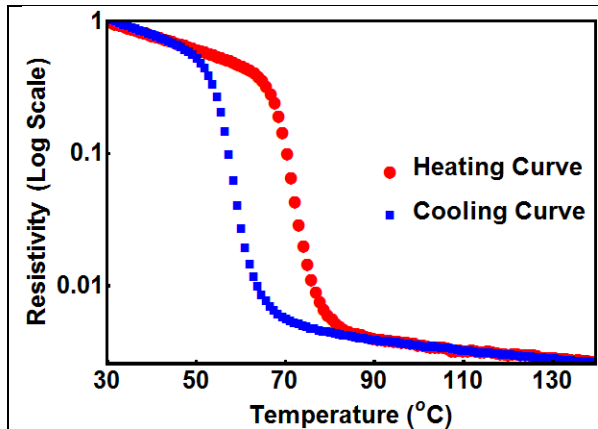


Figure 1.25 - Resistivity of 52 nm RF-M sputtered VO₂ thin film on glass. Data were obtained using a four point probe setup.

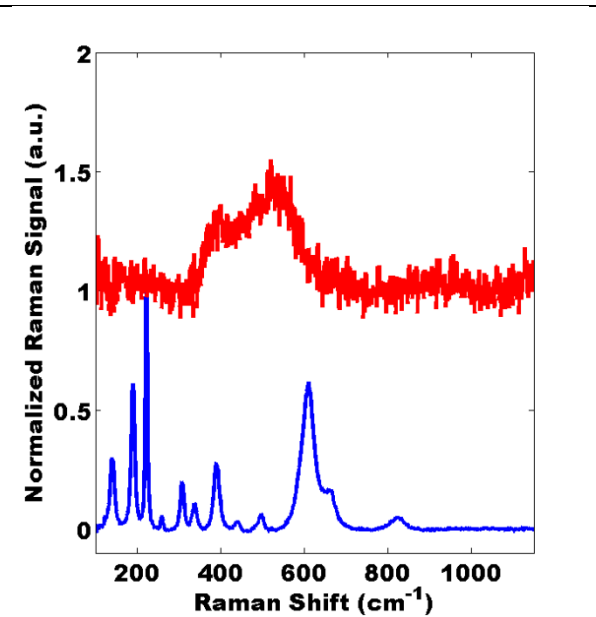


Figure 1.26 - Raman spectra on a VO₂ single crystal grown on Si, as described Chapter 2, both above (red) and below (blue) the SPT. Figure courtesy of Kent Hallman.

The IMT and SPT do not occur simultaneously. The IMT occurs in less than 60 fs [71]. During the transition from the monoclinic to the rutile crystal structure the SPT has a fluence-dependent onset time ranging from less than a picosecond to a few picoseconds,[72] and during the transition from the rutile to the monoclinic crystal structure the SPT takes hundreds of picoseconds to nanoseconds to complete.[65, 73, 74] These can be separated so that only the IMT occurs, leaving the VO₂ in a monoclinic metallic state which can recover to a monoclinic insulating state much quicker than if the SPT also occurred and it was necessary for the atoms to shift back to their M1 positions as well. This was first shown through simultaneous probing of the thermally-induced IMT and SPT of a VO₂ thin film.[75] Other work probing both the thermally- and ultrafast laser pulse-induced IMT and SPT of VO₂ thin films as well as work probing the thermally-induced IMT and SPT of VO₂ single crystals has also shown the existence of a monoclinic metallic phase of VO₂. [71, 76-78]

1.3.5 - Influence of VO₂ Fabrication on Material Properties

The properties of the VO₂, such as surface morphology and critical temperature, are influenced by the fabrication of the VO₂. Parameters such as growth method, substrate, and the addition of dopants can have large effects on the resultant VO₂, as described below.

Different thin film deposition methods (pulsed laser deposition, electron beam evaporation, and radio frequency magnetron sputter) and different surface energies associated with different growth substrates (glass, silicon, and sapphire) alter the size and shape of grains in the resulting film as well as the film roughness.[79]

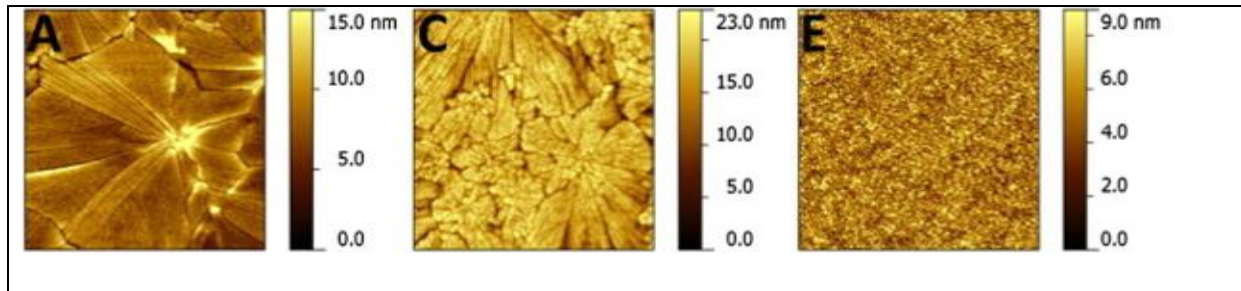


Figure 1.27 - Atomic force microscopy (AFM) scans of VO₂ thin films grown by (A) pulsed laser deposition on glass, (C) electron beam evaporation on c-cut sapphire, and (E) radio frequency magnetron sputtering on silicon. AFM data have a 5 μm by 5 μm scan size. Figure reproduced from Ref. [79].

Changing the growth substrate for thin films from glass or silicon to sapphire (Al₂O₃) or titanium dioxide (TiO₂) causes epitaxial growth of VO₂. The substrate serves as a seed layer and transfers its orientation and lattice structure to the VO₂ film growing atop this seed layer.[54] All of the individual VO₂ grains are oriented in the same direction, forming an epitaxial film as opposed to a randomly oriented film which is obtained when growing VO₂ on substrates such as glass and Si.

Doping VO₂ shifts T_c up (low valence atoms like Ti⁴⁺, Cr³⁺, and Al³⁺) or down (high valence atoms like W⁶⁺, Mo⁶⁺, and Nb⁵⁺) depending on the number of valence electrons the dopant has compared to the number of valence electrons the V⁴⁺ cation has, as the V⁴⁺ cation is being replaced by the dopant.[53-55] This can also alter the insulating phase of the VO₂ at room temperature from M1 to M2 or T phase.[53] The shifts in transition temperature and insulating VO₂ crystal structure can be seen in Table 1.1 and Figure 1.28, respectively.

Dopant	Concentration (at. %)	Transition temperature decreases by	<p> $M = \text{Nb}^{5+}, \text{Mo}^{6+}, \text{W}^{6+}$ $M = \text{Al}^{3+}, \text{Cr}^{3+}, \text{Fe}^{3+}, \text{Ga}$ $y < 0$ ← reduction V^{4+} → oxidation $y > 0$ uniaxial $[110]_R$ stress → </p>
Tungsten (W)	1.0	22-28 °C	
Molybdenum (Mo)	1.5	35 °C	
Niobium (Nb)	1.0	11 °C	
Table 1.1 - Shifts in the T_c of VO_2 with different dopants. Table redrawn from Ref. [54].			Figure 1.28 - Shifts in the T_c and insulating crystal phase of VO_2 with high (red) and low (blue) valence dopants. Figure reproduced from Ref. [53].

1.4 – Active Plasmonics

1.4.1 - Motivation for Combining a LSPR and a Phase-Change Material

Combining plasmonics with phase-change materials yields active plasmonics because of the controllable changing local dielectric environment that the phase-change material provides.[80-82] This, as discussed in Section 1.2.6, shifts the plasmon resonance of the nanoparticle with a speed dependent on the transition time of the PT material and a shift dependent on the magnitude of the change in the dielectric environment in the wavelength range of the plasmon resonance. This opens up the possibility for constructing reconfigurable systems using phase-change materials. It is also possible to achieve active plasmonics using methods besides a phase-change material to controllably alter the plasmon resonance, as discussed in Ref. [83]. These include altering the plasmonic material geometry by fabricating the nanostructure on

a stretchable substrate,[84] and altering the depletion region and thus the plasmon resonance of nanoparticles to create a spatial light modulator in the terahertz spectrum.[85]

1.4.2 - Benefits of Combining VO₂ and Au Plasmonic Particles

Combining VO₂ and Au plasmonic particles primarily allows for two things. It is possible to (1) tune the plasmon resonance of the nanoparticles by switching the VO₂. This has been demonstrated by heating the entire sample,[60, 61, 86-90] by using current to locally heat the VO₂,[91, 92] and using the high local electric field of plasmonic particles on a VO₂ film which are excited on the ps timescale to induce heating.[93] Using the sensitivity of plasmonic particles to their local dielectric environment, it is also possible to (2) use the plasmon-resonance frequency and FWHM as a sensitive local probe of the properties of the VO₂ and the PT in VO₂. [94]

1.5 - Structure of Dissertation

The rest of the dissertation is structured as follows:

Chapter 2

Methods are demonstrated to integrate VO₂ and lithographically patterned Au nanoparticles as well as how to grow VO₂ and use electron beam lithography to make Au nanoparticles. Basic ways of characterizing VO₂ (WL transmission) and Au nanoparticles (WL spectroscopy setup and 5s) are also discussed.

Chapter 3

The phase coexistence pattern in low aspect-ratio VO₂ single crystals is demonstrated to be different from the previously observed pattern seen in high aspect-ratio crystals. Using plasmonic particles as probes, it is demonstrated that the phase coexistence pattern in the low aspect-ratio VO₂ single crystals is depth-dependent.

Chapter 4

Hydrogen doping of VO₂ films is monitored by changes in the plasmon resonance of Au dimers embedded in a low-scattering VO₂ film as a function of time.

Chapter 5

Near-IR plasmon-induced transparency is demonstrated in simulations of stacked Au-VO₂ dolmen structures. This PIT can be actively controlled with temperature and is polarization dependent.

Chapter 6

The major results of this work and future work that these results suggest are summarized.

CHAPTER 2

FABRICATION AND CHARACTERIZATION OF AU-VO₂ NANOSTRUCTURES

2.1 – Introduction

This chapter describes the sample design, fabrication, and characterization of Au-VO₂ nanostructures. The contents of this chapter are divided into four sections: sample design, basic sample fabrication, basic sample characterization, and contributed fabrication developments. The sample design section contains discussion of using finite-difference time-domain (FDTD) simulations to design Au-VO₂ structures. This includes the principles of FDTD simulations, doing FDTD simulations using Lumerical FDTD Solutions, interfacing FDTD Solutions with the heat transport solver in Lumerical Device, and specific considerations for simulations of Au and VO₂. The basic sample fabrication section describes how hybrid Au and VO₂ nanostructures are fabricated. A discussion of why indium tin oxide-coated glass was used as a substrate for these Au-VO₂ nanostructures, sample cleaning, VO₂ thin film deposition methods and annealing, VO₂ single crystal growth, Au deposition, spin-coating, EBL, development, and liftoff are included here. The sample characterization section contains descriptions and details of the major tools used in this work to characterize VO₂ and Au nanoparticles. Scanning electron microscopy, AFM, the temperature-dependent transmission setup, and the 5s are included. Characterization techniques specific to individual projects in this document are discussed in their respective chapters. The contributed fabrication developments section contains my innovations in the fabrication of Au-VO₂ hybrid nanostructures. This includes depositing non-scattering VO₂ films, patterning nanoparticles on VO₂ single crystals using EBL, and using a single layer of

EBL to fabricate stacked Au-VO₂ nanostructures. These contributions provide solutions to challenges that occur when interfacing Au and VO₂, such as scattering and diffusion. These contributed methods will allow for simpler fabrication of high-quality Au-VO₂ nanostructures for a wide variety of applications, from gas sensing to all-optical ultrafast switches.

2.2 - Sample Design

The Au-VO₂ nanostructure geometries examined in this work were designed using three-dimensional full-field FDTD simulations. The expected optical response of fabricated nanostructures was also simulated using FDTD with the nanostructure dimensions imported into the simulations. For descriptions of how FDTD simulations can output the broadband transmission from a region given Maxwell's equations, an electromagnetic wave, a structure with a given geometry and material properties, and the boundary conditions of the simulation regions, see Refs. [12] and [18]. These simulations of an electromagnetic wave interacting with a structure of interest were carried out with the Lumerical FDTD commercial software package. The package FDTD Solutions from Lumerical can also be easily interfaced with the heat transport solver in Lumerical DEVICE to simulate coupled physics problems such as the temperature rise in a plasmonic nanoparticle due to the optical absorption of the nanoparticle at its plasmon resonance.[95]

Lumerical has an extensive online reference guide,[96] including tutorials, to answer questions about setting up, running, and interpreting the results of simulations. In order to set up a simulation in FDTD Solutions, the steps detailed below can be followed. A simulation region is created to define the region of space where the FDTD solver will calculate a solution, with a

precision governed by the mesh accuracy. The boundary conditions, such as periodic or perfectly matched layer (PML), at each boundary of the simulation region are set. The details of periodic and PML boundary conditions are discussed in Refs. [12] and [18]. Exploiting structure geometry using symmetric and antisymmetric boundary conditions, as described here in online reference guide provided by Lumerical in Ref. [97], can be used to reduce the size of the simulation region and, thus, the time required to simulate the response of the structure by a factor of up to four. The shapes, sizes, positions, and optical properties of the components comprising the structure of interest are defined. It is possible to import structures from experimental images such as scanning electron microscopy (SEM) micrographs, as well as to create the structures with the shapes available in the program. Following this, an override mesh can be created to increase the spatial precision of the simulation in the region of interest – such as a nanoparticle – without the necessity to increase the precision used for the entire simulation region. Determining the appropriate override mesh size is discussed in Ref. [12]. An excitation source (a plane wave for this work) is added to the simulation region and the position, polarization, incident angle, and wavelength range are set. Frequency-domain field and power monitors are then placed in the simulation region to collect data (which, in this work, are transmission and local electric field) when the simulation is run. For this work, transmission measured from a monitor placed in the substrate beneath the nanostructure of interest and local electric field is measured from a different monitor, which slices through the nanostructure of interest at a height of half the thickness of the nanostructure. At this point, the simulation is run and results can be viewed. Script files can be used to automate modifications of nanostructure geometry, the running of simulations, the analysis of spectra, and the extraction of data, but these tasks may also be done by hand. Scripts used to do these tasks are included in an appendix.

Two considerations, the first regarding simulating nanostructures on a VO₂ film, and the second regarding the simulation converging, are now addressed. First, when simulating the transmission of nanostructures on a VO₂ film, it is helpful to normalize the response of the full structure to that of the full geometry without the nanostructures. For VO₂ thin films, which have significant losses, this allows the response to the nanoparticle to be observed without the background VO₂ losses, but still with VO₂ as part of the local dielectric environment of the nanoparticle. This method is akin to how transmission spectra are measured experimentally, in which a bright-field spectrum is taken on the sample away from the region of interest so that the effect of the substrate can be removed from the spectrum taken at the region of interest. Second, it is important that the automatic shutoff level in the simulation is reached before the maximum simulation time is reached. Since the automatic shutoff level is a measure of how much the simulation has converged, a simulation that ends before this level (10^{-5} at minimum for the nanostructures simulated here) has not fully converged and the results of this simulation are not trustworthy. This can occur when high aspect ratio nanoparticles, such as the Au nanorod from Chapter 3, are simulated. If the automatic shutoff level is not reached, the simulation time can be increased until the level is reached.

2.3 - Basic Sample Fabrication

2.3.1 - Substrate Details

Samples, with the exception of the single crystal VO₂ samples, were made on 5 x 5 x 0.5 mm indium tin oxide (ITO) coated glass substrates from Delta Technologies. The 15-30 nm ITO coating served to minimize the buildup of electrons on the surface of the substrate

during electron beam lithography so that the position of the electron beam was not shifted due to electrons accumulating on the surface being patterned. Glass and ITO, a transparent conductive oxide, were employed because the experimental geometry to measure the samples in transmission in the visible to near-IR wavelength range is less complex than the geometry to measure samples in reflection. For lithographically patterned samples, these materials were also preferable to silicon (Si) because of their lower refractive indices in comparison to Si. This means that a nanoparticle designed to be resonant at 800 nm when on an ITO-coated glass substrate would be larger than a nanoparticle designed to be resonant at the same wavelength on Si, thus decreasing the difficulty of the EBL patterning.

2.3.2 - Cleaning Substrates

Substrates were cleaned by submerging them in room-temperature tetrachloroethylene (TCE) and both the top and bottom surfaces of the substrates were wiped in a circular motion using a cotton tipped applicator. This process was repeated in acetone, methanol, and deionized water. The substrates were then dried using compressed air and visually inspected for debris. The process was repeated until no debris was observed.

2.3.3 - VO₂ Thin Film Deposition Mechanisms

Radio frequency magnetron (RF-M) sputtering of VO₂ takes place in an Ångström Engineering Inc. Amod deposition system. A 5 cm diameter vanadium metal target is used as the sputtering source, and is sputtered at 180 Watts at a pressure of 6 mTorr in an atmosphere comprising 20 sccm of argon and 1 sccm of O₂. The resulting plasma is verified to have set up before the shutter is opened and the deposition begins. The deposition rate is kept constant at

1 Å/s. The sample holder rotates during the deposition.

Electron beam evaporation (EBE) of VO₂ takes place in the same Ångstrom Engineering Inc. Amod deposition system used for sputtering. An electron beam is rastered across a VO₂ powder precursor at 5x10⁻⁶ Torr. The power of the electron beam is increased until the deposition rate is determined to be stable at 1 Å/s by a quartz crystal microbalance (QCM). At this point, the shutter opens and the deposition begins. The deposition rate is monitored during the deposition and the power is adjusted to maintain a deposition rate of 1 Å/s. The sample holder rotates during the deposition.

Pulsed laser deposition (PLD) of VO₂ takes place in an Epion PLD-3000 system with a Lambda Physik (Coherent COMPex) krypton fluoride (KrF) excimer laser ablating a vanadium metal target. The KrF laser has a wavelength of 248 nm and operates at 385 mJ per pulse with a 25 Hz repetition rate. The deposition occurs in a 10 mTorr O₂ atmosphere with a 2 sccm flow rate. The laser is rastered across the rotating target and the ablated material deposits on onto samples 8 cm above the target, which are also rotating during the deposition.

2.3.4 - Annealing Samples

Vanadium dioxide grown at room temperature via EBE, PLD, and sputtering require thermal annealing to crystallize the material. The VO₂ will not exhibit a phase transition if this annealing is not done. This is accomplished in a horizontal tube furnace. The samples are placed in the tube furnace which is pumped down to 30 mTorr before the samples are annealed for 10 minutes at 450 °C in 250 mTorr of O₂ and removed, without breaking vacuum, to a room-temperature region of the furnace to cool for an additional 10 minutes, at which point vacuum is broken and the samples are removed.

2.3.5 - VO₂ Single Crystal Growth

Single crystals of VO₂ are grown on Si and quartz substrates by physical vapor transport in a horizontal tube furnace at 1.7 Torr and 825 °C in an argon gas environment for 1 hour using vanadium pentoxide (V₂O₅) powder loaded upstream of a 10 × 1 × 1 cm³ crucible with substrates loaded between 5 and 7 cm downstream. After growth, the furnace is allowed to cool to 100 °C, vacuum is broken, and then the samples are removed. This method was developed by Dr. Bob Marvel [98] following the synthesis described in Refs. [99] and [100]. There is little control over the nucleation of single crystals, their precise size, or the distance between them.[98, 100, 101] On average, the single crystals that grow on quartz substrates are larger than those grown on Si substrates, as shown below.

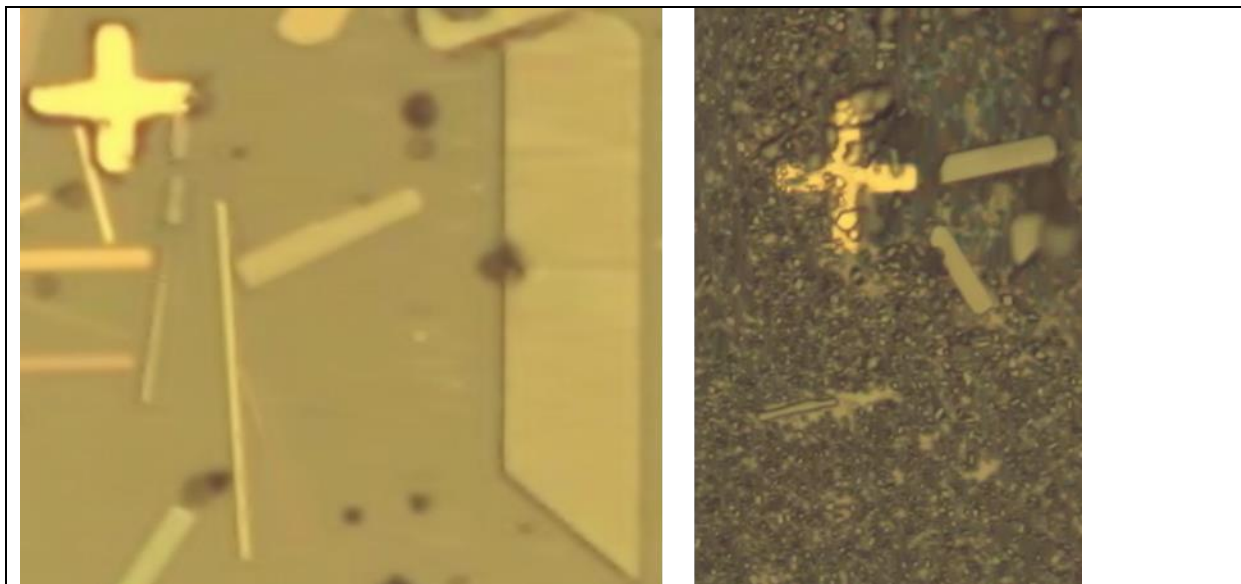


Figure 2.1 - Optical microscopy of typical VO₂ single crystals grown on quartz (left) and Si (right). Photolithographically patterned cross markers are 30 μm by 30 μm.

2.3.6 - Spin-coating Resist onto Samples

For electron beam lithography, spin-coating is used to coat the sample with a uniform layer of the EBL resist polymethyl methacrylate (PMMA) which is in an anisole solvent. The percentage of PMMA to anisole alters the thickness range into which the final PMMA layer can fall, and the molecular weight of the PMMA controls how sensitive the polymer is to the electron beam during EBL.[102] It is ideal for the total thickness of the PMMA to be approximately three times the thickness of the final fabricated nanostructures so that bad liftoff results are not as likely to occur as they would for thinner PMMA. With a three to one ratio, the resolution is not as low as it would be for thicker PMMA. The thickness of a layer of PMMA with a given molecular weight and percent PMMA is controlled by the speed at which the sample is spinning, with higher speeds yielding thinner PMMA. After the PMMA is spun-coated on to a sample, the sample is baked at 180 °C for 90 seconds on a hot plate to remove residual anisole.

2.3.7 - Electron Beam Lithography

Electron beam lithography (EBL) is used to pattern nanoparticles of arbitrary shapes and spacings with feature sizes as small as 5 nm,[103] which is below what is achievable with photolithography. The Heidelberg Instruments uPG101 Laser Writer has a minimum feature size of 600 nm, for example.[104] For use with positive resists such as PMMA, the electron beam is incident on the sample in the locations where a nanoparticle is desired. The PMMA in these locations is damaged by the electron beam and, therefore, easier to remove chemically than undamaged regions. The electron beam can be steered to desired locations within a given write field by deflecting the beam, and to reach areas outside of this write field, a translation stage moves the sample. The EBL system used in this work is a Raith eLINE system. The working

distance for this work is 10 mm and the aperture used was the 10 μm aperture. A step size of 0.004 μm and a settling time of 2 ms are also used. For this work, a write field of 100 μm by 100 μm is used, as the maximum array size used is less than this write field and thus the array could be written without needing to move the stage. The accelerating voltage varied with sample and is specified when discussing each specific sample.

2.3.8 - Development

Development is done to remove the damaged polymer from EBL. The sample is submerged in MIBK:IPA so the patterned side is perpendicular to the ground (vertically) and agitated to ensure that all damaged polymer is removed from the sample. Agitation can be done by placing a magnetic stir bar in the beaker being used and setting it to stir at 300 rpm for one minute, or by alternating between holding the sample steady with tweezers while shaking the beaker of MIBK:IPA sideways and pipetting MIBK:IPA at the sample in 30 second intervals for 90 seconds. After agitation, the sample is rinsed with IPA to halt the development, rinsed with DI water, and dried using compressed air. After the sample is dry, it can be baked on a 100 $^{\circ}\text{C}$ hotplate for 90 seconds to sharpen the edges of the resist.

2.3.9 - Gold deposition

Thermal evaporation of Au was carried out in a Kurt J. Lesker Nano 36 in vacuum at a rate of 1 $\text{\AA}/\text{s}$ with an Au pellet as the precursor. The thickness of the Au was monitored by a quartz crystal microbalance.

2.3.10 - Liftoff

Liftoff is done to remove the undamaged PMMA and the deposited material on top of the PMMA so that only nanoparticles of the desired material remain on the sample. There are multiple ways to achieve this depending on factors such as the adhesion between the nanoparticles and the substrate, the density of nanoparticles, the feature size, and the ratio of PMMA thickness to nanoparticle thickness. In general, the sample is submerged vertically into heated liftoff liquid (100 °C for PG remover and 80 °C or 60 °C for acetone), left to soak until the film appears puckered on the substrate from the PMMA dissolving (anywhere from 10 minutes to 4 hours or more), pipetted with clean liftoff liquid to remove large pieces of PMMA, and left to soak for another period of time in liftoff liquid. After this, the sample is rinsed in room temperature acetone, IPA, and DI water and dried with compressed air. If this proves to be insufficient to remove all of the PMMA, the sample can be sonicated before rinsing.

2.4 - Sample Characterization

2.4.1 - Scanning Electron Microscopy

Scanning electron microscopy is used to image the fabricated samples, which provides contrast between different materials dependent on their conductivities. This was done on the Raith eLINE and the Zeiss Merlin systems using a 10 kV accelerating voltage and a working distance of 10 mm. For the Raith, the 10 μm aperture was used. The Raith has less difficulty imaging samples on ITO-coated glass substrates than the Merlin does because electrons from the electron beam build up on the sample surface and cause larger beam deflections in the Merlin than in the Raith. If carbon tape can be placed on the top of the sample, this charging can be

alleviated when using the Merlin because the carbon tape provides conductive pathways for the electrons to leave the sample surface. Tilted SEM measurements can be done on the Merlin for angles between 0 and 55 degrees to provide information about the thickness of multilayer samples and single crystals, whereas the Raith lacks this capability. Thus, both SEMs have their advantages and uses for characterizing the samples described in this work.

2.4.2 - Atomic Force Microscopy

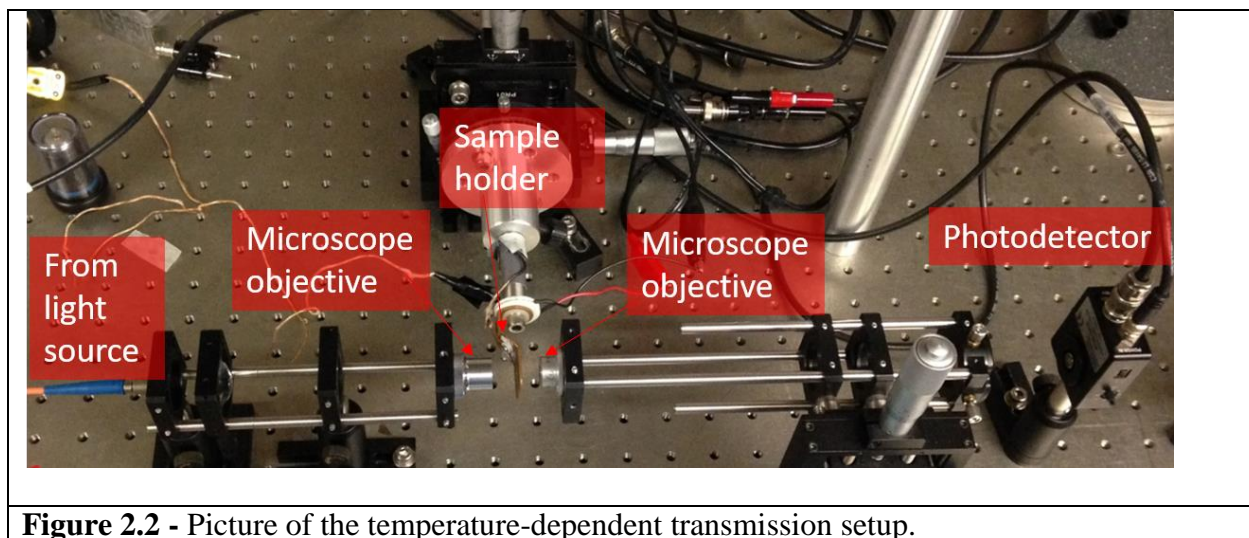
Atomic force microscopy (AFM) is used to image some of the fabricated samples, providing contrast between different areas depending on their relative heights. This was done on the Bruker Dimension Icon in tapping mode. Image post-processing, including leveling AFM scans and measuring nanoparticle heights, was done using Gwyddion software.[105]

2.4.3 – Temperature-Dependent Transmission Setup

The optical transmission as a function of temperature through samples containing VO₂ is measured using a home-built temperature-dependent transmission setup in the Haglund lab. The transmission of 1550 nm laser light or of light from a broadband white-light source (Spectral Products High Power Tungsten-Halogen light source with a 3000 K bulb) is measured. Using 1550 nm laser light is helpful for samples with small amounts of VO₂ (films less than 20 nm thick or VO₂ nanoparticle arrays) because the switching contrast is high at 1550 nm.

The essential components of this setup are a fiber-coupled light source, a 5x microscope objective to focus the light to a 100 μm diameter beam spot on the sample, a sample holder with a Peltier heater for temperature control and a hole through the center of the holder to allow for the transmission of light, a second microscope objective to collect the transmitted light and focus

it, and a Thorlabs PDA10CS InGaAs amplified detector. It is important to check that the beam is not clipped going into either of the microscope objectives by holding up a piece of paper before each objective and verifying that the entire spot is collected by the objective. A piece of paper can also be held up after each objective to verify that the spot on the paper is still circular after passing through each objective. It is also important to check that the beam is well-focused on the photodetector by moving the three-dimensional translation stage attached to the second microscope objective to maximize the current from the photodetector measured using a Labview program on a desktop computer next to this setup in Stevenson Center room 6517. The temperature of the Peltier heater is swept from 30 °C to 90 °C and back to 30 °C, and is managed by a voltage supply, which can be computer-controlled. The temperature of the sample, as monitored by a thermocouple placed on top of a glass reference slide on the sample holder, and the transmission detected at the photodetector are monitored and recorded using the same LabView program mentioned above, which exports this information to a text file.



The hysteresis parameters described section 1.3.4, such as switching contrast and critical

temperature, are extracted by fitting the temperature-dependent transmission to two sigmoids describing the optical transmission during heating and cooling of the sample, respectively. A sigmoidal fitting curve for transmission as a function of temperature is described below.

$$T(t) = min + \frac{C}{1 + E^{s(t-t_{c,dir})}} \#(2.1)$$

In this curve, T is the transmission, t is the temperature, min is the minimum transmission for the curve, C is the switching contrast, s is the steepness of the sigmoid which indicates the abruptness of the VO₂ PT, and $t_{c,dir}$ is the temperature associated with half of the switching contrast. Curves like this are fit to both the heating and cooling parts of the data. The C values for the two curves are averaged to extract the average value of C for the hysteresis curve, the $t_{c,dir}$ values are averaged to find T_c for the hysteresis, and the difference of the $t_{c,dir}$ values is taken to find the hysteresis width.

This setup can be modified in a variety of ways. A lens can be added between the light source and the microscope objective to collimate the beam. Adding a beam-splitter between the light source and first microscope objective allows for the reflected light from the sample to be measured when the photodetector is placed in the reflected beam path. This also allows for hysteresis measurements on nano-patterned samples if a camera attached to a monitor is placed in the reflected beam path and the photodetector remains in the transmitted beam path. It is also possible to switch out the photodiode with a fiber-coupled spectrometer such as the Avantes AvaSpec-2048-2-USB2 (referred to as the “Avantes” hereafter) or the Princeton Instruments Acton SP2300 (referred to as the “Princeton” hereafter) for white-light spectroscopy in the visible to near-IR regime on films or nanoparticle samples with large (at least 100 μm x 100 μm,

as constrained by the spot size at the sample) arrays. A polarizer can be added before the sample if the sample response is polarization-dependent.

2.4.4 - Small Spot-Size Spectroscopy Setup

The small spot-size spectroscopy setup (“5s” device) is an optical setup built by the Haglund lab at Vanderbilt University and used to do white-light spectroscopy in the visible to near-IR regime on nanoparticle arrays that are less than 100 μm x 100 μm in size. Modification to the hysteresis allows for some white-light spectroscopy on nanoparticles, but this is constrained to large arrays, which are time-consuming to fabricate on the Raith. The 5s is a dedicated nanoparticle spectroscopy setup that can do spectroscopy on arrays as small as 10 μm x 10 μm in size.

The essence of this setup is similar to that of the temperature-dependent transmission setup with the necessary modifications to do spectroscopy. A fiber-coupled light source is put through a 50 μm aperture to reduce the object size being focused, collimated with a lens, polarized, focused onto the sample with an apochromatic 20x microscope objective with a long working distance, a sample holder with resistors for temperature control and a hole through the center of the holder to allow for the transmission of light, an apochromatic 5x microscope objective with a long working distance to collect the light, and a second lens to focus the light on to an optical fiber connected to either the Avantes or the Princeton. A second apochromatic 5x microscope objective with a long working distance is affixed to a Watec America Corp LCL-902C camera connected to a monitor is used to image the sample and position the array of interest at the location of the beam of light. An image of this setup is included below.

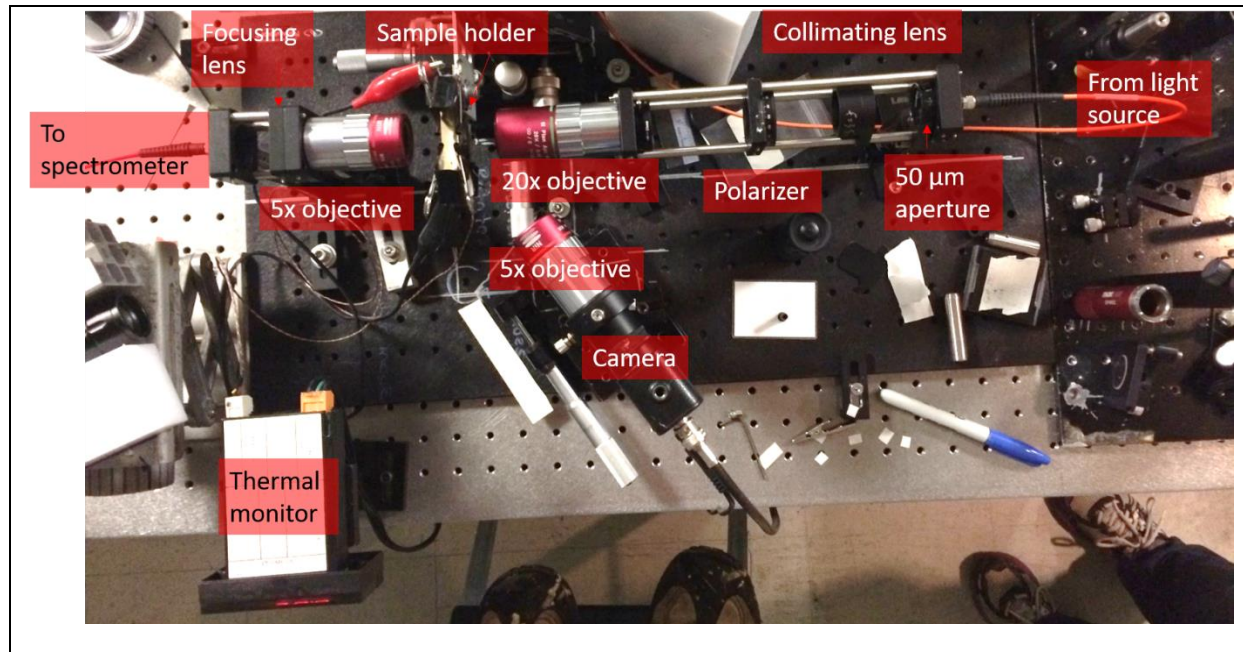


Figure 2.3 - Image of the small spot size spectroscopy setup (“5s”) with relevant components labeled.

A few comments about these components are included below. The optical fibers are changed as appropriate based on the wavelength region of interest to be sure that this region is transmitted through the fibers to the spectrometer. Apochromatic microscope objectives are used because they reduce the chromatic aberration of the light source and thus the spot size of the light source of the wavelength range of interest.[106] The spot size is reduced because the wavelengths are focused much closer to the same position, as opposed to the focal location being strongly wavelength dependent as it is in achromatic lenses.[107] This is critical for obtaining a spot small enough for spectroscopy on $10\ \mu\text{m} \times 10\ \mu\text{m}$ sized nanoparticle arrays. The high-power (10 W) $1\ \Omega$ resistors are wired in parallel and attached to an Epsco D-612T Filtered DC power supply to heat the sample to $90\ ^\circ\text{C}$, which requires approximately 4.5 A and 2.2–2.3 V. The sample holder is used because its thermal expansion is low, so the arrays remain in approximately the same location with respect to the focal plane as the sample is heated and cooled.

2.5 - Contributed Fabrication Developments

2.5.1 - Non-scattering VO₂ thin films

As discussed in Chapter 4, the scattered optical signal of Au dimers embedded in a VO₂ thin film can be used to detect hydrogen. Hydrogen doping of VO₂ alters its dielectric function, which in turn influences the Au dimers. The effect of the hydrogen doping is detected as a shift in the scattering signal from the dimers because their plasmon resonance has been altered by this change in local dielectric environment. To detect these modifications of the Au dimer scattering signal, it is necessary that the VO₂ in which the dimers are embedded has low scattering so that the film scattering signal is negligible compared to the dimer scattering signal.

Scattering of Au dimers embedded in VO₂ thin films was measured using dark-field microscopy at Vanderbilt University and using single-particle-dark-field microscopy at MPI-IS. Vanadium dioxide films grown using PLD, EBE, and sputtering were tested for this application. The results of these tests are described in the remainder of this section.

Vanadium dioxide thin films were deposited at various thicknesses on Si and ITO-coated glass substrates via PLD. Thin films of VO₂ 110 nm thick were deposited on Si and both 100 nm and 50 nm VO₂ thin films were deposited on ITO-coated glass. All of these samples had Au dimers on the substrates, so that the VO₂ deposition embedded the dimers. Based upon dark-field scattering measurements taken at MPI-IS, films made via this deposition method scatter strongly in comparison to the scattering from the individual Au dimers. Thinner PLD VO₂ films appear more highly scattering than thicker films, but it is either impossible or nearly impossible to see scattering from any Au dimers embedded in these PLD films. This can be seen below,

with a fourth image for low-scattering VO₂ showing the locations of 25 Au dimers with scattering signals clearly distinguishable from that of the overlying film.

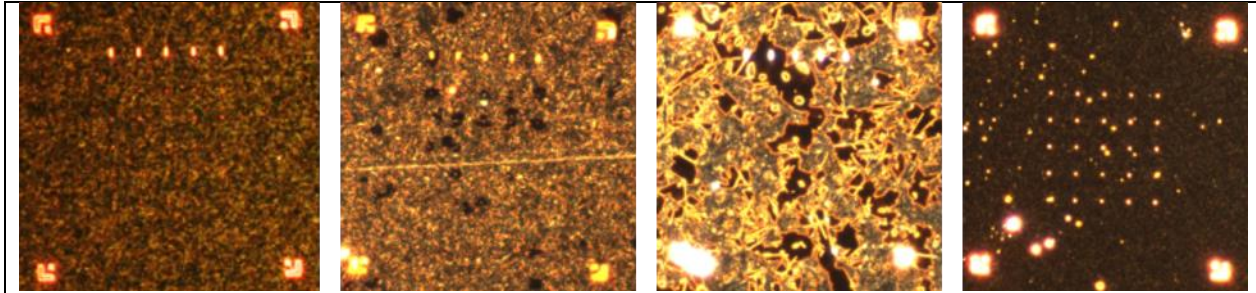


Figure 2.4 – Dark-field scattering of Au dimers embedded in PLD VO₂ films which are 110 nm thick and on Si, 100 nm thick and on ITO-glass, and 50 nm thick and on ITO-glass. The fourth scattering image shows Au dimers covered with low-scattering VO₂. This is included as a reference image, so that the locations of the Au dimers in the other images are known and it is evident what the dimers would look like if their scattering is visible. For the 110 nm VO₂ thin film, scattering from the dimers is barely visible. For the 100 and 50 nm films, scattering from the dimers is completely hidden by scattering from the VO₂ thin films.

Vanadium dioxide thin films 105 and 106 nm thick were deposited via EBE on ITO-coated glass substrates decorated with Au dimers. The two depositions were done two years apart but using the same deposition parameters, as described in Section 2.3.3. The earlier 105 nm EBE VO₂ deposition yielded low-scattering VO₂, but the later deposition yielded high-scattering VO₂. The results of Ref. [79] indicate that EBE VO₂ will be less rough, as measured by AFM, if annealed for a shorter period of time. Under the assumption that a decrease in film roughness decreases film scattering, a second sample from the later 106 nm deposition was annealed for 5 minutes instead of the typical 10 minute anneal. A shorter annealing time did produce a decrease in the VO₂ film scattering to the point where the scattering from the Au dimers is visible, as can be seen in Figure 2.5. However, this still results in VO₂ which is much more highly scattering than the film at the left and is undesirable for detecting changes in the Au

dimer scattering signal. Overall, the results from EBE VO_2 depositions indicated a lack of reproducibility as well as high scattering, both of which are undesirable for this application.

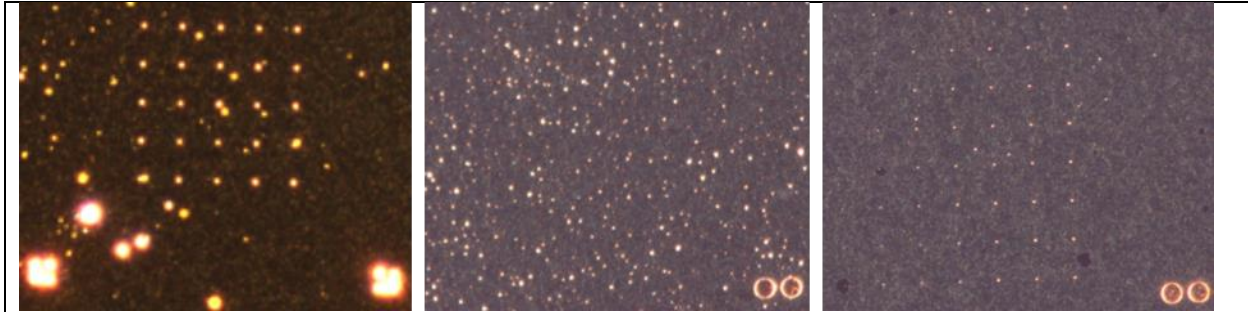


Figure 2.5 – Dark-field scattering of Au dimers embedded in EBE VO_2 films which are 105 nm thick (left) and 106 nm thick (center and right) with a slightly different Au dimer EBL pattern on ITO-coated glass. The left and center films were annealed for 10 minutes and the right film was annealed for 5 minutes. The scattering from the Au dimers is clearly visible (left), not visible (center), and somewhat visible (right).

Vanadium dioxide thin films 100 nm, 108 nm, and 93 nm thick were deposited on ITO-glass via sputtering. The samples from all three of these depositions (one sample, four samples, and 19 samples, respectively) had low-scattering VO_2 such that the scattering from the underlying Au dimers was clearly visible with dark-field scattering. Representative dark-field scattering images on samples from these three depositions are shown below. These results indicate that RF-M sputtering VO_2 is a reproducible process with which to fabricate low-scattering VO_2 on top of plasmonic nanoparticles such that scattering from the plasmonic nanoparticles can be clearly seen.

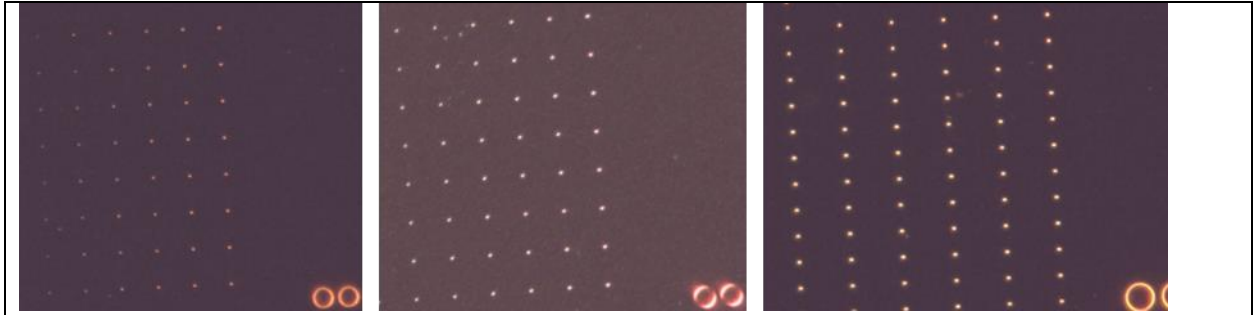


Figure 2.6 – Dark-field scattering of Au dimers embedded in RF-M sputtering VO₂ films which are 100 nm thick (left), 108 nm thick (center), and 93 nm thick (right). The scattering from individual Au dimers can be clearly seen in all three of the images.

2.5.2 - EBL on VO₂ Single Crystals

It can be useful to lithographically pattern nanoparticles on top of arbitrarily shaped and positioned materials with variable thicknesses because for many applications the materials of interest can exist at random locations on a sample surface. Patterning Au nanoparticles on top of VO₂ single crystals is one such case. Gold nanoparticles in the form of dipole antennas (nanorods, nanodisks) or bow-tie antennas can probe and report upon their local dielectric environment and thus provide information about the growth of the metallic phase of VO₂ in single crystals that coexists with the insulating phase of VO₂. With a high enough local electric field generated by the nanoparticles, it may even be possible to influence the growth of these metallic regions. Patterning Au nanoparticles atop VO₂ single crystals has two major challenges. First, the crystals nucleate at random positions on any given substrate, grow to arbitrary sizes, and are arbitrarily oriented such that some samples have no crystals that are large enough to fit the Au nanoparticles on their top surface. For this reason, it is difficult to locate a particular single crystal that can be used for EBL. Second, the single crystals have random thicknesses, which can be as thick as hundreds of nanometers. This poses an issue for EBL, since the focus position where the top of the crystal is in focus is different from the focus position where the

substrate is in focus and it is undesirable to focus on the top of the crystal and expose the PMMA coating the top before EBL is carried out.

These challenges are overcome by modifying the conventional EBL steps described in the prior EBL section. The first challenge is circumvented with a combination of optical microscopy and photolithographically patterned alignment markers. Each substrate on which single crystals are grown, as described above, is examined via optical microscope to determine if there are large enough single crystals for EBL which are not located at the corners or edges of the sample. Substrates containing good single crystals are covered with Cr alignment markers every 200 μm , as can be seen in Figure 2.7. The alphanumeric grid accompanying the cross markers is used to locate individual single crystals of interest and the crosses are used for alignment when doing EBL. The second challenge is mitigated by spin-coating thick PMMA and focusing on the corners of single crystals. To ensure that PMMA coats the tops of the single crystals which are hundreds of nanometers high so that EBL can occur, a thick coat of PMMA is used at the price of decreased resolution during EBL. To focus the electron beam to the height of the top of an individual single crystal during EBL without exposing the resist before patterning, the beam is used to scan only a small corner of the crystal and that corner is focused upon without exposing the majority of the single crystal. This is justified because individual single crystals are uniform in height.

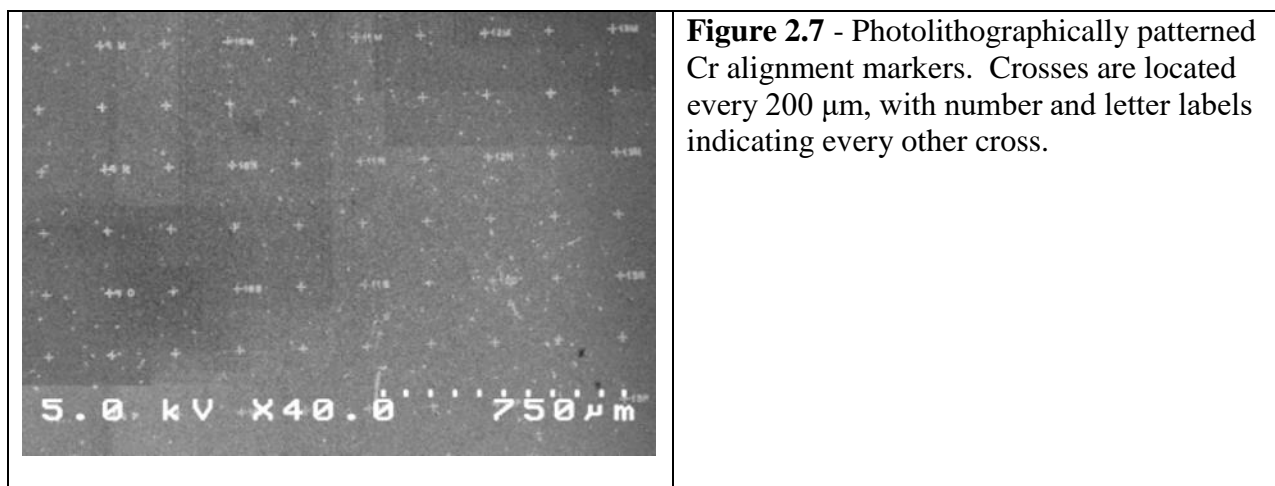


Figure 2.7 - Photolithographically patterned Cr alignment markers. Crosses are located every 200 μm , with number and letter labels indicating every other cross.

Below, the steps to pattern nanoparticles on top of VO_2 single crystals are described. More detail for aligning EBL to write on top of a single crystal is provided in an appendix. Vanadium dioxide single crystals are grown on quartz or Si substrates, as described VO_2 Single Crystal Growth section, and examined with optical microscopy to check crystal sizes. Photolithography is carried out using a Heidelberg Instruments uPG101 Laser Writer. Shiply 1813 is used as the photoresist and is spun at a spin speed of 2000 rpm for a total thickness of approximately 2 μm . Chromium is deposited at 1 $\text{\AA}/\text{s}$ to a thickness of 100 nm using a Kurt J. Lesker Nano 36 and liftoff is done using room temperature acetone and a stir bar at 300 rpm. Single crystals appropriate for EBL are located using an optical microscope. Images are taken of each appropriate crystal and the alphanumeric marker nearest to each crystal to be used for EBL is noted to allow for easy location and identification of these crystals. The polymer used for the EBL process is 950 A4 PMMA. A blob of PMMA is applied onto the sample, covering the entire sample, when it is in the spincoater but is not spinning. The spin parameters to obtain good coverage of the polymer on the tops of the single crystals are a spin speed of 1000 rpm and a spin time of 45 seconds with a 5 second acceleration up to 1000 rpm. A bake on the hotplate at 180 $^\circ\text{C}$ for 5 minutes is necessary to evaporate the solvent. Due to the slow spin speed, regions

of thicker PMMA exist at the edges and corners of the samples, making these areas unusable for EBL. The Kurt J. Lesker Nano 36 is used to deposit a 10 nm dissipation layer of Cr at a rate of 1 Å/s. A metal clip is used to hold the sample to the holder to keep the sample in good thermal contact with the holder and not cook the PMMA. A pump-down time of 30-40 minutes is sufficient to create a high enough quality film to serve as a dissipation layer. The dissipation layer makes EBL patterning on the non-conductive VO₂ single crystals easier. Electron beam lithography is carried out on the sample (920 kV accelerating voltage, 10 mm working distance, 10 μm aperture), blanketing each single crystal of interest and the nearby area with the desired nanoparticle pattern.

After EBL patterning, the sample is held vertically in small beaker of Cr etch for 15-20 s to remove the Cr dissipation layer. The sample is then rinsed with DI water and gently blown dry with compressed air. The development is achieved by placing the sample in MIBK-IPA for 1 minute. To maintain consistent polymer removal from sample to sample, agitation is done using a magnetic stir bar set to 300 rpm placed in the MIBK-IPA beaker in the center of the hot plate where the magnet is located. The sample is held vertically with tweezers and placed such that it is on the edge of the beaker and the front of the sample is faces the direction of the fluid agitation due to the magnetic stir bar during this process, as seen below. The sample is then rinsed with IPA followed by DI water and gently blown dry with compressed air. The Kurt J. Lesker Nano 36 is used to deposit 50 nm of Au at a rate of 1 Å/s, which will form the Au nanoparticles at the locations written with EBL. Due to potential liftoff issues for small particles, a 2 nm Cr adhesion layer may be deposited before the Au so that the Cr is between the VO₂ single crystals and the Au. The Cr layer is deposited at a rate of 0.5 Å/s. Hot acetone is used for liftoff on the sample. Acetone is heated to 80 °C for around 10 minutes on a hot plate in

a beaker with a magnetic stir bar set to 300 rpm. The sample, held and positioned the same way as was described previously in the development step, is placed in this agitating acetone for 5 minutes. To remove the larger pieces of the polymer, after the first 5 minutes, the sample is raised out of the solution and pipetted with hot acetone. The sample is placed back in the agitating acetone for 5 more minutes, after which it is lifted out and pipetted with hot acetone. The sample is then rinsed with clean acetone, followed by IPA, followed by DI water and gently blown dry with the air gun.

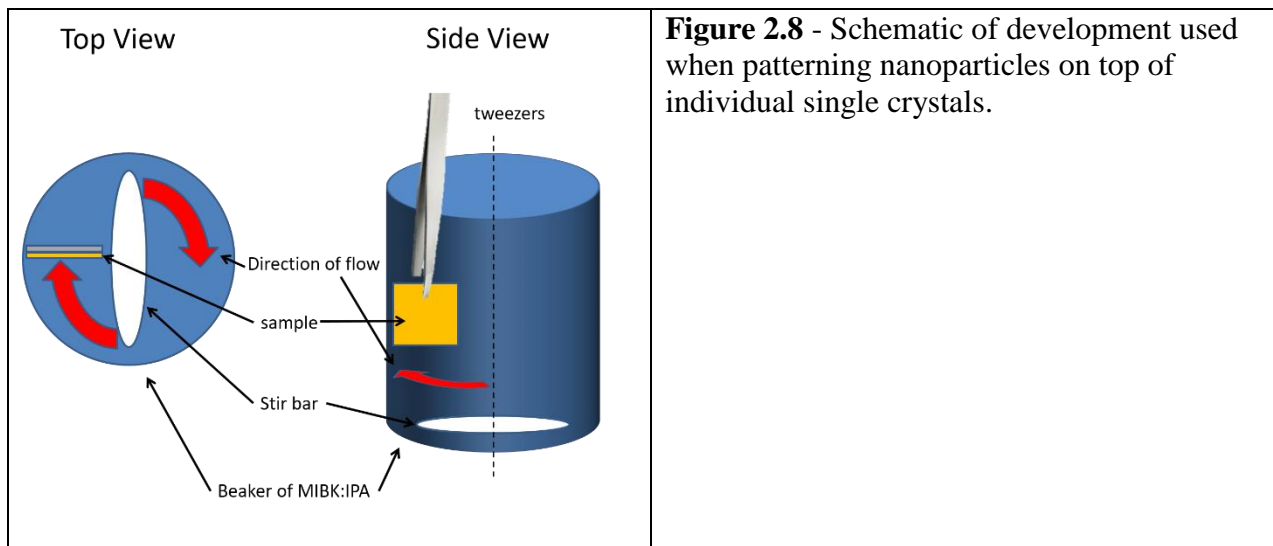


Figure 2.8 - Schematic of development used when patterning nanoparticles on top of individual single crystals.

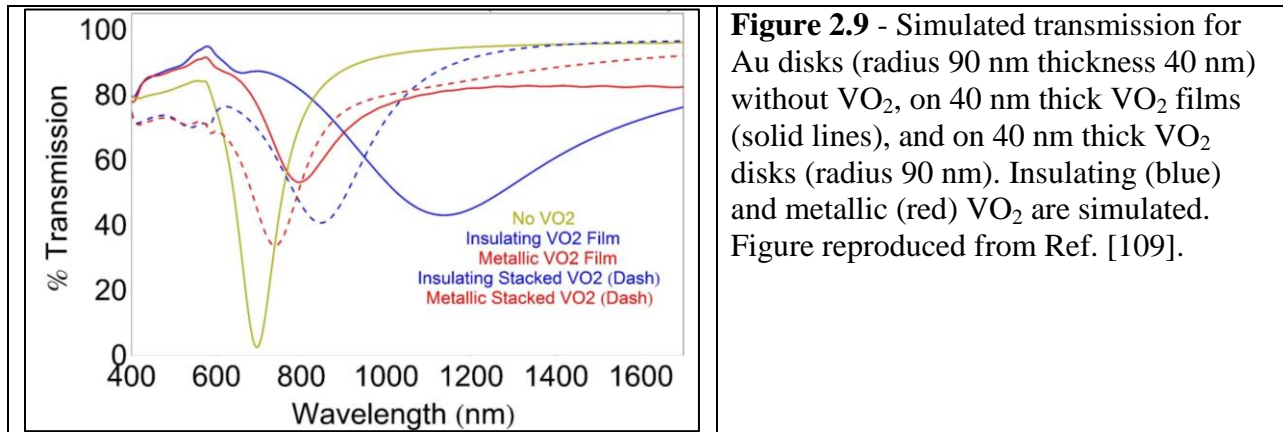
2.5.3 – Stacked-Structure Fabrication

2.5.3.1 - Introduction

To maintain active modulation of Au plasmon resonances while reducing the losses, which come about from using a VO₂ thin film, it is desirable to fabricate Au and VO₂ nanoparticles conformally and in close proximity to each other. This can be achieved using multilayer EBL to pattern first one material and then the second, either stacked on top of each other or close together in-plane which has been demonstrated in Ref. [108]. The influence of

VO₂ thin films and VO₂ nanoparticles on an Au disk plasmon resonance can be seen in Figure 2.9. The resonance is broadened more for thin films than for nanoparticles of VO₂, for which a measurable plasmon-resonance shift still exists when using VO₂ nanoparticles. Using multilayer lithography to fabricate such structures with nanometer precision is challenging, so layering Au and VO₂ in the wells defined by a single step of EBL is an easier fabrication process. This stacked-structure fabrication process is termed “SSF” hereafter.

Applying this method to Au-VO₂ hybrid structures is challenging due to the difficulties of interfacing a low melting point material (Au) with a material which requires processing at 450 °C. This is also difficult because the two materials are deposited using different methods, thus making the dynamics of the material plumes during deposition different.



Previous work on SSF focused on fabricating VO₂-Au stacked disks with a variety of diameters.[110] In these samples, the VO₂ was deposited via PLD and, after Au deposition and liftoff, annealed for 20 minutes. A single layer of PMMA 180 nm thick was used for EBL. When compared with simulations of similar nanostructures, the experimentally measured resonance shifts (insulating to metallic VO₂) for disks with diameters of 122 nm or less were significantly smaller. This deviation increased with decreasing disk diameter. Only for disks

with a diameter of 148 nm was there agreement between the simulated and experimental resonance shift. A summary of the experimental and simulated response of these stacked disks can be seen in Figure 2.10. It is suggested that this may be due to the Au and VO₂ intermixing, Au doping the VO₂, or the VO₂ not being perfectly stoichiometric. It is suggested that the annealing time (20 minutes) and/or the annealing temperature (450 °C) be decreased to reduce these effects. More details regarding the fabrication, simulation, and characterization of this previous work on SSF can be seen in Ref. [110].

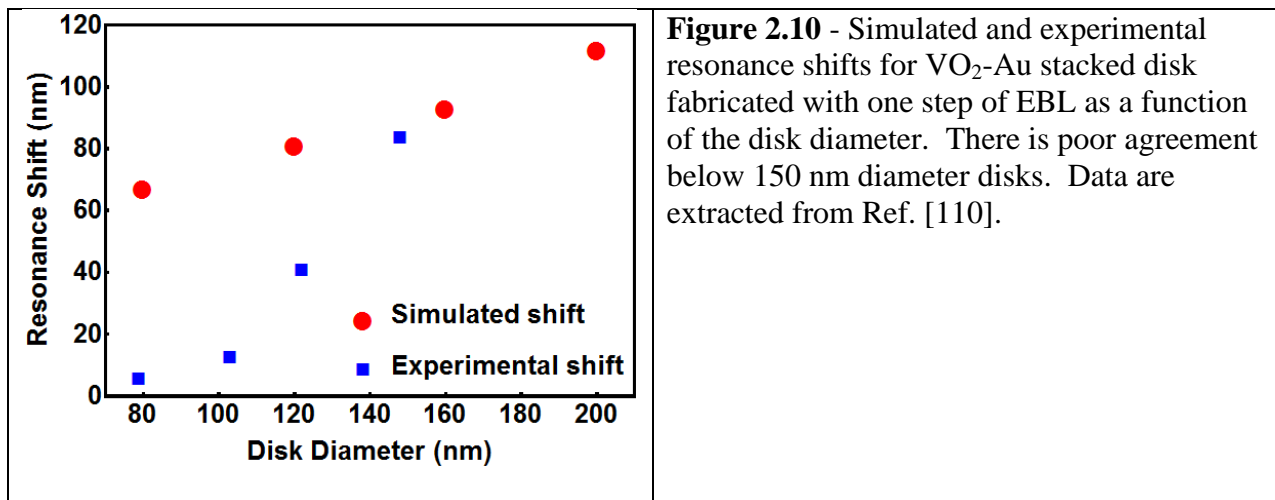


Figure 2.10 - Simulated and experimental resonance shifts for VO₂-Au stacked disk fabricated with one step of EBL as a function of the disk diameter. There is poor agreement below 150 nm diameter disks. Data are extracted from Ref. [110].

Here, VO₂-Au, Au-VO₂, and Au-VO₂-Au stacked structures are fabricated and the processes used are modified to optimize the SSF method. The samples fabricated with the SSF method are characterized with a variety of tools. SEM is used to verify that the EBL was successful and measure the in-plane dimensions of the various Au and VO₂ layers, which can be distinguished thanks to their different conductivities. AFM is used to measure the height of the composite structure. Based on the heights of pure Au nanoparticles, the height of the VO₂ in a composite structure can be determined. To verify that there were no errors during the VO₂ deposition process such as an incorrect gas atmosphere or RF-M sputtering target, a VO₂ thin

film witness sample deposited at the same time that the VO₂ nanoparticles are fabricated is annealed and measured in the temperature-dependent transmission setup. If a hysteresis with a reasonable contrast and critical temperature is obtained, then characterization of the sample containing VO₂ nanoparticles is continued. The 5s or the temperature-dependent transmission setup with spectroscopy modifications is used to measure the transmission spectrum of the hybrid Au-VO₂ nanoparticle sample both above and below the VO₂ phase transition. The choice of spectroscopy setup is determined by the size of the nanoparticle arrays being measured. For small arrays where the expected resonance shift over the VO₂ phase transition is small, transmission spectra above and below the VO₂ phase-transition temperature are measured both before and after annealing to isolate the effects of the VO₂ phase transition from other temperature-dependent effects. The simulated transmission spectra of the nanoparticles above and below the phase transition are also determined by simulating the nanostructure in Lumerical FDTD using the experimental dimensions measured via SEM and AFM. Thus, the simulated and experimental spectra of the nanoparticles can be compared.

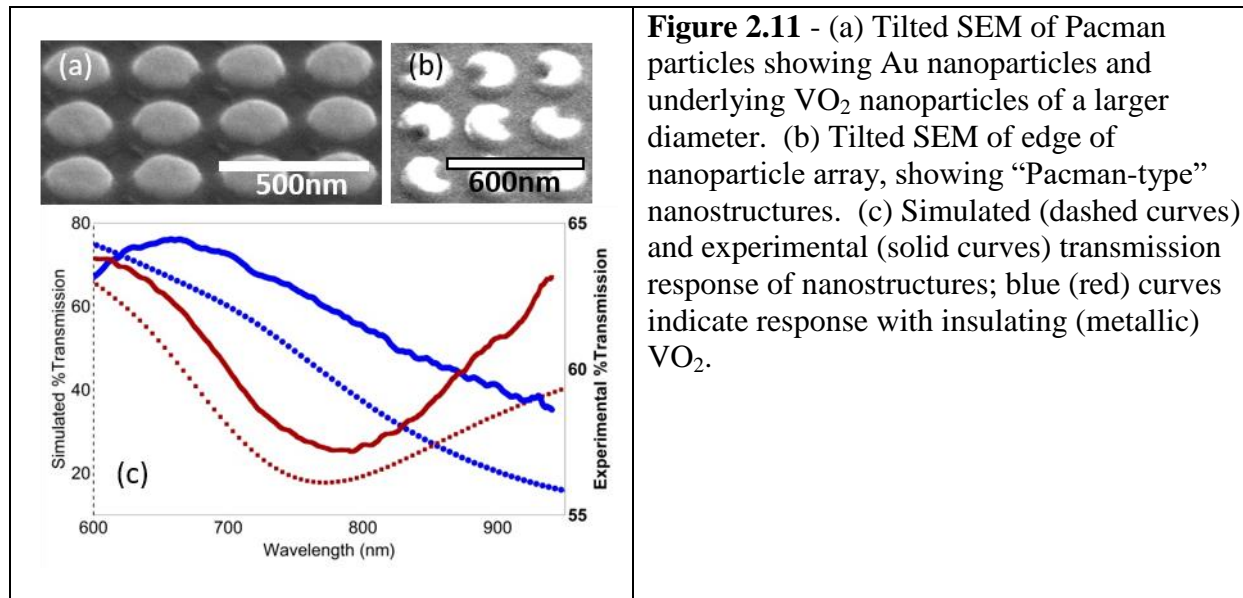
2.5.3.2 Fabrication Process and Rationale

A description of the steps taken to fabricate Au-VO₂-Au stacked disk nanostructures, named “nano wedding cakes” because the top Au disk has a smaller diameter than the VO₂ or bottom Au disk, and the rationale for these steps follows. The ITO-glass substrate is spin-coated with 90 nm of 495 A2 PMMA and 70 nm of 950 A2 PMMA and baked after each layer is spin-coated. After EBL and development, Au is evaporated as described above, to a thickness of 20 nm. Radio frequency magnetron sputtering of VO₂ is done using a tilted sample holder raised up 40 mm from its lowest position with the samples faced towards the sputtering source. The sample holder does not rotate for this deposition. The QCM setpoint is 45 nm, yielding a VO₂

nanoparticle thickness of 26 nm. A second layer of Au is evaporated, also to a thickness of 20 nm. A long-duration liftoff is carried out on the sample to remove the residual PMMA.

The sample is suspended vertically in a beaker of acetone heated to 60 °C on a hot plate. The beaker is covered with parafilm, and the sample soaks in this heated acetone for four hours. The sample is pipetted with acetone while still submerged to remove large chunks of polymer, then removed from this beaker and placed in a beaker of clean acetone with the lithography facing upwards, and sonicated for 10 seconds. The sample is then removed from the beaker, rinsed with DI water, and gently blown dry with compressed air. The sample is annealed as described above.

Radio frequency magnetron sputtering is used to deposit VO₂ instead of electron beam evaporation (EBE) or pulsed laser deposition (PLD). Using EBE to make VO₂ nanoparticles leads to large shadowing, producing particles with smaller dimensions than intended. Thus, EBE is not used here. Pulsed laser deposition is neglected in favor of RF-M sputtering, as PLD is a longer and more complex process than RF-M sputtering. Pulsed laser deposition-made VO₂, though, has been used to produce VO₂-Au nanoparticle disk stacks, named Pacman particles for the shape of particles around the edge of the array. These nanoparticles were used to verify that Au and VO₂ can be used to fabricate stacked structures where the Au and VO₂ properties (plasmon resonance and phase transition) are both maintained after annealing. The Pacman particles are fabricated through the following process. First, the ITO-glass sample is spin-coated with 100 nm of 495 A2 PMMA and 140 nm of 950 A2 PMMA and baked after each layer is spin-coated. After EBL and development, 40 nm of PLD VO₂ followed by 2 nm of thermally evaporated Cr and 40 nm of thermally evaporated Au are deposited onto the sample. After liftoff, the sample is annealed as described in the earlier annealing samples section.



In this case, the substrates were mounted on a tilted holder instead of a flat holder for RF-M sputtering. The tilted holder is angled such that the sample surface is oriented perpendicular to the direction of sputtered atoms coming from the sputter gun and raised 40mm from the lowest position. In contrast, sputtered atoms from the sputter gun strike the flat holder (rotating) at an angle. Thus, fewer atoms of VO₂ reach the bottom of the wells in PMMA patterned by EBL when the flat holder is used instead of the tilted holder, reducing the thickness of the resultant VO₂ nanoparticles. Images of the flat and tilted holders and their orientations in the RF-M sputtering system are included in Figure 2.12.

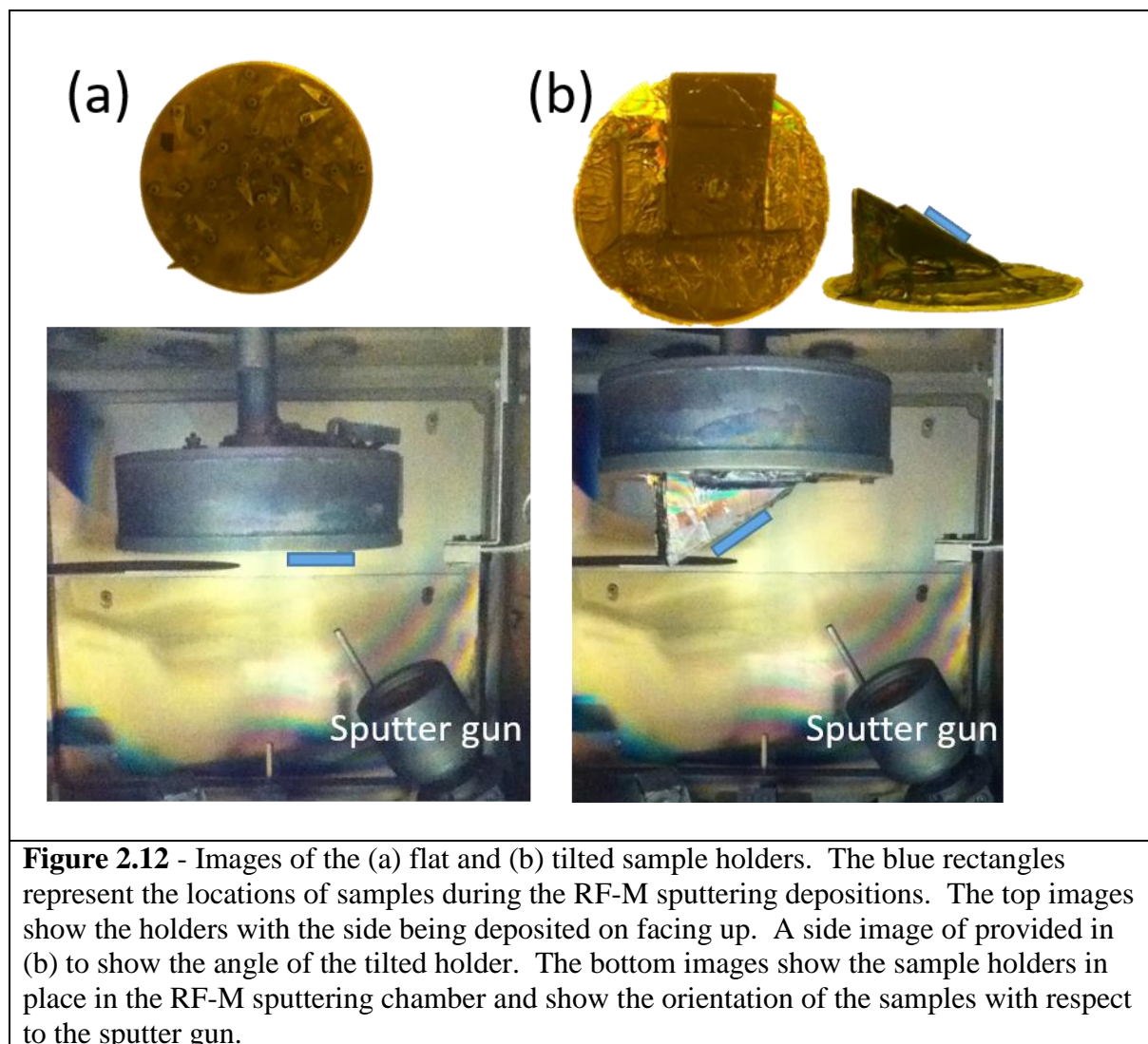


Figure 2.12 - Images of the (a) flat and (b) tilted sample holders. The blue rectangles represent the locations of samples during the RF-M sputtering depositions. The top images show the holders with the side being deposited on facing up. A side image of provided in (b) to show the angle of the tilted holder. The bottom images show the sample holders in place in the RF-M sputtering chamber and show the orientation of the samples with respect to the sputter gun.

A thin (160 nm) double layer of PMMA was used instead of a thicker (300 nm) double layer when depositing RF-M sputtered VO_2 using the tilted sample holder, even though a lower PMMA to nanostructure thickness ratio increases liftoff difficulties. The thin double layer consisted of 90 nm of 495 A2 PMMA and 70 nm of 950 A2 PMMA, and the thick double layer consisted of 100 nm of 495 A2 PMMA and 200 nm of 950 A4 PMMA. The thick double layer did not permit fabrication of RF-M sputtered VO_2 nanoparticles thicker than 7 – 10 nm as measured by AFM, which is too thin to cause a measurable plasmon-resonance shift in the

underlying Au nanoparticles due to the small change in the local dielectric environment. The thin double layer permitted fabrication of 30 nm thick VO₂ nanoparticles, which is sufficient to induce a measureable plasmon-resonance shift in the underlying Au nanoparticles. A geometric argument is suggested to explain the effect of the PMMA thickness on the VO₂ nanostructure thickness. EBL-patterned wells of the same radius have a higher angle of acceptance if they are shallower, permitting the deposition of more RF-M sputtered VO₂. A schematic of this is shown in Figure 2.13. Using the thicknesses of the 950 PMMA layer for the thick (200 nm A4 PMMA) and thin (70 nm A2 PMMA) double layer processes, described above, as the well depths and 100 nm as the well radius, the angle of acceptance is calculated. The θ_{acc} values are 55° and 27° for 70 nm and 200 nm thick wells, respectively.

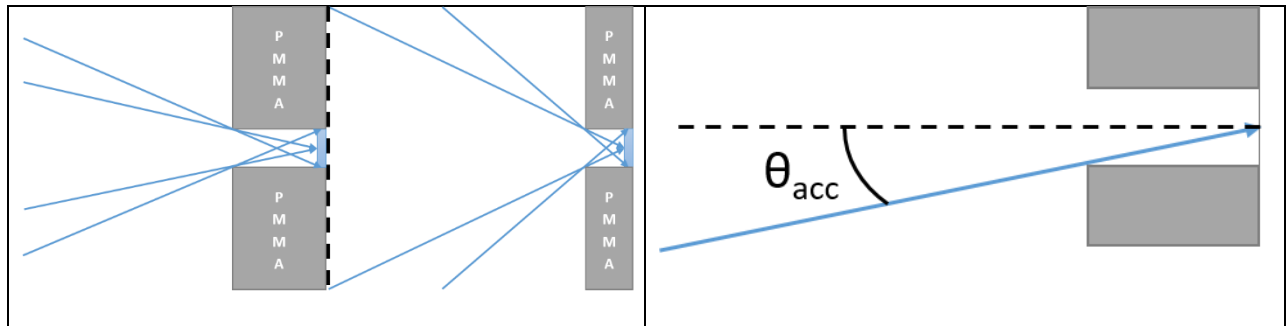
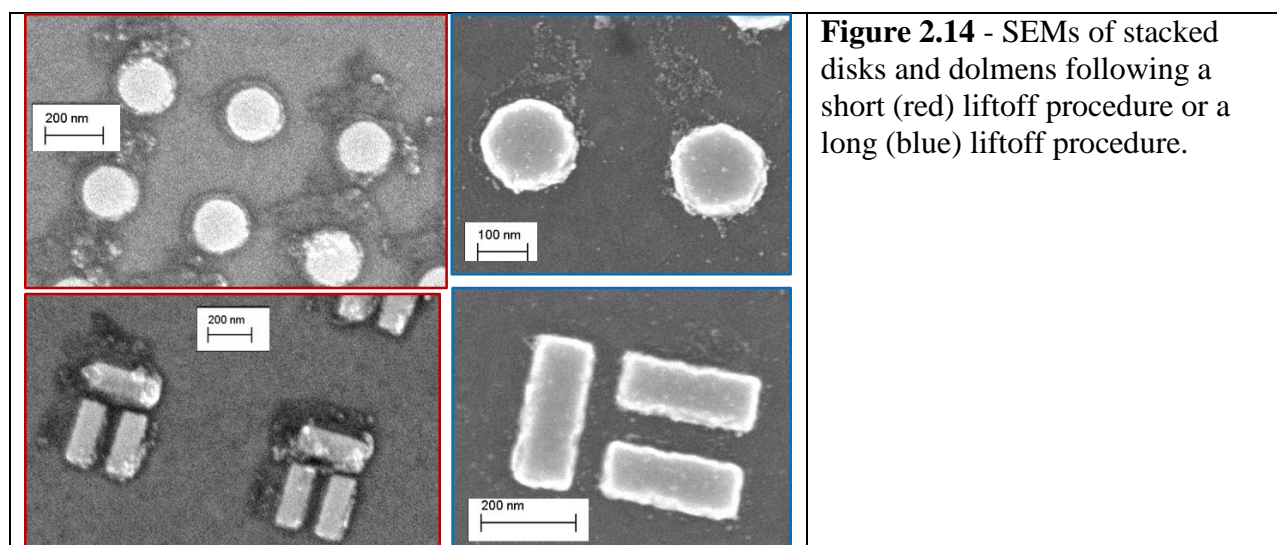


Figure 2.13 - Schematic showing the largest angles which depositing material (blue lines) can have and still reach the bottom of the EBL-patterned wells in the PMMA and deposit there to form a nanoparticle (blue). The angle of acceptance is clearly smaller for a deeper PMMA well than for the shallower well. Schematic indicating θ_{acc} is in the right panel.

A long liftoff process including sonication was used for these samples instead of a short process, when the samples were spin-coated with 90 nm of 495 A2 PMMA and 70 nm of 950 A2 PMMA. The short process is suitable when thicker PMMA is used, as the liftoff is easier when the ratio of the PMMA height to nanostructure height is higher. The short process is unsuitable for use with this thinner PMMA, as significant residual PMMA remains on the sample surface

following liftoff. A long process yields a far cleaner surface while not being aggressive enough to remove the Au-VO₂ structures. A comparison of the samples where liftoff was short vs long can be seen in Figure 2.14, with irregularly shaped dark regions indicating areas where PMMA remains on the sample surface. The short liftoff process consists of soaking the sample in 80 °C acetone for 10 minutes with a magnetic stir bar rotating at 300 rpm, pipetting the sample with clean acetone, soaking the sample in heated acetone for a further 5 minutes, pipetting the sample with clean acetone, rinsing the sample with IPA followed by DI water, and blowing the sample dry with compressed air.



The fabrication results of the nano wedding cake structures are discussed below. From AFM, it is determined that the bottom and top Au layers are both 20 nm thick and that the VO₂ layer is 26 nm thick, which is sufficiently thick to cause a measurable plasmon-resonance shift in the surrounding Au disk nanoparticles, shown in Figure 2.15. From the SEM, shown in Figure 2.15, it is evident that the bottom Au layer and the VO₂ layer have different diameters than the

top Au layer. At the edges of the arrays, the top Au layer is also offset from the bottom two layers, as shown below. This smaller diameter ranges from 55% to 63% of the bottom layer diameter as the bottom diameter ranges from 158 to 197 nm. It is suspected that the difference in PMMA molecular weight, and thus volume of PMMA exposed and removed, between the top layer (950 PMMA) and the bottom layer (495 PMMA) is the cause of this wedding cake effect. As the nanostructure thickness gets close to the thickness of the 495 A2 PMMA, there is less room for the deposited material to expand radially and fill the footprint of the well, as shown in Figure 2.16. This may explain the wedding cake shape of these nanoparticles.

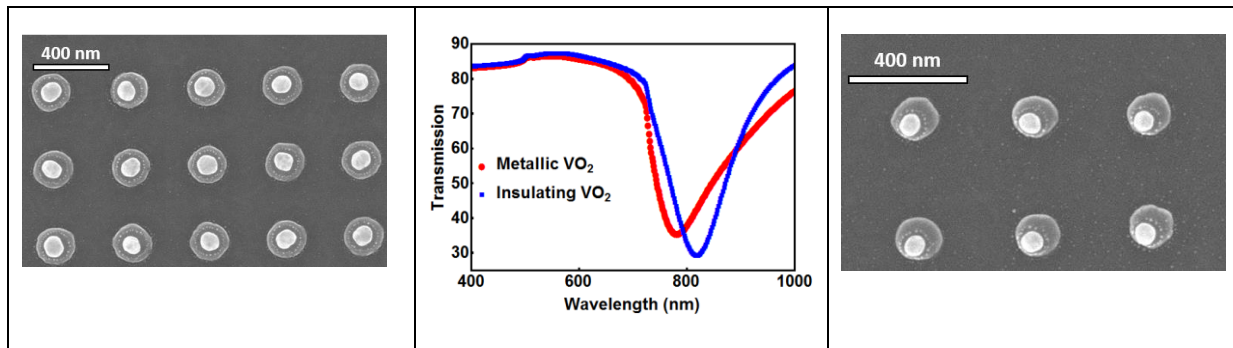


Figure 2.15 - Nano wedding cakes. On the left is an SEM of nano wedding cakes with the top Au layer (diameter 124 nm) centered on underlying VO₂ and Au layers (diameter 197 nm). In the center are the simulated transmission spectra for metallic and insulating VO₂. The dimensions are those of the experimentally fabricated samples at the left. On the right is an SEM of nano wedding cakes with top Au layer (87 nm) offset from the center of the underlying VO₂ and Au layers (diameter 158 nm).

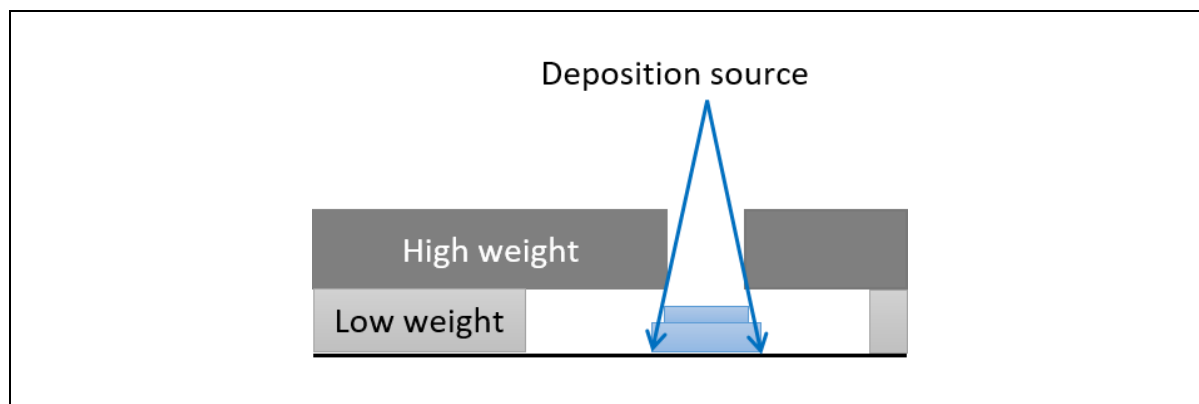


Figure 2.16 - Diagram showing the radius of a particle (blue) with increasing height in a two layer EBL-defined well. High molecular weight PMMA (950 PMMA) is shown in dark gray and low molecular weight PMMA (495 PMMA) is in light gray. Blue arrows show the angle of acceptance for material deposited into this well. The nanoparticle decreases in diameter as the nanoparticle thickness increases.

Based on these results, a few modifications could be made to the SSF process to improve the resultant Au-VO₂ hybrid nanoparticles. Coupled usage of a single layer of PMMA and a longer liftoff time than employed here may reduce the nano wedding cake effect without decreasing the quality of the liftoff. Changing the VO₂ deposition method back from RF-M sputtering to PLD may reduce the likelihood of the VO₂ thickness during deposition cutting off at a thickness that is too thin for the desired nanostructures due to geometric constraints. A thin diffusion barrier, such as sapphire (Al₂O₃), between all Au and VO₂ layers should also prevent any intermixing or doping between the two materials. Simulations would need to be run to determine the influence of diffusion barrier layers on the optical properties of an Au-VO₂ hybrid nanostructure before implementing this modification.

2.5.4 - Significance of Contributed Fabrication Developments

The fabrication developments described here - fabricating non-scattering VO₂ films, patterning nanoparticles atop VO₂ single crystals, and fabricating stacked Au-VO₂

nanostructures – provide new sample geometries for examining the interactions of the phase-change material VO₂ with Au plasmonic nanoparticles. These developments allow for the hydrogen doping of VO₂ thin films probed by embedded Au nanoparticles and the phase coexistence of VO₂ single crystals to be examined as well for stacked Au-VO₂ dolmen nanostructures to be fabricated, as discussed in the following three chapters.

CHAPTER 3

VO₂ SINGLE CRYSTAL PHASE COEXISTENCE

The results of this work are published in *Nanotechnology* with DOI: 10.1088/1361-6528/aa5652.

The citation for this paper is as follows:

McGahan C, Gamage S, Liang J, Cross B, Marvel R E, Haglund R F and Abate Y 2017
Geometric constraints on phase coexistence in vanadium dioxide single crystals
Nanotechnology **28** 085701

3.1 – Introduction

The appearance of ordered, coexisting phases during a phase transition is characteristic of VO₂ single crystals. Stripes of metallic (M) and insulating (I) VO₂, as well as their associated atomic structures, have been examined in VO₂ single crystals as a function of strain, doping, temperature, and electrical current, among others. In these studies, the M and I stripes are oriented perpendicular to the long axis of the VO₂ single crystals. With a single exception in literature, though, all the research looking at ordered coexisting M and I phases in VO₂ single crystals has been done using high aspect-ratio crystals and assuming that the coexistence is the same as a function of depth, leaving the physics of M/I phase coexistence on low aspect-ratio VO₂ single crystals and the depth-dependent M/I phase coexistence of VO₂ single crystals unexamined. The M/I phase coexistence for a low aspect-ratio single crystal was shown here to have a different pattern of M and I domains than previously observed and to be depth-dependent. A novel herringbone pattern of coexisting M and I domains (seen at the right in the schematic below) altered by ferroelastic domains was found in a low aspect-ratio single crystal probed via

s-SNOM and far field optical microscopy, in contrast to stripes seen in high aspect-ratio single crystals. The well-known perpendicular stripe pattern were reproduced in high-aspect-ratio nanobeams, as can be seen on the left part of Figure 3.1.[111] Furthermore, it was discovered that M domains nucleate below the crystal surface using the response of plasmonic antennas placed on the crystal surface, suggesting that M domains nucleate at the substrate-crystal interface and grow towards the surface with increasing temperature as opposed to being the M/I phase coexistence being depth-independent. The results suggest that aspect ratio alters the pattern of phase coexistence in VO₂ single crystals and that the phase coexistence is depth-dependent. This herringbone pattern of M/I phase coexistence may be related to the absence of an aspect-ratio-related geometric constraint [50, 112] and to substrate-induced strain that is relieved by the formation of ferroelastic domains.[113] This work is a starting point for more sophisticated probing of phase coexistence in VO₂ single crystals as a function of depth within an individual crystal and as a function of crystal aspect ratio. For example, a plasmonic bow-tie or other structured antenna placed upon thin VO₂ single crystals would be sensitive to M domains nucleating at the substrate-crystal interface and the growth of an M domain could be probed using the plasmon-resonance shift of the antenna as a function of temperature.

3.2 - Background

Single crystals of VO₂ exhibit coexisting, ordered metallic (M) and insulating (I) domains in thermal equilibrium that have been observed using scattering-scanning near-field optical microscopy (s-SNOM),[111, 114] pump-probe s-SNOM,[115, 116] scanning near-field microwave microscopy,[113, 117] and optical microscopy.[117, 118] Coexisting, ordered

monoclinic (M1 and/or M2) or triclinic (T) and rutile (R) domains have been observed in thermal equilibrium via Raman spectroscopy,[53, 113, 116, 119] with insulating VO₂ observed to have M1, M2 or T crystal structure and metallic VO₂ observed to have a rutile crystal structure. Rutile and M1 structural domains have been shown to correspond with the locations of coexisting M and I domains imaged with reflected white light, respectively.[120] Transient coexisting metallic and insulating domains have also been observed in nanobeams using optical pump-THz probe s-SNOM even below the fluence threshold required to initiate the completed phase transition.[116] Ordered phase coexistence of stripes perpendicular to the c_R axis or in a herringbone structure has also been observed in cracked epitaxial VO₂ films on TiO₂ which form ribbons[112, 121, 122] as well as single crystals both on their growth substrate [50, 111, 113, 117, 118, 123] and clamped on a different substrate [119] due to strain. However, with a single exception in the literature,[50] these experiments have been carried out on micro- or nanobeams with high aspect ratios and, until now, no one has investigated in detail the critical issue of stripe phases in geometries with low aspect ratios typical of bulk single crystals.

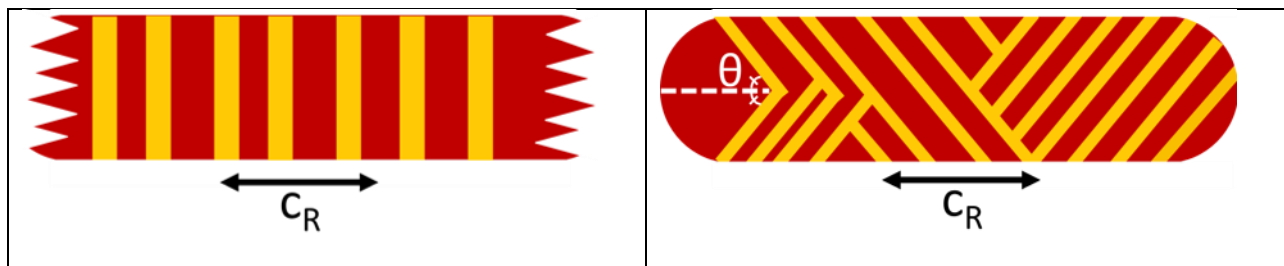


Figure 3.1 - Phase coexistence patterns for VO₂ single crystals. Perpendicular stripe pattern shown on the left and pure herringbone pattern shown on the right. All the herringbone domains form at θ from the c_R direction. Yellow domains indicate metallic VO₂ and red domains indicated insulating VO₂. Arrows indicate the direction of the rutile c crystal axis of VO₂.

3.3 - Materials and Methods

Coexisting M and I phases in VO₂ single crystals were examined during the thermally induced IMT using a commercial (neaspec.com) s-SNOM integrated with a laboratory-built heater (Figure 3.2-a). A platinum-iridium-coated atomic force microscope (AFM) tip, oscillating at a resonance frequency of 280 KHz, was illuminated by a focused CO₂ laser ($\lambda=10.7 \mu\text{m}$) at 45° with respect to the sample surface.[124, 125] A fraction of this light was focused by the AFM tip to a nanoscale light source at the apex of the tip. The excitation laser was polarized perpendicular to the plane of incidence (s-polarized) and the scattered signal was detected in the plane of incidence (p-polarized). The scattered signal from the tip-sample interface was demodulated at harmonics of the tip frequency to suppress the background from the light not focused by the AFM tip and detected via pseudoheterodyne interferometry. By raster scanning the sample surface, concurrent topographical (Figure 3.2-b) and near-field optical (Figure 3.2-c) images of VO₂ single crystals and Au nanoantennas were recorded as a function of temperature with 15 nm resolution. Vanadium dioxide switches from I to M at an applied electric field of order 2×10^7 V/m to 7×10^7 V/m[62, 126] and also when exposed to a picosecond pulse of alternating current (AC) terahertz electric field with a peak value of 1×10^8 V/m,[127] both of which are initiated and driven by the Poole-Frenkel effect. These threshold values are orders of magnitude higher than the 6×10^5 V/m electric field of the CO₂ laser used to excite the plasmon.

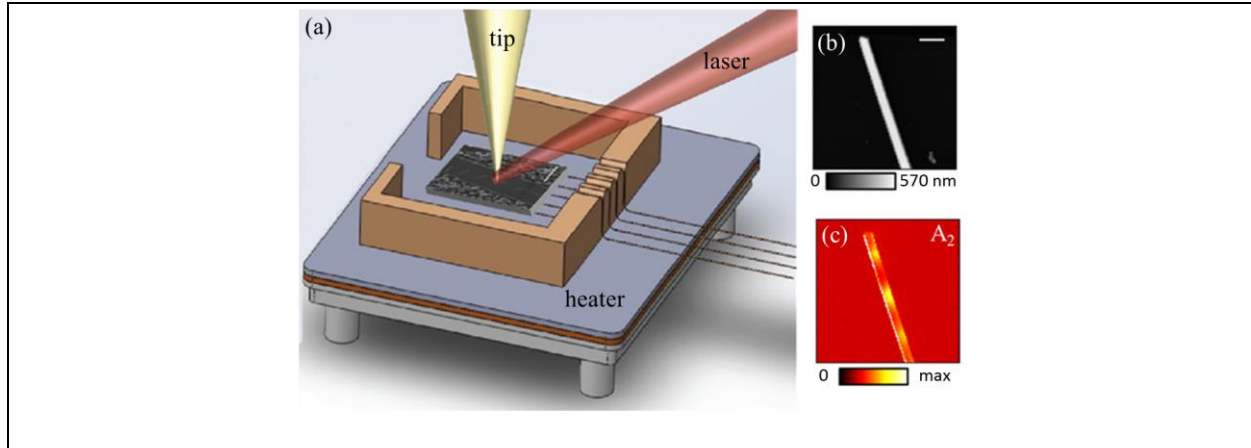


Figure 3.2 - Schematic of the s-SNOM setup (a), topographic (b) and second harmonic near-field amplitude (c) images of a single crystal VO₂ nanobeam grown on sapphire substrate recorded at temperature 50°C and laser wavelength, $\lambda=10.7 \mu\text{m}$. Scale bar at top of (b) represents 50 nm and applies to (b) and (c). Optical amplitude image of the strained beam displays the formation of coexisting metallic (bright) and insulating (dark) domains even below the critical temperature. Figure reproduced from Ref. [128].

The topographic image of a VO₂ nanobeam (Figure 1b) shows a uniform crystal, free of defects and grain boundaries, indicating that the optical contrast in Figure 3.2-c is not due to the existence of multiple grains. The strong contrast in scattering amplitude in s-SNOM at 10.7 μm is due to local variations in the polarizability of the sample [59, 124] due to differences between the optical constants of VO₂ in M and I regions. From ellipsometry, the values $\epsilon_1=2.4$ and $\epsilon_2=2.9$ for I VO₂ and $\epsilon_1=-3.3$ and $\epsilon_2=45$ for M VO₂ are measured. Based upon the VO₂ optical constants, the M regions are expected to have strong scattering amplitudes due to the large negative ϵ_1 and large positive ϵ_2 , whereas I regions are expected to have weaker scattering amplitudes due to the moderate ϵ_1 and small ϵ_2 . [129] In this way, s-SNOM can image the phase coexistence in VO₂ using a CO₂ laser and M and I domains can be identified based upon their relative scattering amplitudes.

Figure 3.2-c shows the s-SNOM amplitude image of a VO₂ nanobeam below the critical temperature for the IMT. Regions with strong scattering amplitudes are coded as bright

(represented by yellow) and correspond to scattering from metallic VO₂ domains, whereas regions with weak scattering amplitudes are assigned as dark (represented by red) and correspond to insulating domains. Since s-SNOM images the local permittivity of the sample within the optical near-field of the tip at the excitation wavelength, the probe volume extends into the bulk of the crystal [124, 130-135] within the penetration depth of both insulating and metallic VO₂. Thus, at 10.7 μm, the s-SNOM is sensitive to the phases of VO₂ domains well below the surface of a single crystal.

Vanadium dioxide single-crystal microbeams were fabricated as described in Chapter 2. The VO₂ crystals were grown on a silicon substrate covered with its native thermal oxide, typically 2 nm thick as measured by ellipsometry. Chromium alignment markers were patterned photolithographically after crystal growth, allowing specific crystals to be located by scanning electron microscopy (SEM) and s-SNOM as described in Chapter 2. Due to the strong contrast of the IMT in s-SNOM at mid infrared frequencies, the gold antennas (3.2 μm by 300 nm nominal dimensions) were designed to be resonant with 10.7 μm light and fabricated atop individual single crystals via EBL with a Raith eLINE system as described in Chapter 2. The crystal chosen for this experiment has an aspect ratio of 5:1, which differs from that of the nanobeams examined in Figure 3.2-b and 3.2-c and that of nanobeams with aspect ratios of order 20:1 examined in previous work with the exception of one previous study where a low-aspect-ratio crystal was imaged.[50] The resulting structures are shown in Figure 3.3. Identical Au rods were oriented on an individual single crystal at 18° angular increments over a 90° range of angles to permit in-plane polarization-dependent measurements, as the excitation laser in-plane polarization direction cannot be modified in this apparatus. Fabricating Au antennas resonant with the CO₂ laser also allowed for simultaneous imaging of the M/I phase coexistence and the

Au plasmon resonance.[59] A plasmon resonance can be observed by s-SNOM as having increased scattering compared with its surroundings. This is because the incident electric field induces the dipole plasmon resonance of the nanoparticle, which has its own electric field. These fields combine and are scattered into a detector to produce a high scattering signal. When imaging the out-of-plane field of the nanoparticle, bright regions are expected at the tips of the nanorod, which are basically out of phase with each other.[136] This can be seen in the experimental 3rd harmonic amplitude and phase images of an individual resonant Au nanorod in Figure 3.4.

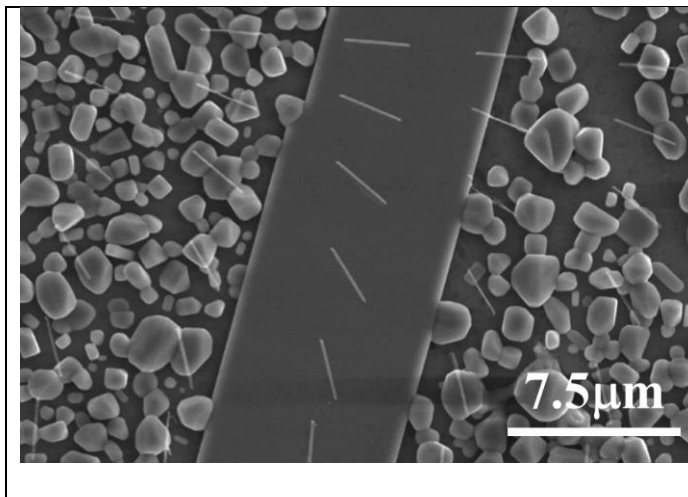


Figure 3.3 - Scanning electron micrograph of VO₂ single-crystal microbeam grown on silicon substrate. Gold nanorods were fabricated on top of the single crystal via electron beam lithography. Figure reproduced from Ref. [128].

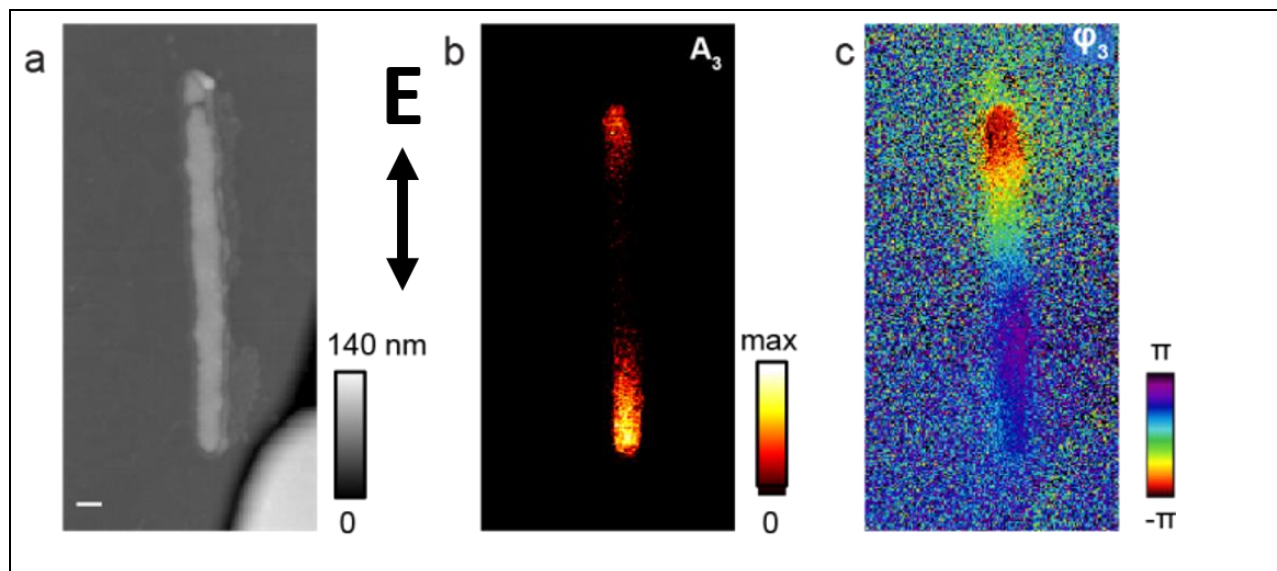


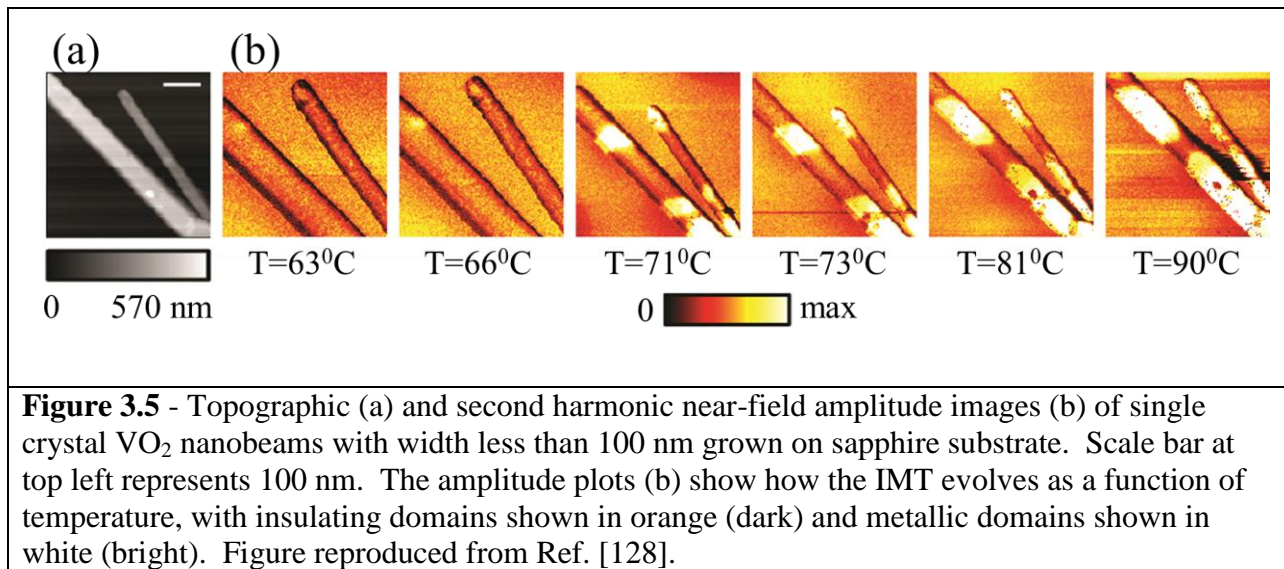
Figure 3.4 - Topographic (a) third harmonic near-field amplitude (b), and third harmonic phase images (c) of an individual Au nanorod resonant with the excitation laser. Amplitude and phase patterns characteristic of a dipole antenna are seen, with regions of high scattering at the rod ends in the amplitude image and a phase shift over the length of the rod. Scale bar at bottom left represents 300 nm.

3.4 - Results and Discussion

3.4.1 - Phase Coexistence in High-Aspect-Ratio Single Crystals

First, the insulating and metallic domains in narrow (~80 nm), high-aspect-ratio VO₂ single-crystal nanobeams (Figure 3.5) grown by vapor phase transport [118, 123] on a sapphire substrate were investigated as the coexisting phases evolved in temperature. The uniformity of the single crystals was verified via topographic measurements (Figure 3.5-a). The nucleation of M phases during the IMT can begin at random locations on a single crystal, as in the onset of the IMT in polycrystalline thin films.[129] Due to the high-aspect-ratio and the crystallinity of nanobeams, strain at the crystal-substrate interface causes the domain structure to evolve by forming well-defined and periodic metallic rutile and insulating non-rutile domains perpendicular to the c_R (along the long dimension of the crystal) axis which span the width of the

crystal.[118] At the onset of the IMT ($T_c \sim 63^\circ\text{C}$) in the nanobeams examined, bright metallic nanodomains form perpendicular to the c_R axis and grow in size as temperature increases, forming a periodic pattern of stripes evolving towards a dominating bright phase at high temperature ($T \sim 90^\circ\text{C}$, Figure 3b). The ordered coexistence of M and I domains is ideal for determining the effect of the nanorod plasmon on the IMT; however, it is not feasible to fabricate $3.2\ \mu\text{m}$ long Au nanorods resonant at the excitation laser wavelength on these nanobeams due to their narrow width.



3.4.2 - Phase Coexistence in Low-Aspect-Ratio Single Crystals

To explore interactions of the Au nanoantennas with single crystal VO_2 , a VO_2 microbeam (estimated thickness 250-500 nm from tilted SEM) was grown on Si. The microbeam was wide enough (lateral dimension $8.5\ \mu\text{m}$) to allow for fabrication of $3.2\ \mu\text{m}$ -long dipole antennas resonant with the excitation laser. Figure 3.6 displays topographical (Figure 3.6-a), near-field amplitude (Figure 3.6-b), and polarized optical microscopy (Figure 3.6-c) images of Au antennas on this microbeam. The smooth topography in

Figure 3.6-a indicates a uniform single crystal. As with nanobeams, stripes are seen in the amplitude image (Figure 3.6-b), indicating the formation of coexisting M and I domains in this microbeam. The gradations in brightness of the M stripes indicate variation in the M domain scattering signal which may be caused by different M domains being buried at a variety of depths beneath I domains at crystal surface. This suggests that in Figure 3.6-b, the rightmost metallic domain is farther from the crystal surface and buried deeper in an I domain than the bottom portion of the leftmost metallic domain because the bottom region of the leftmost domain exhibits more scattering than the rightmost metallic domain. The s-SNOM technique, however, is unsuitable for quantitatively probing the depths of buried domains, as the scattering signal is generated from a nanoscale light source whose interaction with the phase-change material within the source near field extends to depth which is difficult to predict and will change as the M domains grow.

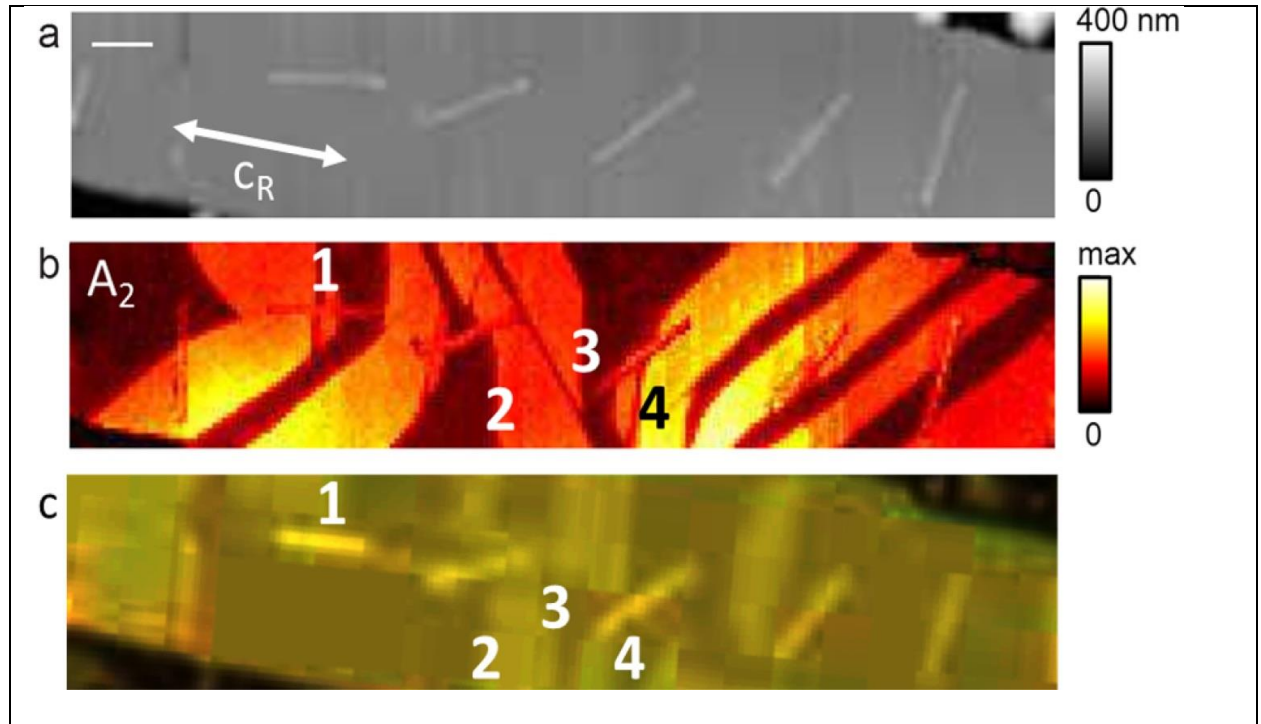


Figure 3.6. S-SNOM topography (a), second-harmonic near-field amplitude imaged at $T \sim 73^\circ\text{C}$ and recorded at laser wavelength $\lambda = 10.7 \mu\text{m}$ (b), and optical microscope (c) images of Au rods fabricated on a VO_2 microbeam grown on silicon. Scale bar at top right of (a) represents $1.5 \mu\text{m}$. Arrow in (a) indicates the direction of the c_R axis in all three figures. Regions in (b) where the metallic domain walls deviate from the herringbone structure are labelled 1, 2, 3 and 4. Large alternating regions of bright and dark rectangles in (c) are ferroelastic domains. Ferroelastic domain walls corresponding to interruptions in the herringbone structure are labelled 1, 2, 3 and 4 to match the labels in (b). Figure adapted from Ref. [128].

In the low-aspect-ratio microbeam, metallic rutile and insulating non-rutile domains primarily form a herringbone pattern oriented at 50 ± 5 degrees with respect to the c_R axis (marked in Figure 3.6-a). Mirror symmetry occurs in M1 VO_2 because both directions are energetically equivalent and correspond to the energy-equivalent orientations of the monoclinic c -axis (described in Refs. [112, 122] and observed in a VO_2 crystal in Ref. [50]). This ties the atomic-scale response of VO_2 to mesoscale properties. It is posited that the low aspect ratio of the microbeam is responsible for the observation of the herringbone pattern here and in Ref. [50] as opposed to the domain pattern of stripes perpendicular to the c_R axis observed in high-aspect-

ratio nanobeams.[111, 113, 117, 118, 123] However, in the microbeam some M domain walls are oriented at 50 ± 5 degrees with respect to the c_R axis in one region but bend to become perpendicular to the c_R axis, in a deviation from a pure herringbone pattern.

The deviations from the herringbone pattern are correlated with the positions of ferroelastic domains. Ferroelastic domains were first observed in VO_2 at room temperature using polarized far-field optical microscopy and scanning microwave microscopy to examine nanoplatelets comparable in width to the microbeam studied here.[113, 117] Ferroelastic domains were further examined at room temperature on single crystals with M1, M2, and T crystal structures, and confirmed by Raman spectroscopy.[53] These ferroelastic domains form in reaction to stress in the monoclinic phase of VO_2 . In M1 VO_2 , as the temperature is increased, the ferroelastic domains switch between energy-equivalent orientations of the same monoclinic crystal structure. The large-scale ferroelastic domain patterns that form in M1 VO_2 are related to the crystal width and the strength of the interaction between the crystal and the substrate.[113] The ferroelastic domains in M1 VO_2 and the M/I stripe phases couple due to their mutual interaction with strain; walls between parallel-plane ferroelastic domains in M1 VO_2 oriented perpendicular to the c_R axis serve as nucleation sites for metallic rutile domains of VO_2 [113] that do not conform to the herringbone pattern of M/I phase coexistence.

Polarized optical microscopy of the VO_2 microbeam decorated with Au nanorods in Figure 4c shows the positions of ferroelastic domains and nanoantennas on the crystal probed with s-SNOM in Figures 3.6-a and 3.6-b. The Au nanoantennas can be seen in Figure 3.6-c as narrow bright areas at locations corresponding to the bright regions in Figure 3.6-a. The ferroelastic domains are manifest as bright rectangular regions and a dark background. As the ferroelastic domains are oriented perpendicular to the c_R axis of the microbeam, they are of the

parallel-plane type and can serve as nucleation sites for metallic rutile domains.[113] The ferroelastic domain boundaries that nucleate metallic domains are marked in Figure 3.6-c. These labels correspond to numerical labels in Figure 4.6-b which indicate locations where the herringbone structure is interrupted by metallic domains perpendicular to the c_R axis.

For example, consider the region marked “2” in Figures 3.6-b and 3.6c. In Figure 3.6-b, a domain wall located at “2” is oriented perpendicular to the c_R axis in the bottom half of the figure and oriented at 50 ± 5 degrees with respect to the c_R axis in the top half of the figure. The part of the domain wall oriented at 50 ± 5 degrees with respect to the c_R axis follows the herringbone pattern, but the domain wall labelled as “2” deviates from this pattern in the bottom part of the figure. In Figure 3.6-c, there is a boundary between a bright and a dark ferroelastic domain at the location marked “2” running perpendicular to the c_R axis in the bottom half of the figure. This is evidence that the ferroelastic domain wall has nucleated the M/I domain wall labelled as “2”. By comparing numbered regions in Figures 3.6-b and 3.6-c, it can be seen that the numbered ferroelastic domain walls line up with those M-I boundaries that differ from the herringbone structure. This indicates that the ferroelastic domains influence the formation of metallic rutile domains and, thus, cause deviation from the herringbone structure, as the metallic domain walls nucleated at each of the four numerically labelled positions would not have occurred if not for the ferroelastic domain wall at each labelled position.

Microbeams of VO_2 exhibit ordered, coexisting M and I phases that should in principle interact with plasmonic Au nanorods by altering the plasmon-resonance frequency, which will change the amplitude contrast observed via s-SNOM. Nevertheless, in Figure 3.6-b, we do not observe detectable modification of the nanorod plasmon resonance. This indicates that Au nanorod antennas are not influenced by the phase coexistence, though the Au nanorods were

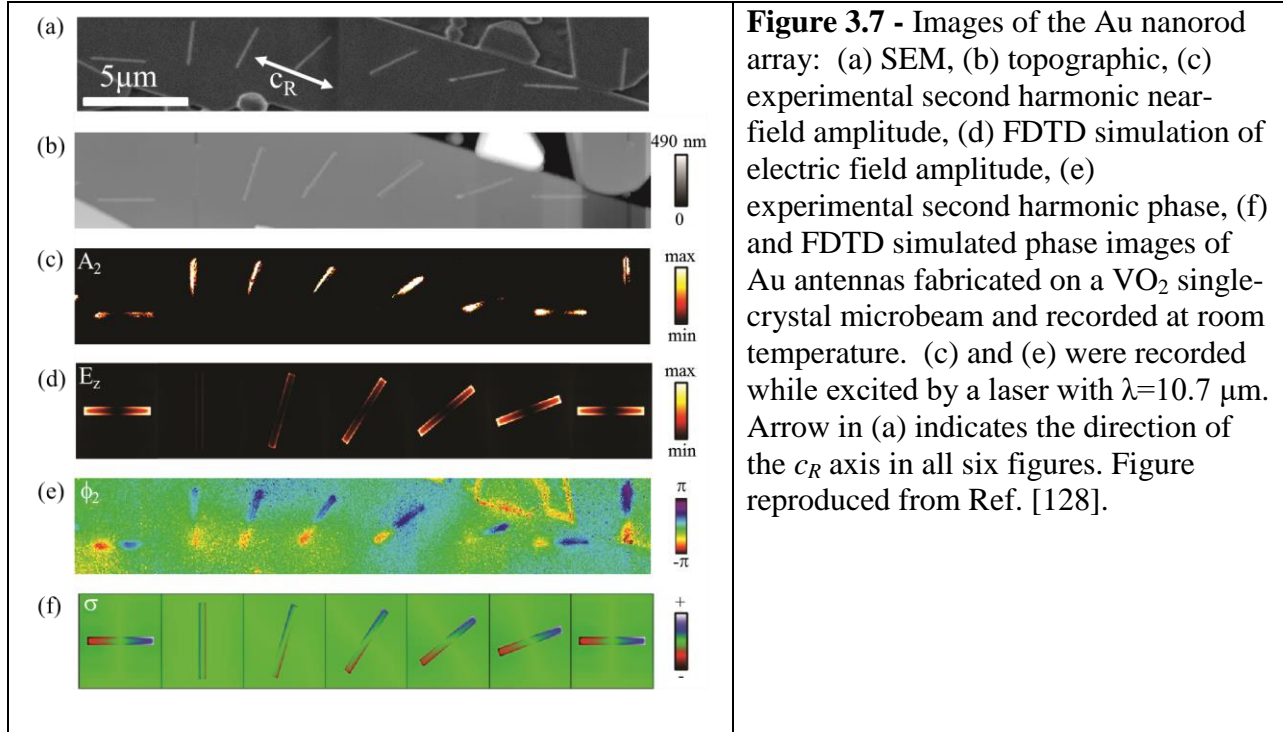
simulated to be resonant with the exciting laser. This is unexpected given the quenching of the Au nanoantenna plasmon resonance seen in Au nanorod plasmons in direct contact with M domains of thin films.[59] The next portion of this chapter explores the reasons for this lack of interaction, based both on experiments and simulations.

3.4.3 - Verification that Plasmonic Particles are Resonant with Excitation Source

Verification that the Au antennas are resonant with 10.7 μm light by examining their amplitude and phase response at room temperature using s-SNOM is carried out. When a nanorod antenna is oriented parallel to the laser polarization and resonant with the laser wavelength, the laser excites the plasmonic dipole mode of the rod, giving rise to a distinctive amplitude and phase contrast at the rod ends.[137] Figure 3.7 shows experimental topographic (b), 2nd harmonic near-field optical amplitude (c), and phase (e) images of Au nanorods on a VO₂ microbeam taken at $\lambda=10.7 \mu\text{m}$ and at room temperature. The direction of the c_R axis is indicated in the SEM in Figure 3.7-a. We observed the characteristic amplitude and phase contrast when the nanorod antenna and laser field are parallel, and at other rod orientations the dipolar signature is weak. This is expected due to the contribution to the scattered light from the metallized AFM tip used to image the IMT simultaneously with the Au plasmons. As a result of strong local antenna-field distortions caused by the metallic AFM tip, even Au rods oriented perpendicular to the laser polarization showed bright optical amplitude and phase contrast.

The orientation-dependent excitations were simulated using finite-difference, time-domain (FDTD) computations shown in Figures 3.7-d and 3.7-f, which exhibit decreased field intensity and reduced phase contrast at the nanorod ends, as the angle between the nanorod long axis and polarization of the laser is rotated from 0° to 90°. Taken together, these images indicate

clearly that the antennas have resonant excitation wavelengths close to the incident 10.7 μm laser light.

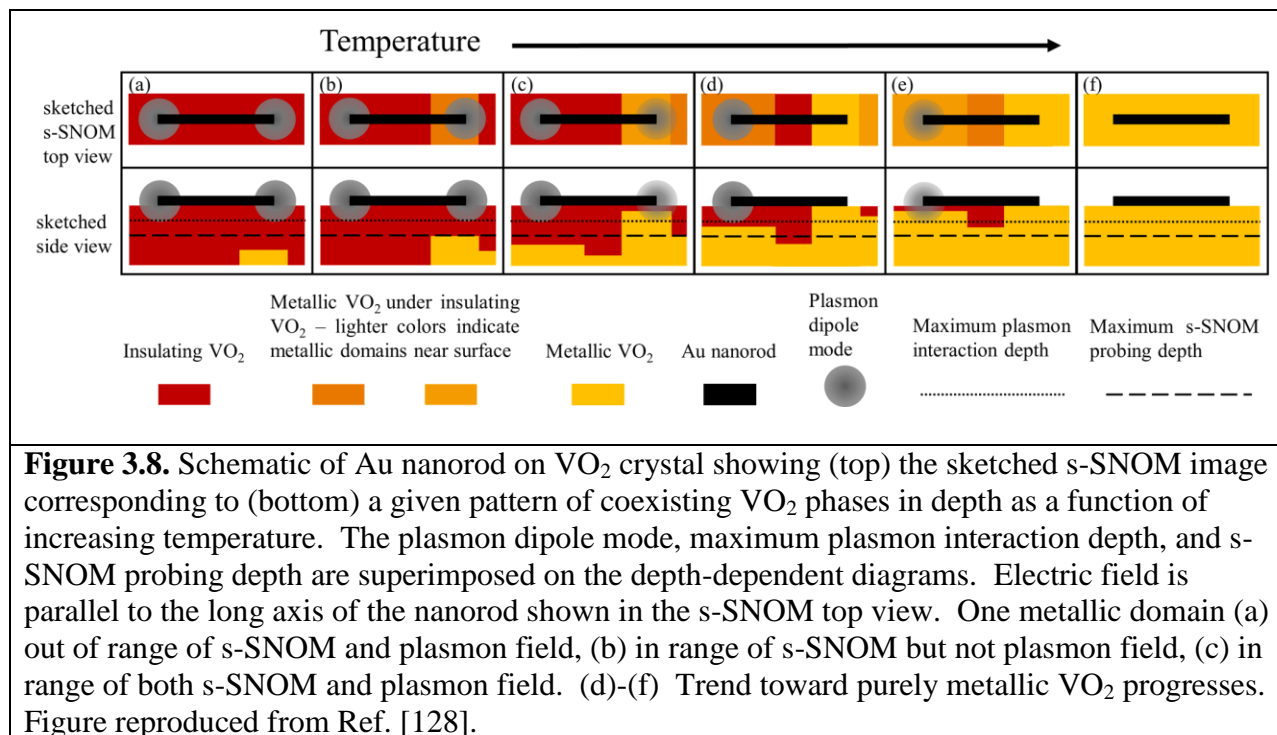


3.4.4 - Depth Dependence of Phase Coexistence

Results from s-SNOM imply that the metallic rutile stripes in the microbeam form at the crystal-substrate interface and are not within the plasmon interaction range of the Au nanorods on the surface of the VO₂ as soon as the M domains nucleate. A measure of the plasmon range for Au nanoparticles resonant at near-IR wavelengths using Lumerical FDTD can be seen in Appendix F. Though metallic domains more than several nanometers below the surface of the single-crystal microbeam can in principle be probed using s-SNOM,[124, 130-134] the metallic domains are too far beneath the crystal surface to interact with the Au nanorods due to the rapid decay of the out-of-plane plasmon field. Thus, the Au nanoantennas do not show the measurable quenching seen in previous thin film studies.[59]

Figure 3.8 demonstrates this principle, showing the growth of M domains toward the top surface of the crystal as the temperature varies, how the difference between the s-SNOM probing depth and the maximum plasmon interaction depth alters the s-SNOM image formation, and how the dipole plasmon is altered by the IMT. Figure 3.8-a represents a plasmon dipolar mode on top of the insulating phase of VO₂ with an M domain located far from the crystal surface and s-SNOM probe range. More heating (Figure 3.8-b) causes the metallic domain to grow nearer to the crystal surface and within the probing depth of s-SNOM but not within the interaction range of the plasmon supported by the metal nanorod, leaving the plasmon resonance unaltered from Figure 3.8-a. The M domains imaged in Figure 3.8-b can be seen in this stage of growth, in range of the s-SNOM but not of the plasmons and, thus, the M domains do not alter the plasmon resonance. Further heating (Figure 3.8-c) brings a metallic domain into the plasmon interaction region, altering the plasmon resonance from that seen in Figure 3.8-a, represented here as a decrease in the strength of the electric near field on the right side of the nanorod and a possible shifting of the plasmon resonance. This was observed for plasmonically resonant nanorods on VO₂ thin films.[59] The process continues in Figure 3.8-d with the electric near field on the right side of the nanorod being completely quenched and in Figure 3.8-e where the near field on the right is completely quenched and the near field on the left is weakened. In Figure 3.8-f the entire VO₂ crystal is metallic and the plasmon resonance corresponds to that which would be seen for the Au antenna on metallic VO₂, completing the process. Our observation that metallic domains nucleate beneath the crystal surface is further supported by three-dimensional s-SNOM imaging of VO₂ polycrystalline ribbons thinner than our 250-500 nm microbeams, being only 30 - 300 nm thick.[112] Metallic rutile domains were shown to preferentially nucleate at the VO₂-substrate interface to reduce the strain, which is the highest at that interface. The metallic

domains were observed to grow towards the surface of the VO₂ and only occasionally appeared as stripes on the polycrystalline ribbon surface.[112]

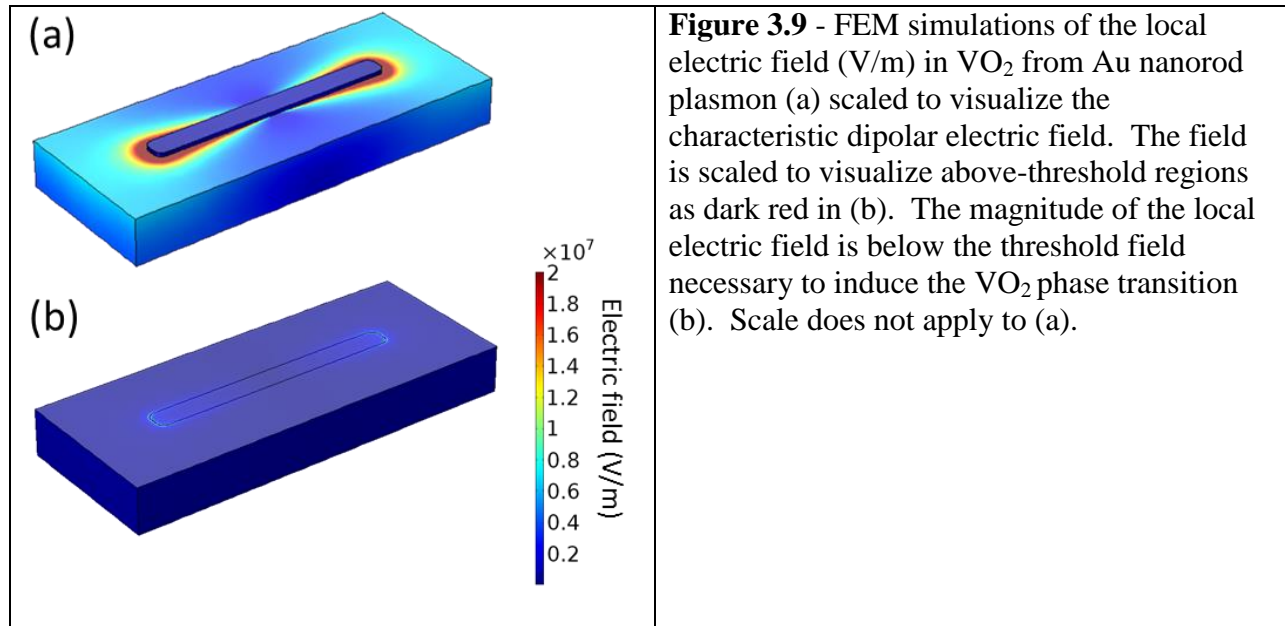


A logical future step will be to investigate the interaction of plasmons with few nanometer thick VO₂ single crystals such that Au nanoparticle plasmons would be sensitive to M domains even at the crystal-substrate interface and act as local probes. Etching methods, as recently described in Ref. [138], have been used to reduce the thickness of VO₂ thin films. Neither these methods, nor any others, have not been tested to thin VO₂ single crystals. Unwanted etching of the sides of single crystals must be considered and minimized in addition to the desirable etching of the top of the crystal to obtain a thin crystal while preserving the original footprint of the crystal. Significant process development will be needed to adapt these etching methods for the purpose of thinning but not shrinking VO₂ single crystals while maintaining crystals free of grain boundaries and switching VO₂. The M domains in thinner crystals than

considered in the current work could also be detected by s-SNOM as soon as the domains nucleate and modify the gold plasmons on the surface of the crystal.

3.4.5 - Simulated Influence of Plasmon Resonance on VO₂

It has been demonstrated that for the sample temperature at which the amplitude image shown in Figure 3.6-b was measured that the VO₂ phase coexistence does not influence the response of the Au nanorod plasmon resonance because the M domains are not within the plasmon interaction region. The next investigation is whether the Au plasmon resonance could influence the VO₂ and locally induce the PT. The CO₂ laser incident upon bare VO₂ does not provide a high enough electric field to induce the VO₂ switch on its own, but plasmonic particles at resonance have enhanced local electric fields in comparison to the incident electric field. Finite-element method (FEM) simulations were used to determine the magnitude of the local electric field of an Au nanoantenna on top of insulating VO₂ when excited with the electric field of the CO₂ laser used in these experiments. For a discussion on the FEM technique, see Ref. [12]. As can be seen below, Figure 3.9-a shows the local electric field at the surface of the VO₂ from the Au nanorod plasmon excited by a CO₂ laser, scaled to visualize the plasmon. The characteristic dipolar electric field is observed in Figure 3.9-a. On the other hand, Figure 3.9-b shows that there are no regions in the VO₂ that are above the threshold field needed to switch VO₂ (2×10^7 V/m).[62] Near-threshold fields (field strength greater than 1×10^7 V/m) only exist beneath the ends of the Au nanoantennas on the VO₂ surface and to a depth less than 10 nm.



The bowtie antenna is one plausible nanostructure that could provide sufficient local electric field to switch the VO₂. The bowtie geometry in this set of simulations can be seen in Figure 3.10-a with dimensions $G=10$ nm, $L=3400$ nm, $W_1=600$ nm, $W_2=20$ nm, and thickness 20 nm. An electric near-field pattern characteristic of a bowtie plasmon resonance is observed in Figure 3.10-b at the surface of the VO₂. The region of high electric field at the center of the bowtie is shown in Figure 3.10-c as a function of depth ($-z$) with the electric field scaled to illustrate, in red, regions of VO₂ experiencing above-threshold field. The VO₂ region experiencing above-threshold electric field from the bowtie plasmon has a maximum in-plane area of 40 nm by 30 nm as indicated by white arrows in Figure 3.10-c and extends 10 nm only into the VO₂. This indicates that it is possible to generate a local electric field sufficient to switch a small region of VO₂, but that the fabrication necessary to do so might be difficult and would outweigh the potential insight gained from conducting that experiment.

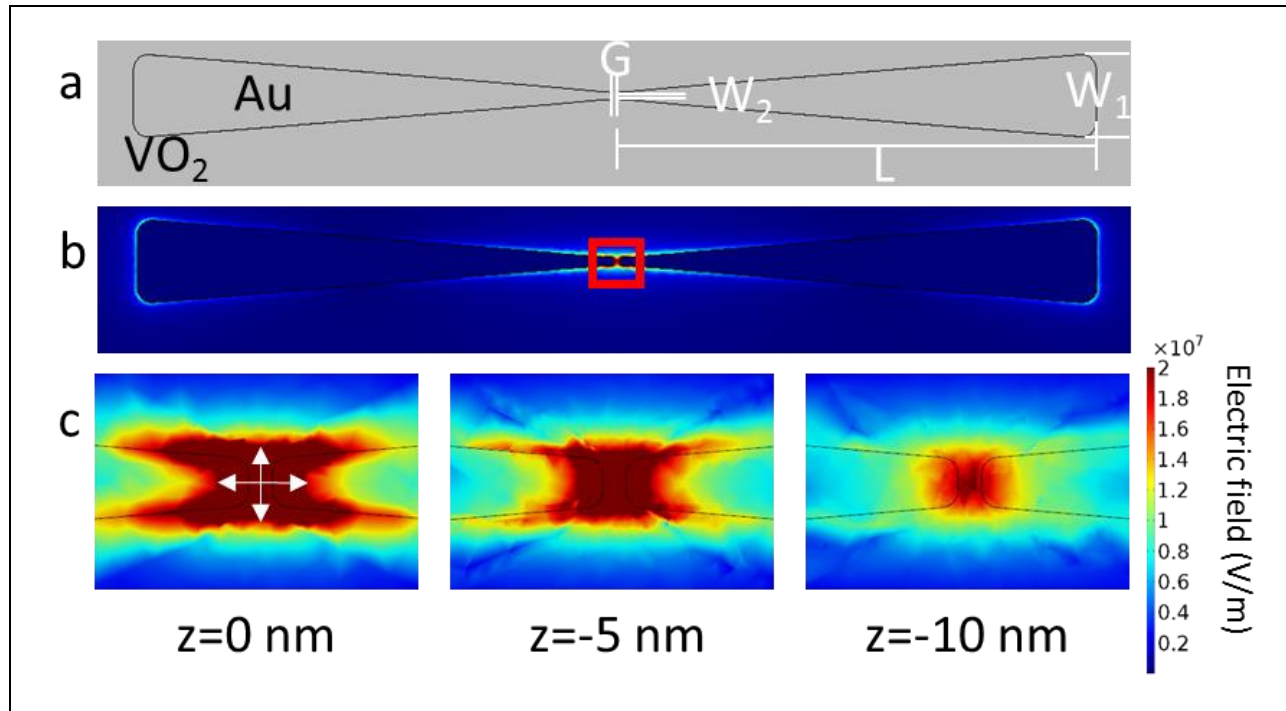


Figure 3.10 - Geometry of bowtie (a) and FEM simulations of the local electric field (V/m) in VO₂ from Au bowtie plasmon (b,c). In (b) the field at the surface of the VO₂ is scaled to show the plasmonic response characteristic of a bowtie antenna. Close-ups of region in red box are shown in (c). Slices of the antenna gap electric field scaled to display above-threshold field in red are shown in (c) as a function of depth (-z) below the VO₂ surface. Scale only applies to (c).

3.5 – Conclusions and Outlook

For the first time, the thermally induced IMT and the structure of the phase coexistence in a low-aspect-ratio VO₂ single-crystal microbeam decorated with plasmonic Au nanorod antennas have been studied to examine the inhomogeneous response of the crystal to the insulator-to-metal transition. A herringbone-like M/I phase coexistence pattern with deviations due to ferroelastic domains has been observed, confirming that a phase coexistence pattern other than the commonly observed stripe pattern perpendicular to the c_R axis is possible in VO₂ single crystals and that the pattern observed may be determined by the crystal aspect ratio. These experimental measurements also suggest a connection between the M/I phase coexistence seen in

strained epitaxial thin film ribbons and single crystals of VO₂. It was observed that the herringbone structure is modified by the presence of ferroelastic domain walls that serve as nucleation sites for those M phase regions that deviate clearly from the herringbone pattern. This interaction cannot be seen in the polycrystalline VO₂ ribbons.

Decoration of single crystals with resonant Au plasmonic nanostructures establishes the possibility of using nanostructures as non-destructive plasmon probes of the VO₂ phase coexistence in the bulk of the crystal to compliment s-SNOM measurements. Using the Au nanorod plasmon resonance, depth-dependent inhomogeneity in VO₂ single crystals is demonstrated because M domains nucleate beneath the VO₂ crystal surface and do not immediately extend throughout the entire depth of the crystal. With sufficiently thin single crystals, the M domains would be within the range of the plasmon field as they nucleate. In this case, the plasmon could serve as a non-invasive probe of the growth of M domains with temperature due to the temperature-dependent growth of M domains modifying the local dielectric environment of the plasmon in a manner detectable via s-SNOM.

A survey of the phase coexistence patterns of single crystals of various aspect ratios will provide further information on the role of aspect ratio on the development of stripes or a herringbone pattern and how one pattern transitions to the other around a critical aspect ratio. This would not require the use of Au nanorod probes, so the single crystals used here would not need to be as large as those used for this work and thus easier to find on any given sample. This could be done using a precision temperature stage and either an s-SNOM or an optical microscope since there is contrast in the color of the VO₂ single crystal above and below the PT as well as contrast in the scattering amplitude which can be measured via s-SNOM.

Using the sample described in this work, examining the temperature evolution of the modified herringbone structure and the evolution of the nanorod plasmon resonance would demonstrate if, with sufficient heating, the entire single crystal does become metalized. Monitoring the plasmon resonance in conjunction with the evolution of the herringbone structure would indicate if the surface of the single crystal does undergo the phase transition with sufficient heating. Also, using the sample described in this work, examining the ferroelastic domain pattern before heating the crystal and imaging the phase coexistence and repeating this procedure multiple times would provide information about how fixed the ferroelastic domain locations are and, thus, how the deviations from the herringbone pattern are altered or not altered upon repeated temperature cycling.

CHAPTER 4

HYDROGEN DOPING OF VO₂ PROBED VIA PLASMONIC PARTICLES

4.1 - Introduction

This chapter describes the use of Au nanoparticles embedded in VO₂ thin films to monitor the atomic hydrogen doping of the films by tracking changes in the plasmon resonance. This work was done in collaboration with the Max Planck Institute for Intelligent Systems and Rice University. The contents of this chapter are divided into seven sections: background, sample fabrication, experimental setup and methods, thermal hysteresis data and analysis, dynamics data and analysis, integrating thermal and dynamic results, and conclusions and outlook. The background section provides information about hydrogen doping of VO₂, previous experiments, and differences between the present work and earlier research. The sample fabrication section describes the complex route to the preparation of the VO₂ films with plasmonic hydrogen probes. The experimental setup and methods section describes how the temperature-dependent hydrogen doping of VO₂ is probed. The thermal hysteresis data and analysis section (Section 4.5) discusses the plasmon-resonance hysteresis curves obtained by monitoring the Au nanoparticle plasmon resonance as the sample is heated from below the pure VO₂ critical temperature to above the critical temperature and then cooled back to room temperature for samples prepared by hydrogen doping at different temperatures. The dynamics data and analysis section discusses the time evolution of the plasmon-resonance wavelength of the Au nanoparticle while the VO₂ is doped with atomic hydrogen at different temperatures. The final section discusses the information that can be gathered by combining the thermal and

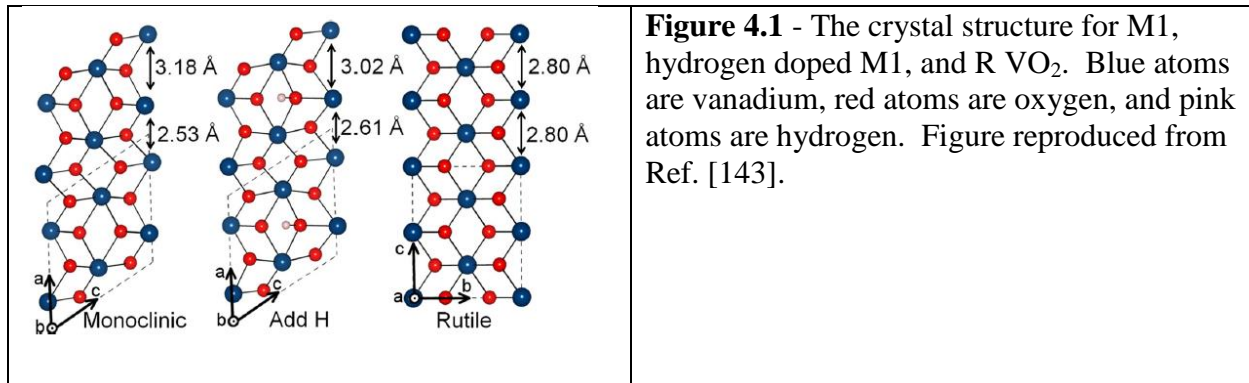
dynamics data on hydrogen doping of VO₂ thin films. The conclusions and outlook section details what has been learned from this research and possible future directions of interest based upon this research.

4.2 - Background

Atomic hydrogen acts as a reversible dopant of VO₂. The metallic state of VO₂ has been shown to be stable below 2 K in single crystals of VO₂ doped with hydrogen.[139] The metallic state of VO₂ can also be stabilized below the critical transition temperature T_c for pure VO₂ if other dopants are used,[53-55] but the metallic state cannot be stabilized to temperatures anywhere near 2 K. Using 7 atomic percent Mo, T_c for a VO₂ thin film can be decreased to 24 °C at the cost of reduced resistivity contrast;[140] W doping of VO₂ thin films to 8 at% reduces T_c to 32 °C. For VO₂ nanoparticles in silica glass, doping with 3 at% W decreases T_c to -25 °C (248K).[141] Due to the sensitivity of VO₂ to atomic hydrogen, VO₂ is also used as a hydrogen gas sensor – an important technology since hydrogen gas is explosive but also a byproduct of many chemical reactions. Before using hydrogen doped VO₂ as the basis for such devices, it is necessary to understand the physics of the VO₂ interactions with atomic hydrogen. These aspects include how atomic hydrogen alters T_c , the VO₂ optical properties, and the influence of hydrogenation on these properties of the VO₂ PT with time.

Vanadium dioxide can be doped with atomic hydrogen in either the M1 and R states, but atomic hydrogen diffuses much more rapidly when VO₂ is in the R state,[139] because H will diffuse readily along the channels lined with oxygen atoms along the rutile c (c_R) axis.[68, 142] The H atoms diffuse down the channel by hopping from one O site to the next.[142] Hydrogen

atoms do not readily diffuse perpendicular to these channels.[142] For VO₂ in the M1 state, these channels also exist but are distorted along the *a* M1 axis compared to the channels along the *c* axis of R VO₂, as seen in figure 4.1. Thus, atomic hydrogen diffuses preferentially along the monoclinic *a* (*m_a*) axis of VO₂ in comparison to other M1 axes [143] but also diffuses three orders of magnitude faster along the *c_R* axis than equivalent *m_a* axis.[139] In M1 VO₂, the presence of H also distorts the crystal lattice such that the short and long bond lengths between V atoms shift from 2.53 Å and 3.18 Å to 2.61 Å and 3.02 Å. This brings the crystal structure closer to that of R VO₂, which has one a bond length of 2.80 Å between V atoms, and stabilizes the metallic phase.[143] The crystal structures of M1, hydrogen doped M1, and R VO₂ can be seen in Figure 4.1.



These changes on the atomic scale dramatically alter the optical and electronic properties of the VO₂. With increased H doping, the insulating bandgap decreases until it disappears.[142] The resistance of the VO₂ decreases [144] and the current through the VO₂ increases for a given voltage.[51] The color of the VO₂ also changes from that of I VO₂ to that of M VO₂ with hydrogenation, which has been used to calculate the diffusion constant of atomic hydrogen into VO₂ single crystals.[139, 142] With light H doping, *T_c* drops [142] approximately 10 °C.[144]

With increased H doping, the conductivity increases with no change in T_c . [144] The metallic phase of VO_2 is stable at room temperature, [142] and even down to 2K. [139] With sufficient H doping, the pure insulating state VO_2 will change to metallic H doped VO_2 and then to a heavily H doped insulating state based upon the changes in sheet resistance of VO_2 as a function of time in a hydrogen atmosphere.

Previous research on hydrogenation of VO_2 has been carried out with a variety of tools and geometries. A commonly used method is to take an individual VO_2 single crystal and pattern metal contacts for electrical measurements. In this geometry, I-V curves and conductivity have been examined during [144] or after hydrogen doping using gold or palladium as a catalyst to dissociate molecular hydrogen to atomic hydrogen. [68, 144] Conductance has been monitored after hydrogen doping directly with atomic hydrogen to verify that the hydrogen-induced metallic state of VO_2 is stable down to 2K. [139] The electrical response was also probed during gas cycling of H_2 and air to show the reproducibility and reversibility of the response while Pd was employed to create H from H_2 . [51, 144] The dynamics of the hydrogenation were also probed in this geometry, using the current across the single crystal during hydrogen doping as a probe of the VO_2 . [51] Two other common methods of examining VO_2 during hydrogenation are optical. The first uses Raman spectroscopy on VO_2 single crystals to probe how the crystal structure changes for hydrogenated and unhydrogenated regions of crystals and how the hydrogenated structure compares to the unhydrogenated structure. [68, 139] The second method uses the color change of VO_2 during H doping to calculate the diffusion constant for H into VO_2 single crystals [68, 139, 142] and show visually that H preferentially diffuses into VO_2 along the c_R axis after being dissociated from H_2 using a Pd catalyst. [142] The presence of H in the channels along the c_R axis of VO_2 has also been shown

experimentally for epitaxial VO₂ thin films using high-angle annular dark-field and annular bright-field scanning transmission electron microscopy. The molecular hydrogen is dissociated to create atomic hydrogen with a platinum catalyst.[145]

Here, the hydrogenation of a polycrystalline VO₂ thin film is probed by tracking the plasmon-resonance shift of Au nanoparticles embedded in a VO₂ film changes. Gold disk dimers and monomers are buried in a VO₂ thin film, which is decorated with Pd nanoparticles to induce the dissociation of H atoms from H₂ molecules. As the electronic properties of VO₂ are altered due to H doping and the resonance of a plasmonic particle is sensitive to its local dielectric environment, shifts in the plasmon resonance of individual nanoparticles provide information about the changing phase of the VO₂. The effect of H on VO₂ is probed as a function of temperature after hydrogenation as well as at a fixed temperature as a function of time during hydrogenation. This provides information about how the PT is altered after hydrogenation and also provides information about the dynamics of VO₂ hydrogenation.

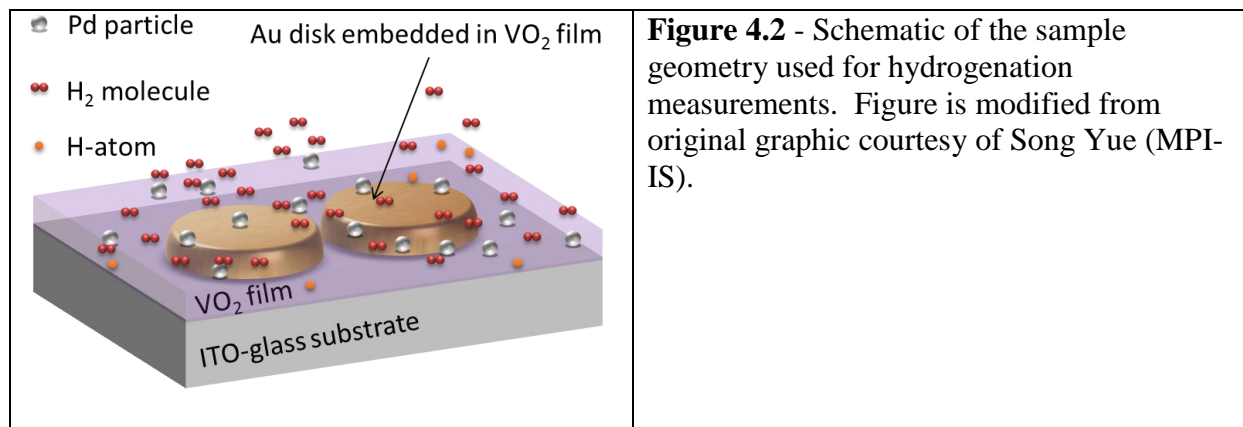
This experimental program is different from previous work on atomic hydrogen doping of VO₂ because the hydrogenation is being *locally* tracked by the plasmon-resonance shift of embedded plasmonic particles instead of on a more global scale using the I-V response of single crystals, the VO₂ color change, or Raman spectroscopy. Using the shift in the plasmon resonance of a plasmonic particle also provides a sensitive optical method for probing the hydrogenation in contrast to previous work. This method allows measurement of the temperature dependent VO₂ hysteresis for different amounts of H doping, similar to other measurements of the switching of VO₂ in the literature on the effect of H doping, and has the potential for precise tracking of the hydrogenation dynamics of VO₂. In this way, it is possible to compare the thermal hysteresis results with other methods of probing the electronic changes in

VO₂ over the PT to verify that the same trends are observed and then use this same method to probe the dynamics in more detail than has been previously investigated. Many of the previous studies on the dynamics of hydrogen doping of VO₂ only detect one process by tracking the color change and provide a diffusion coefficient based upon that. Some of the previous studies show that the response of the VO₂ to H can be cycled but do not analyze the properties of the VO₂ while the properties of the materials are changing. Two previous studies on the dynamics of hydrogen doping of VO₂ do analyze the properties of the VO₂ while the material properties are changing due to the hydrogen, see evidence that two processes are involved in the hydrogen doping of VO₂, and discuss the physical meanings of these two processes. By analyzing the dynamical data using equations to fit this data and determining the physical meanings behind the fit values, the work described here can examine the relative contributions of the two processes involved in hydrogen doping of VO₂.

4.3 - Sample Fabrication

Fourteen identical samples were prepared for this work in collaboration with the Max Planck Institute for Intelligent Systems. Arrays of 35 nm thick Au disk dimers (component disk diameter 250 ± 10 nm, gap 20 ± 5 nm) and monomers (diameter 350 ± 10 nm) were patterned via EBL on ITO-glass substrates. These samples were all coated in 93 ± 6 nm of VO₂ film by RF-magnetron sputtering and annealed at 450 °C in 250 mTorr O₂ to get switching, non-scattering VO₂ films as detailed in the Chapter 2 sections on RF-M sputtered VO₂ and obtaining non-scattering VO₂. The samples were then decorated with 3.3 to 3.4 nm of palladium (Pd) and baked to create Pd nanoparticles atop the VO₂ film which are used to dissociate the H₂ molecules

into atomic hydrogen. A schematic of the sample geometry for an Au disk dimer can be seen below.



4.4 - Experimental Setup and Measurements

Single-particle dark-field microscopy was used (MPI-IS) to measure the dark-field scattering signal from individual Au nanoparticles embedded in a non-scattering VO₂ film. A schematic of the dark-field microscope used for these measurements can be seen in Figure 4.3. The center of the light source is blocked so that only light far from the center of the beam reflects off an annular mirror. This light is passed into the periphery of a dark-field objective and focused onto the sample. Light scattered from the sample is collected by the objective lens of the dark-field objective, passed through the center of the annular mirror, and directed to a spectrometer so that scattering spectra can be detected. The sample is placed on a temperature-controlled stage to allow for temperature-dependent measurements. A gas cell built at MPI-IS with a quartz-glass window on the top side allows for dark-field scattering measurements at variable temperatures in a pressure-controlled H₂ atmosphere during hydrogen doping.

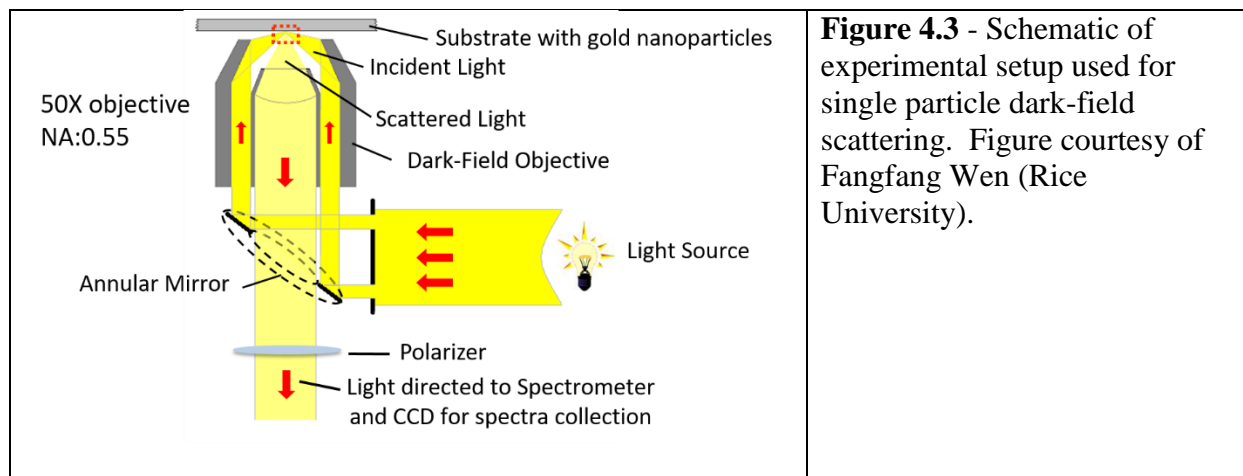


Figure 4.3 - Schematic of experimental setup used for single particle dark-field scattering. Figure courtesy of Fangfang Wen (Rice University).

In the following results, the scattering spectrum measured at each time or temperature point is collected and the peak in the scattering signal is considered the resonant wavelength for the Au nanoparticle being examined. The peak is located using a centroid detection method, as described in Ref. [146]. Two types of measurements are carried out using this experimental setup. In the first, the plasmon resonance of an Au nanoparticle is monitored in air as the temperature of the sample is swept from 25 °C up to 120 °C and down to as low as 0 °C. This occurs for samples before and after Pd deposition as well as after hydrogenation at a variety of temperatures. In the second type of measurement, the plasmon resonance of an Au nanoparticle (monomer or dimer) is monitored as the sample is held at a constant temperature in a controlled atmosphere varying concentrations of H₂.

4.5 - Thermal Hysteresis Data and Analysis

4.5.1 - Thermal Hysteresis Background

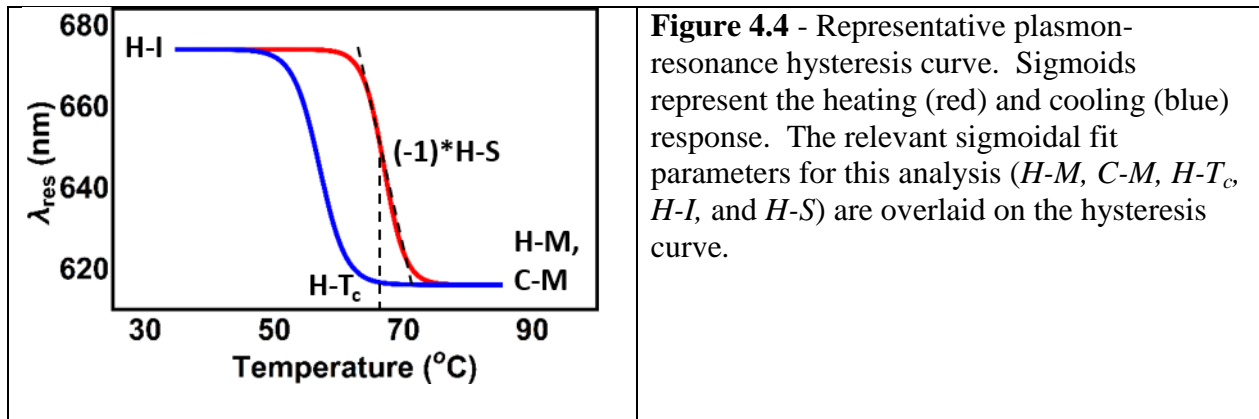
The system under examination is Au disk dimers and monomers covered in a VO₂ thin film decorated with Pd nanoparticles which are used to split the molecular hydrogen into atomic

hydrogen that is incorporated into the VO₂ thin film and alter the VO₂ electronic and structural properties. The Au nanoparticles are deployed as sensitive local reporters of the VO₂ properties through their changing plasmon resonance. As the VO₂ is heated and cooled and undergoes the PT from I to M back to I, the plasmon resonance shifts in a manner which resembles a thermal VO₂ hysteresis curve comprised of two sigmoidal curves. This is termed the plasmon-resonance hysteresis. A sigmoidal curve has the form

$$\lambda_{res} = M + \frac{I - M}{1 + e^{S*(T-T_c)}} \#(4.1)$$

and describes the wavelength of the plasmon resonance, λ_{res} , as a function of temperature, T . The parameter M is the minimum of the sigmoid, and for the plasmon-resonance hysteresis it represents the wavelength of the plasmon resonance when the surrounding VO₂ is completely metallic. The parameter I is the maximum of the sigmoid, and for the plasmon-resonance hysteresis it represents the wavelength of the plasmon resonance when the surrounding VO₂ is completely insulating. The parameter T_c is the temperature around which the sigmoid is centered, and for the plasmon-resonance hysteresis it represents the critical switching temperature for the VO₂ phase transition when the sample is switched either from the insulating state to the metallic state or vice versa. The parameter S is the negative of the slope of the sigmoid at T_c , and for the plasmon-resonance hysteresis is determined by the variation in T_c for individual VO₂ grains. If all of the grains in the local environment of an Au nanoparticle undergo the PT at exactly the same temperature, the slope S will be infinite. If, though, the VO₂ grains in the local environment of the Au nanoparticle switch over a range of temperatures, S will have a smaller value.

The plasmon-resonance hysteresis curves considered here consist of two sigmoids, which pertain to the response when the sample is heated from the insulating state to the metallic state (heating curve, red) and when the sample is cooled from the metallic state to the insulating state (cooling curve, blue), as can be seen in Figure 4.4. To distinguish between the sigmoidal fit parameters for the heating and cooling curves, “H” is added in front of a fit parameter to denote it as the fit parameter for the heating curve and “C” is added in front of a fit parameter to denote it as the fit parameter for the cooling curve. For example, *H-M* represents the wavelength of the plasmon resonance when the surrounding VO₂ is completely metallic when the sample is heated from the insulating state to the metallic state.

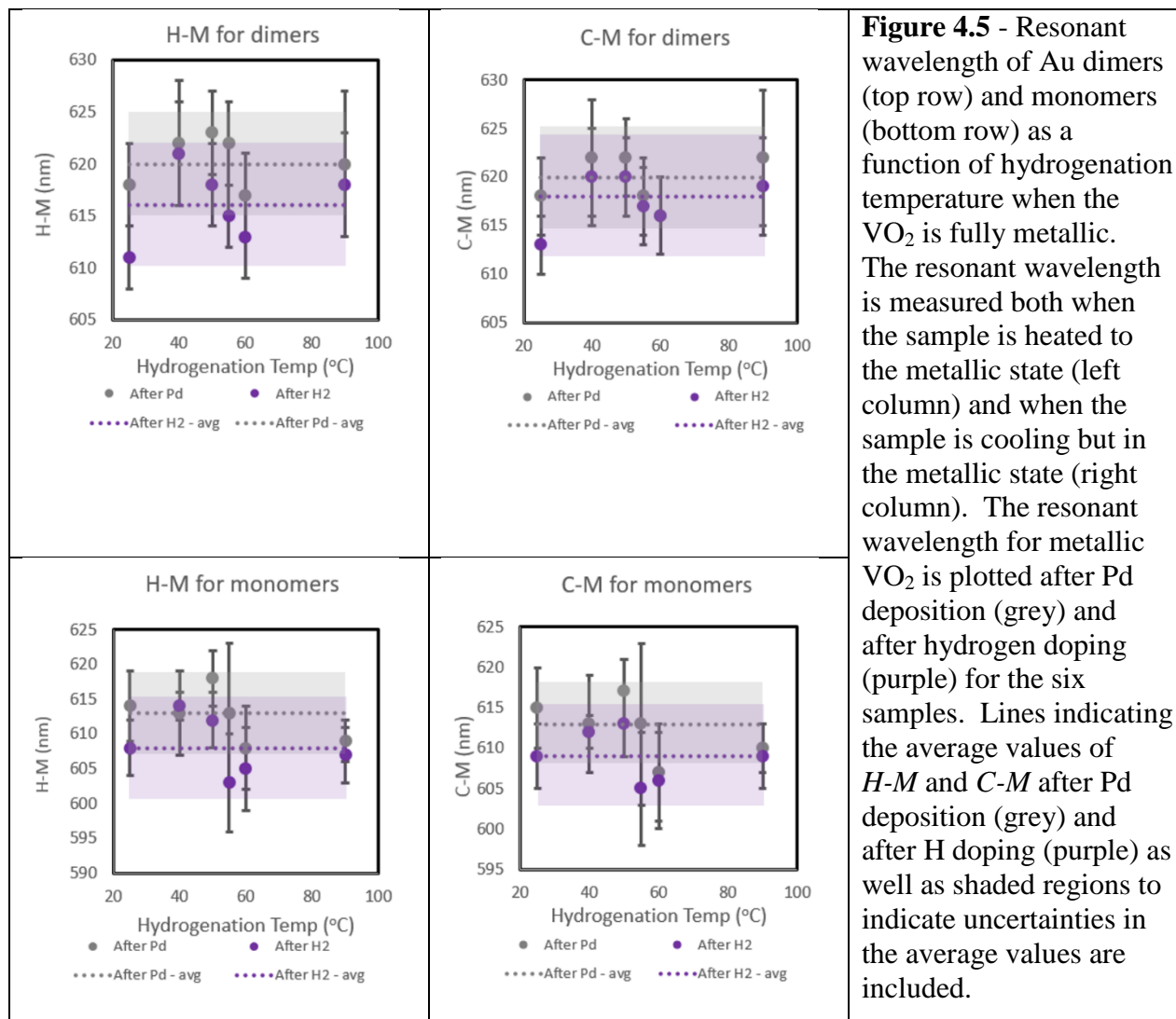


The plasmon-resonance hysteresis curve tracks with the transmission hysteresis curve measured on the VO₂ film away from the nanoparticles. The effect of the Pd nanoparticles on the plasmon hysteresis is minimal, causing a slight blue-shift and a narrowing of the hysteresis. The data supporting these statements can be found in an appendix.

4.5.2 - Thermal Hysteresis Fits to Data and Analysis

In this section, the sigmoid fit parameters that persist through atomic hydrogen doping of VO₂ are compared with the values of the fit parameters after Pd deposition but before hydrogen doping. These parameters are *H-M*, *C-M*, *H-T_c*, *H-I*, and *H-S*. The metallic state is stabilized down to 20 °C after hydrogenation and heating over the PT into the M state, so the cooling curve for the plasmon-resonance spectroscopy is flat instead of having a sigmoidal shape, similar to the conductivity of a VO₂ single crystal after mild hydrogen doping.[68] Thus, the only cooling curve parameter considered is *C-M*. The five aforementioned parameters are determined for each sample by fitting the plasmon-resonance hysteresis for each nanoparticle to two sigmoids and averaging the resulting parameter values of the Au disk dimers and disk monomers separately. The error bars in the following plots show the standard error of the mean in each fit parameter for the ten Au dimers and/or nine Au monomers measured for each sample. Each of the six relevant samples was placed in a molecular hydrogen gas environment for 30 minutes at a different temperature. The sample hydrogenation temperatures are as follows: ITO-10 at 25 °C, ITO-12 at 40 °C, ITO-13 at 50 °C, ITO-14 at 55 °C, ITO-15 at 60 °C, and ITO-16 at 90 °C.

The plots of *H-M* and *C-M*, seen in Figure 4.5, for nanoparticle dimers and monomers before and after hydrogenation at different temperatures indicate that there is no statistically significant variation in these parameters for samples hydrogenated at different temperatures or even between samples pre- and post-hydrogenation. The metallic state of hydrogenated VO₂ is indistinguishable from that of pure (unhydrogenated) VO₂ as probed by Au nanoparticle reporters.



The plots of the heating sigmoid critical temperature ($H-T_c$) for nanoparticle dimers and monomers before and after hydrogenation at different temperatures can be seen in Figure 4.6 and indicate that there is a decrease in $H-T_c$ after hydrogenation that cannot be explained by uncertainty in experimental measurements. Counter to expectations that $H-T_c$ would decrease with hydrogenation at increasingly high temperatures, $H-T_c$ drops from its pre-hydrogenated value for hydrogenation temperatures of 25 °C and 40 °C, increases until it is close to the pre-hydrogenated value for hydrogenation at 50 °C, and decreases for hydrogenation at 55 °C and 60 °C, though not to the point where they are below $H-T_c$ for low-temperature

hydrogenation. This indicates that there is a critical concentration of hydrogen causing $H-T_c$ of VO_2 to increase nearly back to the undoped temperature. On either side of this critical concentration, $H-T_c$ decreases.

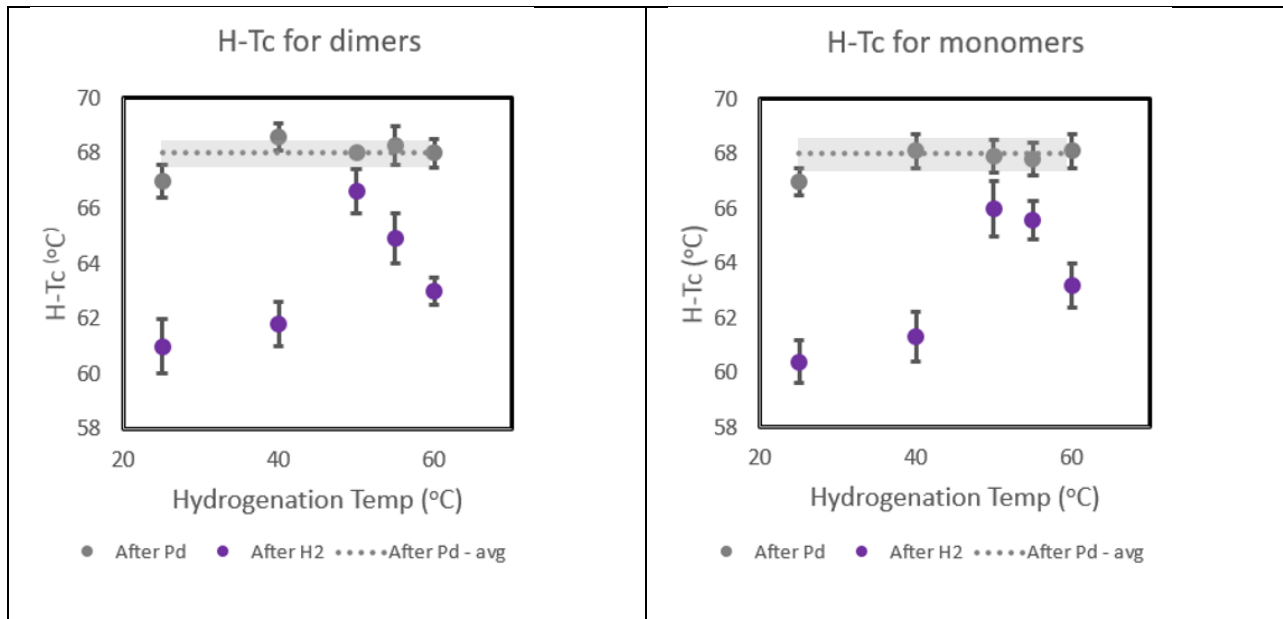


Figure 4.6 - Critical temperature for the heating curve ($H-T_c$) for disk dimers and disk monomers as a function of hydrogenation temperature. The critical temperature of VO_2 under heating is plotted after Pd deposition (grey) and after hydrogen doping (purple) for the five samples which exhibit heating sigmoids after hydrogenation. A line indicating the average value of $H-T_c$ after Pd deposition (grey) as well as shaded regions to indicate uncertainties in the average value are included.

The plots of $H-I$ for nanoparticle dimers and monomers in Figure 4.7 before and after atomic hydrogen doping at different temperatures indicate that there is also a decrease in $H-I$ due to hydrogenation that cannot be explained by uncertainty in experimental measurements. With increased hydrogenation, $H-I$ smoothly decreases to the metallic state resonant wavelength (red). This indicates that the insulating state of VO_2 is influenced by hydrogenation at temperatures as low as 25 °C – nearly room temperature.

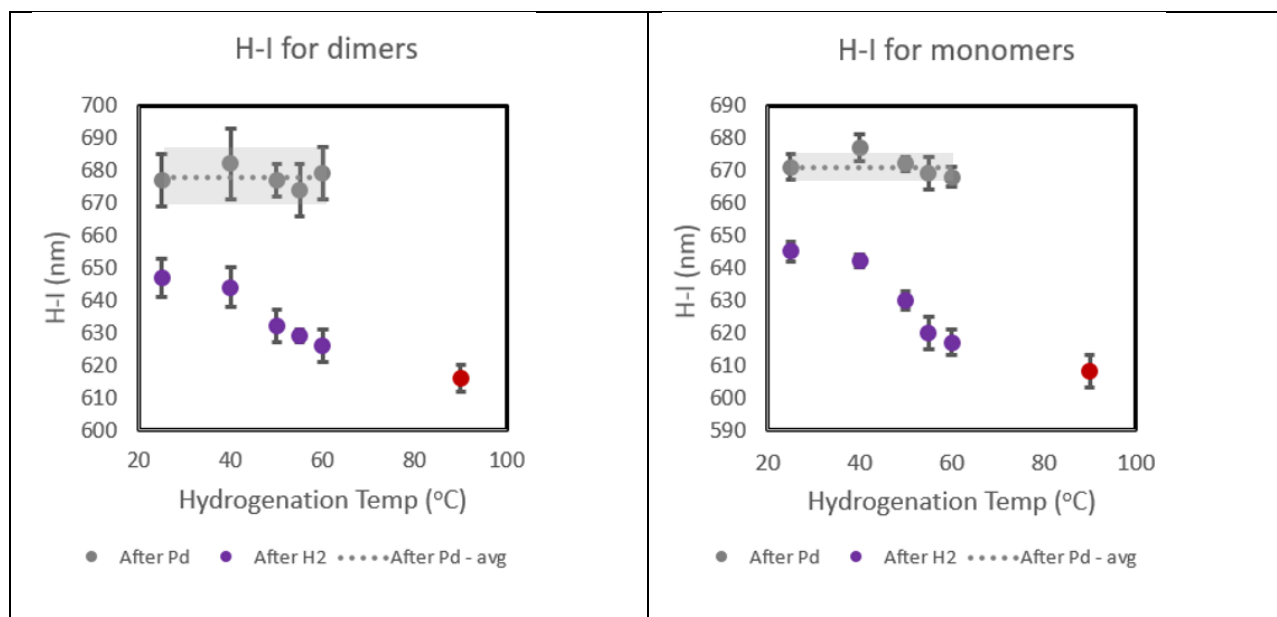


Figure 4.7 - Resonant wavelength when VO₂ is in an insulating state (*H-I*) and the sample is being heated for disk dimers and disk monomers as a function of hydrogenation temperature. The resonant wavelength for insulating VO₂ is plotted after Pd deposition (grey) and after hydrogen doping (purple) for the five samples which exhibit heating sigmoids after hydrogenation. A line indicating the average value of *H-I* after Pd deposition (grey) as well as shaded regions to indicate uncertainties in the average value are included. The red points indicate the resonant wavelength value for Au disks and dimers after hydrogenation at 90 °C.

The plots of *H-S* for nanoparticle dimers and monomers in Figure 4.8 before and after hydrogenation at different temperatures indicate that there is a *decrease* in *H-S* due to hydrogenation that cannot be explained by uncertainty in experimental measurements; the only exception is sample ITO-10 for dimers in which the pre-hydrogenated sharpness of the hysteresis has a large variation from dimer to dimer and thus a large uncertainty. As a function of hydrogenation at different temperatures, although *H-S* remains constant. The plasmon-resonance hysteresis tracks the VO₂ thin film hysteresis,[94, 147]: therefore the cause of changes to the slope at T_c of the sigmoids in the plasmon-resonance hysteresis is related to the cause of the changes to *H-S* of the sigmoids in the VO₂ thin film transmission hysteresis. It is known for VO₂ hystereses that VO₂ nanoparticles of larger sizes switch at lower temperatures because they contain more potent defects that can nucleate the phase transition.[148] Thus, a film containing

VO₂ domains that all have the same switching temperature would exhibit a large value of S over the PT because all of the domains would switch together. The hysteresis loop would have steeper slopes on both the heating and cooling cycles, that is, more like the hysteresis in a bulk single crystal. A film with domains of various sizes would have a smaller value of S because the VO₂ domains would not switch simultaneously; rather each domain would switch when the VO₂ reached the transition temperature for that specific domain. The change in the values of S for the sigmoids measured under hydrogen doping suggests that hydrogenation increases the variance in the number of defects in the different VO₂ crystal grains compared to the variance in the number of defects in the VO₂ grains before hydrogen doping. This would reduce the value of S to decrease, because the VO₂ grains with different numbers of defects due to hydrogen doping would switch at different temperatures. This would in turn make the slope of the hysteresis curve less steep.

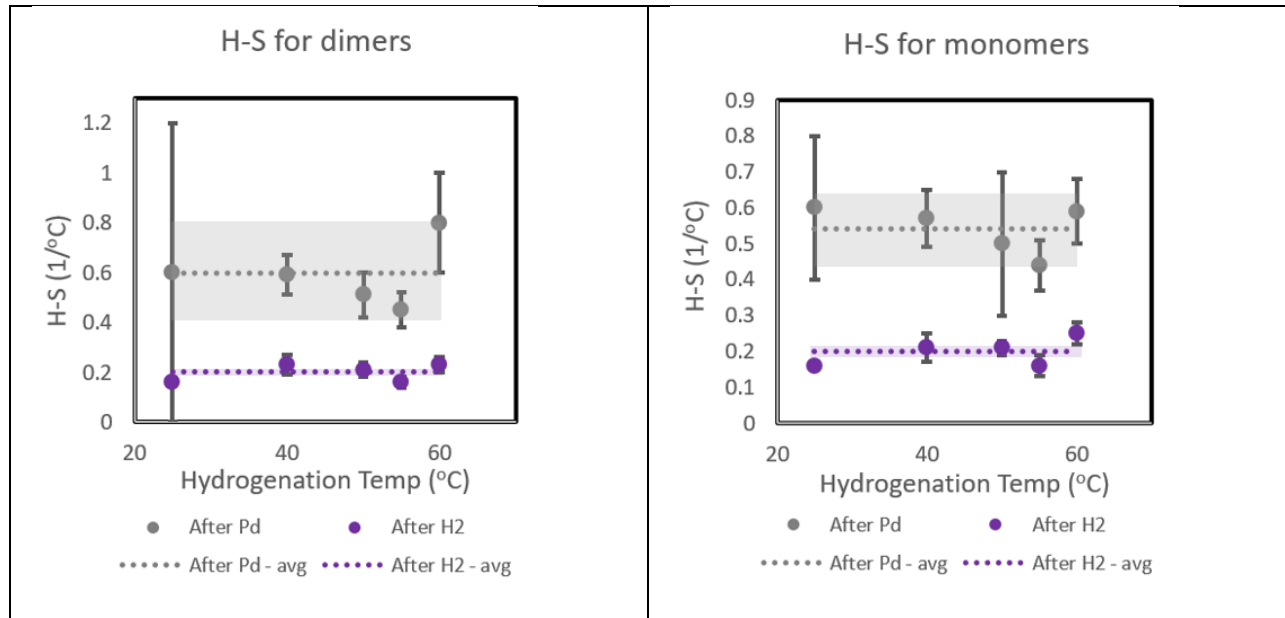


Figure 4.8 - Sigmoid parameter governing the slope of the heating sigmoid ($H-S$) for disk dimers and disk monomers as a function of hydrogenation temperature. $H-S$ is plotted after Pd deposition (grey) and after hydrogen doping (purple) for the five samples which exhibit heating sigmoids after hydrogenation. Lines indicating the average values of $H-S$ after Pd deposition (grey) and after H₂ doping (purple) as well as shaded regions to indicate uncertainties in the average values are included.

Overall, the thermal hysteresis data showed that with increased hydrogenation, the VO₂ T_c decreases and then the VO₂ switching contrast decreases to zero as the metallic phase stabilize, comparable to observations of VO₂ electrical properties on hydrogenated single crystals in previous work.[68, 142, 144] Having established confidence in the plasmon-resonance spectroscopy as a way to track the VO₂ thermal hysteresis after hydrogenation, the dynamics of hydrogen doping in VO₂ thin films are now considered.

4.6 - Dynamics Data and Analysis

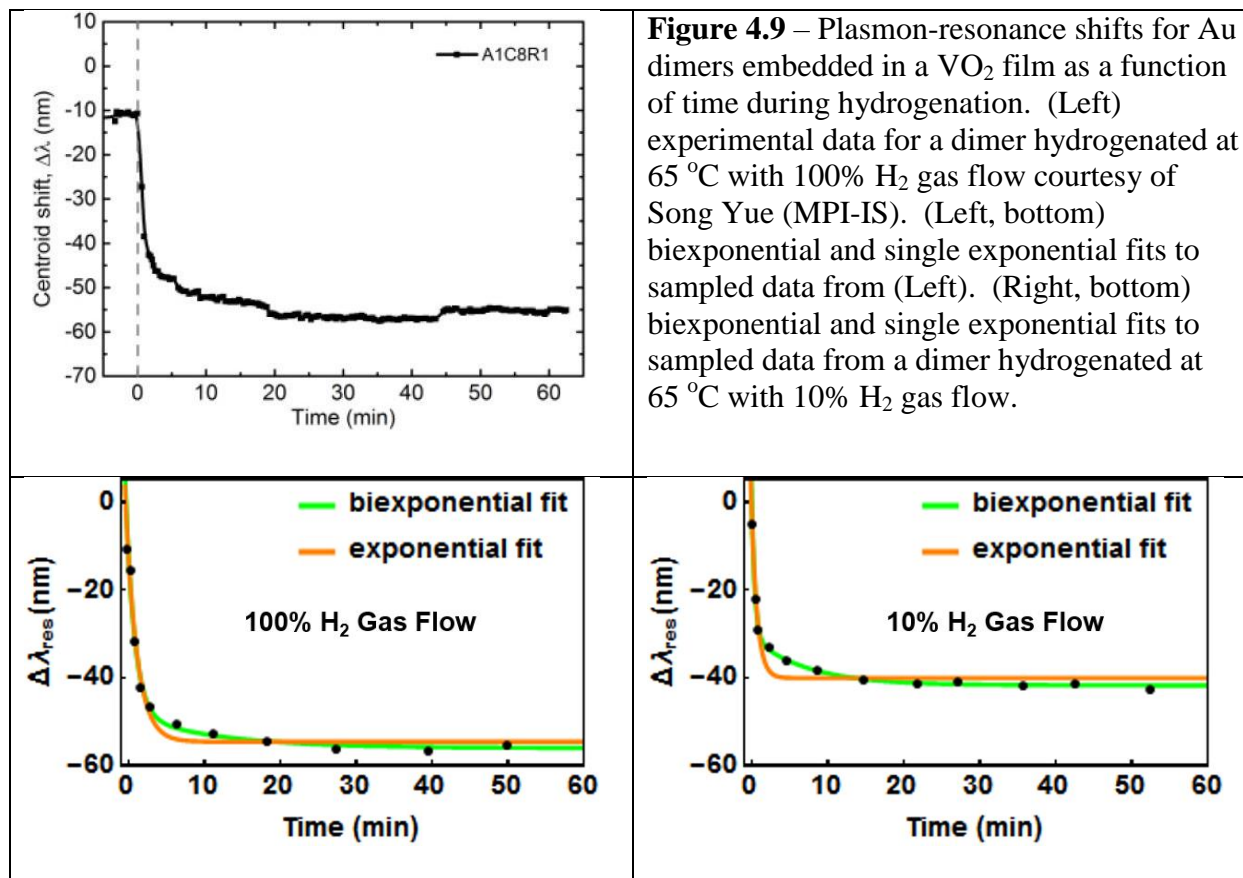
To examine the dynamics of the VO₂ thin film hydrogenation, the plasmon resonance of individual Au disk dimers and monomers are tracked as a function of time. Changes in the

plasmon resonance of the nanoparticles indicates changes in the VO₂ dielectric properties in the local dielectric environment of the nanoparticles. This is examined at a variety of atomic hydrogen doping temperatures both above and below the PT as well as over a variety of hydrogen concentrations.

From looking at dynamical data for individual Au nanoparticles, the response resembles an exponential decay. This can be seen in the top left of Figure 4.9 for the resonance of an Au dimer probed during hydrogenation at 65 °C with 100% H₂ gas flow. The dotted line at zero minutes is when the molecular hydrogen gas begins to flow. Data are extracted from this graph and as well as a plot of the resonance of an Au dimer during hydrogenation at 65 °C with 10% H₂ gas flow. These data (black, small) are fit in the bottom graphics in Figure 4.9 to a single exponential (orange) and a biexponential (green). The forms of these equations are displayed below.

$$\text{single exponential fit: } \Delta\lambda = aE^{-bt} + c \#(4.2)$$

$$\text{biexponential fit: } \Delta\lambda = aE^{-bt} + c + dE^{-ft} \#(4.3)$$



To quantify which of the fits, biexponential or single exponential fit, represents a set of dynamical data more closely, the value of $\Delta\lambda_{\text{res}}$ for each experimentally measured data point is compared to the value of $\Delta\lambda_{\text{res}}$ predicted for the time associated with that data point for the biexponential fit and the single exponential fit. These differences are called residuals. The residuals are calculated for all of the measured data points. The residuals associated with the biexponential fit are each squared and summed, and the residuals associated with the single exponential are likewise squared and summed. These sums are normalized to the number of data points for which residuals were calculated and then the square root is taken. A single number quantifying the goodness of the fit to the data is obtained in this way, and one is obtained for each of the two fits (biexponential fit and single exponential fit). This number will be referred to here as the *GoF* (goodness of fit)

For 100% H₂ gas flow, both fits provide reasonable representations of the data, though the biexponential fit follows the data points slightly more closely than the single exponential fit. The *GoF* of the data from the single exponential fit is 1.8 whereas the standard deviation of the same data from the biexponential fit is 1.3. For 10% H₂ gas flow, it is clear that the biexponential fit represents the data points better than the single exponential fit. The *GoF* of the data for the 10% H₂ gas flow from the single exponential fit is 2.5 but is 1.0 for the biexponential fit. This, though, could be due to having more fit parameters in the biexponential fit than the single exponential fit or due to these sets of data having two decay times due to some physical reason, which would necessitate the use of a biexponential fit.

To justify the validity of using a biexponential fit instead of a single exponential fit, it is important to establish a precedent and/or physical reasons for this observation of multiple time scales for atomic hydrogen doping of VO₂. Hydrogenation of VO₂ single crystals has been studied by placing a single crystal across electrical contacts to probe the response of the VO₂ to hydrogen as a function of time and voltage.[51, 144] In this work, the conductance of the VO₂ single crystal increases with time under hydrogenation over two different timescales. For Ref. [51], the first timescale is slow (several minutes) and is related to the formation of H atoms from H₂ due to interaction with the Pd, the diffusion of the H atoms into the VO₂ surface, and further diffusion into the bulk of the VO₂. During this time, the current increases linearly. The second timescale is rapid (nanosecond to microsecond range) and causes a sharp increase in the current by a factor of 10³, indicating that a metallic state of VO₂ has been achieved. For Ref. [144], the fast process (1-5 minutes) occurs first, followed by a slow process where many hours are required to reach a constant current. This is described as being due to fast splitting of H₂ into H in the presence of Pd followed by H atoms flowing over the VO₂ surface and diffusing into the

bulk of the VO₂ single crystal.[144] The results from Ref. [144], probing the electrical conductance during hydrogen doping, indicate two timescales similar to what is observed in this work and justify the use of a biexponential fit to the dynamics data of the plasmon-resonance shift during hydrogenation.

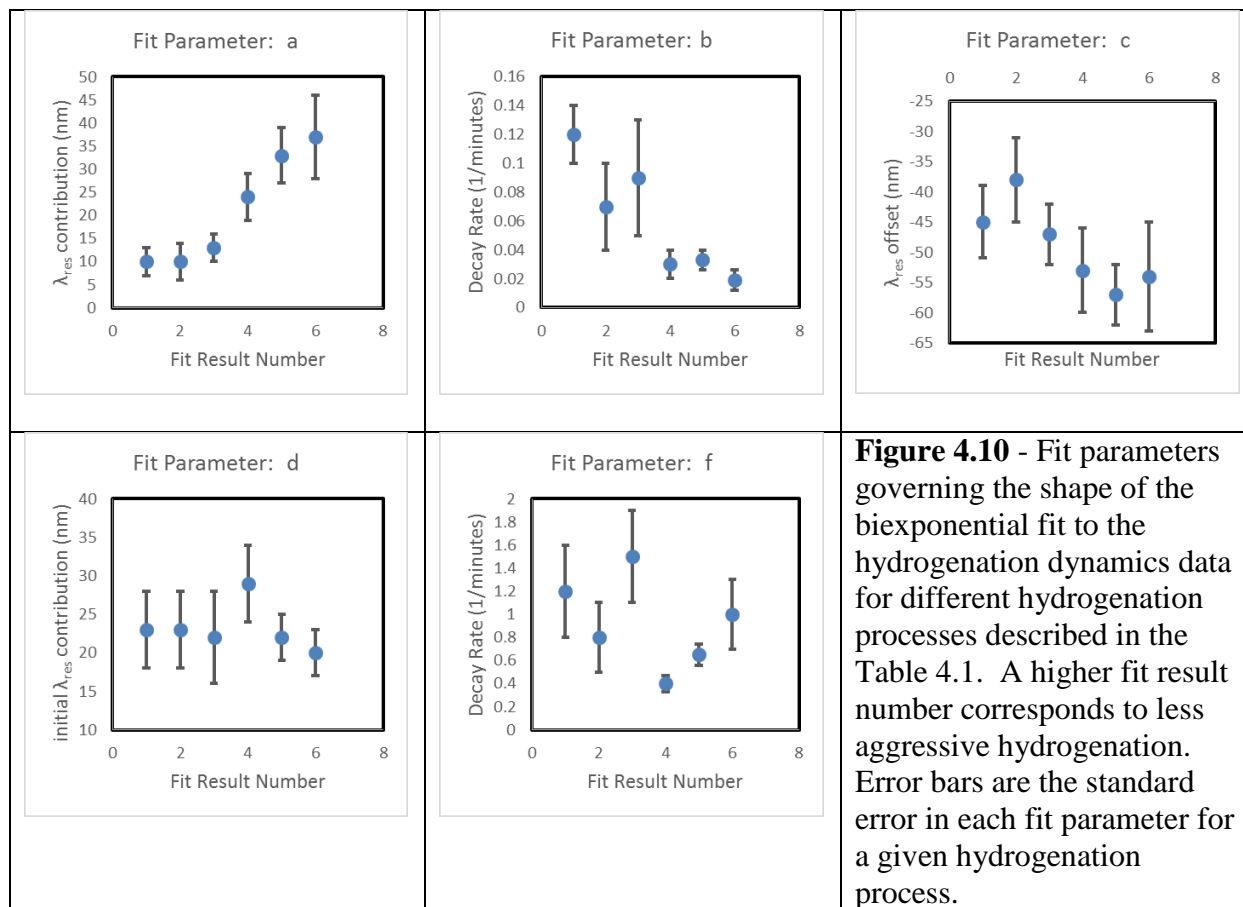
Eight samples are used to examine the dynamics of hydrogenation in VO₂ thin films. The details of the hydrogenation processes for these samples are described now. The results for two of the samples, ITO-17 and ITO-19, do not follow a biexponential curve, which is not surprising. The dynamics of these two samples will be discussed later in this chapter. The hydrogenation processes used on the remaining samples do result in data that follow biexponential curves.

Sample Name	Number for Biexponential Fit Results	Hydrogenation Temperature (°C)	Hydrogen Flow Percentage (%)
ITO-17	NA	25	100
ITO-18	1	65	100
ITO-19	NA	100	100
ITO-20	2	65	50
ITO-21	3	65	10
ITO-22	4	55	10
ITO-23	5	55	1
ITO-24	6	55	0.1

Table 4.1 - Details of the samples and parameters used for hydrogen dynamics studies.

With increasing biexponential fit number from 1 to 6, as detailed in Table 4.1, the hydrogenation becomes less aggressive due to the decrease in hydrogenation temperature and/or H₂ flow percentage. For each of the samples, the sample is heated to the hydrogenation temperature. That temperature is maintained while H₂ gas is introduced to the atmosphere in the gas cell for 60 minutes. The plasmon resonance of an individual Au disk dimer or monomer is monitored before and during hydrogenation to probe how the resonance is modified with time

due to the presence of atomic hydrogen. For each sample, this monitoring occurs on ten individual disk dimers and nine individual disk monomers. These curves are fit to a biexponential curve and the five fit parameters obtained for each curve are averaged to obtain average fit parameters for each hydrogenation process. Data sets are rejected if the biexponential fitting function is unable to converge to a solution. The error bars in the following plots show the standard error in each fit parameter for the ten Au dimers and/or nine Au monomers measured for each sample, barring those data sets that were rejected because the curve fitting in Mathematica was unable to converge upon a solution to fit those sets of data to a biexponential equation. The average fit parameters for each of the samples with the exception of ITO-17 and ITO-19 are plotted so that the influence of the hydrogenation process on each individual fit parameter can be determined.



Individually, these fit parameters do not provide much information. The value of the fit parameter a , from equation 4.3 lacks a consistent trend. The parameter a is constant within uncertainty for hydrogenation at 65 °C for 100%, 50%, and 10% H₂ gas flow. The value of a increases for hydrogenation at 55 °C compared to 65 °C and is constant within uncertainty for H₂ gas flows of 10%, 1%, and 0.1%. The value of b is constant within uncertainty for hydrogenation at 65 °C and 55 °C, regardless of H₂ gas flow percentage. The values of c and d are constant within their uncertainties for the fit results shown. The value of f does not appear to have one distinct trend. The parameter f is constant within uncertainty for hydrogenation at 65 °C for 100%, 50%, and 10% H₂ gas flow. The value of f decreases in comparison to the values for atomic hydrogenation at 65 °C and increases with decreased gas flow from 10%, 1%,

and 0.1% H₂ for hydrogenation at 55 °C.

Meaningful information, though, can be extracted when comparing the parameters corresponding to the two exponential decays. A comparison of the decay rates of b and f shows on average an order-of-magnitude difference. This indicates that there is a fast (less than three minutes) hydrogenation effect described by d and f and also a slow (between 7 and 70 minutes) hydrogenation effect described by a and b . The fast timescale is comparable to the 1 – 5 minute fast timescale observed in Ref. [144] for a VO₂ single crystal with a radius of order 100 nm, though the low timescale observed in that work was of order 18 hours. The ratio of the fast (f) and slow (b) process decay rates for the hydrogenation processes which result in data that can be fit using a biexponential function is plotted in Figure 4.11. The ratio of f to b is, on average, 20. This ratio is increased for hydrogenation at 55 °C with a 0.1% hydrogen flow rate. This arises because although f has a comparable decay rate for this process as for other processes, b is decreased for this least aggressive hydrogen doping process.

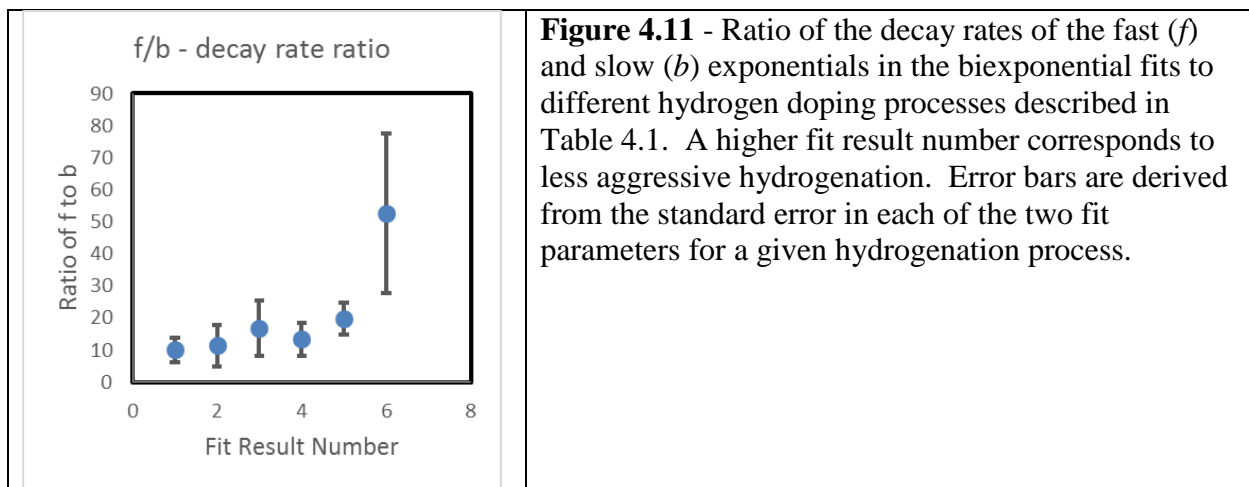


Figure 4.11 - Ratio of the decay rates of the fast (f) and slow (b) exponentials in the biexponential fits to different hydrogen doping processes described in Table 4.1. A higher fit result number corresponds to less aggressive hydrogenation. Error bars are derived from the standard error in each of the two fit parameters for a given hydrogenation process.

Comparing the values of d and a , which correspond to the fast and slow hydrogenation effects, can provide an idea of the contribution of each of these effects to the overall

hydrogenation dynamical response. Thus, the ratio of the fast (d) and slow (a) process contributions for the hydrogenation processes which result in data that can be fit using a biexponential function is plotted in Figure 4.12. As the hydrogenation becomes less aggressive, the ratio of the contributions of the fast and slow exponential decays changes from greater than one (fits results one through three), to one (fit results four), to less than one (fit results five and six). Though d remains constant, a increases as hydrogenation becomes less aggressive. Functionally, the fast decay plays less of a role in determining the hydrogenation dynamics of the VO₂ than the slow decay as the hydrogenation process becomes less aggressive. Also, the slow decay time becomes slower with the decrease in hydrogenation process aggression.

Taking these results together, as the hydrogenation becomes less aggressive, the slow decay becomes slower and plays a larger role in contributing to the overall hydrogenation dynamics than with more aggressive hydrogenation where the fast decay dominates the behavior.

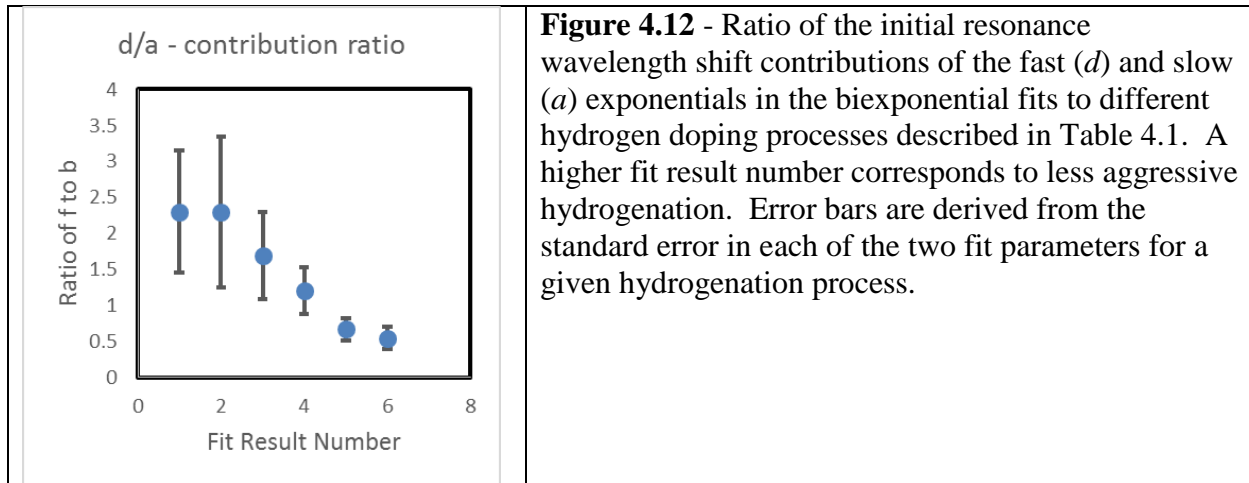
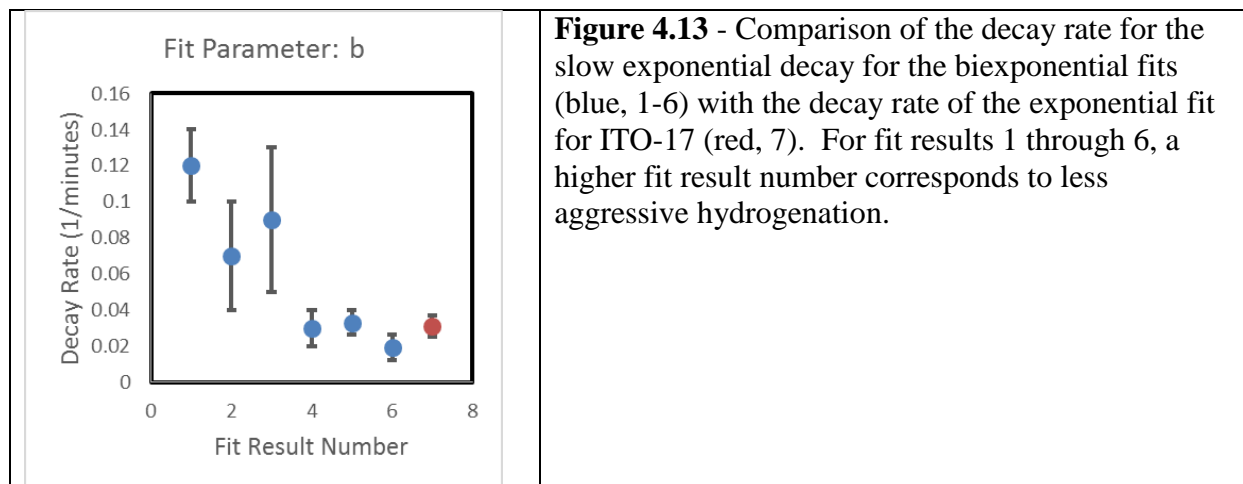


Figure 4.12 - Ratio of the initial resonance wavelength shift contributions of the fast (d) and slow (a) exponentials in the biexponential fits to different hydrogen doping processes described in Table 4.1. A higher fit result number corresponds to less aggressive hydrogenation. Error bars are derived from the standard error in each of the two fit parameters for a given hydrogenation process.

The sample ITO-17 was hydrogenated with a process that was not very aggressive, given that hydrogenation was done at 25 °C. The resulting data do not fit a biexponential equation, but it does fit a single exponential equation better than a linear equation. For the previously

discussed samples in this section, the slow decay term contributed more to the overall hydrogenation dynamics for less aggressive hydrogenation processes for the six samples where the results could be fit to biexponentials. If that trend continues, there will be some hydrogenation process which will cause the fast process to play little role in the hydrogen dynamics and leave only the slow process. This is what is observed when the exponential decay rate for sample ITO-17 is compared with the fit values of b for the biexponential fit. In Figure 4.13, the graph of the fit parameter b is reproduced (blue) with the addition of the exponential decay rate for ITO-17 (red). As can be seen in Figure 4.13, the decay rate for ITO-17 is comparable to that of fit results four through six for samples hydrogenated at 55 °C at a variety of H₂ flow rates. This suggests that with a sufficiently non-aggressive hydrogenation process, the fast decay rate is completely absent and only the slow decay rate remains.



The sample ITO-19 was hydrogenated at 100% H₂ flow at 90 °C. At this temperature, the VO₂ is well above the PT and is expected to be in the metallic, rutile state where hydrogen has been shown in previous work to dope the VO₂ more easily than in the insulating, monoclinic state.[139] A representative graph of the plasmon-resonance shift as a function of time under a

H₂ atmosphere can be seen in Figure 4.14. Data sets from Au nanoparticles measured on this sample do not have a biexponential or exponential character, but rather can best be approximated as flat lines for the first 15 minutes of hydrogenation and approximated as linear fits during the remaining 45 minutes of hydrogenation, as can be seen in Figure 4.15. Using the average slope from these fits, a plasmon-resonance shift due to hydrogenation while the VO₂ is in a metallic state the entire time can be determined. The average slope from the linear fits to the dynamics data for 19 Au disks and dimers is 0.20 ± 0.03 1/min, resulting in an average resonance shift during hydrogenation at 100 °C of 9 ± 1 nm.

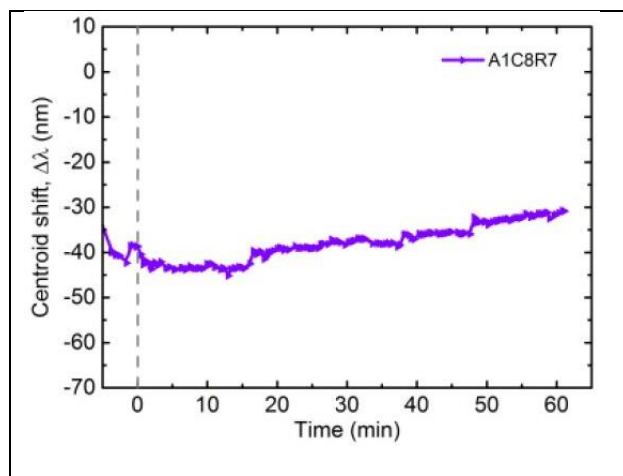


Figure 4.14 – Plasmon-resonance shift for an Au dimer embedded in a VO₂ film as a function of time during hydrogenation. Experimental data for a dimer hydrogenated at 90 °C with 100% H₂ gas flow courtesy of Song Yue (MPI-IS).

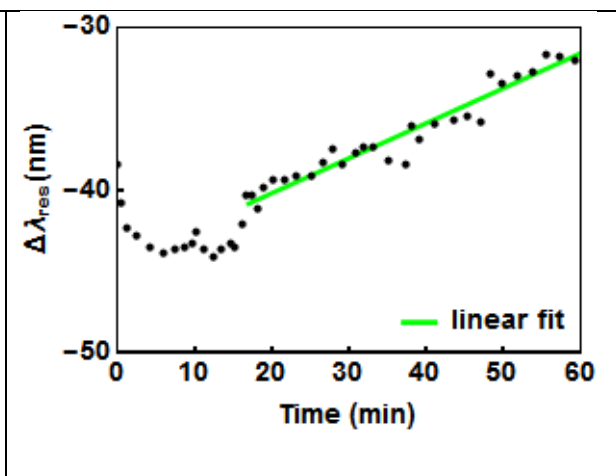


Figure 4.15 - Linear fit to sampled data for Figure 4.14. The y-axis is zoomed-in for ease of visualization. A positive slope with increasing time can be seen starting at a time of 15 minutes.

4.7 - Integrating Thermal and Dynamic Results

For the hydrogenation dynamics for 100% H₂ flow, the 25 °C data fit an exponential decay with a decay time of 30 minutes. This means that after 30 minutes only 63% of maximum

hydrogenation has been achieved. Thus, the thermal hysteresis data acquired after hydrogenation at 25 °C for 30 minutes is not the thermal hysteresis which would result from a fully hydrogenated sample.

4.8 - Conclusions and Outlook

This preliminary work on atomic hydrogen doping of VO₂ probed by plasmon-resonance spectroscopy indicates that plasmonic resonators provide a sensitive platform for probing changes in the VO₂ material properties due to hydrogen doping. This work was done using polycrystalline non-epitaxial VO₂ thin films, in contrast to other work on VO₂ hydrogenation using VO₂ single crystals or epitaxial thin films. This means that for the first time the preferential axis of atomic hydrogen diffusion into the VO₂ was random and not solely from the surface of the VO₂ towards the substrate. It would be interesting to use plasmon-resonance spectroscopy of embedded nanoparticles for epitaxial thin films of VO₂ to determine the role of the orientation of the hydrogen diffusion axis versus the role of grain boundaries in the diffusion of hydrogen in VO₂ thin films. It may prove challenging to obtain epitaxial VO₂ films that also have sufficiently low scattering so that the film scattering does not overpower the nanoparticle scattering. It would also be interesting to determine why the hydrogen doping in sputtered VO₂ thin films is not fully reversible whereas it has been shown to be reversible in all other studies of hydrogenated VO₂, including previous work done while developing a non-scattering VO₂ film where plasmon-resonance spectroscopy was carried out for Au nanoparticles embedded in electron beam evaporated VO₂.

CHAPTER 5

ACTIVE PIT IN STACKED AU-VO₂ DOLMENS

5.1 - Introduction

Nanoparticles exhibit resonances dependent on properties such as particle shape, resonator lossiness, and dielectric environment. The plasmon resonances of metallic nanoparticles can be sharp based upon their damping such as if the mode is a bright or a dark mode, but the resonance positions cannot be changed after fabrication. Vanadium dioxide (VO₂) has been used to actively tune the plasmon resonance of metal nanoparticles in the visible to terahertz regime because the phase transition in VO₂ is accompanied by a large change in dielectric function. Vanadium dioxide is lossy in the visible and near-IR, broadening and damping the plasmon resonances of metallic nanostructures placed on VO₂ films. It is desirable to use VO₂ nanoparticles in the plasmonic near field of metallic nanostructures to minimize the broadening but retain the active plasmonic nature of Au nanoparticles on a VO₂ film. As this causes the resonance shift over the PT to be small,[108] nanostructures that exhibit sharp resonances, such as dolmens exhibiting PIT, have the potential to increase the switching contrast in the presence of VO₂ due to the sharp resonances.

In this Chapter, tunable plasmon-induced transparency (PIT) is demonstrated through simulations in the near-IR by switching the phase of VO₂ in a stacked Au-VO₂ dolmen nanostructure geometry. A stacked dolmen nanostructure which was experimentally fabricated using a single layer of EBL was also shown through simulations to exhibit PIT when the dimensions of the fabricated structure were used in the simulations. The parameter space of the

stacked Au-VO₂ dolmen nanostructures was also explored to optimize the contrast in the transmission over the PT. It was determined that a sharp plasmon resonance due to reduced VO₂ in the local environment of a plasmon resonator also brings a reduction in the plasmon-resonance shift over the PT such that it was not possible to simultaneously optimize both the resonance shift and narrowness of the resonance. This places limits on the switching contrast that can be obtained using this geometry. The results suggest that using VO₂ nanoparticles coupled with complex plasmonic nanostructures, such as dolmens, can produce tunable plasmon resonances but that these are still limited by the lossiness of VO₂ and the small change in the effective dielectric environment of the Au dolmen due to the PT of VO₂ nanoparticles. Gold-vanadium dioxide dolmen nanostructures using “just enough” VO₂ provide resonances that are actively tunable and can be switched, potentially on the ultrafast timescale, with a 26% contrast. This contrast is not suitable for an optical switch where contrasts near 100% are necessary. This would be acceptable as an optical sensor, but the resonance is broad compared to other sensor designs, which is not optimal when attempting to detect small shifts in resonance. These results indicate that it is possible to design an Au-VO₂ nanostructure with active PIT, but that this geometry did not prove to provide the improvements to Au-VO₂ active plasmonics that were initially envisioned.

5.2 - Theory

5.2.1 - Bright and Dark Plasmon Modes

Plasmon modes can be grouped into two categories based on their ability to couple to incident light. Bright modes, such as dipole modes, can couple to incident light. This also

means that they have high radiative decay rates, so these resonances are short-lived and spectrally broad. Dark modes, such as a quadrupolar mode, cannot couple to incident light but can be excited through other means. Due to this, dark modes can only decay through non-radiative processes and by losing energy due to intrinsic losses in the metal. The non-radiative decay is far slower than the radiative decay and the loss of energy in the plasmon mode, and both the dipole mode and quadrupole mode lose energy due to intrinsic losses in the metal nanoparticles supporting the dipole and quadrupole resonances. For this reason, these modes are long-lived and spectrally narrow.[149, 150]

5.2.2 - What is Plasmon-Induced Transparency?

Plasmon-induced transparency (PIT) is the classical analog of electromagnetically induced transparency. In PIT, the coupling of a broad and a narrow plasmon resonance excited with incident light causes the plasmonic structure to become transparent to light within a narrow band of wavelengths,[61, 109, 149-153] as can be seen in Figure 5.1. This can occur in a variety of nanostructures such as dolmens, concentric and non-concentric ring-disk systems, asymmetric rings, and plasmonic clusters such as heptamers and hexamers.[151, 154] The dolmen structure, shown schematically in Figure 5.2, will be considered here.

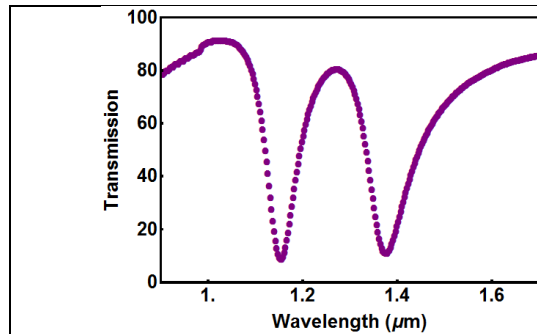


Figure 5.1 - Simulated transmission spectrum showing PIT.

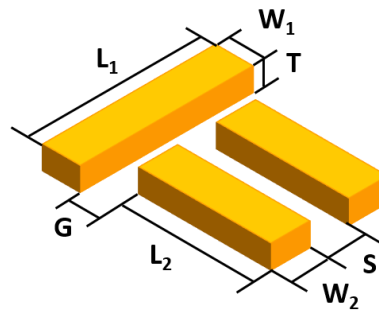


Figure 5.2 - Schematic of a dolmen structure.

The coupling of a dipolar and a quadrupolar plasmon resonance in a dolmen structure can cause PIT because of the coupling between the dipolar mode and both the quadrupolar mode and the light incident on the resonators. The single nanorod with the long axis parallel to the direction of the electric field of the incident light supports the dipolar plasmon resonance, which causes the electrons to oscillate along the long axis of the nanorod in a mode that can be excited by the incident light. The pair of nanorods with their long axes perpendicular to the direction of the electric field supports a quadrupole resonance where the electrons in the two nanorods are counterpropagating. This resonance cannot be directly excited by the incident light. If, though, the dipole and quadrupole resonances are close in wavelength and the nanorods supporting the dipole and quadrupole modes are spatially close together, the plasmon oscillation in the dipole antenna can couple to and excite the quadrupolar resonance in the quadrupole antenna. At this point, the dipolar plasmon resonance is being driven by both the electric field of the incident light and the electric field created by the quadrupole plasmon resonance. Plasmon-induced transparency occurs when these electric fields are equal in magnitude and opposite in sign so that the dipole plasmon resonance does not form and absorb light at its resonant wavelength.[152] Instead, light in a narrow band of wavelengths around the resonant wavelength of the dipole antenna is transmitted through the nanostructure as though the nanostructure is transparent over

that band of wavelengths. The width and strength of the PIT region is governed by the coupling between the dipolar and quadrupolar modes,[149] and the sharpness of the PIT region is governed by the losses in the quadrupolar mode.[61]

In the dolmen nanostructure, the coupling between the dipole and quadrupole modes is dictated by the size of the gap G (labeled in Figure 5.2), with a smaller gap leading to higher coupling between the component modes. This can be seen in Figure 5.3 in the simulated transmission curves, where the gap G is altered from 20 nm to 100 nm without changing any other features of the dolmen structure. Here, the transmission in the PIT region decreases with increasing gap size and the wavelength range over which PIT occurs also shrinks. The PIT region does remain centered about the bonding and antibonding mode wavelength positions, indicating that the resonant wavelengths of the component dipole and quadrupole resonators remain matched with each other as G is altered. Interestingly, the long wavelength bonding mode blue-shifts noticeably more with increasing G than the short wavelength antibonding mode red-shifts.

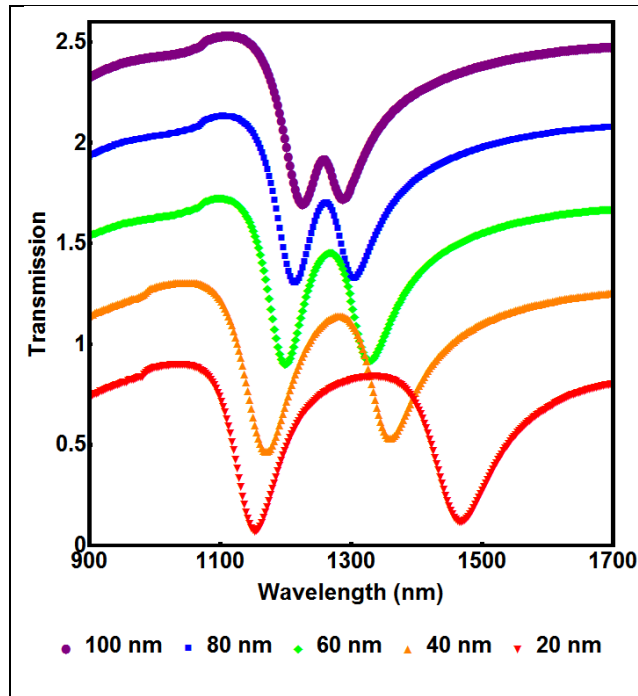


Figure 5.3 - Simulated transmission for Au dolmens on glass with decreasing gap size G . Stronger PIT is observed as G decreases. The spectra are each offset by 0.4 in transmission for clarity. Incident electric field polarized parallel to the dipole antenna, along the length of L_1 . In this set of simulations, the dimensions of the dolmen are $L_1 = 320$ nm, $W_1 = 135$ nm, $L_2 = 300$ nm, $W_2 = 125$ nm, $S = 50$ nm, and $T = 60$ nm.

The PIT mechanism is primarily described in the literature by using the concepts used to describe analog of electromagnetically induced transparency (EIT), as PIT is the classical analog of EIT. In EIT, the transition probability amplitudes from the ground state to a bright state and from a dark state to a bright state form two separate transition pathways which interfere destructively so that there is no probability of being in that bright state and, therefore, light will not be absorbed but instead transmitted. In the case of PIT with a dolmen nanostructure, these interacting transition probability amplitudes are plasmon resonances and the dipole antenna plasmon oscillation is canceled out by the influence of the quadrupole mode and the driving field from the incident light.[149, 150, 153]

As the dolmen structure consists of spatially separate dipole and quadrupole resonators, the dolmen response can be considered as the hybridization of dipole and quadrupole component modes using the plasmon hybridization theory described above.[19, 152] A hybridization diagram is shown in Figure 5.4. A low energy bonding mode forms with the local charges on

either side of the dipole-quadrupole gap having charges of different signs, creating a region of high electric field in the gap between the dipole and quadrupole antennas. A higher energy antibonding mode forms with the local charges on either side of the gap having charges with the same sign, causing the local electric field to be stronger both at the outer corners of the dolmen which are farther from the gap and also near the gap between the nanorods that form the quadrupole antenna. At approximately the energy of the component dipolar and quadrupolar modes, the state associated with PIT forms where the local electric field is weak around the single nanorod compared to the field around the quadrupole mode. The local electric field patterns associated with these three hybrid plasmon modes are verified via simulations, as seen in Figure 5.4, and have also been observed experimentally via s-SNOM.[152] A far more detailed treatment of the charge distribution of the dolmen nanostructure, considering both the real and imaginary components of the charge distribution to examine the time evolution of the plasmon resonances is provided in Ref. [155]. Using this method that does not discard the imaginary part of the charge distribution, it is clear that the dipole and quadrupole resonators that comprise the hybridized plasmon modes do not oscillate in phase, where disregarding the imaginary part of the charge distribution would not provide this information.

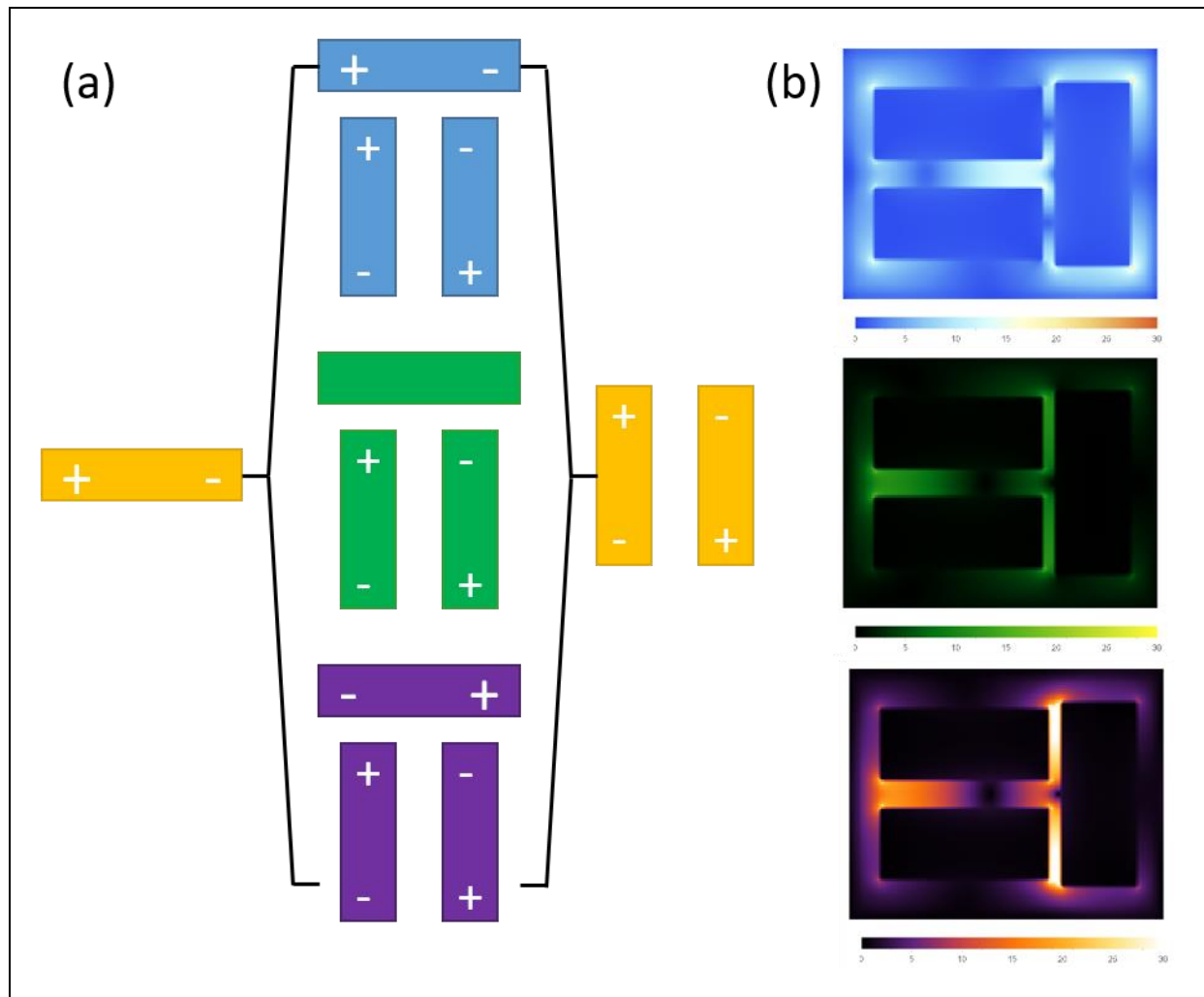
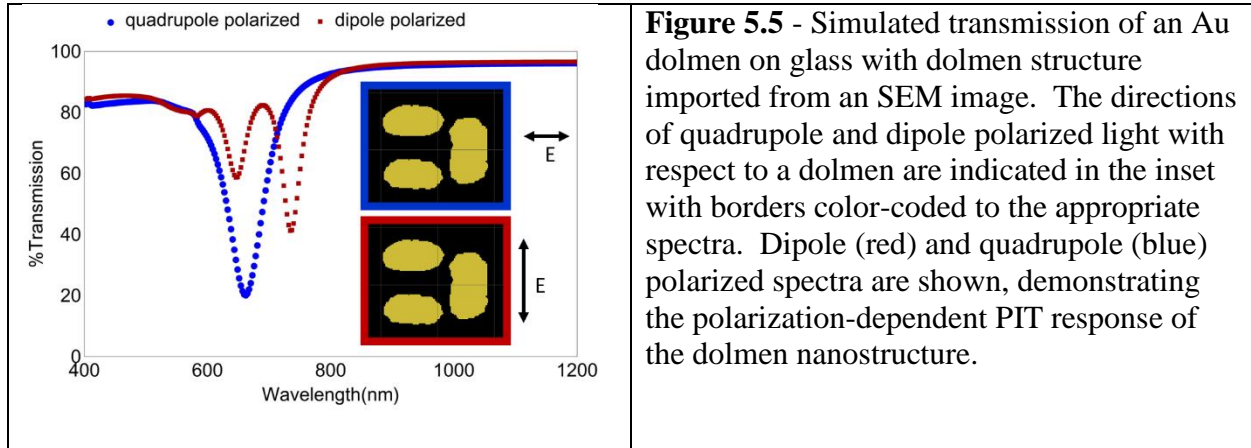


Figure 5.4 - (a) Plasmon mode hybridization diagram for an Au dolmen formed from a dipole and a quadrupole antenna showing the bonding (purple), PIT (green), and antibonding (blue) mode charge distributions. (b) The simulated local electric field maps at each of the hybrid modes described in (a) with the same color scheme. The PIT mode has no local field around the dipole antenna and the bonding mode has high electric field in the gap between the dipole and quadrupole antennas, as expected from the charge distributions. Incident electric field polarized parallel to the dipole antenna, along the length of L_1 for electric field maps.

5.2.3 - Sample Design Logic

It is desirable to actively tune PIT because it provided a sharp, tunable spectral response. Using a dolmen structure allows for a polarization-dependent PIT response. In previous work in this area, an Au dolmen on glass designed such that the PIT was centered at 690 nm when simulating with the dimensions of the fabricated dolmens and an identical Au dolmen on a VO_2

film were examined in an attempt to achieve this aim.[61] Figure 5.5 shows the simulated spectra for Au dolmens on glass with dimensions defined from importing SEMs of the fabricated structure and with light polarized parallel to the long axis of the dipole antenna and with light polarized parallel to the long axis of the quadrupole.



When the optical transmission of the experimentally fabricated Au dolmens on a 50 nm EBE VO₂ film was measured as a function of wavelength using the Avantes spectrometer as a detector, the plasmon resonance that was observed was blue-shifted as the VO₂ PT from I to M was induced by heating the sample, as seen in Figure 5.6. A plot of the data using in Figure 5.6 that does not take a running average to reduce experimental noise can be found in Ref. [61]. This was expected due to the change in the dielectric function of VO₂ over the PT. Only one resonance was observed in the experimental spectra for Au dolmens on M and I VO₂, which was identified as the antibonding mode of the dolmen since that antibonding mode has a higher resonant energy and thus a shorter resonant wavelength than the bonding mode of the dolmen. The bonding mode resonance was presumed to be at a longer wavelength and thus out of the wavelength range of the Avantes spectrometer. Using Lumerical FDTD to simulate the optical

transmission from the nanostructure between 400 nm and 1200 nm which is seen in Figure 5.7, the bonding mode resonance was not observed. Instead, a single dipole mode was observed from the dolmen nanostructure simulated atop a metallic VO₂ film, and a broad mode was observed when the dolmen was simulated on top of an insulating VO₂ film. This indicated that the dipole and quadrupole modes were not hybridizing to create PIT and suggested that the VO₂ may have been influencing the dipole and quadrupole modes differently. This also suggested that using less VO₂ may disturb the dipole and quadrupole modes that make up the hybrid modes of the dolmens less and thus allow for PIT to be observed.

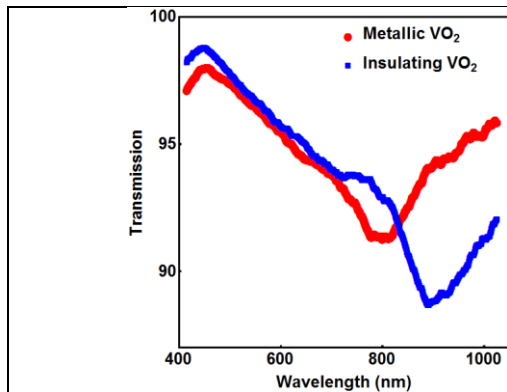


Figure 5.6 – Experimentally measured optical transmission of an Au dolmen on a VO₂ film. The light is dipole polarized. The orientation of dipole polarized light with respect to a dolmen is described in the inset of Figure 5.5.

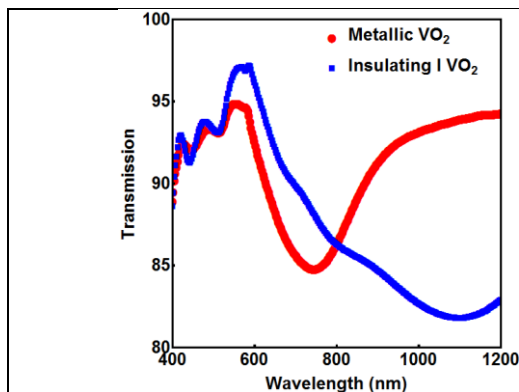


Figure 5.7 – Simulated transmission of an Au dolmen on a VO₂ film the with dolmen structure imported from an SEM image of the sample measured in Figure 5.6. The light is dipole polarized. The orientation of dipole polarized light with respect to a dolmen is described in the inset of Figure 5.5.

In a second iteration, the Au dolmen was fabricated on top of a VO₂ dolmen using the SSF method and tuned such that the PIT is in the near-IR. The shift to the near-IR is carried out

to take advantage of the increased contrast in the dielectric function of VO₂ over the PT in comparison to the dielectric contrast at lower wavelengths. The amount of VO₂ is decreased, as discussed in Chapter 2, to decrease the losses and the broadening of the plasmon resonance while maintaining active tuning capabilities, though it should be noted that the tuning range will be decreased from what would be observed using a VO₂ film.

5.3 - Simulations

5.3.1 – Simulation Overview

The simulated response of stacked dolmens consisting of Au and VO₂ is examined as a function of parameters such as G , T for the VO₂, and the pitch of the stacked dolmen array. For these various geometries, the transmission spectrum, contrast over the PT, and maximum local electric field in the dipole-quadrupole gap at the bonding mode plasmon-resonance wavelength are used as characterization tools. Unless otherwise mentioned, the simulation geometry consists of a glass substrate, a plane wave light source with emission from 900 to 1700 nm, a 60 nm thick Au dolmen, and a 20 nm thick VO₂ dolmen on top of the Au dolmen. The Au and VO₂ dolmens have the same in-plane dimensions, which are listed in Table 5.1 and apply to all of the following simulations unless otherwise stated. The boundary conditions for the top and bottom of the simulation region, where the light enters and exists the simulation region, are perfectly matched layers, which means that all light incident on those boundaries of the simulation region is absorbed. The in-plane boundary conditions for the simulation regions are periodic boundary conditions, which means that the electromagnetic fields on the opposite boundaries of the simulation region (the left and right boundaries, for example) must be equal and that the optical

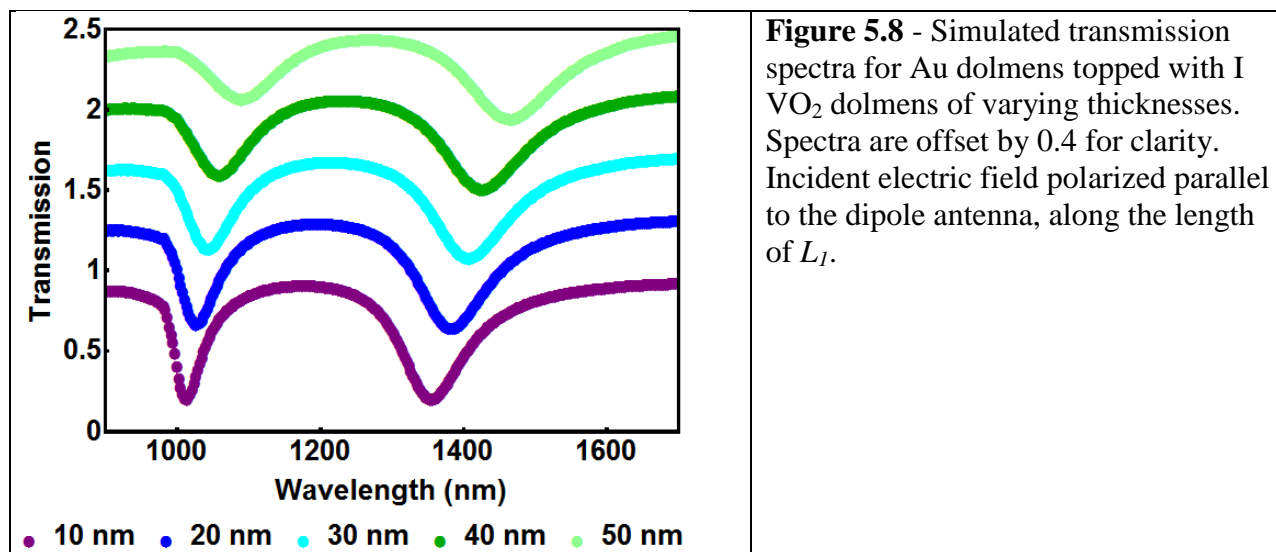
response of the simulations corresponds to the response of an infinite array of the nanostructure inside of the simulation regions. The local electric field is measured as a slice through the Au dolmen at a fixed height, half the thickness of the Au. The purpose of this exploration of the stacked dolmen parameter space is to determine if there is an optimal geometry to obtain remarkable contrast or change in local electric field over the phase transition, or to obtain an uncharacteristically sharp resonance while using this stacked dolmen platform.

L ₁ (nm)	W ₁ (nm)	L ₂ (nm)	W ₂ (nm)	G (nm)	S (nm)	X-pitch (nm)	Y-pitch (nm)
260	115	230	100	13	50	600	680

Table 5.1 – In-plane dimensions and pitch for stacked Au-VO₂ dolmen nanostructures in the simulations discussed in Section 5.4. These dimensions are applicable unless it is specifically stated otherwise in one of the following simulations.

5.3.2 - Effect of VO₂ Thickness

In this set of simulations, the thickness of the VO₂ on top of the Au dolmen is varied between 10 nm and 50 nm while holding all other parameters constant. As the VO₂ thickness is increased, the transmission spectrum showing PIT is damped, with a noticeable decrease in depth and increase in the broadness of the resonance. This is expected due to the lossiness of VO₂. The PIT is also red-shifted with increased thickness. This is because thicker VO₂ causes more VO₂ in the local dielectric environment of the Au dolmen, which increases the effective dielectric environment and, thus, causes a red-shift. This trend is illustrated in Figure 5.8 for an Au dolmen topped with insulating VO₂, but the same trend holds for metallic VO₂ as well. The resonance shift over the PT does increase with increasing VO₂ thickness, but the broadening and damping of the spectra with increasing VO₂ thickness counteract this benefit.



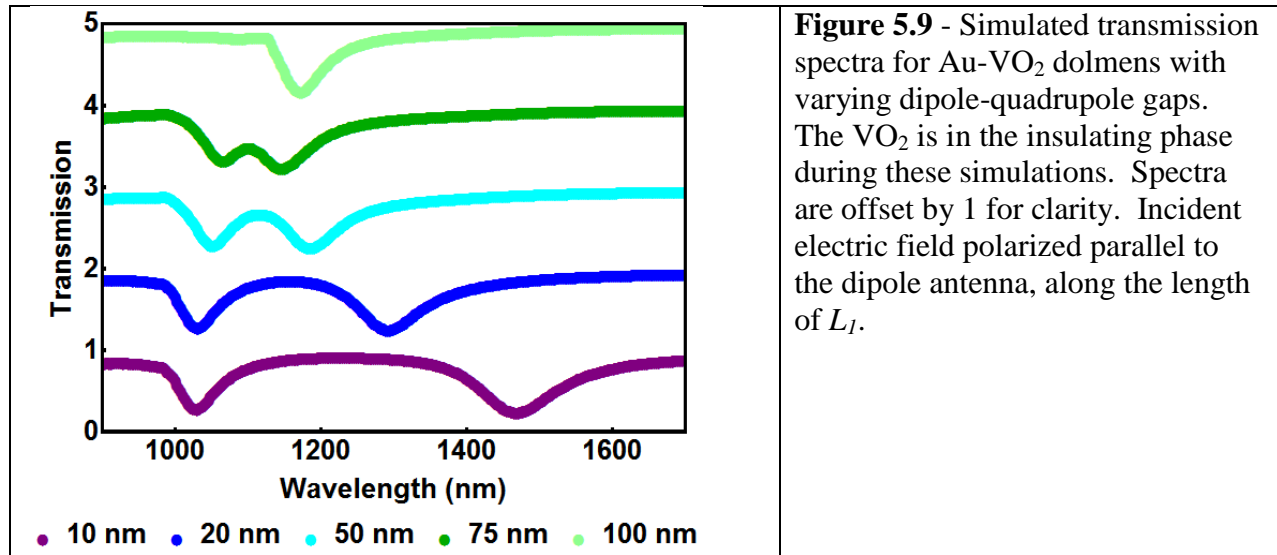
As seen in Table 5.2, the maximum contrast in the transmission spectrum over the PT increases with increasing VO₂ thickness and then levels off. The contrast increases with thickness because thicker VO₂ means that the local dielectric environment of the Au nanoparticles is comprised of more VO₂. Thus, the change in the local dielectric environment is larger for thicker VO₂. This trend holds until the thickness of the VO₂ is larger than the sensing depth of the Au plasmon and the contrast levels off because the VO₂ farther away from the Au dolmen is no longer in the local dielectric environment of the Au plasmon.

VO ₂ Thickness (nm)	10	20	30	40	50
Maximum transmission contrast	0.16	0.23	0.25	0.26	0.26

Table 5.2 - Maximum change in simulated transmission over the VO₂ phase transition for Au dolmens topped with VO₂ dolmens of varying thicknesses.

5.3.3 - Effect of Dipole-Quadrupole Gap G

In this set of simulations, the dipole-quadrupole gap G is varied between 10 nm and 100 nm while holding all other parameters constant. As G is increased, the window of PIT is reduced in wavelength range and the transmission in the window of PIT is decreased, as seen in the spectra in Figure 5.9. This is expected, as the dipole-quadrupole coupling strength influences the strength of the PIT and the physical gap between the two resonators controls this coupling strength. In addition, the wavelength of the antibonding mode red-shifts slightly and the wavelength of the bonding mode blue-shifts significantly. This occurs until G is so large that the coupling between the dipole and quadrupole modes weakens to the point that mode hybridization no longer occurs. This can be seen in the $G = 100$ nm curve below, where a single dip in transmission characteristic of a purely dipolar mode is observed. This is further confirmed when looking at the local electric field for the $G = 100$ nm resonance, seen in Figure 5.10. An electric field pattern characteristic of a dipole antenna can be seen around the single nanorod, separate from the local electric field pattern of the nanorod quadrupole. These trends are illustrated in Figures 5.9 and 5.10 for an Au dolmen topped with insulating VO_2 , but the same trends also hold for metallic VO_2 . The distance at which the dipole and quadrupole modes stop coupling can also be seen as a measure of the range of the plasmon field. A second method of measuring the range of the plasmon field using Lumerical FDTD can be seen in Appendix F.



As G is increased, the magnitude of the local electric field enhancement in the gap between the dipole and quadrupole antennas decreases. This can be seen in Figure 5.10 in the local electric field maps of Au-VO₂ dolmens taken at the wavelength associated with the bonding mode of the nanostructure as G is increased. Insulating VO₂ is used in these simulations, but the same trend holds for metallic VO₂. The ratio of the magnitude of the local electric fields in the gap for insulating and metallic VO₂ also decreases with increasing G , as can be seen in Table 5.3. For $G = 100$ nm, the ratio is 1:1 because a pure dipolar mode has been formed on the single nanorod at this gap. The maximum change in transmission over the PT also decreases with an increase in G , which can be seen in Table 5.4.

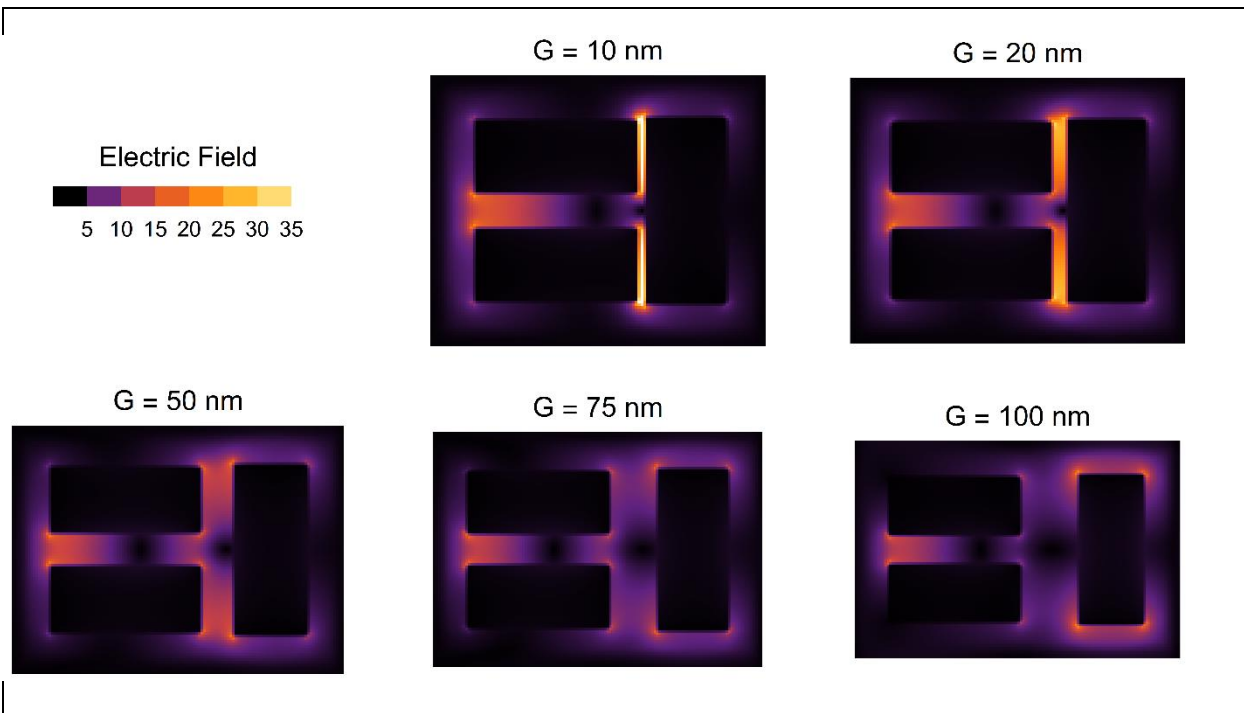


Figure 5.10 - Simulated local electric field maps for Au-VO₂ dolmens taken at the wavelength of the bonding mode of nanostructure with varying values of G . The maps are taken at a height of 30 nm. A scale of electric field enhancement is provided at the top left. Incident electric field polarized parallel to the dipole antenna, along the length of L_1 .

Gap (nm)	10	20	50	75	100
Electric field ratio (I:M)	1.79:1	1.69:1	1.56:1	1.37:1	1:1

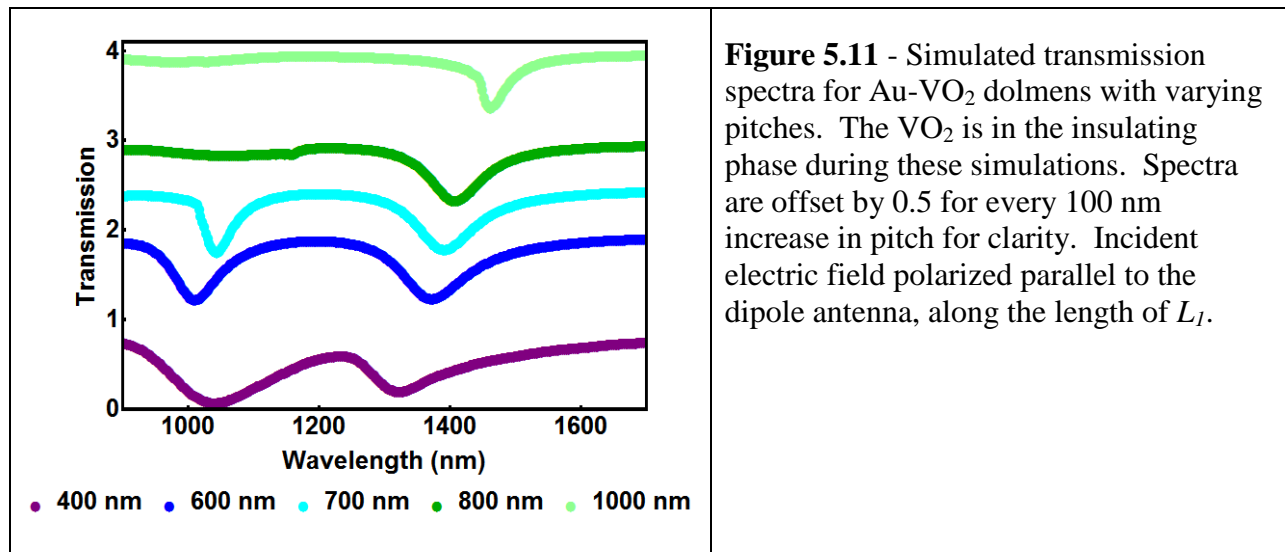
Table 5.3 - Ratio of maximum local electric field values for I and M VO₂ for Au-VO₂ dolmens with varying values of G , the dipole-quadrupole gap.

Gap (nm)	10	20	50	75	100
Maximum transmission contrast	0.24	0.21	0.18	0.16	0.16

Table 5.4 - Maximum change in simulated transmission over the VO₂ phase transition for Au-VO₂ dolmens with varying values of G , the dipole-quadrupole gap.

5.3.4 - Effect of the Pitch of the Array:

In this next set of simulations, the pitch is varied between 400 nm and 1000 nm while holding all other parameters constant. As the pitch is increased from 400 to 700 nm for Au dolmens topped with insulating VO₂ dolmens, the PIT region shifts to become centered in wavelength between the bonding and antibonding mode dips in the transmission spectrum, as can be seen in Figure 5.11. The transmission in the region of PIT increases, as does the wavelength range over which PIT is occurring. For this geometry, 700 nm is the optimal pitch in terms of the shape of the simulated PIT spectrum. Increasing the pitch to 800 nm destroys the characteristic PIT spectrum while maintaining the bonding mode as identified through the local electric field map. Further increases in pitch sharpen this mode. This destruction of the PIT and sharpening of the bonding mode that remains as the pitch increases are attributed to the Wood's anomaly, which is described in Section 1.2.8. For the range of pitches examined, the resonance position for the bonding mode for PIT also red-shifts with increasing pitch.



The maximum change in transmission over the PT increases slightly with increasing pitch, as can be seen in Table 5.5. As the pitch is increased, the magnitude of the local electric field enhancement in the gap between the dipole and quadrupole antennas increases, with a large increase for the 800 and 1000 nm pitches. This suggests that these pitches are more effectively concentrating electric field in the dipole-quadrupole gap. This can be seen in Figure 5.12 in the local electric field maps of Au-VO₂ dolmens taken at the wavelength of the bonding mode of nanostructure where the pitch is increased. The ratio of the magnitude of the local electric fields in the gap for insulating and metallic VO₂ increases slightly with increasing pitch, as can be seen in Table 5.6.

Pitch (nm)	400	600	700	800	1000
Maximum transmission contrast	0.2	0.22	0.23	0.24	0.24
Table 5.5 - Maximum change in simulated transmission over the VO ₂ phase transition for Au-VO ₂ dolmens with varying pitches.					

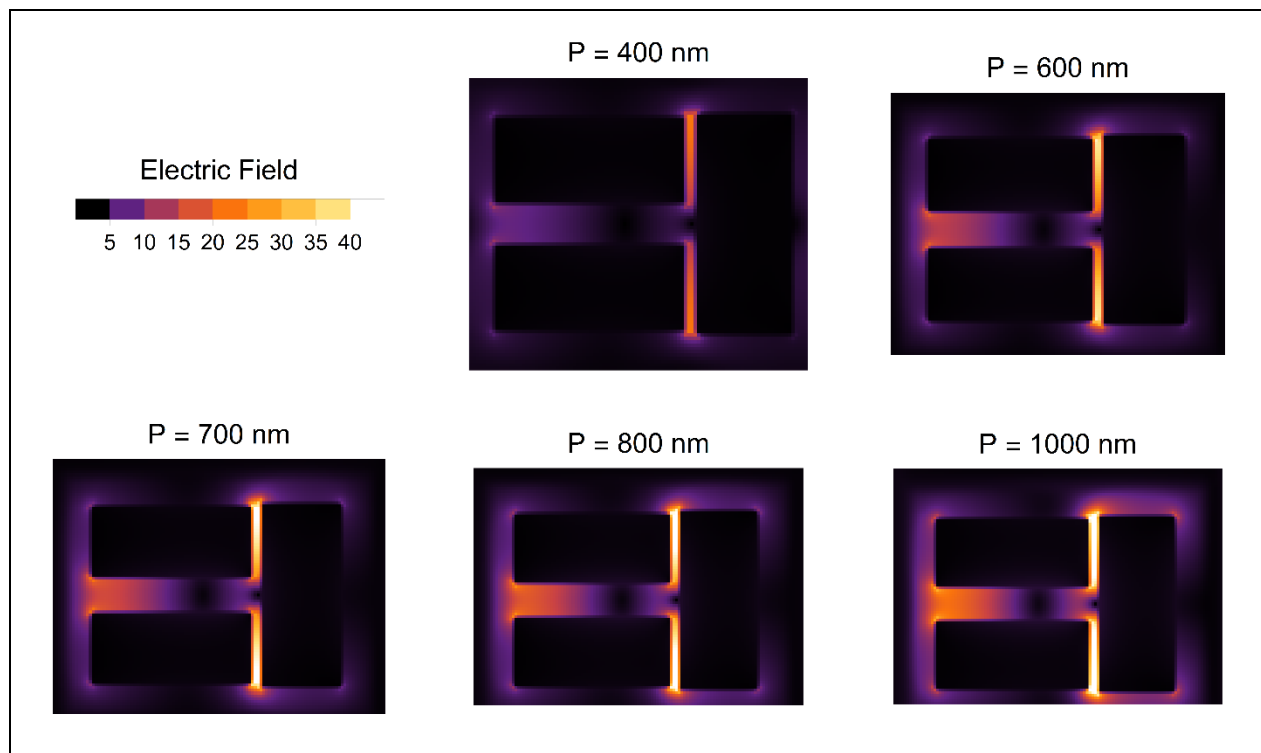


Figure 5.12 - Simulated local electric field maps for Au-VO₂ dolmens taken at the wavelength of the bonding mode of nanostructure with varying values of pitch. The maps are taken at a height of 30nm. A scale of electric field enhancement is provided at the top left. Incident electric field polarized parallel to the dipole antenna, along the length of L_I .

Pitch (nm)	400	600	700	800	1000
Electric field ratio (I:M)	1.77:1	1.75:1	1.82:1	1.88:1	1.93:1

Table 5.6 - Ratio of maximum local electric field values for I and M VO₂ for Au-VO₂ dolmens with varying pitches.

5.4 - Proof-of-Principle Fabrication and Characterization of Structures

Following these simulations, stacked dolmens were fabricated in 5 μm square arrays with varying gaps G as a proof-of-principle fabrication test. The stacks consist of 18 nm of VO₂ deposited by RF-M sputtering on top of 60 nm of Au on an ITO-coated glass substrate. The

ITO-glass substrate was coated with PMMA by spin-coating, using the thin PMMA method described in the stacked-structure fabrication section of Chapter 2. The dolmen array was patterned by EBL as described in Chapter 2 with a 20 keV accelerating voltage. Development was done as described in Chapter 2, using a stir bar rotating at 300 rpm. Gold was deposited as described in Chapter 2. Vanadium dioxide was deposited as described in the stacked-structure fabrication section of Chapter 2 with at QCM setpoint of 45 nm yielding 18 ± 2 nm, as measured by AFM shown below. Liftoff was carried out as described in the stacked-structure fabrication section of Chapter 2, except that pipetting with acetone occurred with the sample in air and not submerged in acetone. SEMs of stacked dolmens with $G = 54$ nm are shown in Figure 5.13.

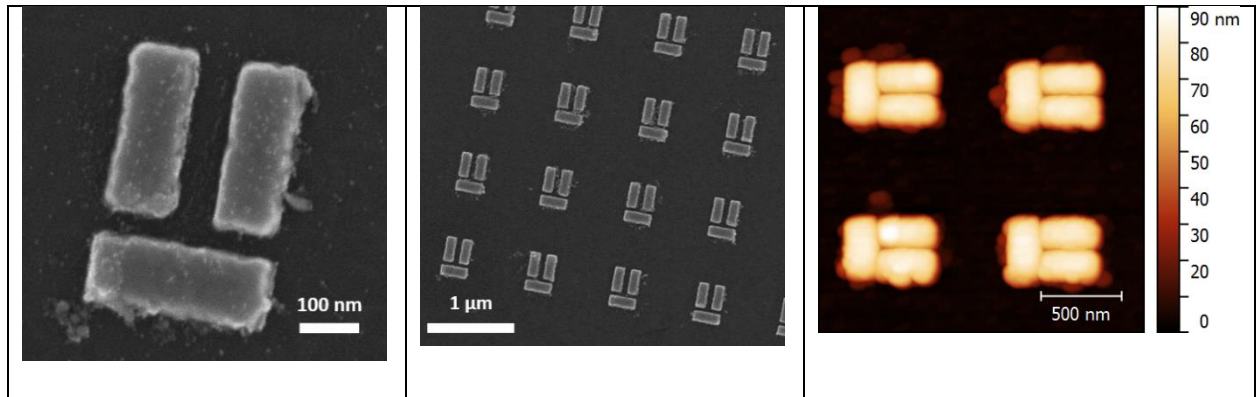


Figure 5.13 - Left and center - SEMs of stacked dolmens. Left is a magnified images of an individual dolmen and center is an array of dolmens with a pitch of 1110 nm. Right -AFM of stacked dolmen. Line profiles indicate that the full structure thickness is 78 ± 2 nm. As the Au is 60 nm thick based upon previous Au nanoparticle thickness calibration via AFM, the VO_2 layer is 18 ± 2 nm thick.

The transmission spectra based upon the dolmen dimensions of this fabricated sample are determined through simulations. The dimensions of the fabricated dolmen are put into Lumerical FDTD in two ways – 1) using dimensions measured from SEM images using ImageJ and reproduced in Lumerical FDTD with three rectangles and 2) importing a “cleaned-up”

version of the SEM image to Lumerical with appropriate scaling. The simulated transmission spectra for Au dolmens created in these two ways are shown in Figure 5.12.

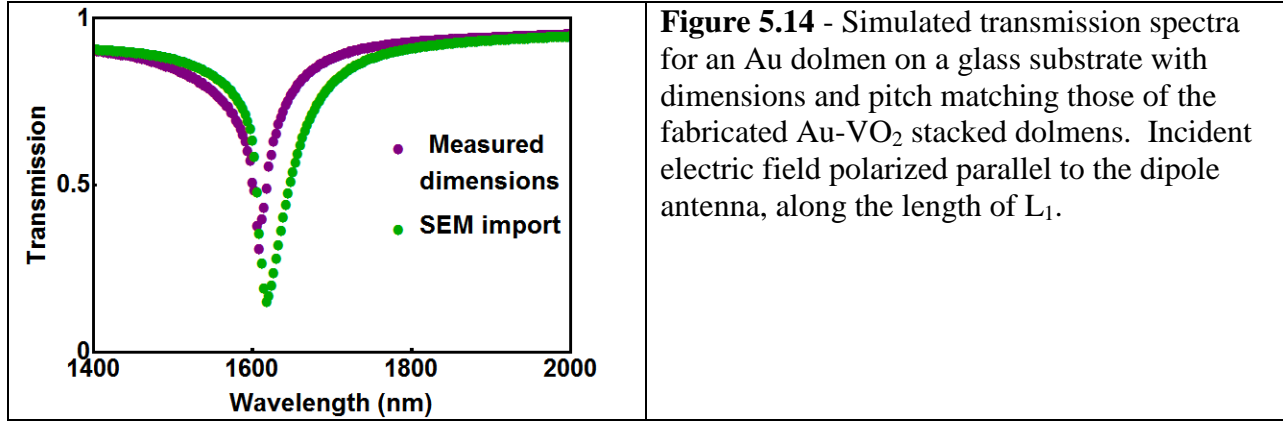
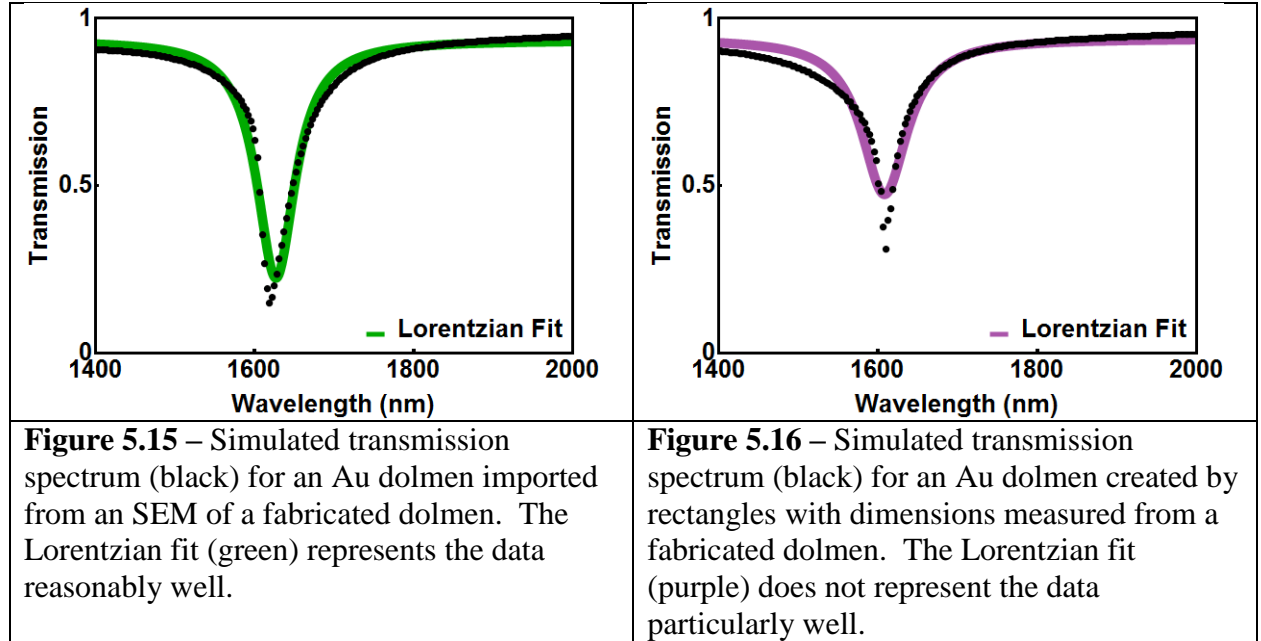


Figure 5.14 - Simulated transmission spectra for an Au dolmen on a glass substrate with dimensions and pitch matching those of the fabricated Au-VO₂ stacked dolmens. Incident electric field polarized parallel to the dipole antenna, along the length of L₁.

The transmission spectra are fit to a Lorentzian of the form shown in Equation 5.1, as this is the form of a dipolar resonance, which these curves resemble.

$$y = a - b \frac{0.5\Gamma}{(x - c)^2 + (0.5\Gamma)^2} \quad \#(5.1)$$

All three of the fit parameters are allowed unfixed during the fitting so that each can vary in order to obtain the best fit for each set of data. The transmission spectrum obtained by importing an SEM image of a fabricated dolmen and simulating the response of that dolmen can be reasonably fit to a Lorentzian, as seen in Figure 5.15. The transmission spectrum obtained by measuring the dimensions of an experimentally fabricated dolmen, reproducing the dolmen in the simulation with three rectangles, and simulating that dolmen does not fit a Lorentzian very well. This can be seen in Figure 5.16. Due to this, the fit values of b and Γ for the measured dimensions transmission curve do not represent the data well.



The maximum y value, a , is nearly identical for the transmission from the measured dimensions (0.94) and SEM import (0.93). The resonance positions are similar, though c is smaller for the measured dimensions at 1608 nm than for the SEM import at 1627 nm. The fit parameter b is related to the depth of the plasmon resonance and is 21 for the SEM import and 16 for the measured dimensions. The width of the plasmon resonance is described by Γ and is 59 nm for the SEM import and 70 nm for the measured dimensions. Though the plasmon resonances obtained using these methods are not equally well-described by a Lorentzian, the general shape of the plasmon resonance is the same for the dolmens created using method 1 and method 2. That is, a narrow, deep resonance such as that observed in Figure 5.11 for a 1000 nm pitch. The local electric fields at the resonance positions for the dolmens are similar in strength and pattern. The map associated with the SEM import has less uniformity in the dipole-quadrupole gap (G) than the map associated with the measured dimensions, as can be seen below in Figure 5.17. This is due to imperfections in the fabricated nanostructures. This suggests that

simulating fabricated structures with method 1, while not reproducing all the nuances of the fabricated structure, provides a good idea of the resonance character. Thus, method 1 was employed below.

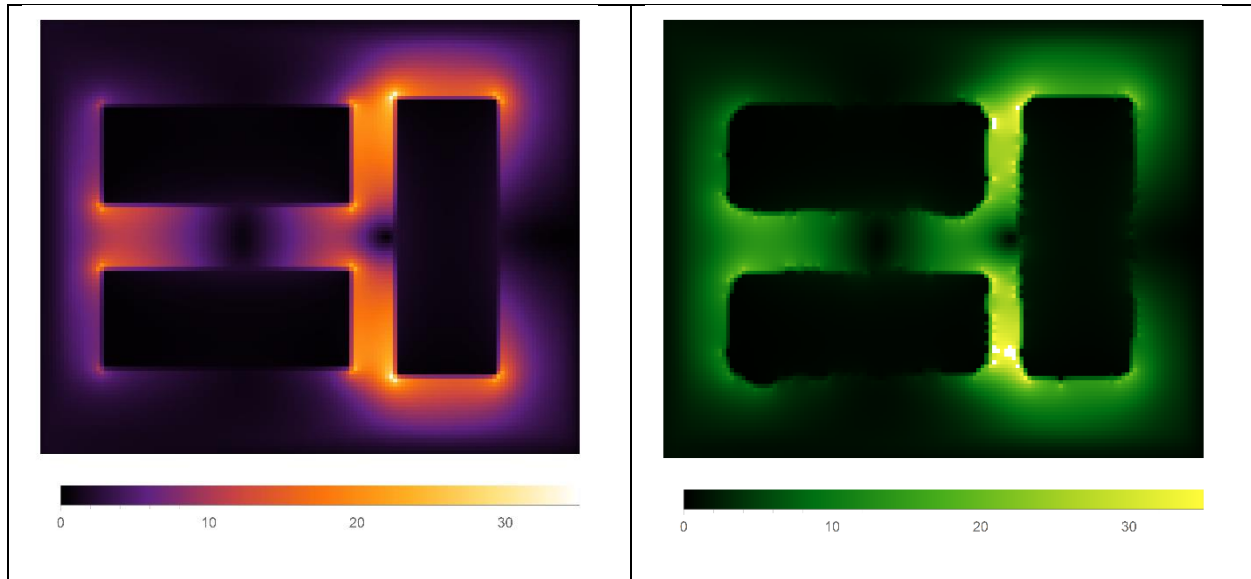
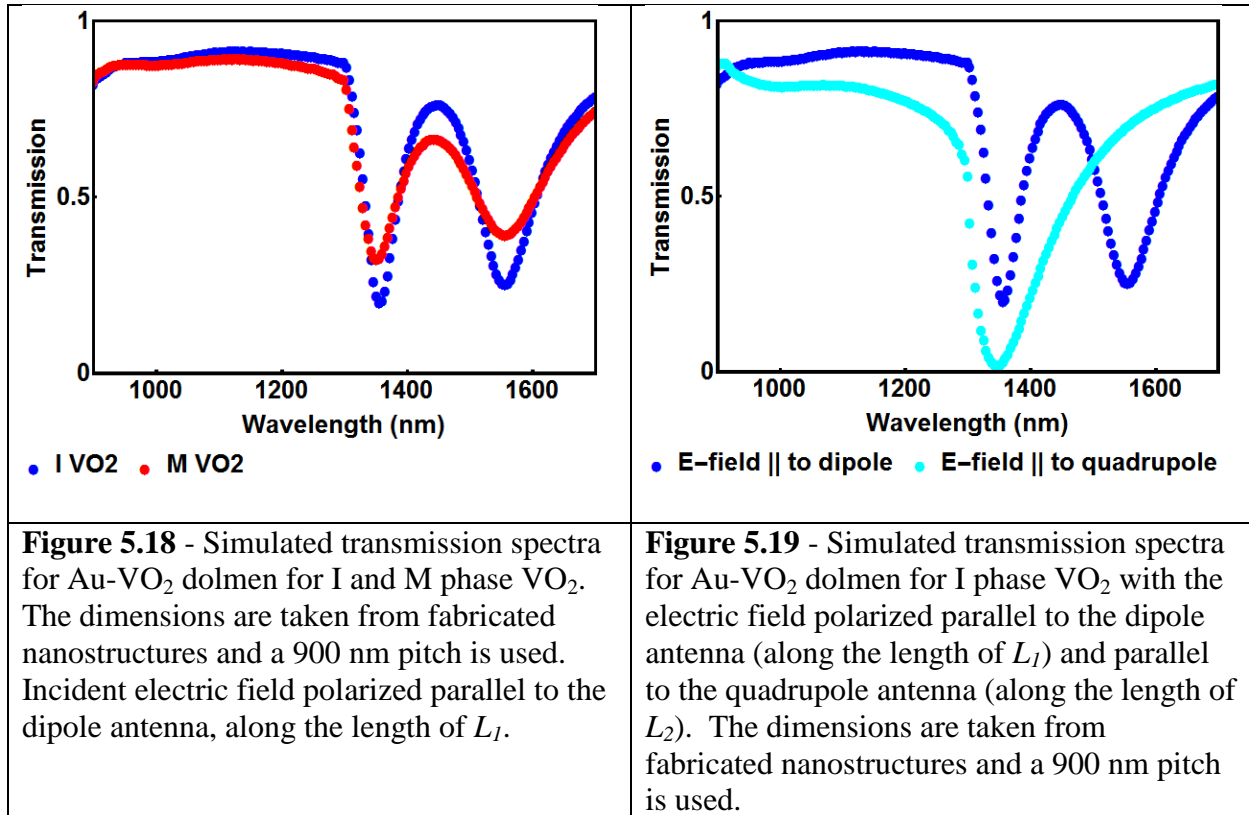


Figure 5.17 - Local electric field maps at resonance for each of the two spectra. The purple map corresponds to the measured dimensions and the green map corresponds to the SEM import. Incident electric field polarized parallel to the dipole antenna, along the length of L_1 .

Using method 1, the fabricated dolmens with 18 nm thick VO_2 are simulated for both I and M VO_2 and for light polarized both parallel to the dipole antenna (vertical in Figure 5.17) and parallel to the quadrupole antenna (horizontal in Figure 5.17). The pitch is modified from the fabricated pitch of 1110 nm to 900 nm, which was determined to produce PIT in simulations. This is done to evaluate the performance based on the positions of the individual Au bars, as the pitch is easier to modify in future samples than the precise positions of the Au bars comprising the dolmen. The simulated transmission as a function of VO_2 phase and polarization can be seen in Figures 5.18 and 5.19, respectively. There is a distinct difference in the spectra depending the phase of VO_2 for dipole polarized light, with a maximum difference in transmission over the PT

of 0.14. The effect of polarization is distinct as well, going from PIT for dipole polarized light to a broad dipole resonance for quadrupole polarized light, which is expected for a dolmen nanostructure where the observation of PIT is polarization-dependent.



5.5 - Conclusions and Outlook

In this chapter, Au-VO₂ stacked dolmens are examined via simulations based upon the results of previous experiments on dolmen nanostructures,[61] Au-VO₂ disk nanomodulators,[108] and preliminary simulations [109] with the goal of developing a nanostructure exhibiting active PIT with large contrast over the PT. Active PIT is obtained with a measurable contrast over the PT using the nanoparticle dimensions of proof-of-principle

experimentally fabricated dolmen stacks. The maximum change in transmission over the PT is 0.26, the resonance is still rather broad due to the use of metal plasmonic particles and VO₂ which both have non-trivial losses, the maximum change in electric field enhancement over the PT is only a change of a factor of two, and neither the PIT resonance position nor the bonding or antibonding mode resonance positions shift significantly over the PT due to the small amount of VO₂ in the local dielectric environment of the plasmonic particles. These results do not sufficiently advance the state-of-the-art and suggest that this specific platform of an Au dolmen topped with a VO₂ dolmen is not suitable as a high-contrast nanostructure, or one with a large resonant wavelength shift. This platform may be suitable for applications where a small but detectable change in contrast is acceptable and a polarization dependent response is desirable.

Based upon this sweep of the stacked dolmen parameter space, there are a few avenues of potential research. Due to the sensitivity of the PIT to the gap G , actively tuning the gap size through use of a stretchable substrate similar to what is demonstrated here with split ring resonators [84] or reversibly chemically depositing and removing metal on the surfaces of the dipole and quadrupole to shift the plasmon resonance and alter the gap size may be more promising than using the tunable, though small, change in the local dielectric environment from a VO₂ dolmen atop an Au dolmen. A method for reversibly altering the dimensions of metallic particles, using electrodeposition to increase the nanoparticle size and stripping to decrease the nanoparticle size, is described in Ref. [156]. Using VO₂ nanoparticles and an Au dolmen, it may be promising to place nanoscale VO₂ in a region where the local electric field is high to induce a large change in the plasmon response over the PT with a small patch of VO₂, such as in the gap between the dipole and quadrupole antennas. In this way, the dipole-quadrupole coupling would also be modified over the PT. This effect has been demonstrated for Au bowties with a VO₂

nanoparticle positioned in the gap and bridging the two triangles.[157]

CHAPTER 6

CONCLUSIONS AND OUTLOOK

In Chapter 2, processes for making non-scattering VO₂, plasmonic nanoparticles on top of VO₂ single crystals, and Au-VO₂ stacked nanostructures are discussed. These fabrication developments make the experiments discussed in the rest of the dissertation possible and open the door for new experiments and physics to investigate. One such example is the nano wedding cake structure, consisting of a VO₂ disk sandwiched between two Au disks of different radii. This structure has the potential to exhibit active second harmonic generation. Breaking the symmetry of the nano wedding cake by having the top Au disk off-center may also yield an interesting polarization-dependent response.

In Chapter 3, the phase coexistence of a low aspect ratio VO₂ single crystal is examined and found to be different from that of high aspect ratio single crystals. Using the plasmonic particles decorating the crystal surface, the nucleating M phase is also determined for the first time in VO₂ single crystals to nucleate below the crystal surface instead of extending through the entire thickness of the crystal. Thin VO₂ crystals decorated with plasmonic particles should be investigated with increasing temperature to determine if that the M domains do reach to the VO₂ crystal surface and shift the plasmon resonance of the nanoparticles with sufficient temperature. The role of aspect ratio on the observed phase coexistence pattern should also be examined in more detail to determine if there are other factors besides aspect ratio that influence the pattern of M and I domains.

In Chapter 4, doping of a polycrystalline VO₂ thin film with hydrogen and examining the influence of hydrogen on the VO₂ properties using embedded plasmonic particles is described. This proves to be a sensitive probe of the VO₂ hysteresis after different amounts of hydrogen

doping and of the VO₂ properties change while hydrogen doping is occurring such that two distinct diffusion time scales can be observed. This film is non-epitaxial and thus the preferred diffusion direction for hydrogen changes from grain to grain. Thus, a comparison of these results to the dynamics of hydrogen doping for an epitaxial VO₂ film with embedded plasmonic particles may indicate the respective roles of the grain orientation and grain boundaries in describing hydrogen doping of VO₂ thin films.

In Chapter 5, a design for active PIT using a stacked Au-VO₂ dolmen nanostructure is described. It is also determined that there is a limit to the switching contrast over the PT achievable with this geometry. Placing VO₂ in the gap between the dipole and quadrupole antennas to reversibly tune the coupling between these modes and thus tune the PIT may prove to increase the contrast over the VO₂ PT. Due also to the sensitivity of the PIT response to the dipole-quadrupole gap size, a manner of actively alter the gap size such as using a stretchable substrate or reversible growth and removal of material on the dipole and quadrupole antennas could be a fruitful direction for active plasmonics.

Based upon the work detailed in this dissertation, I propose some new directions, applications, and fabrication developments using VO₂, or VO₂ and metal plasmonics.

Hydrogen doping of VO₂ alters the crystal structure of the VO₂ by changing the bond lengths between neighboring V atoms. Especially in a single crystal, this should, in principle, alter the strain in the VO₂ and thus influence the ferroelastic domains and the phase coexistence pattern when the sample is heated. The influence of atomic hydrogen on the ferroelastic domains of VO₂ in a single crystal could be determined by optically imaging the crystal during hydrogen doping with a polarized optical microscope, since both ferroelastic domains and the effect of hydrogen doping produce contrast in the color of the crystal. The catalyst necessary to split the

molecular hydrogen into atomic hydrogen could also be deposited only on certain parts of the crystal to attempt to control which parts of the crystal become doped with atomic hydrogen.

Atomic hydrogen is known to passivate surfaces. The vanadium dioxide surface is known to have a higher fraction of V^{3+} and V^{5+} than in the bulk of the material which has more V^{4+} . Combining these two facts, it would be interesting to see how the vanadium valence on the film surface changes with hydrogen doping. The vanadium valence, for example, could be measured both before and after hydrogen doping to determine the effects of atomic hydrogen on the vanadium. These valence states are conventionally measured using X-ray photoelectron spectroscopy (XPS) under ultra-high vacuum (UHV).[158] It would not be feasible to measure changes in XPS during hydrogen doping, since the gas atmosphere would alter the detected photoelectron energies. For this reason, XPS would be done on the sample under UHV before hydrogen doping, the sample would be removed to a gas cell for hydrogen doping, and then sample would returned to UHV so that XPS could be done after the hydrogen doping.

To obtain narrow optical resonances from nanoparticle structures, metal plasmonics are not a suitable choice due to their high free electron densities that contribute to the losses in these metals, as described in Ref. [13]. Instead, dielectric metasurfaces using materials such as silicon could be used due to the low losses from absorption in the material which results in very narrow plasmon resonances. These dielectric metasurfaces can even be composed of multiple resonator components exhibiting both dark and bright modes which can couple and produce a metasurface analogy to PIT, as described in Ref. [159]. Dielectric metasurfaces have also been demonstrated to be sensitive to their local dielectric environment.[159] Thus, combining a dielectric metasurface with VO_2 should yield active tuning of a sharp optical resonance. This may

represent a path toward a nanoscale optical switch which can be controlled on the ultrafast timescale with light, as the VO₂ phase transition can be induced in this manner.

A strength of metal plasmonics that has not been employed in this work is that metal plasmons locally generate heat related to the absorption in the material. The shape of the nanoparticle can alter the amount by which the temperature of the material is increased when illuminated by light, as seen experimentally.[160] The role of absorption and thus local heating by plasmonic particles can be simulated using simulation software from Lumerical[®], specifically by calculating the absorption in the nanostructure using Lumerical FDTD and calculating the increase in temperature based on this absorption using the heat transport solver from Lumerical DEVICE.[95] This local heating may be sufficient to locally switch VO₂ nanoparticles or a thin film next to the metal plasmonic particles based on the simulated temperature rise. If light were incident upon these nanostructures, the local increases in temperature from the metal plasmonic particles could switch just parts of a VO₂ thin film and create patterns like a diffraction grating depending on the placement of the plasmonic particles, where the patterns would disappear after the PT is reversed. If the insulating VO₂ dielectric function depends on has temperature, heating the material above room temperature but below the PT could produce a temperature gradient which would produce a gradient in the refractive index that could focus or defocus light incident on that region of the sample. This could lead to a lensing effect in which the focus can be tuned. Designing the nanoparticles to have polarization-dependent absorption could also create a multifunctional material where light of one polarization could be focused while not altering light of a different polarization, for example.

This idea is a way to fabricate hybrid plasmonic-VO₂ nanostructures using one layer of EBL and placing VO₂ only in the regions around the nanoparticle that have a high local electric

field when the plasmon resonance is excited. In short, the nanoparticle is covered with a polymer sensitive to high electric field and four-photon absorption in the polymer damages the regions of high electric field, as described in Refs. [161, 162]. The nanoparticle is covered in PMMA and the plasmon resonance of the nanoparticle is excited. Due to four-photon absorption, the high electric field generated at specific places on the nanoparticle will expose the PMMA if the resonant wavelength is appropriately tuned. The power of the laser and the exposure time influence the size of the exposed region. The sample can then be developed to remove the exposed areas, leaving wells in the PMMA which can be filled with VO₂. Liftoff will remove the unexposed PMMA, leaving VO₂ where the local electric field from the plasmon is the highest. More details of the process used to expose the regions in the PMMA that experience the high electric field from the plasmons, called PMMA mapping, are described in Ref. [163], which extends the work of Ref. [161] from nanorod monomers and dimers to bowtie antennas.

The previous idea creates precisely positioned metal and VO₂ nanoparticles in close proximity using a single step of EBL. This last idea envisions the fabrication of hybrid metal nanoparticle-VO₂ film active broadband absorbers without using EBL or a thin film deposition method that requires a deposition chamber, such as RF-M sputtering or thermal evaporation, allowing for cheap fabrication of devices. Metal nanoparticles of various sizes can be grown chemically or purchased from commercial sources. This removes the need for EBL and provides access to particles with precise plasmon-resonance wavelengths. Vanadium dioxide can be deposited as a thin film using a sol-gel method, as described in Ref.[164]. In this method, a solution is prepared and spin-coated onto a substrate. The coated substrate is then baked in a furnace to remove the solvent and create a VO₂ film. A sol-gel method for creating VO₂ thin

films and W-VO₂ films has been developed at Vanderbilt by Hanu Arava using the tube furnace to bake the coated substrates. It should be possible to combine the chemically fabricated metal nanospheres with the solution for the VO₂ sol-gel process to create a VO₂ film with metal nanoparticles embedded in the film. This creates an active plasmonic device without complex lithographic fabrication, as seen in the top left of Figure 6.1. Changing the size of the chemically fabricated nanoparticles will change the plasmon resonance of the nanoparticles, as can be seen in the schematic in the bottom left of Figure 6.1. Thus, combining chemically fabricated nanospheres of different sizes with the VO₂ solution should create broadband absorption that is tunable by inducing the phase transition of VO₂. With careful design of the device, inducing the PT should open a window of transparency within the region of broadband absorption as can be seen on the right of Figure 6.1, so that the device would act as a controllable filter. This is because the change in the dielectric function of the VO₂ over the PT, and thus the resonance shift of the plasmonic particles over PT, is wavelength-dependent.

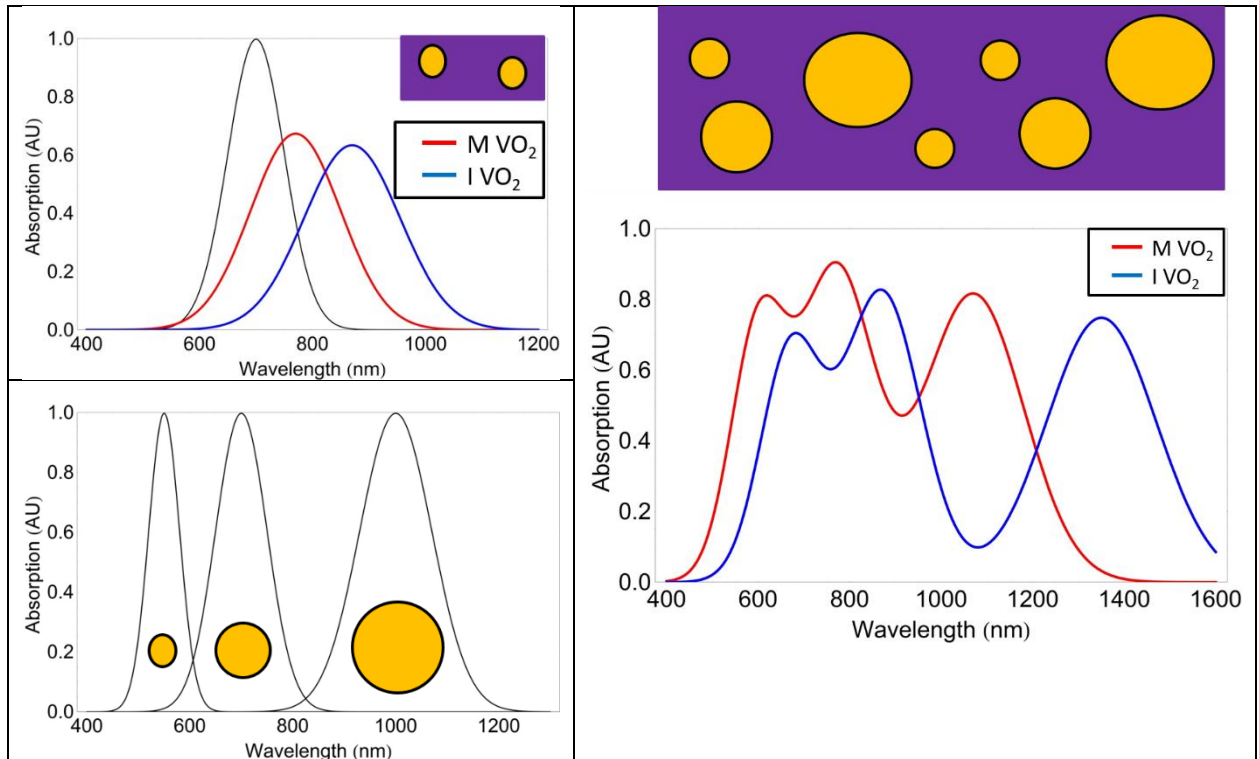


Figure 6.1 – Schematics illustrating the principles for a broadband absorber which is actively tunable. In the top left, the absorption of nanoparticles of the same size embedded in M and I VO₂ (red and blue, respectively) are shown in comparison to the absorption of those nanoparticles in air (black). In the bottom left, the absorption of nanoparticles of different sizes in air are shown. On the right, the absorption of nanoparticles of different sizes embedded in M and I VO₂ (red and blue, respectively) are shown.

APPENDICES

Appendix A

Useful Lumerical Scripts

A.1 – Parameter Sweeps using Scripting

A parameter in a simulation, such as the length of a nanorod, can be swept over by hand by creating many simulations which each have a different value of this parameter. It is simpler to create all of these simulations and modify a parameter in the simulations using a script. A script provided below modifies the length of a nanorod in the x direction over a defined range and saves each file with a name defined in the script. In line 1, the one dimensional array called *xspan* is defined to have values ranging from 100×10^{-9} to 200×10^{-9} in three steps. These values, then, are 100×10^{-9} , 150×10^{-9} , and 200×10^{-9} . The rest of the script consists of a for loop. The second line sets up the for loop to iterate over values of the counter variable *i*, starting from 1 and going until the *i* is larger than the number of values in *xspan*. The third line changes the open simulation from the result viewing mode to the layout mode where the values of parameters can be modified. The fourth line sets the parameter of x span in the object named nanorod to the value of *xspan* at the position *i* in that one dimensional array. The fifth line defines a parameter called *f_name* to be the words nanorod length test combined with the current value of the counter variable *i*. In this script, for example, if the counter *i* was 2 then the parameter x span for the nanorod would be set to 150×10^{-9} nm and the name of the file would be nanorod length test 2. The last line saves the simulation to the file name defined in the fifth line.

```

xspan=linspace(100e-9, 200e-9, 3);
for (i=1:length(xspan)) {
Switchtolayout;
setnamed("nanorod", "x span", xspan(i));
f_name="nanorod length test "+num2str(i);
save(f_name); }

```

A.2 – Script to run Multiple Simulations in a Row

Simulations can be manually run by clicking the green run button for an open simulation. When it is necessary to run multiple simulations, it can be helpful to place them all in the simulation queue and then run all of the jobs one after the other. A simple script such as that shown below permits a list of simulations to be run in manner. In this script, three simulation files (file 1, file 2, and file 3) are added to the simulation queue in lines one through 3. In line four, the simulations in the queue are run.

```

addjob("file 1");
addjob("file 2");
addjob("file 3");
runjobs;

```

A.3 - Exporting Data from a Monitor

Data can be exported manually from a monitor by viewing the relevant data and clicking the appropriate buttons to export those data. When it is preferable to process or scale the data before exporting it, or when the data are to be imported into a program for analysis that does not parse headings well, a script can be used to export data from a specific monitor. A script showing how to export a transmission spectrum from a monitor is shown below. The first line defines the variable T as having the list of transmission values held in the monitor called *TransmissionMonitor* in the simulation from which data are being exported. The second line

defines the variable f as having the list of frequency values held in the *TransmissionMonitor* monitor. The third line defines a new variable λ as the speed of light c (a known constant in Lumerical FDTD) divided by f and multiplied by 10^9 so that the frequency values are converted to wavelength values. The fourth line defines an array names *data_to_print* to contain the values of λ and of T multiplied by 100. In this way, this array contains the percent transmission at each wavelength point, where the wavelength is in nanometers. In the last line, the data in *data_to_print* are converted to a string and written to the file named *transmission spectrum.txt*.

```
T=transmission("TransmissionMonitor");  
f=getdata("TransmissionMonitor", "f");  
lambda=c/f*1e9;  
data_to_print=(lambda,T*100);  
write("transmission spectrum.txt", num2str(data_to_print));
```

Appendix B

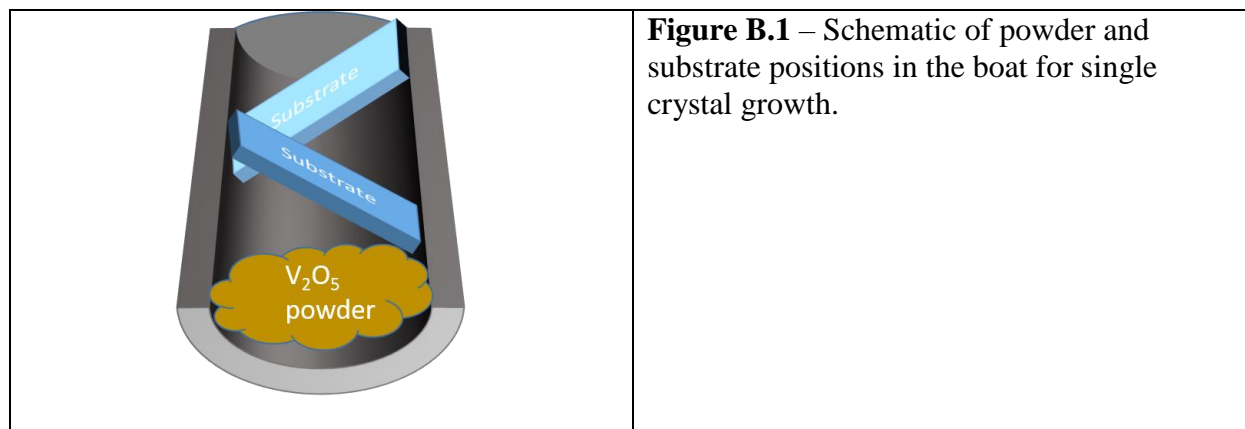
Detailed Process for Single Crystal Growth

In Appendix B, the detailed process and considerations from growing VO₂ single crystals in the tube furnace in the Haglund lab are discussed. Topics such as substrate constraints, sample loading for single crystal growth, and a heating recipe are covered here.

As the growth temperature for VO₂ single crystals is 825 °C, with crystals also growing between 810 °C and 850 °C, the melting temperature of the substrate on which the crystals will grow must be high enough that the substrate will not melt during growth. SiO₂, for example, should not be used as a substrate for this crystal growth. Silicon and quartz approximately 1 cm in size both work nicely, and the Si doping does not influence the crystal growth in any noticeable manner. Silicon is conductive whereas quartz is not, but growth on quartz yields larger single crystals. Cleaning the substrates before the crystals growth does not influence the resulting crystals, so it is unnecessary to clean the substrates before growth.

Boats are used to hold the V₂O₅ powder and the substrate on which the material will condense. The boats are loaded such that the V₂O₅ powder is upstream (loading side of the tube) and the samples are downstream (vacuum pump side). For the powder, approximately a teaspoon is placed in one end of each boat using a spatula. Fresh powder is used for each single crystal growth. A maximum of two samples are placed at alternating angles away from where the powder has been placed in each boat, as seen in Figure B.1. For Si samples with one side polished, the polished side is placed face down in the boat. The two boats are then placed into the small quartz tube which is colored black from previous single crystal growths. The small quartz tube is used to confine the vapor and make it easier to remove the boats from the main

tube in the furnace. The boats tend to get stuck to the bottom of the tube if they are put directly into the main tube.



The small quartz tube is loaded into the main tube by placing the small tube in the main tube and pushing it as far into the main tube as possible with a hand. A steel rod with distanced marked with marker is used to push the small tube into the main tube until the red mark on the rod is in line with the beginning of the furnace. While doing this, it is important to push on the small tube and not the boats inside the tube. Inserting the rod into the main tube at an angle makes this easier, since then it is possible to push on the side of the small tube. Due to previous single crystal growths, the main tube is rough inside of the furnace, so care must be taken to prevent the boats in the small tube from flipping over.

As this process uses Ar gas instead of O₂, the vacuum pump that is not suitable for use with O₂ is used to save the pump that can operate with O₂ gas for VO₂ annealing. The exhaust hose must be swapped to the vacuum pump being used. At this point, the tube can be sealed as is done for VO₂ annealing – by placing the end piece on the tube and pumping down the tube using the vacuum pump. Once the tube is under a sufficient vacuum that the end piece will stay on without being held, the split ring holder is removed so that it is safe to leave the tube furnace

unattended during this growth process. To monitor the pressure inside the tube, a vacuum that can measure pressures up to 2 Torr is used. Once the pressure in the main tube is less than 30 mTorr, Ar gas is flowed into the tube furnace to reach a pressure of 1.7 Torr. It is necessary to verify on the computer that the Ar mass flow controller is being used for this process instead of the O₂ mass flow controller. The pressure in the tube will take some time to equilibrate, but the temperature ramping should be started at this point because nothing will occur in terms of single crystal growth until the high 700 to low 800 °C range.

Before heating the tube, the fans below the tube should be turned on to prevent the tube and the fittings from becoming too hot. The temperature is ramped up to the growth temperature of 825 °C in stages so to not overshoot the growth temperature. The tube is first ramped to 250 °C. It can be left to heat for 10 minutes during the temperature ramping and at this point the mass flow controller can be adjusted if needed. The tube is then ramped to 450 °C, which should take approximately 15 to 20 minutes, and, then to 650 °C, which should also take approximately 15 to 20 minutes. The timing is not as critical up to this temperature, and if a temperature is within 20 °C of the target temperature on the ramp the next step can be carried out. Above 650 °C the timing becomes more critical because this is becoming close to the growth temperature. The final step in the heating ramp is heating the tube to 825 °C for 15 to 20 minutes and starting a timer when the temperature reaches 825 °C. After one hour of single crystal growth at 825 °C, the furnace can be turned off and let to cool for at least four hours or until the temperature reaches 100 °C and can be handled. At this point, a copper rod with a hook at one end can be slid into the main tube past the end of the small quartz tube to hook the downstream end of the small tube and pull the small tube out of the tube.

Appendix C

Detailed Process for Writing Nanoparticles on VO₂ Single Crystals

In Appendix C, the process of writing an EBL pattern on a specific location of a non-uniform sample is described. This process has many steps in common with doing the second layer of a two layer EBL process.

If an electron beam lithography (EBL) pattern is to be written on a uniform sample (bare substrate, substrate with a film on it, etc), a basic EBL writing procedure can be used for positioning the sample, where a scratch is made in the bottom left corner of the sample and the pattern is written some user-set distance (typically millimeters up and to the right) from the end of the scratch. This works with no issue on a uniform sample, since as long as the pattern is written approximately where it was placed, then the pattern can be easily located to check lithography quality under an SEM and to be measured in an experimental setup. If, though, multilayer lithography or writing on specific features on the underlying sample is necessary, the above method lacks the requisite precision. The following description of steps will focus on writing Au nanorods on randomly located VO₂ single crystals, though comments about adapting the procedure to conventional double layer EBL are also made throughout.

Writing Au nanostructures on VO₂ single crystals poses a few challenges. They are randomly located on the sample, as can be seen in Figure C.1 on the right, so it is difficult to locate a specific single crystal identified via optical microscopy on the Raith. Once the pattern is written, it is also difficult to go back and find the written area. Another challenge is that writing specifically on the single crystals requires precision and also focus adjustments as the single

crystals are significantly taller than the substrate on which they are grown. To make locating specific crystals easier, photolithography markers are written on the sample comprised of crosses as well as alphanumeric coordinates, seen in Figure 1 on the left. The markers can be seen underneath the PMMA and Cr conduction layer, so they make locating crystals easy during EBL as well as before and after EBL.

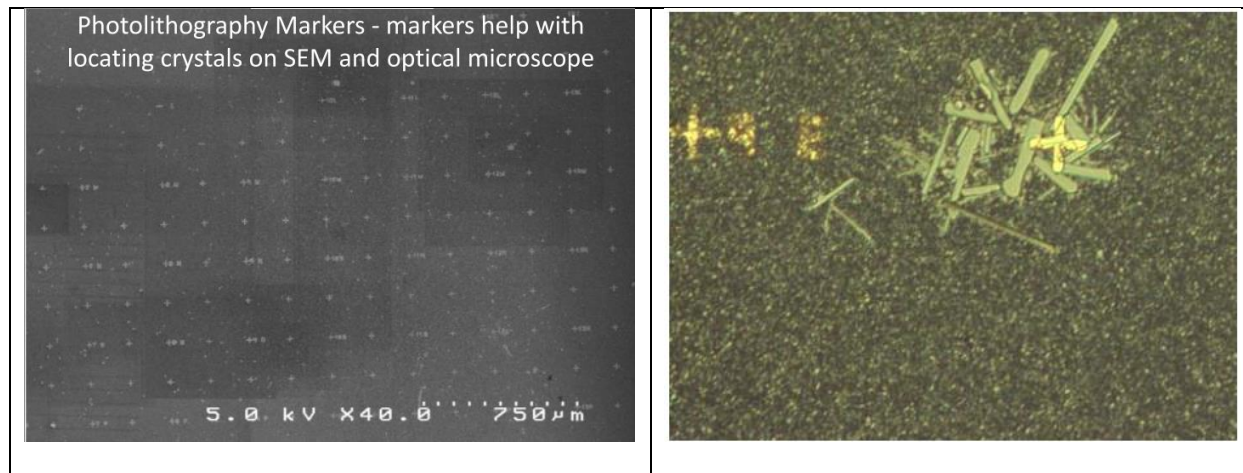
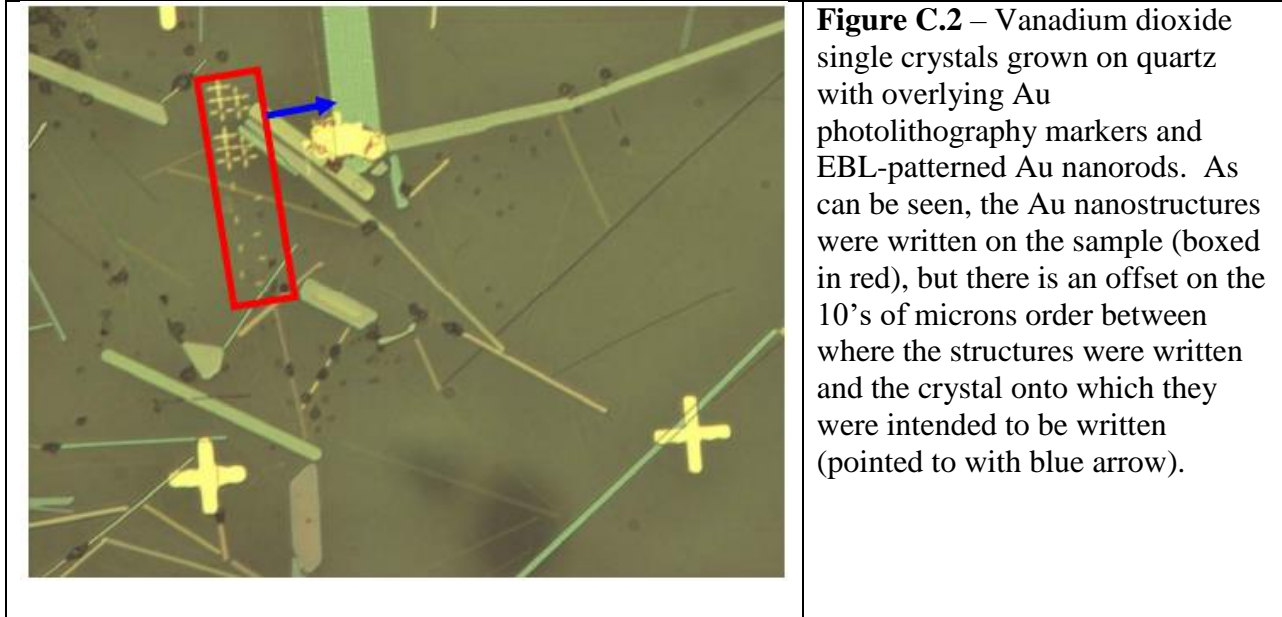


Figure C.1 – Vanadium dioxide single crystals grown on Si with overlying Au photolithography markers. The left SEM shows the regularly spaced Au crosses with numbers and letters, with PMMA and Cr on top, demonstrating their visibility for EBL. The right optical micrograph shows VO₂ single crystals on the micrometer scale randomly oriented and shaped near one particular set of photolithography markers.

A naïve attempt to remedy the precise position problem might be to define a corner of the crystal of interest to be (0,0) using the set origin feature on the Raith and then write the pattern at (0,0). While this will put the Au nanostructures in generally the right place on the sample, this may not be precise enough to achieve the desired outcome, as can be seen in Figure C.2.



Aligning to three points (defining a plane) allows for more precise positioning than aligning to one point with the set origin feature. For the sake of clarification, it should be noted that aligning to three points is a separate thing from aligning the write fields. That is to prevent/minimize stitching errors when a pattern being written is more than a single write-field in size, whereas aligning to three points is to set up a coordinate system used to position the pattern to be written on the sample. For this process, a GDSII file containing the already written alignment markers with the appropriate dimensions and separations is required. In this case, 30 micron crosses spaced 200 microns apart and fabricated via photolithography are used, and the alignment locations are at centers of three crosses out of the four that make a square. The markers in the GDSII file can be written on a different layer than the pattern to be written, as one way to make sure that only the pattern is written instead of also writing the markers a second time. A mark (green flag numbered 1, 2, or 3) is placed at the center of each of the three alignment markers being used in the GDSII file. Once these are set, the equivalent points on the sample are navigated to and selected in the “3-points” alignment under “adjust UVW” (with the

eyedropper) so to align the coordinate system in the GDSII with that of the sample. Care is taken to not expose the sample except areas for very close the markers. This can be accomplished by moving from marker to marker by control + right clicking the desired location in the GDSII file, and zooming in just on the marker so to locate its center for alignment. The “adjust” button will be clicked once all three marks have been placed in order to modify the U-V coordinates based on these mark positions. The U-V coordinates on the bottom right will change once “adjust” has been clicked. For multilayer EBL where the position of one written layer to the one being written is critical because the size scale for permissible misalignment is quite small, there is an automated alignment process to more precisely than may be possible by hand locate the center of each of the alignment markers.

At this point, there is another difference between multilayer EBL and placing a lithography pattern precisely on a randomly oriented and located area of the sample, in this case, on single crystals of VO₂. For multilayer EBL, each layer of the pattern has been put into a single GDSII beforehand as a separate layer so that the layers will match up when they are written on the sample. For writing on the crystals or any other non-uniform features, especially those which are difficult to see under the SEM, the pattern to be written can be placed into the GDSII file relative to the flagged markers. This placement is based upon the distance from and position of a flagged marker to the single crystal, which can be determined via optical microscopy images and a program like ImageJ to measure distances, or in the Raith SEM where the method is described below. After the markers have been set, a SEM image of the 3 markers and the crystal to be written on is taken, and the length and width cursors are used to determine the distance from the bottom left cross (0,0) to the center of the crystal. With the distances from the bottom left marker measured, the array to be written can be placed such that its center is at

the coordinates given by these distances.

As the terms writefield and working area are both being introduced below and are similar, it is beneficial to specify the differences between them and what each one means to avoid confusion. The writefield is the area on which the electron beam can write without moving the stage. The size of this area can be altered, with the size of the area and the resolution of the pattern being inversely proportional. The working area, in contrast, is defined by the user and is the area of the pattern desired to be written. This can comprise multiply writefields, be the same area as a writefield, or be an area less than that of a full writefield.

It is necessary to set up the working area and make sure that it is centered on the pattern to be written. This is done in “Exposure Properties” using the “Working Area” button (blue rectangles) by setting the center of the working area based the coordinates of the pattern to be written and the size of the working area desired. In this case, the working area is the size a single writefield and is the size of pattern to be written. Once the working area is set, the pattern can be dragged and dropped into a positionlist. The properties of the pattern (such as the location, exposed layer, and dose parameters) can be modified using the “Properties” option by clicking on the pattern in the positionlist. The location of the pattern to be written in the positionlist can be set directly from the location of the working area using the bottommost right button in exposure properties (green box with cross, and nearby cyan and black boxes). The layers to be exposed are set in the positionlist for the pattern to be written by clicking the “Exposed Layer” button (a series of parallel colored planes). The dot, line, and area doses for the pattern are set by clicking the “Exposure Parameter” button after the beam current on the Faraday cup has been measured.

With this general method, it is advisable to make the pattern to be written larger than strictly necessary (assuming that pattern writing times are not prohibitively long) to guarantee that the crystal is covered. To write on top of objects like the crystals, which have non-trivial heights, it is also advised to focus (at a low magnification) on the top of the crystal so that the electron beam is focused during writing.

From this point, the EBL process required to pattern on non-uniform substrates is identical to that of the process for a uniform substrate. This process, once complete, will produce lithographically patterned particles on a non-uniform substrate, such as the Au nanorods fabricated on top of VO₂ single crystals which can be seen in Figure C.3.

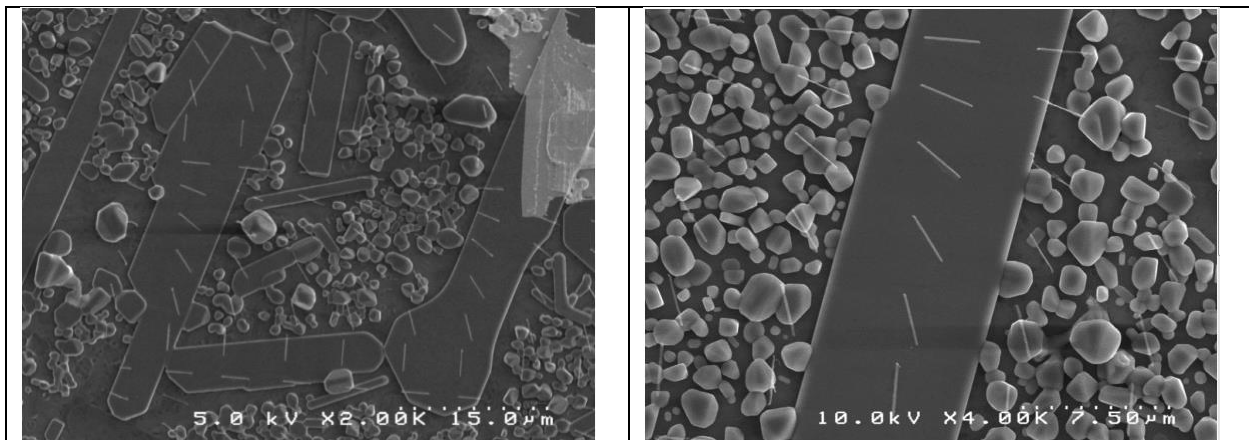


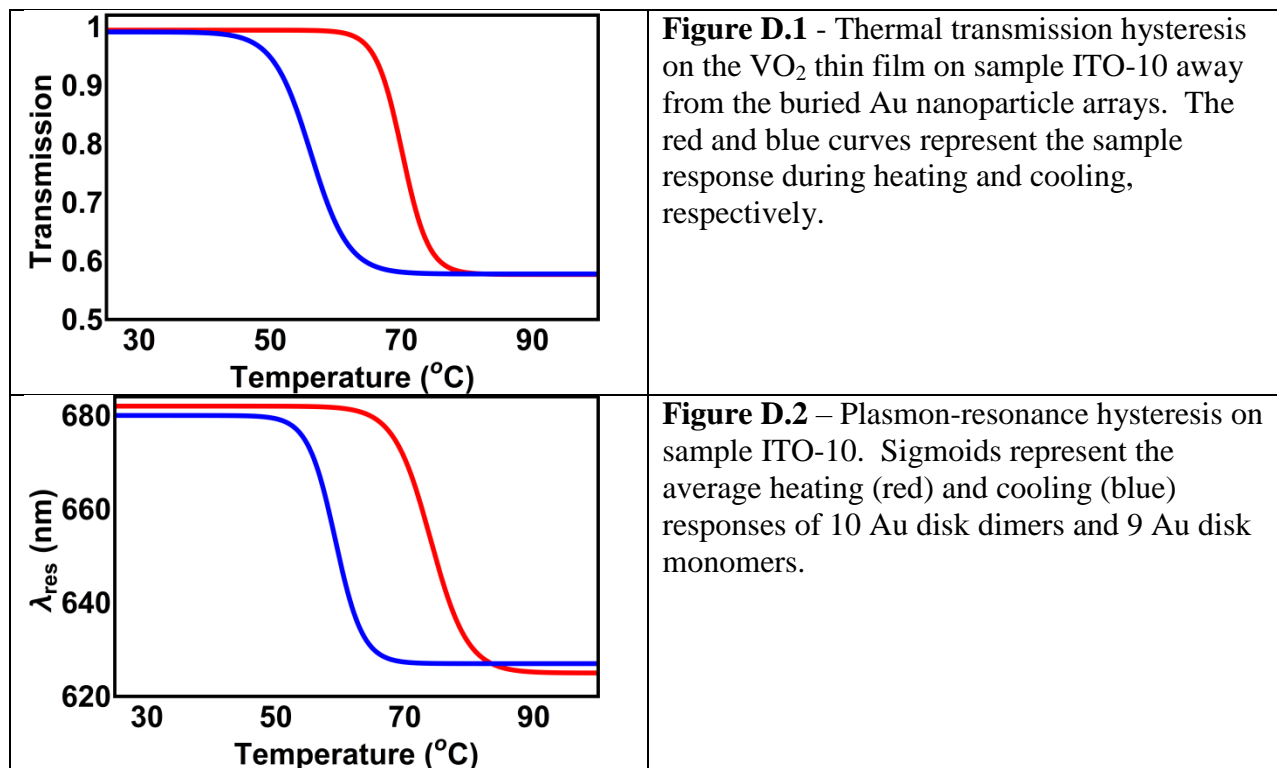
Figure C.3 – Vanadium dioxide single crystals grown on Si with overlying Au photolithography markers and EBL-patterned Au nanorods. As can be seen, the Au nanostructures have been successfully written on the sample directly on top of VO₂ crystals.

Appendix D

Details of the Plasmon-Resonance Hysteresis

In Appendix D, the plasmon-resonance hysteresis described in Chapter 4 is discussed further. The plasmon-resonance hysteresis for Au nanoparticles embedded in an undoped VO₂ thin film is compared with the thermal transmission hysteresis of this same VO₂ thin film. The plasmon-resonance hystereses for Au nanoparticles embedded in an undoped VO₂ thin film both before and after Pd are also compared.

A comparison of a thermal VO₂ transmission hysteresis curve and a plasmon-resonance hysteresis curve taken on the same sample before Pd deposition or hydrogen doping can be seen below in Figures D.1 and D.2 respectively. Red and blue curves represent heating and cooling respectively. The hysteresis widths for the thermal and plasmon-resonance curves are similar, at 14 °C and 15 °C respectively. The critical switching temperatures for both the heating and cooling curves, though, are at lower temperatures for the thermal hysteresis than for the plasmon-resonance hysteresis. For the thermal hysteresis these temperatures are 70 °C and 56 °C whereas the temperatures are 75 °C and 60 °C for the plasmon-resonance hysteresis.



Next, the effect of putting 3 nm of Pd on top of the VO₂ film and annealing that to create Pd nanoparticles is determined. A comparison of the plasmon resonance-hysteresis can be seen before and after Pd deposition in Figures D.3 and D.4 respectively. The plasmon-resonance hysteresis curves for ten individual disk dimers and nine individual disk monomers are recorded for temperatures between 20 °C and 120 °C both before and after Pd deposition. There is no measureable difference between the plasmon-resonance hystereses of the disk dimers and disk monomers, so these 19 data sets are averaged together. Due to the Pd deposition, the critical temperature T_c as well as the central temperatures for both the heating and cooling curves decreases (5 ± 2 °C, 7 ± 2 °C, and 2 ± 1 °C respectively) and the hysteresis width narrows by 5 ± 3 °C. The overall resonance shift over the PT is consistent for the system before and after Pd deposition within uncertainty. With the Pd deposition, the metallic state resonance position blue-shifts by 9 ± 9 nm and the insulating state resonance position is consistent before and after Pd

deposition within experimental uncertainty. The heating sigmoid slope at T_c after Pd deposition and the slope of the cooling sigmoid at T_c remains the same within uncertainty. Overall, there are small though measurable changes in the plasmon-resonance hysteresis of the system due to Pd deposition, as can be seen below in the comparison of the average sigmoidal fits for the plasmon-resonance hysteresis curves before and after Pd deposition.

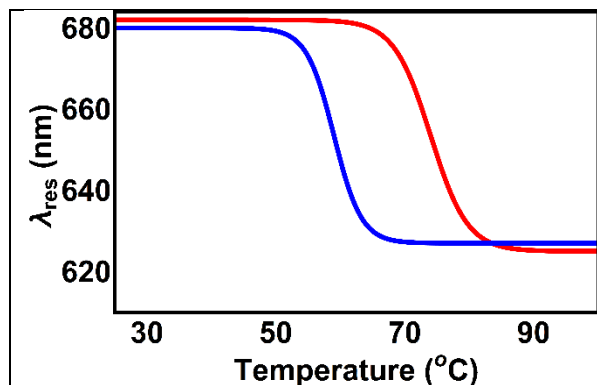


Figure D.3 – Plasmon-resonance hysteresis on sample ITO-10 before Pd deposition. Sigmoids represent the average heating (red) and cooling (blue) responses of 10 Au disk dimers and 9 Au disk monomers.

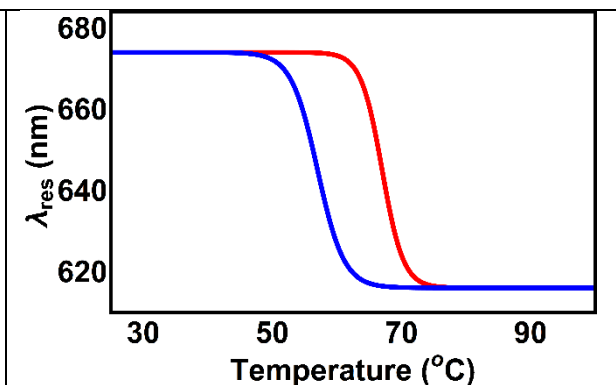


Figure D.4 - Plasmon resonance-hysteresis on sample ITO-10 after Pd deposition. Sigmoids represent the average heating (red) and cooling (blue) responses of 10 Au disk dimers and 9 Au disk monomers.

Appendix E

Contributions to the Understanding of VO₂ Not Discussed in this Dissertation

My contributions extend beyond the topic discussed in the body of this dissertation, the interactions between gold plasmons and VO₂. Thus, two papers which provide new information about the properties of VO₂ from experiments using samples fabricated by me are discussed briefly below.

The first of these contributions pertains to the speed of the VO₂ IMT and its relation with the SPT. This work is published in PRL under the title “Instantaneous Band Gap Collapse in Photoexcited Monoclinic VO₂ due to Photocarrier Doping”. In this work, the bandgap of a PLD VO₂ thin film grown by me was probed using time-resolved photoelectron spectroscopy during ultrafast excitation of the material. This method allows for time resolution high enough to resolve the dynamics of the VO₂ IMT as well as the ability to isolate changes in the dielectric function from changes in the bandgap. It was previously thought that the IMT would not immediately begin upon excitation, but rather that there would be a delay due to the SPT. With the high time resolution in this work, this was demonstrated to be incorrect. Instead, the IMT begins nearly immediately and indicates that the IMT can finish before the atoms in the VO₂ begin to move during the SPT. This demonstrates that the SPT is not required for the IMT to occur and that in the time before the SPT occurs that the VO₂ is in a monoclinic metallic state.

The second of these contributions pertains to the role of the bandgap in the stopping power of the electrons in metal oxides such as VO₂ for protons. This work will be submitted to Physical Review A under the title “Scaling properties of electronic stopping power of slow protons in oxides”. In this work, metal oxides (VO₂, HfO, Ta₂O₅, and ZnO) were hit with

protons to determine the effect of different material properties of these metal oxides on the interactions of the electrons in these oxides with the incident protons. A variety of oxides were used to determine which parameters alter the electronic stopping. Vanadium dioxide was used to determine the effect of the bandgap on the stopping power, since the bandgap collapses over the PT from insulating to metallic. I grew RF-M sputtering VO₂ films between 8 and 16 nm thick on Si for this application. I verified that the films had a phase transition using temperature-dependent transmission, as can be seen in Figure E.1. As expected, the change in transmission over the PT increases with increasing VO₂ thickness. Characteristic SEM and AFM images are also included in Figures E.2 and E.3, showing that the films are generally continuous but have voids as can be seen in the differences in conductivity and differences in height using SEM and AFM imaging respectively. Using VO₂, the scattering cross section was determined to not be influenced by the bandgap of the material, as the VO₂ scattering cross section for the protons at a given energy was the same for insulating and metallic VO₂. The density of the valence electrons of the different oxides also did not influence the scattering cross section. The scattering cross section for metal oxides was instead related to the number of occupied states in the valence band of the material, thus with the number of oxygen atoms in the material.

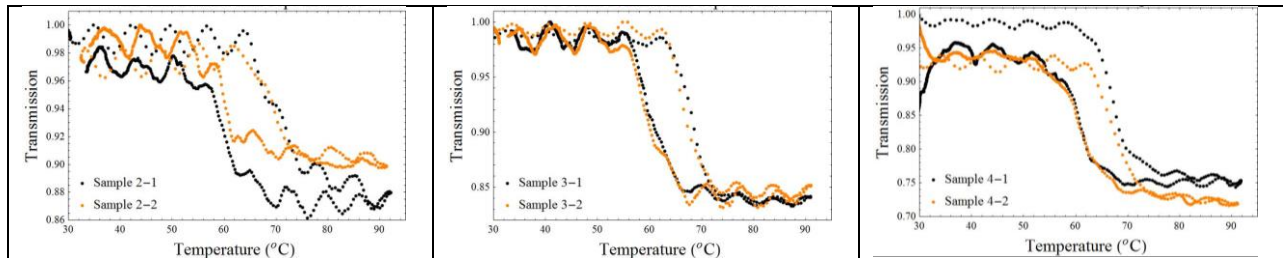


Figure E.1 - Temperature-dependent transmission measured using a 1550 nm laser light for 8 nm, 12 nm, and 16 nm (left to right) RF-M sputtering VO₂ films grown on Si. The oscillations in the hysteresis curves are due to the thermoelectric effect in silicon, and appear in these curves due to the underlying Si substrates.

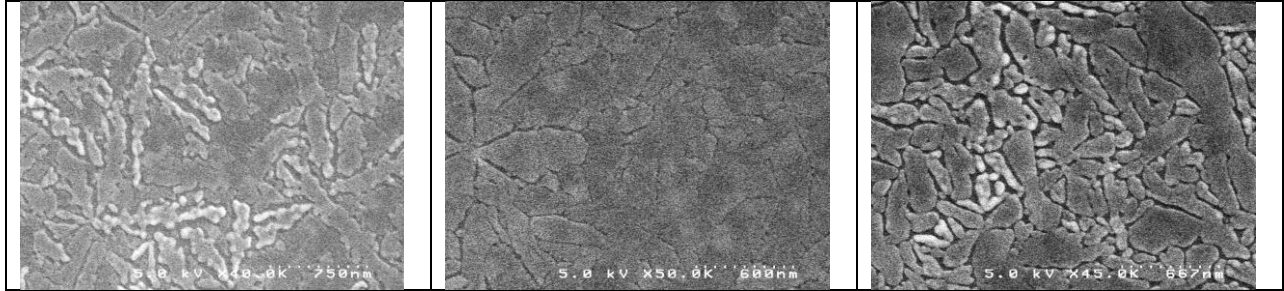


Figure E.2 – Representative SEM images for 8 nm, 12 nm, and 16 nm (left to right) RF-M sputtering VO₂ films grown on Si. Individual grains with differences in conductivity are seen.

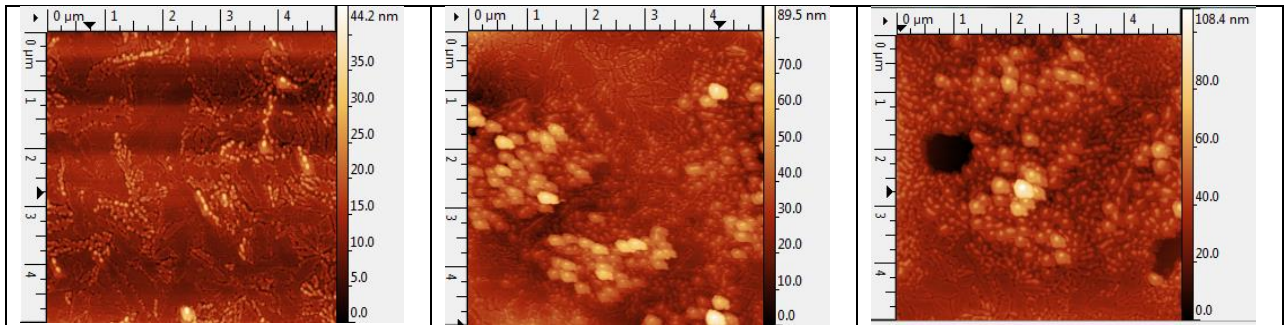


Figure E.3 – Representative AFM images for 8 nm (left) and 16 nm (center and right) RF-M sputtering VO₂ films grown on Si. The samples are film-like, with distinct grains and regions where the material appears to be balled-up. Some regions on the samples have voids, as seen in the right image.

Appendix F

Sensing Depth for LSPR in with Resonance in the Near-IR Wavelength Range

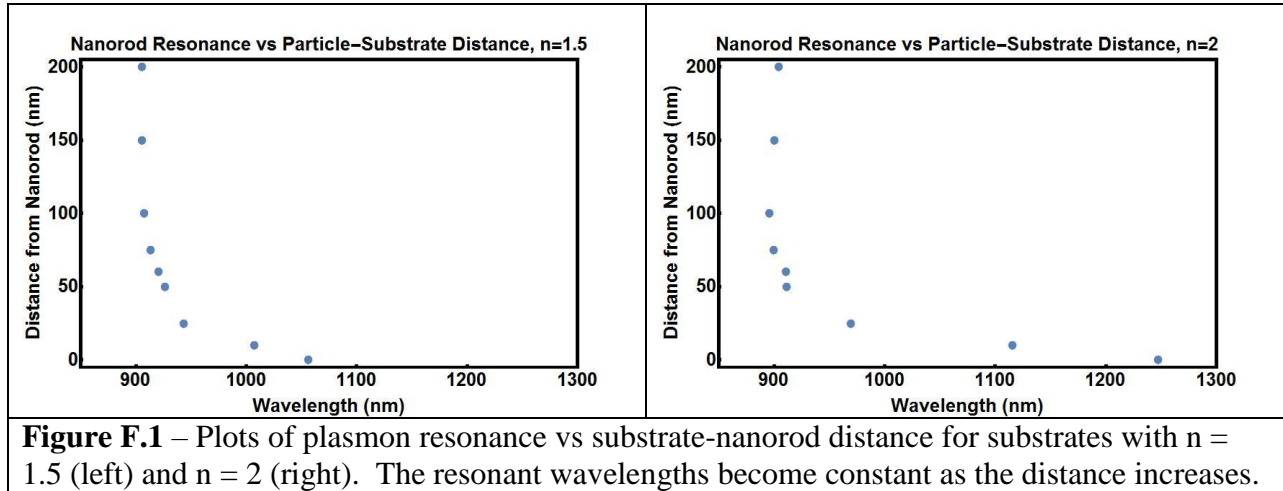


Figure F.1 – Plots of plasmon resonance vs substrate-nanorod distance for substrates with $n = 1.5$ (left) and $n = 2$ (right). The resonant wavelengths become constant as the distance increases.

In Appendix F, one measure of the sensing depth of an Au plasmonic particle is discussed based upon simulations using Lumerical FDTD. The plasmonic particle used in this set of simulations is an Au nanorod that is resonant in the near-IR. The nanorod is placed on top of a substrate with a given refractive index and the simulated optical transmission is determined. The wavelength of the plasmon resonance is extracted for this spectrum. To examine sensing depth of the plasmon, the distance between the substrate and the nanorod is varied from 0 nm to 200 nm and a transmission spectrum with an associated resonant wavelength is obtained at each distance. The resonant wavelength is plotted as a function of distance. This is done for substrates with real refractive indices of 1.5 and 2, and can be seen in Figure F.1.

For substrate-nanorod distances between 200 nm and 75 nm, the resonant wavelength for the nanorods above either of the two substrate refractive indices remains rather constant. As the distance decreases and the substrate is brought into the plasmon interaction range, the resonant wavelength sharply but smoothly red-shifts towards the resonant wavelength for the

nanoparticle on a substrate with $n = 1.5$ or $n = 2$. The red-shift is larger for the nanorod on a substrate with $n = 2$ than for a substrate with $n = 1.5$ because the larger refractive index causes the plasmon resonance to occur at a longer resonant wavelength, as discussed in Section 1.2.6. This indicates that the spatial extent of the plasmon simulated here is between 60 nm and 75 nm.

BIBLIOGRAPHY

- [1] Freestone I, Meeks N, Sax M and Higgitt C 2007 The Lycurgus Cup — A Roman nanotechnology *Gold Bulletin* **40** 270-7
- [2] Mizera K 2009 Gothic stained rose window of Notre-Dame de Paris. (<https://en.wikipedia.org/wiki/Plasmon#/media/File:GothicRayonnantRose003.jpg>)
- [3] Faraday M 1857 The Bakerian Lecture: Experimental Relations of Gold (and Other Metals) to Light *Philosophical Transactions of the Royal Society of London* **147** 145-81
- [4] Thompson D 2007 Michael Faraday's recognition of ruby gold: the birth of modern nanotechnology *Gold Bulletin* **40** 267-9
- [5] Mie G 1908 Beitrage zur Optik truber Medien, speziell kolloidaler Metallosungen *Annalen der Physik, Series Four* **25** 377-445
- [6] Lorenz L V 1896 *Oeuvres Scientifiques de L. Lorenz* vol 1 (Copenhagen: Librairie Lehmann)
- [7] Logan N A 1965 Survey of some early studies of the scattering of plane waves by a sphere *Proceedings of the IEEE* **53** 773-85
- [8] Twersky V 1964 Rayleigh Scattering *Appl. Opt.* **3** 1150-62
- [9] Kreibig U and Vollmer M 1995 *Optical Properties of Metal Clusters*: (Springer)
- [10] Bohren C and Huffman D 2007 *Absorption and scattering of light by small particles*: (Wiley-VCH Verlag GbH & Co)
- [11] van de Hulst H C 1957 *Light Scattering by Small Particles* (New York John Wiley & Sons, Inc.)
- [12] Ferrara D W Plasmonic Interactions in Gold::Vanadium Dioxide Hybrid Nanostructures. In: *Physics*: Vanderbilt University
- [13] Boltasseva A and Atwater H A 2011 Low-Loss Plasmonic Metamaterials *Science* **331** 290-1
- [14] Sönnichsen C, Franzl T, Wilk T, von Plessen G, Feldmann J, Wilson O and Mulvaney P 2002 Drastic Reduction of Plasmon Damping in Gold Nanorods *Physical Review Letters* **88** 077402
- [15] Zorić I, Zäch M, Kasemo B and Langhammer C 2011 Gold, Platinum, and Aluminum Nanodisk Plasmons: Material Independence, Subradiance, and Damping Mechanisms *ACS Nano* **5** 2535-46

- [16] Tam F, Chen A L, Kundu J, Wang H and Halas N J 2007 Mesoscopic nanoshells: Geometry-dependent plasmon resonances beyond the quasistatic limit *The Journal of Chemical Physics* **127** 204703
- [17] Fox M 2011 *Optical Properties of Solids*: (Oxford University Press)
- [18] Ziegler J I 2011 Complex Plasmonic Behavior of Archimedian Nanospirals. In: *Physics*: Vanderbilt University
- [19] Prodan E, Radloff C, Halas N J and Nordlander P 2003 A Hybridization Model for the Plasmon Response of Complex Nanostructures *Science* **302** 419-22
- [20] Hessel A and Oliner A A 1965 A New Theory of Wood's Anomalies on Optical Gratings *Appl. Opt.* **4** 1275-97
- [21] Murdin P 1990 Wood's Anomalies in the INT spectrograph. In: *ING La Palma Technical Note*
- [22] Maystre D 2012 *Plasmonics*
- [23] Nikitin A G, Kabashin A V and Dallaporta H 2012 Plasmonic resonances in diffractive arrays of gold nanoantennas: near and far field effects *Opt. Express* **20** 27941-52
- [24] Liu Z and Ye J 2016 Highly controllable double Fano resonances in plasmonic metasurfaces *Nanoscale* **8** 17665-74
- [25] Yang S, Liu Z, Xia X, E Y, Tang C, Wang Y, Li J, Wang L and Gu C 2016 Excitation of ultrasharp trapped-mode resonances in mirror-symmetric metamaterials *Physical Review B* **93** 235407
- [26] Zhao L, Kelly K L and Schatz G C 2003 The Extinction Spectra of Silver Nanoparticle Arrays: Influence of Array Structure on Plasmon Resonance Wavelength and Width *The Journal of Physical Chemistry B* **107** 7343-50
- [27] Jain P K, Huang X, El-Sayed I H and El-Sayed M A 2007 Review of Some Interesting Surface Plasmon Resonance-enhanced Properties of Noble Metal Nanoparticles and Their Applications to Biosystems *Plasmonics* **2** 107-18
- [28] Brongersma M L, Halas N J and Nordlander P 2015 Plasmon-induced hot carrier science and technology *Nat Nano* **10** 25-34
- [29] Liu N, Tang M L, Hentschel M, Giessen H and Alivisatos A P 2011 Nanoantenna-enhanced gas sensing in a single tailored nanofocus *Nat Mater* **10** 631-6
- [30] Atwater H A and Polman A 2010 Plasmonics for improved photovoltaic devices *Nat Mater* **9** 205-13

- [31] Kristensen A, Yang J K W, Bozhevolnyi S I, Link S, Nordlander P, Halas N J and Mortensen N A 2016 Plasmonic colour generation *Nature Reviews Materials* **2** 16088
- [32] Wu M K, Ashburn J R, Torng C J, Hor P H, Meng R L, Gao L, Huang Z J, Wang Y Q and Chu C W 1987 Superconductivity at 93 K in a new mixed-phase Y-Ba-Cu-O compound system at ambient pressure *Physical Review Letters* **58** 908-10
- [33] Macià F, Abril G, Hernández-Mínguez A, Hernandez J M, Tejada J and Parisi F 2008 Magnetic fingerprints of the very fast jumps of colossal magnetoresistance in the phase-separated manganite $\text{La}_{0.225}\text{Pr}_{0.40}\text{Ca}_{0.375}\text{MnO}_3$ *Physical Review B* **77** 012403
- [34] Dernier P D and Marezio M 1970 Crystal Structure of the Low-Temperature Antiferromagnetic Phase of V_2O_3 *Physical Review B* **2** 3771-6
- [35] Waldecker L, Miller T A, Rude M, Bertoni R, Osmond J, Pruneri V, Simpson R E, Ernstorfer R and Wall S 2015 Time-domain separation of optical properties from structural transitions in resonantly bonded materials *Nat Mater* **14** 991-5
- [36] Morin F J 1959 Oxides Which Show a Metal-to-Insulator Transition at the Neel Temperature *Physical Review Letters* **3** 34-6
- [37] Eyert V 2002 The metal-insulator transitions of VO_2 : A band theoretical approach *Annalen der Physik* **11** 650-704
- [38] Wang W, Luo Y, Zhang D and Luo F 2006 Dynamic optical limiting experiments on vanadium dioxide and vanadium pentoxide thin films irradiated by a laser beam *Appl. Opt.* **45** 3378-81
- [39] Gao Y, Luo H, Zhang Z, Kang L, Chen Z, Du J, Kanehira M and Cao C 2012 Nanoceramic VO_2 thermochromic smart glass: A review on progress in solution processing *Nano Energy* **1** 221-46
- [40] Li S Y, Niklasson G A and Granqvist C G 2012 Thermochromic fenestration with VO_2 -based materials: Three challenges and how they can be met *Thin Solid Films* **520** 3823-8
- [41] Wang X, Cao Y, Zhang Y, Yan L and Li Y 2015 Fabrication of VO_2 -based multilayer structure with variable emittance *Applied Surface Science* **344** 230-5
- [42] Briggs R M, Pryce I M and Atwater H A 2010 Compact silicon photonic waveguide modulator based on the vanadium dioxide metal-insulator phase transition *Opt. Express* **18** 11192-201
- [43] Ryckman J D, Diez-Blanco V, Nag J, Marvel R E, Choi B K, Haglund R F and Weiss S M 2012 Photothermal optical modulation of ultra-compact hybrid Si- VO_2 ring resonators *Opt. Express* **20** 13215-25

- [44] Ryckman J D, Hallman K A, Marvel R E, Haglund R F and Weiss S M 2013 Ultra-compact silicon photonic devices reconfigured by an optically induced semiconductor-to-metal transition *Opt. Express* **21** 10753-63
- [45] Cao J, Fan W, Zhou Q, Sheu E, Liu A, Barrett C and Wu J 2010 Colossal thermal-mechanical actuation via phase transition in single-crystal VO₂ microcantilevers *Journal of Applied Physics* **108** 083538
- [46] Liu K, Cheng C, Suh J, Tang-Kong R, Fu D, Lee S, Zhou J, Chua L O and Wu J 2014 Powerful, Multifunctional Torsional Micromuscles Activated by Phase Transition *Advanced Materials* **26** 1746-50
- [47] Tselev A, Budai J D, Strelcov E, Tischler J Z, Kolmakov A and Kalinin S V 2011 Electromechanical Actuation and Current-Induced Metastable States in Suspended Single-Crystalline VO₂ Nanoplatelets *Nano Letters* **11** 3065-73
- [48] Liu K, Cheng C, Cheng Z, Wang K, Ramesh R and Wu J 2012 Giant-Amplitude, High-Work Density Microactuators with Phase Transition Activated Nanolayer Bimorphs *Nano Letters* **12** 6302-8
- [49] Chen C, Yi X, Zhao X and Xiong B 2001 Characterizations of VO₂-based uncooled microbolometer linear array *Sensors and Actuators A: Physical* **90** 212-4
- [50] Strelcov E, Lilach Y and Kolmakov A 2009 Gas Sensor Based on Metal–Insulator Transition in VO₂ Nanowire Thermistor *Nano Letters* **9** 2322-6
- [51] Byon J W, Kim M-B, Kim M H, Kim S Y, Lee S H, Lee B C and Baik J M 2012 Electrothermally Induced Highly Responsive and Highly Selective Vanadium Oxide Hydrogen Sensor Based on Metal–Insulator Transition *The Journal of Physical Chemistry C* **116** 226-30
- [52] Verleur H W, Barker A S and Berglund C N 1968 Optical Properties of VO₂ between 0.25 and 5 eV *Physical Review* **172** 788-98
- [53] Strelcov E, Tselev A, Ivanov I, Budai J D, Zhang J, Tischler J Z, Kravchenko I, Kalinin S V and Kolmakov A 2012 Doping-Based Stabilization of the M2 Phase in Free-Standing VO₂ Nanostructures at Room Temperature *Nano Letters* **12** 6198-205
- [54] Nag J and R. F. Haglund J 2008 Synthesis of vanadium dioxide thin films and nanoparticles *Journal of Physics: Condensed Matter* **20** 264016
- [55] Béteille F and Livage J 1998 Optical Switching in VO₂ Thin Films *Journal of Sol-Gel Science and Technology* **13** 915-21
- [56] Cao J, Gu Y, Fan W, Chen L Q, Ogletree D F, Chen K, Tamura N, Kunz M, Barrett C, Seidel J and Wu J 2010 Extended Mapping and Exploration of the Vanadium Dioxide Stress-Temperature Phase Diagram *Nano Letters* **10** 2667-73

- [57] Park J H, Coy J M, Kasirga T S, Huang C, Fei Z, Hunter S and Cobden D H 2013 Measurement of a solid-state triple point at the metal-insulator transition in VO₂ *Nature* **500** 431-4
- [58] Aetukuri N B, Gray A X, Drouard M, Cossale M, Gao L, Reid A H, Kukreja R, Ohldag H, Jenkins C A, Arenholz E, Roche K P, Durr H A, Samant M G and Parkin S S P 2013 Control of the metal-insulator transition in vanadium dioxide by modifying orbital occupancy *Nat Phys* **9** 661-6
- [59] Abate Y, Marvel R E, Ziegler J I, Gamage S, Javani M H, Stockman M I and Haglund R F 2015 Control of plasmonic nanoantennas by reversible metal-insulator transition *Scientific Reports* **5**
- [60] Dicken M J, Aydin K, Pryce I M, Sweatlock L A, Boyd E M, Walavalkar S, Ma J and Atwater H A 2009 Frequency tunable near-infrared metamaterials based on VO₂ phase transition *Opt. Express* **17** 18330-9
- [61] McGahan C, Appavoo K, Haglund R F and Shapera E 2013 Switchable plasmon-induced transparency in gold nanoarrays on vanadium dioxide film *Journal of Vacuum Science & Technology B, Nanotechnology and Microelectronics: Materials, Processing, Measurement, and Phenomena* **31** 06FE1
- [62] Markov P, Marvel R E, Conley H J, Miller K J, Haglund R F and Weiss S M 2015 Optically Monitored Electrical Switching in VO₂ *ACS Photonics* **2** 1175-82
- [63] Mayer B, Schmidt C, Grupp A, Bühler J, Oelmann J, Marvel R E, Haglund R F, Oka T, Brida D, Leitenstorfer A and Pashkin A 2015 Tunneling breakdown of a strongly correlated insulating state in VO₂ induced by intense multiterahertz excitation *Physical Review B* **91** 235113
- [64] Wall S, Wegkamp D, Foglia L, Appavoo K, Nag J, Haglund Jr R F, Stähler J and Wolf M 2012 Ultrafast changes in lattice symmetry probed by coherent phonons *Nature Communications* **3** 721
- [65] Cavalleri A, Tóth C, Siders C W, Squier J A, Ráksi F, Forget P and Kieffer J C 2001 Femtosecond Structural Dynamics in VO₂ during an Ultrafast Solid-Solid Phase Transition *Physical Review Letters* **87** 237401
- [66] Kübler C, Ehrke H, Huber R, Lopez R, Halabica A, Haglund R F and Leitenstorfer A 2007 Coherent Structural Dynamics and Electronic Correlations during an Ultrafast Insulator-to-Metal Phase Transition in VO₂ *Physical Review Letters* **99** 116401
- [67] Pashkin A, Kübler C, Ehrke H, Lopez R, Halabica A, Haglund R F, Huber R and Leitenstorfer A 2011 Ultrafast insulator-metal phase transition in VO₂ studied by multiterahertz spectroscopy *Physical Review B* **83** 195120
- [68] Wei J, Ji H, Guo W, Nevidomskyy A H and Natelson D 2012 Hydrogen stabilization of metallic vanadium dioxide in single-crystal nanobeams *Nat Nano* **7** 357-62

- [69] Cavalleri A, Dekorsy T, Chong H H W, Kieffer J C and Schoenlein R W 2004 Evidence for a structurally-driven insulator-to-metal transition in VO₂: A view from the ultrafast timescale *Physical Review B* **70** 161102
- [70] Srivastava R and Chase L L 1971 Raman Spectrum of Semiconducting and Metallic VO₂ *Physical Review Letters* **27** 727-30
- [71] Wegkamp D, Herzog M, Xian L, Gatti M, Cudazzo P, McGahan C L, Marvel R E, Haglund R F, Rubio A, Wolf M and Stähler J 2014 Instantaneous Band Gap Collapse in Photoexcited Monoclinic VO₂ due to Photocarrier Doping *Physical Review Letters* **113** 216401
- [72] Appavoo K, Wang B, Brady N F, Seo M, Nag J, Prasankumar R P, Hilton D J, Pantelides S T and Haglund R F 2014 Ultrafast Phase Transition via Catastrophic Phonon Collapse Driven by Plasmonic Hot-Electron Injection *Nano Letters* **14** 1127-33
- [73] Baum P, Yang D-S and Zewail A H 2007 4D Visualization of Transitional Structures in Phase Transformations by Electron Diffraction *Science* **318** 788-92
- [74] Hada M, Okimura K and Matsuo J 2010 Characterization of structural dynamics of VO₂ thin film on c-Al₂O₃ using in-air time-resolved x-ray diffraction *Physical Review B* **82** 153401
- [75] Nag J, Jr. R F H, Payzant E A and More K L 2012 Non-congruence of thermally driven structural and electronic transitions in VO₂ *Journal of Applied Physics* **112** 103532
- [76] Laverock J, Kittiwatanakul S, Zakharov A A, Niu Y R, Chen B, Wolf S A, Lu J W and Smith K E 2014 Direct Observation of Decoupled Structural and Electronic Transitions and an Ambient Pressure Monocliniclike Metallic Phase of VO₂ *Physical Review Letters* **113** 216402
- [77] Morrison V R, Chatelain R P, Tiwari K L, Hendaoui A, Bruhács A, Chaker M and Siwick B J 2014 A photoinduced metal-like phase of monoclinic VO₂ revealed by ultrafast electron diffraction *Science* **346** 445-8
- [78] Tao Z, Han T-R T, Mahanti S D, Duxbury P M, Yuan F, Ruan C-Y, Wang K and Wu J 2012 Decoupling of Structural and Electronic Phase Transitions in VO₂ *Physical Review Letters* **109** 166406
- [79] Marvel R E, Harl R R, Craciun V, Rogers B R and Haglund Jr R F 2015 Influence of deposition process and substrate on the phase transition of vanadium dioxide thin films *Acta Materialia* **91** 217-26
- [80] Sámson Z L, MacDonald K F, Angelis F D, Gholipour B, Knight K, Huang C C, Fabrizio E D, Hewak D W and Zheludev N I 2010 Metamaterial electro-optic switch of nanoscale thickness *Applied Physics Letters* **96** 143105

- [81] Nishi H, Asahi T and Kobatake S 2009 Light-Controllable Surface Plasmon Resonance Absorption of Gold Nanoparticles Covered with Photochromic Diarylethene Polymers *The Journal of Physical Chemistry C* **113** 17359-66
- [82] Michel A K U, Chigrin D N, Mass T W W, Schonauer K, Salinga M, Wuttig M and Taubner T 2013 Using Low-Loss Phase-Change Materials for Mid-Infrared Antenna Resonance Tuning *Nano Letters* **13** 3470-5
- [83] Zheludev N I and Kivshar Y S 2012 From metamaterials to metadevices *Nat Mater* **11** 917-24
- [84] Pryce I M, Aydin K, Kelaita Y A, Briggs R M and Atwater H A 2010 Highly Strained Compliant Optical Metamaterials with Large Frequency Tunability *Nano Letters* **10** 4222-7
- [85] Chan W L, Chen H-T, Taylor A J, Brener I, Cich M J and Mittleman D M 2009 A spatial light modulator for terahertz beams *Applied Physics Letters* **94** 213511
- [86] Xu G, Huang C-M, Tazawa M, Jin P and Chen L-H 2009 Tunable optical properties of nano-Au on vanadium dioxide *Optics Communications* **282** 896-902
- [87] Suh J Y, Donev E U, Ferrara D W, Tetz K A, Feldman L C and R. F. Haglund J 2008 Modulation of the gold particle-plasmon resonance by the metal-semiconductor transition of vanadium dioxide *Journal of Optics A: Pure and Applied Optics* **10** 055202
- [88] Driscoll T, Palit S, Qazilbash M M, Brehm M, Keilmann F, Chae B-G, Yun S-J, Kim H-T, Cho S Y, Jokerst N M, Smith D R and Basov D N 2008 Dynamic tuning of an infrared hybrid-metamaterial resonance using vanadium dioxide *Applied Physics Letters* **93** 024101
- [89] Earl S K, James T D, Davis T J, McCallum J C, Marvel R E, Haglund R F and Roberts A 2013 Tunable optical antennas enabled by the phase transition in vanadium dioxide *Opt. Express* **21** 27503-8
- [90] Earl S K, James T D, Gómez D E, Marvel R E, Haglund Jr. R F and Roberts A 2017 Switchable polarization rotation of visible light using a plasmonic metasurface *APL Photonics* **2** 016103
- [91] Goldflam M D, Driscoll T, Barnas D, Khatib O, Royal M, Jokerst N M, Smith D R, Kim B-J, Seo G, Kim H-T and Basov D N 2013 Two-dimensional reconfigurable gradient index memory metasurface *Applied Physics Letters* **102** 224103
- [92] Driscoll T, Kim H-T, Chae B-G, Kim B-J, Lee Y-W, Jokerst N M, Palit S, Smith D R, Di Ventra M and Basov D N 2009 Memory Metamaterials *Science* **325** 1518-21
- [93] Muskens O L, Bergamini L, Wang Y, Gaskell J M, Zabala N, de Groot C H, Sheel D W and Aizpurua J 2016 Antenna-assisted picosecond control of nanoscale phase transition in vanadium dioxide *Light Sci Appl.* **5** e16173

- [94] Ferrara D W, Nag J, MacQuarrie E R, Kaye A B and Haglund R F 2013 Plasmonic Probe of the Semiconductor to Metal Phase Transition in Vanadium Dioxide *Nano Letters* **13** 4169-75
- [95] Lumerical Solutions I 2015 Photothermal Heating in Plasmonic Nanostructures. (https://kb.lumerical.com/en/sp_photothermal-heating-in-plasmo.html)
- [96] Lumerical Solutions I 2015 Lumerical Knowledge Base. (<https://kb.lumerical.com/en/index.html>)
- [97] Lumerical Solutions I 2015 Symmetric and anti-symmetric BCs (https://kb.lumerical.com/en/ref_sim_obj_symmetric_anti-symmetric.html)
- [98] Marvel R 2015 Physics and Processing of Vanadium Dioxide for Optical Devices. In: *Interdisciplinary Materials Science: Vanderbilt University*
- [99] Guiton B S, Gu Q, Prieto A L, Gudixsen M S and Park H 2005 Single-Crystalline Vanadium Dioxide Nanowires with Rectangular Cross Sections *Journal of the American Chemical Society* **127** 498-9
- [100] Cheng C, Liu K, Xiang B, Suh J and Wu J 2012 Ultra-long, free-standing, single-crystalline vanadium dioxide micro/nanowires grown by simple thermal evaporation *Applied Physics Letters* **100** 103111
- [101] Kim I S and Lauhon L J 2012 Increased Yield and Uniformity of Vanadium Dioxide Nanobeam Growth via Two-Step Physical Vapor Transport Process *Crystal Growth & Design* **12** 1383-7
- [102] 2001 NANO PMMA and Copolymer. ed MicroChem
- [103] Vieu C, Carcenac F, Pépin A, Chen Y, Mejias M, Lebib A, Manin-Ferlazzo L, Couraud L and Launois H 2000 Electron beam lithography: resolution limits and applications *Applied Surface Science* **164** 111-7
- [104] μ PG 101 Tabletop Micro Pattern Generator. ed H Instruments
- [105] Nečas D and Klapetek P 2012 Gwyddion: an open-source software for SPM data analysis *Central European Journal of Physics* **10** 181-8
- [106] Jacobson D 2016 What do APO and Apochromat mean. In: *Lenses FAQ*, (<http://stason.org/TULARC/recreation/photography/lenses-faq/31-What-do-APO-and-Apochromatic-mean.html>: StasoSphere.com)
- [107] Zügge D H 2000 Achromat, Apochromat, Superachromat - What is the Difference? In: *Camera Lens News*, (<http://www.dantestella.com/zeiss/achromat.html>)
- [108] Appavoo K and Haglund Jr R F 2014 Polarization selective phase-change nanomodulator *Scientific Reports* **4** 6771

- [109] Beier N F 2016 Nanoscale Dolmen Structure Exhibiting A Tunable Fano Resonance. In: *Physics*: Vanderbilt University
- [110] Appavoo K 2012 Hybrid Phase-Changing Nanostructures: From Reconfigurable Plasmonic Devices to Ultrafast Dynamics. In: *Interdisciplinary Materials Science*: Vanderbilt University
- [111] Jones A C, Berweger S, Wei J, Cobden D and Raschke M B 2010 Nano-optical Investigations of the Metal–Insulator Phase Behavior of Individual VO₂ Microcrystals *Nano Letters* **10** 1574-81
- [112] Liu M, Wagner M, Zhang J, McLeod A, Kittiwatanakul S, Fei Z, Abreu E, Goldflam M, Sternbach A J, Dai S, West K G, Lu J, Wolf S A, Averitt R D and Basov D N 2014 Symmetry breaking and geometric confinement in VO₂: Results from a three-dimensional infrared nano-imaging *Applied Physics Letters* **104** 121905
- [113] Tselev A, Meunier V, Strelcov E, Shelton W A, Luk'yanchuk I A, Jones K, Proksch R, Kolmakov A and Kalinin S V 2010 Mesoscopic Metal–Insulator Transition at Ferroelastic Domain Walls in VO₂ *ACS Nano* **4** 4412-9
- [114] O'Callahan B T, Jones A C, Hyung Park J, Cobden D H, Atkin J M and Raschke M B 2015 Inhomogeneity of the ultrafast insulator-to-metal transition dynamics of VO₂ *Nat Commun* **6**
- [115] Dönges S A, Khatib O, O'Callahan B T, Atkin J M, Park J H, Cobden D and Raschke M B 2016 Ultrafast Nanoimaging of the Photoinduced Phase Transition Dynamics in VO₂ *Nano Letters* **16** 3029-35
- [116] Huber M A, Plankl M, Eisele M, Marvel R E, Sandner F, Korn T, Schüller C, Haglund R F, Huber R and Cocker T L 2016 Ultrafast Mid-Infrared Nanoscopy of Strained Vanadium Dioxide Nanobeams *Nano Letters* **16** 1421-7
- [117] Tselev A, Strelcov E, Luk'yanchuk I A, Budai J D, Tischler J Z, Ivanov I N, Jones K, Proksch R, Kalinin S V and Kolmakov A 2010 Interplay between Ferroelastic and Metal–Insulator Phase Transitions in Strained Quasi-Two-Dimensional VO₂ Nanoplatelets *Nano Letters* **10** 2003-11
- [118] Cao J, Ertekin E, Srinivasan V, Fan W, Huang S, Zheng H, Yim J W L, Khanal D R, Ogletree D F, Grossman J C and Wu J 2009 Strain engineering and one-dimensional organization of metal-insulator domains in single-crystal vanadium dioxide beams *Nature Nanotechnology* **4** 732-7
- [119] Zhang S, Chou J Y and Lauhon L J 2009 Direct Correlation of Structural Domain Formation with the Metal Insulator Transition in a VO₂ Nanobeam *Nano Letters* **9** 4527-32

- [120] Zhang S, Kim I S and Lauhon L J 2011 Stoichiometry Engineering of Monoclinic to Rutile Phase Transition in Suspended Single Crystalline Vanadium Dioxide Nanobeams *Nano Letters* **11** 1443-7
- [121] Liu M K, Wagner M, Abreu E, Kittiwatanakul S, McLeod A, Fei Z, Goldflam M, Dai S, Fogler M M, Lu J, Wolf S A, Averitt R D and Basov D N 2013 Anisotropic Electronic State via Spontaneous Phase Separation in Strained Vanadium Dioxide Films *Physical Review Letters* **111** 096602
- [122] Liu M, Sternbach A J, Wagner M, Slusar T V, Kong T, Bud'ko S L, Kittiwatanakul S, Qazilbash M M, McLeod A, Fei Z, Abreu E, Zhang J, Goldflam M, Dai S, Ni G-X, Lu J, Bechtel H A, Martin M C, Raschke M B, Averitt R D, Wolf S A, Kim H-T, Canfield P C and Basov D N 2015 Phase transition in bulk single crystals and thin films of VO₂ by nanoscale infrared spectroscopy and imaging *Physical Review B* **91** 245155
- [123] Atkin J M, Berweger S, Chavez E K, Raschke M B, Cao J, Fan W and Wu J 2012 Strain and temperature dependence of the insulating phases of VO₂ near the metal-insulator transition *Physical Review B* **85** 020101
- [124] Nuño Z, Hessler B, Ochoa J, Shon Y-S, Bonney C and Abate Y 2011 Nanoscale subsurface- and material-specific identification of single nanoparticles *Opt. Express* **19** 20865-75
- [125] Keilmann F and Hillenbrand R 2004 Near-field microscopy by elastic light scattering from a tip *Philos T Roy Soc A* **362** 787-805
- [126] Wu B, Zimmers A, Aubin H, Ghosh R, Liu Y and Lopez R 2011 Electric-field-driven phase transition in vanadium dioxide *Physical Review B* **84** 241410
- [127] Liu M, Hwang H Y, Tao H, Strikwerda A C, Fan K, Keiser G R, Sternbach A J, West K G, Kittiwatanakul S, Lu J, Wolf S A, Omenetto F G, Zhang X, Nelson K A and Averitt R D 2012 Terahertz-field-induced insulator-to-metal transition in vanadium dioxide metamaterial *Nature* **487** 345-8
- [128] McGahan C, Gamage S, Liang J, Cross B, Marvel R E, Haglund R F and Abate Y 2017 Geometric constraints on phase coexistence in vanadium dioxide single crystals *Nanotechnology* **28** 085701
- [129] Qazilbash M M, Brehm M, Chae B G, Ho P C, Andreev G O, Kim B J, Yun S J, Balatsky A V, Maple M B, Keilmann F, Kim H T and Basov D N 2007 Mott transition in VO₂ revealed by infrared spectroscopy and nano-imaging *Science* **318** 1750-3
- [130] Engelhardt A P, Hauer B and Taubner T 2013 Visibility of weak contrasts in subsurface scattering near-field microscopy *Ultramicroscopy* **126** 40-3
- [131] Krutokhvostov R, Govyadinov A A, Stiegler J M, Huth F, Chuvilin A, Carney P S and Hillenbrand R 2012 Enhanced resolution in subsurface near-field optical microscopy *Opt. Express* **20** 593-600

- [132] Hauer B, Engelhardt A P and Taubner T 2012 Quasi-analytical model for scattering infrared near-field microscopy on layered systems *Opt. Express* **20** 13173-88
- [133] Taubner T, Keilmann F and Hillenbrand R 2005 Nanoscale-resolved subsurface imaging by scattering-type near-field optical microscopy *Opt. Express* **13** 8893-9
- [134] Govyadinov A A, Mastel S, Golmar F, Chuvilin A, Carney P S and Hillenbrand R 2014 Recovery of Permittivity and Depth from Near-Field Data as a Step toward Infrared Nanotomography *ACS Nano* **8** 6911-21
- [135] Zhu J, Hippalgaonkar K, Shen S, Wang K, Abate Y, Lee S, Wu J, Yin X, Majumdar A and Zhang X 2014 Temperature-Gated Thermal Rectifier for Active Heat Flow Control *Nano Letters* **14** 4867-72
- [136] Hillenbrand R, Keilmann F, Hanarp P, Sutherland D S and Aizpurua J 2003 Coherent imaging of nanoscale plasmon patterns with a carbon nanotube optical probe *Applied Physics Letters* **83** 368-70
- [137] Mastel S, Greife S E, Cross G B, Taber A, Dhuey S, Cabrini S, Schuck P J and Abate Y 2012 Real-space mapping of nanoplasmonic hotspots via optical antenna-gap loading *Applied Physics Letters* **101** 131102
- [138] Yamin T, Wissberg S, Cohen H, Cohen-Taguri G and Sharoni A 2016 Ultrathin Films of VO₂ on r-Cut Sapphire Achieved by Postdeposition Etching *ACS Applied Materials & Interfaces* **8** 14863-70
- [139] Lin J, Ji H, Swift M W, Hardy W J, Peng Z, Fan X, Nevidomskyy A H, Tour J M and Natelson D 2014 Hydrogen Diffusion and Stabilization in Single-Crystal VO₂ Micro/Nanobeams by Direct Atomic Hydrogenation *Nano Letters* **14** 5445-51
- [140] Hanlon T J, Coath J A and Richardson M A 2003 Molybdenum-doped vanadium dioxide coatings on glass produced by the aqueous sol-gel method *Thin Solid Films* **436** 269-72
- [141] Lopez R, Haynes T E, Boatner L A, Feldman L C and Haglund R F 2002 Temperature-controlled surface plasmon resonance in VO₂ nanorods *Opt. Lett.* **27** 1327-9
- [142] Kasirga T S, Jim M C, Jae H P and David H C 2016 Visualization of one-dimensional diffusion and spontaneous segregation of hydrogen in single crystals of VO₂ *Nanotechnology* **27** 345708
- [143] Warnick K H, Wang B and Pantelides S T 2014 Hydrogen dynamics and metallic phase stabilization in VO₂ *Applied Physics Letters* **104** 101913
- [144] Baik J M, Kim M H, Larson C, Yavuz C T, Stucky G D, Wodtke A M and Moskovits M 2009 Pd-Sensitized Single Vanadium Oxide Nanowires: Highly Responsive Hydrogen Sensing Based on the Metal-Insulator Transition *Nano Letters* **9** 3980-4

- [145] Yoon H, Choi M, Lim T-W, Kwon H, Ihm K, Kim J K, Choi S-Y and Son J 2016 Reversible phase modulation and hydrogen storage in multivalent VO₂ epitaxial thin films *Nat Mater* **15** 1113-9
- [146] Li N, Tittl A, Yue S, Giessen H, Song C, Ding B and Liu N 2014 DNA-assembled bimetallic plasmonic nanosensors *Light Sci Appl* **3** e226
- [147] Lei D Y, Appavoo K, Sonnefraud Y, Haglund R F and Maier S A 2010 Single-particle plasmon resonance spectroscopy of phase transition in vanadium dioxide *Opt. Lett.* **35** 3988-90
- [148] Lopez R, Feldman L C and Haglund R F 2004 Size-Dependent Optical Properties of VO₂ Nanoparticle Arrays *Physical Review Letters* **93** 177403
- [149] Zhang S, Genov D A, Wang Y, Liu M and Zhang X 2008 Plasmon-Induced Transparency in Metamaterials *Physical Review Letters* **101** 047401
- [150] Liu N, Langguth L, Weiss T, Kastel J, Fleischhauer M, Pfau T and Giessen H 2009 Plasmonic analogue of electromagnetically induced transparency at the Drude damping limit *Nat Mater* **8** 758-62
- [151] Verellen N, Sonnefraud Y, Sobhani H, Hao F, Moshchalkov V V, Dorpe P V, Nordlander P and Maier S A 2009 Fano Resonances in Individual Coherent Plasmonic Nanocavities *Nano Letters* **9** 1663-7
- [152] Ye Z, Zhang S, Wang Y, Park Y-S, Zentgraf T, Bartal G, Yin X and Zhang X 2012 Mapping the near-field dynamics in plasmon-induced transparency *Physical Review B* **86** 155148
- [153] Taubert R, Hentschel M and Giessen H 2013 Plasmonic analog of electromagnetically induced absorption: simulations, experiments, and coupled oscillator analysis *J. Opt. Soc. Am. B* **30** 3123-34
- [154] Luk'yanchuk B, Zheludev N I, Maier S A, Halas N J, Nordlander P, Giessen H and Chong C T 2010 The Fano resonance in plasmonic nanostructures and metamaterials *Nat Mater* **9** 707-15
- [155] Raziman T V and Martin O J F 2016 Does the real part contain all the physical information? *Journal of Optics* **18** 095002
- [156] Wang G, Chen X, Liu S, Wong C and Chu S 2016 Mechanical Chameleon through Dynamic Real-Time Plasmonic Tuning *ACS Nano* **10** 1788-94
- [157] Zufelt K B 2014 Highly efficient infrared photodetectors based on plasmonic metamaterials and vanadium dioxide. In: *Interdisciplinary Materials Science: Vanderbilt University*
- [158] Laboratory L A N 2000 XPS works.

- [159] Yang Y, Kravchenko I I, Briggs D P and Valentine J 2014 All-dielectric metasurface analogue of electromagnetically induced transparency *Nature Communications* **5** 5753
- [160] Coppens Z J, Li W, Walker D G and Valentine J G 2013 Probing and Controlling Photothermal Heat Generation in Plasmonic Nanostructures *Nano Letters* **13** 1023-8
- [161] Volpe G, Noack M, Aćimović S S, Reinhardt C and Quidant R 2012 Near-Field Mapping of Plasmonic Antennas by Multiphoton Absorption in Poly(methyl methacrylate) *Nano Letters* **12** 4864-8
- [162] Jiang H and Gordon R 2013 Nonlinear Plasmonics: Four-photon Near-field Photolithography using Optical Antennas *Plasmonics* **8** 1655-65
- [163] Engerer K 2016 Mapping the Electromagnetic Near Field of Gold Nanoparticles in Poly(methyl) Methacrylate. In: *Interdisciplinary Materials Science*: Vanderbilt University
- [164] Seyfour M M and Binions R 2017 Sol-gel approaches to thermochromic vanadium dioxide coating for smart glazing application *Solar Energy Materials and Solar Cells* **159** 52-65